Recent Advances in Physical Layer Technologies for 5G-Enabled Internet of Things

Lead Guest Editor: Xingwang Li
Guest Editors: Di Zhang, Hien Quoc Ngo, and Carlos T. Calafate

Recent Advances in Physical Layer Technologies for 5G-Enabled Internet of Things

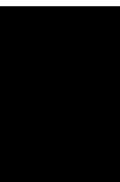# Recent Advances in Physical Layer Technologies for 5G-Enabled Internet of Things

Lead Guest Editor: Xingwang Li
Guest Editors: Di Zhang, Hien Quoc Ngo, and
Carlos T. Calafate

Contents

Research Article

Security Enhancement for Energy Harvesting Cognitive Networks with Relay Selection

Khuong Ho-Van [1,2] **and Thiem Do-Dac** [1,2,3]

[1]*Ho Chi Minh City University of Technology (HCMUT), 268 Ly Thuong Kiet Street, District 10, Ho Chi Minh City, Vietnam*
[2]*Vietnam National University Ho Chi Minh City, Linh Trung Ward, Thu Duc District, Ho Chi Minh City, Vietnam*
[3]*Thu Dau Mot University, 6 Tran Van On Street, Phu Hoa Ward, Thu Dau Mot City, Binh Duong Province, Vietnam*

Correspondence should be addressed to Thiem Do-Dac; thiemdd@tdmu.edu.vn

Relay selection is proposed in this paper as an efficient solution to secure information transmission of secondary users against eavesdroppers in energy harvesting cognitive networks. The proposed relay selection method selects a secondary relay among available secondary relays, which are capable of harvesting radio frequency energy in signals of the secondary transmitter and correctly restore secondary message, to curtail signal-to-noise ratio at the wire-tapper. In order to evaluate the security performance of the suggested relay selection method, an exact intercept outage probability formula accounting for peak transmit power confinement, Rayleigh fading, and interference power confinement is firstly derived. Monte-Carlo simulations are then generated to corroborate the proposed formula. Numerous results expose that positions of relays, the number of relays, and parameters of the energy harvesting method significantly influence the security performance while the power confinements on secondary transmitters cause the performance saturation.

1. Introduction

The explosion of emerging wireless applications, significantly increasing spectrum utilization demand, and green-and-sustainable communication induce energy efficiency and spectral efficiency to become critical design metrics for modern wireless communication networks (e.g., Fifth Generation (5G)) [1–5]. Indeed, one of the 5G system's main use cases is Internet of Things (IoT). IoT finds wide-spread applications in many fields such as electricity, transportation, military, healthcare, public safety, ... A huge number of simultaneously connected devices when deploying IoT will consume an enormous amount of energy [6]. Therefore, it is mandatory to enhance the energy efficiency so as to linger the lifetime of devices and alleviate the energy demand. Furthermore, IoT requires a wide transmission bandwidth to allocate concurrent operation of massive amount of devices. As such, in spectrum scarcity-and-shortage circumstances as nowadays [7], the problem of improving the spectral efficiency needs to be solved. Similar to IoT, meeting the increasing demand

of high speed information transmission and the growing number of mobile users forces the efficient energy-and-spectrum utilization to become a mandatory design requirement for 5G mobile wireless communication systems [8].

The cognitive radio technology is an appropriate and feasible solution to improve the spectral efficiency [9]. Indeed, a cognitive radio network is decomposed into two primary and secondary subnetworks where radio frequencies are solely allotted to primary transmitters in the primary subnetwork. Nonetheless, secondary users (SUs) are also able to access the primary frequency band with interweave, overlay, and underlay mechanisms [10]. As such, the cognitive radio technology considerably enhances the spectral efficiency and overcomes the spectrum shortage problem, better fulfilling the increasing spectrum utilization demand of new wireless applications such as IoT and 5G mobile communication. In the underlay mechanism, SUs are granted access to the licensed spectrum only if SUs bound interference power induced at primary users (PUs) below an endurable threshold. SUs operating in the overlay mechanism utilize

concurrently the licensed spectrum with PUs but information transmission reliability of PUs must be maintained or improved through sophisticated coding methods. Meanwhile, the interweave mechanism solely reserves empty spectrum holes of PUs for SUs' access. Without spectrum sensing implementation for detecting the empty spectrum holes as in the interweave mechanism nor complicated coding methods as in the overlay mechanism, the underlay one is not only simple but also energy-efficient (no extra energy consumption for spectrum sensing or complicated coding). Therefore, the underlay mechanism is investigated in this paper.

Several energy efficiency improving solutions for wireless communications networks have been proposed such as network planning [11], hardware solutions [12], scavenging the energy from available sources (e.g., thermal, radio frequency (RF) powers, solar, wind, ...) [13, 14]. Among these solutions, RF signals based energy harvesting neither depends time-variant energy sources nor requires additional energy harvesting devices (e.g., wind turbines, solar panels). Such advantages which the RF signals based energy harvesting brings make it completely suitable and applicable for small-size mobile devices used in IoT or 5G mobile communication [15]. Therefore, the RF signals based energy harvesting is potential and feasible to supply the energy, prolong the operation time for wireless terminals, and increase the energy efficiency [16]. It can be implemented through Simultaneous Wireless Power and Information Transfer [17–19] or relaying communication [20–22]. Moreover, RF signals based energy harvesting circuits were successfully designed and tested [23, 24].

Energy harvesting cognitive networks (EHCNs) combine two emerging technologies (cognitive radio and RF energy harvesting). Therefore, EHCNs are expected to achieve multiple design criteria of modern wireless communication networks (e.g., 5G), such as high spectral and energy efficiencies [25–27]. However, EHCNs allow both secondary and primary users to utilize the licensed spectrum concurrently. As such, information security in these networks is of great concern. For information security against wire-tappers, physical layer security (PLS) has lately been suggested as a complementary-and-cheap measure to the traditional encryption and cryptographic techniques [28]. Various techniques, such as transmit beam-forming [29], opportunistic scheduling [30], transmit antenna selection [31], jamming [32], on-off transmission [33], and relaying [34], can be applied for PLS. Among them, the relay selection has received considerable attentions because of the following reasons. Firstly, the relay selection achieves higher spectral efficiency than all-relay transmission while the benefits of all-relay transmission, such as diversity order and coding gain, are still maintained for the relay selection [35]. Secondly, the relay selection sustains the secondary transmitter-destination connection through relaying in case that this connection is blocked owing to heavy shadowing or severe fading or the limited transmission range of SUs (It is recalled that the underlay mechanism allocates the transmit power of SUs, which limits the radio coverage of SUs.). Finally, the relay can be selectively-and-purposely chosen in order to not only disrupt the eavesdroppers' signal reception but also enhance the reliability of received signals at the desired desti-

nation. The current paper suggests a relay selection method with the objective of minimizing the overhearing of the eavesdroppers in EHCNs where all relays are self-powered with harvesting radio frequency energy in signals of the secondary transmitter and the transmit powers of all SUs are limited by the peak interference power as well as the peak transmit power.

1.1. Related Works. This subsection solely surveys works pertaining to the relay selection in EHCNs for secure information transmission against eavesdroppers. More specifically, this review relied on notable characteristics (Existing works (e.g., [36–40]), which did not reflect these characteristics, should not be reviewed. For example, [36–38] considered non-cognitive radio networks with energy harvesting; [39, 40] provided the security capability analysis of the relay selection in cognitive radio networks without energy harvesting.) including the relay selection, security performance analysis, the interference power confinement, the energy harvesting, the peak transmit power confinement, the underlay mechanism. Through this survey, our contributions are summarized in successive subsection. Actually, only few works mentioned the relay/path selection in EHCNs for secure information transmission against eavesdroppers. More specifically, the most relevant work is [41] in which the relay selection follows two steps: the successfully decoding set that consists of relays exactly recovering the secondary message is first formed and then the relay (in the successfully decoding set) which creates the largest signal-to-noise ratio (SNR) at the secondary destination is chosen. All secondary relays are self-powered with harvesting radio frequency energy in signals of the secondary transmitter through the time-switching (TS) method [42] where one complete secondary transmitter-to-destination transmission undergoes three phases: energy harvesting at relays, information transmission of the secondary transmitter, and information transmission of the selected relay. Both (peak transmit and interference) power confinements regulate power distribution for the relays and the secondary transmitter. Nevertheless, [41] only provides simulation results on the secrecy outage probability (SOP) of the investigated relay selection in EHCNs. The relatively relevant work is [43] where the path selection, instead of the relay selection as [41], was proposed for multi-hop multi-path EHCNs in which multiple paths, each consisting of multiple hops, connect the secondary transmitter with the secondary destination. Only one path providing the largest SNR is adopted to maintain secondary transmitter-destination connection. In [43], all SUs collect the energy from dedicated beacons through the TS method and their transmit powers are subject to the peak transmit power confinement, the condition that the eavesdropper fails to recover SUs' message, and the interference power confinement. The outage possibility at the secondary destination was analyzed in an accurate closed form under the assumption of all statistically independent end-to-end SNRs of transmission paths. This assumption is not always correct since the transmit power of the secondary transmitter is a common term which appears in all end-to-end SNRs of transmission paths; hence, these end-to-end SNRs are correlated in general.

1.2. Motivation and Contributions. Although the relay selection has several advantages, rare attention has been paid on the relay selection in EHCNs for PLS. This motivates us to further study it in order to have a complete evaluation on many aspects (information security, spectral efficiency, energy efficiency, secondary transmitter-destination connection probability) of EHCNs before practical deployment. This paper reconsiders the system model in [41] but with the below distinctions:

(i) Our paper suggests a different relay selection method in which the chosen relay from the successfully decoding set is the one which minimizes the SNR at the eavesdropper. This prevents the eavesdropper from decoding legitimate information as much as possible

(ii) All relays in this paper harvest the energy with the power splitting (PS) method which differs the TS method in [41].

(iii) This paper analyzes the intercept outage probability (IOP) in an exact form while [41] merely supplied simulation results of the SOP

Our contributions are briefly listed as:

(i) Suggest a relay selection method in EHCNs to hinder the eavesdropper from overhearing as much as possible

(ii) Derive an exact IOP formula for quickly assessing the security measure of the suggested relay selection method in EHCNs under Rayleigh fading channels and the (peak transmit and interference) power confinements

(iii) Prove the existence of optimum key system parameters for the best security performance

(iv) Provide insightful results on the security performance: *i)* IOP is saturated when the peak transmit power of the secondary transmitter is large; *ii)* security performance is significantly enhanced with appropriate selections of relays' positions, information relaying and energy harvesting times, and power partition for energy harvesting and information decoding

1.3. Outline. This paper continues with channel and system models in Part II. Then, Part III derives the IOP in detail. Illustrative results and conclusions are delivered in Part IV and Part V, correspondingly.

1.4. Notations. $c \sim \mathscr{CN}(0, \eta)$ denotes the circularly symmetric complex Gaussian random variable c with η variance and zero mean; $f_{\mathscr{V}}(x)$ and $F_{\mathscr{V}}(x)$ are the probability density function (PDF) and the cumulative distribution function (CDF) of the random variable $\mathscr{V}$, correspondingly; $\Pr\{\mathscr{V}\}$ denotes the possibility of the event $\mathscr{V}$; $\Pr\{\mathscr{V}|\mathscr{M}\}$ is the probability of the event $\mathscr{V}$ conditioned on $\mathscr{M}$; $\binom{n}{k} = n!/k!$
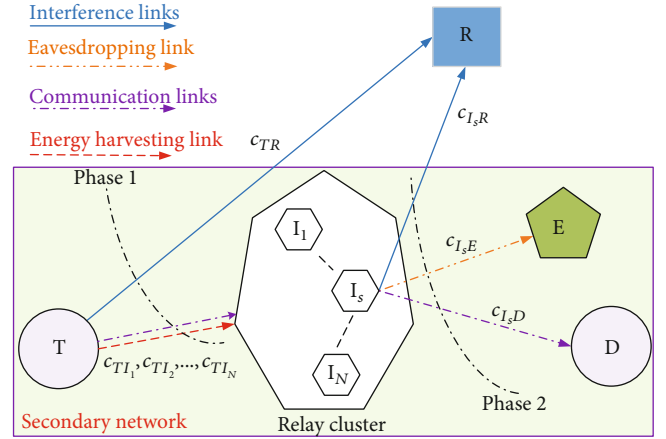
FIGURE 1: System model.

$(n - k)!$ is the binomial coefficient; $\Xi_Y\{\cdot\}$ stands for the expectation with respect to (w.r.t) the random variable Y; $|\mathscr{V}|$ denotes the size of the set $\mathscr{V}$.

2. System and Channel Models

Figure 1 considers the relay selection in EHCNs where the secondary transmitter T communicates the secondary destination D. The secondary message, which is transmitted by T, is illegally extracted by an eavesdropper E. Because of severe fading and heavy shadowing, direct communication between T and D and between T and E may be unavailable. Accordingly, the current paper suggests to choose a relay I_s from a cluster of N relays $(I_1, I_2, ..., I_N)$ between T and D for two purposes: *i)* maintain communication between T and D through relaying; *ii)* limit the eavesdropping of E. For the underlay mechanism under consideration, T and I_r with $r \in [1, N]$ interfere the signal reception at the primary receiver R. This paper assumes (This assumption is commonly accepted in cognitive radio related publications (e.g. [44–46]).) that primary transmitters are far away from D, E and I_r with $r \in [1, N]$ or interferences from primary transmitters are Gaussian-distributed. As such, interferences from primary transmitters are neglected or incorporated into noise terms at corresponding secondary receivers. Moreover, this paper assumes that T is not power-constrained. Therefore, relays with limited power can scavenge the energy in RF signals of T.

In Figure 2(a), β is the time for the secondary message to reach D, which is partitioned into two phases. The Phase 1, which remains $\varepsilon\beta$ where the time splitting ratio is denoted as $\varepsilon \in (0, 1)$, is for T to send the secondary message based on which relays harvest the energy with the power splitting method (e.g., [47, 48]) and decode the secondary message as exposed in Figure 2(b). This method splits the received signal of I_r into two fractions: one fraction $\sqrt{\omega}o_{TI_r}$ for decoding the secondary message (The message decoder is assumed to spend neglected energy. This assumption is popularly accepted in open literature (e.g., [49–55]).) and the other fraction $\sqrt{1 - \omega}o_{TI_r}$ for harvesting the energy, where o_{TI_r} is the received signal of I_r and $\omega \in (0, 1)$ is the power splitting
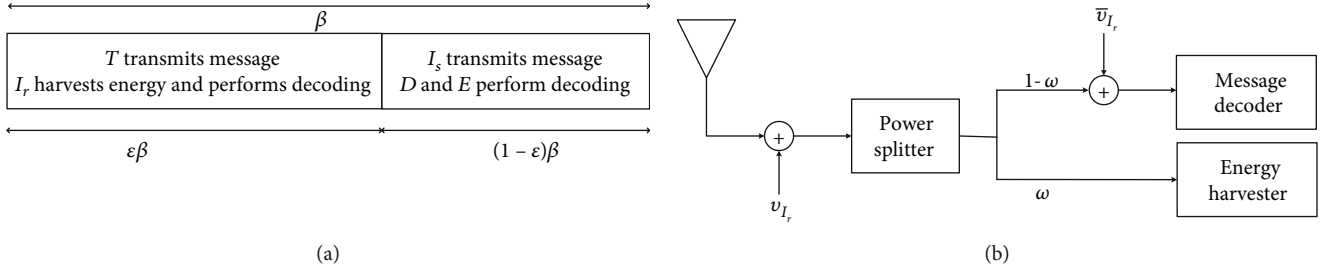
FIGURE 2: Message processing at I_r and phase times. (a) Phase times, (b) Message processing at Ir.

ratio. The Phase 1 ends with the relay selection as follows. First, Δ, which denotes a set of relays that exactly recover the secondary message, is formed. Then, the relay I_s in Δ, which creates the smallest SNR at E, is selected (This paper assumes that each relay can obtain the channel state information (CSI) of channels from and to it (i.e., I_r -E channel, I_r -D channel, and T-I_r channel) such that the SNRs of these channels are available at it [56–58]. Such CSI can be estimated, for example, through the exchange of clear-to-send signal and ready-to-send signal between D and I_r and between T and I_r [59], and through local oscillator power leakage from the wire-tapper's radio frequency front-end [60, 61]. Furthermore, the relay selection method in this paper can be carried out in a distributed manner, for instance, using the timer concept where the relay I_r in Δ sets the value of its timer which is proportional to the SNR of the I_r-E channel. Therefore, the relay whose timer runs out first is selected.). Such a relay selection is to reduce the successful decoding probability of E. The Phase 2, which remains $(1-\varepsilon)\beta$, is for the chosen relay Is to re-encode the decoded secondary message and broadcast the re-encoded message to D and E.

In Figure 1, c_{jk}, $j \in \{T, I_1, I_2, ..., I_N\}$ and $k \in \{I_1, I_2, ..., I_N, E, D, R\}$, signifies the j-k channel coefficient. The current paper models $c_{jk} \sim \mathscr{CN}(0, \eta_{jk})$. Such a model of c_{jk} implies that wireless channels under consideration are Rayleigh-distributed. With incorporating path-loss, η_{jk} is represented as $\eta_{jk} = d_{jk}^{-\zeta}$ where d_{jk} refers the j-k distance and ζ denotes the path-loss exponent. Then, the PDF and the CDF of the channel gain $g_{jk} = |c_{jk}|^2$ are correspondingly expressed as $f_{g_{jk}}(x) = e^{-x/\eta_{jk}}/\eta_{jk}$ and $F_{g_{jk}}(x) = 1 - e^{-x/\eta_{jk}}$, where $x \geq 0$.

The relay I_r receives the following signal in the Phase 1:

$$o_{TI_r} = c_{TI_r}\sqrt{P_T}i_T + v_{I_r}, \tag{1}$$

where i_T is the unit power symbol sent by T, P_T is the transmit power of T, and $v_{I_r} \sim \mathscr{CN}(0, V_{I_r})$ is the receiver noise at I_r. Without loss of generality and for notation simplicity, equal noise variances at relays' receivers are assumed (i.e., $V_{I_r} = V_I, \forall r \in [1, N]$).

The T's transmit power, P_T, must be established in the underlay mechanism as [62].

$$P_T = \min\left(\frac{Q_p}{g_{TR}}, P_p\right), \tag{2}$$

for controlling the interference power induced at R within a bearable level, upper-bounding the transmit power of T by the peak transmit power P_p restricted by hardware implementation, and maximizing the transmission range of T. Here, Q_p is the peak interference power agonized by R.

According to Figure 2(b), I_r harvests the sum energy in the Phase 1 as

$$E_{I_r} = \varphi\omega\left(P_T g_{TI_r} + V_I\right)\varepsilon\beta, \tag{3}$$

where the energy conversion efficiency is $\varphi \in (0, 1)$. Accordingly, the peak power which the relay I_r can transmit signals in the Phase 2 is

$$P_{I_r} = \frac{E_{I_r}}{(1-\varepsilon)\beta} = P_T g_{TI_r}M + L, \tag{4}$$

in which

$$M = \varepsilon\varphi\omega/(1-\varepsilon), \tag{5}$$

$$L = V_I M. \tag{6}$$

Figure 2(b) shows that the input signal of the message decoder of the relay I_r is

$$\bar{o}_{TI_r} = \sqrt{1-\omega}o_{TI_r} + \bar{v}_{I_r}, \tag{7}$$

where $\bar{v}_{I_r} \sim \mathscr{CN}(0, \bar{V}_{I_r})$ is the noise generated by the passband-to-baseband signal conversion. Without loss of generality, equal noise variances at the passband-to-baseband signal converters are assumed (i.e., $\bar{V}_{I_r} = \bar{V}_I, \forall r \in [1, N]$).

Plugging (1) into (7) results in

$$\bar{o}_{TI_r} = \sqrt{(1-\omega)P_T}c_{TI_r}i_T + \sqrt{1-\omega}v_{I_r} + \bar{v}_{I_r}. \tag{8}$$

It is inferred from (8) that the message decoder of the relay I_r obtains the input SNR as

$$\Upsilon_{TI_r} = \frac{P_T g_{TI_r}}{\hat{V}_I}, \tag{9}$$

where

$$\widehat{V}_I = V_I + \frac{\bar{V}_I}{1 - \omega}. \tag{10}$$

The channel capacity that the relay I_r can obtain is $C_{TI_r} = \varepsilon \log_2(1 + \Upsilon_{TI_r})$ bps/Hz where ε preceding the logarithm is because the Phase 1 remains $\varepsilon\beta$. Based on the communication theory, I_r correctly restores the secondary message only if its channel capacity is above the target transmission rate C_t, i.e., $C_{TI_r} \geq C_t$. In other words, i_T is successfully restored at I_r if $\Upsilon_{TI_r} \geq \Upsilon_t$ where $\Upsilon_t = 2^{C_t/\varepsilon} - 1$.

The Phase 1 ends by grouping relays which exactly restore the secondary message into a set Δ as

$$\Delta = \left\{ I_r : Y_{TI_r} \geq Y_t, r \in [1, N] \right\}. \tag{11}$$

Then, the relay in Δ which minimizes the SNR at E is chosen (It is noted that [38] proposed the same relay selection method as ours. Nonetheless, [38] considered the noncognitive scenario while our paper investigated the cognitive scenario. As such, the analysis in our paper differs that in [38].). In other words, the selected relay can be mathematically represented as

$$I_s = \arg \min_{I_r \in \Delta} \Upsilon_{I_r E}, \tag{12}$$

where $\Upsilon_{I_r E}$ is the SNR at E through the $I_r - E$ channel.

Such a relay selection in (12) apparently boosts the IOP at E, improving the security capability.

The Phase 2 is for I_s to broadcast the decoded message i_{I_s}. As such, E receives the signal in the Phase 2 as

$$o_{I_s E} = c_{I_s E} \sqrt{\bar{P}_{I_s}} i_{I_s} + \upsilon_E, \tag{13}$$

in which $\bar{P}_{I_s}$ is the transmit power of I_s and $\upsilon_E \sim \mathscr{CN}(0, V_E)$ is the receiver noise at E.

E obtains the following SNR in the Phase 2, which is computed from (13), as

$$\Upsilon_{I_s E} = \frac{g_{I_s E} \bar{P}_{I_s}}{V_E}. \tag{14}$$

Generally, the SNR at E through the $I_r - E$ channel is derived in a similar manner to (14), i.e.,

$$\Upsilon_{I_r E} = \frac{g_{I_r E} \bar{P}_{I_r}}{V_E}, \tag{15}$$

where the transmit power of I_r is $\bar{P}_{I_r}$.

I_r allocates its transmit power according to the underlay mechanism as

$$\bar{P}_{I_r} = \min \left(\frac{Q_p}{g_{I_r R}}, P_{I_r} \right), \tag{16}$$

which is similar to (2).

The channel capacity at E in the Phase 2 is given by

$$C_{I_s E} = (1 - \varepsilon) \log_2 (1 + \Upsilon_{I_s E}), \tag{17}$$

where $(1 - \varepsilon)$ preceding the logarithm is because the Phase 2 remains $(1 - \varepsilon)\beta$.

3. Intercept Outage Probability Analysis

The IOP is the possibility which the wire-tapper E fails to decode the secondary message. As such, it is a critical performance indicator to assess the security capability of the relay selection in EHCNs. This section proposes an exact IOP formula for quickly measuring the secrecy performance without invoking exhaustive simulations.

The IOP is defined as

$$\Theta = \Pr \left\{ C_{I_s E} \leq C_t \right\}, \tag{18}$$

where C_t is the target transmission rate.

Inserting (17) into (18) results in

$$\Theta = \Pr \left\{ (1 - \varepsilon) \log_2 (1 + \Upsilon_{I_s E}) \leq C_t \right\} = \Pr \left\{ \Upsilon_{I_s E} \leq \Upsilon_e \right\}, \tag{19}$$

where $\Upsilon_e = 2^{C_t/(1-\varepsilon)} - 1$.

It is recalled that I_s is the relay in the set Δ providing the smallest SNR at E. Therefore, $\Upsilon_{I_s E}$ can be represented in terms of $\Upsilon_{I_r E}$ with $I_r \in \Delta$ as

$$\Upsilon_{I_s E} = \min_{I_r \in \Delta} \Upsilon_{I_r E} \tag{20}$$

Additionally, the formation of the set Δ implicitly means that the relays in Δ (i.e., $I_r \in \Delta$) successfully restore the secondary message (i.e., $\Upsilon_{TI_r} \geq \Upsilon_t$) while the relays not in Δ (i.e., $I_k \in \bar{\Delta}$) fail to recover the secondary message (i.e., $\Upsilon_{TI_k} < \Upsilon_t$). By denoting $|\Delta|$ and $|\bar{\Delta}|$ as the sizes of Δ and $\bar{\Delta}$, respectively, it is inferred that $|\Delta| + |\bar{\Delta}| = N$. Therefore, (19) can be explicitly rewritten as

$$\Theta = \Pr \left\{ \min_{I_r \in \Delta} \Upsilon_{I_r E} \leq \Upsilon_e, \bigcap_{I_r \in \Delta} \left\{ \Upsilon_{TI_r} \geq \Upsilon_t \right\}, \bigcap_{I_k \in \bar{\Delta}} \left\{ \Upsilon_{TI_k} < \Upsilon_t \right\} \right\}. \tag{21}$$

Because $|\Delta| = 0$ falls in the range of $[0, N]$, (21) is

further rewritten according to the law of total probability as

$$\Theta = \sum_{|\Delta|=0}^{N} \sum_{\Delta} \Pr\left\{ \min_{I_r \in \Delta} \Upsilon_{I,E} \le \Upsilon_e, \bigcap_{I_r \in \Delta}\{\Upsilon_{TI_r} \ge \Upsilon_t\}, \bigcap_{I_k \in \bar{\Delta}}\{\Upsilon_{TI_k} < \Upsilon_t\} \right\}. \tag{22}$$

Since $|\Delta| = 0$ corresponds to the case which no relay exactly restores the secondary message, the event $\min_{I_r \in \Delta} \Upsilon_{I,E} \le \Upsilon_e$ with $|\Delta| = 0$ always happens with the probability of 1. Therefore, the term in (22) corresponding to $|\Delta| = 0$ can be expressed as

$$\mathcal{R} = \Pr\left\{ \Upsilon_{TI_1} \le \Upsilon_t, \Upsilon_{TI_2} \le \Upsilon_t, \cdots, \Upsilon_{TI_N} \le \Upsilon_t \right\}. \tag{23}$$

Without loss of generality, the current paper assumes that relays are closely located (i.e., $\eta_{TI_r} = \eta_{TI}$, $\eta_{I,D} = \eta_{ID}$, $\eta_{I,R} = \eta_{IR}$, $\eta_{I,E} = \eta_{IE}$, $\forall r \in [1, N]$) for analysis tractability. As such, if $|\Delta| = \mathtt{m}$ is fixed, then $\Pr\{\min_{I_r \in \Delta} \Upsilon_{I,E} \le \Upsilon_e, \bigcap_{I_r \in \Delta}\{\Upsilon_{TI_r} \ge \Upsilon_t\}, \bigcap_{I_k \in \bar{\Delta}}\{\Upsilon_{TI_k} < \Upsilon_t\}\}$ is independent of elements forming the set Δ. Moreover, the total number of sets, each with $|\Delta| = \mathtt{m}$ elements, is $\binom{N}{\mathtt{m}}$. Therefore, (22) is simplified as

$$\begin{aligned}
\Theta &= \mathcal{R} + \sum_{|\Delta|=1}^{N} \binom{N}{|\Delta|} \Pr\left\{ \min_{I_r \in \Delta} \Upsilon_{I,E} \le \Upsilon_e, \bigcap_{I_r \in \Delta}\{\Upsilon_{TI_r} \ge \Upsilon_t\}, \bigcap_{I_k \in \bar{\Delta}}\{\Upsilon_{TI_k} < \Upsilon_t\} \right\} \\
&= \mathcal{R} + \sum_{|\Delta|=1}^{N} \binom{N}{|\Delta|} \underbrace{\Xi_{P_T}\left\{ \underbrace{\Pr\left\{ \min \Upsilon_{I,E} \le \Upsilon_e, \bigcap\{\Upsilon_{TI_r} \ge \Upsilon_t\}, \bigcap\{\Upsilon_{TI_k} < \Upsilon_t\} | P_T \right\}}_{\mathcal{H}} \right\}}_{\mathcal{W}}.
\end{aligned} \tag{24}$$

Now, two terms of (24) are computed to finish the derivation of Θ.

Theorem 1. $\mathcal{R}$ *is expressed in an accurate closed form as*

$$\mathcal{R} = \sum_{l=0}^{N} \binom{N}{l} (-1)^l \left(\frac{1-B}{B} e^{-AB/\eta_{TR}} + e^{-G} \right) \tag{25}$$

where

$$A = \frac{Q_p}{P_p}, \tag{26}$$

$$B = \frac{\eta_{TR} \Upsilon_t \widehat{V}_I l}{\eta_{TI} Q_p} + 1, \tag{27}$$

$$G = \frac{\Upsilon_t \widehat{V}_I l}{\eta_{TI} P_p}. \tag{28}$$

Proof. Please see Appendix A.

Theorem 2. $\mathcal{W}$ *is derived in a precise form as*

$$\mathcal{W} = \int_0^\infty \left[e^{-K|\Delta|/\min\left(\frac{Q_p}{x}, P_p\right)} - \left\{ (S-1)\mathcal{K}\left(U, \min\left(\frac{Q_p}{x}, P_p\right)\right) + \mathcal{K}\left(H, \min\left(\frac{Q_p}{x}, P_p\right)\right) \right\}^{|\Delta|} \right] \\
\times \left(1 - e^{-K/\min\left(\frac{Q_p}{x}, P_p\right)} \right)^{N-|\Delta|} \frac{1}{\eta_{TR}} e^{-x/\eta_{TR}} dx, \tag{29}$$

where $W_{x, y}(z)$ is the Whittaker function [63], eq. (1087.4) built in computational tools (e.g., Mathematica, Matlab) and

$$K = \frac{\Upsilon_t \widehat{V}_I}{\eta_{TI}}, \tag{30}$$

$$U = \frac{\Upsilon_e V_E}{\eta_{IE}} + \frac{Q_p}{\eta_{IR}}, \tag{31}$$

$$S = \frac{Q_p}{\eta_{IR} U}, \tag{32}$$

$$H = \frac{\Upsilon_e V_E}{\eta_{IE}}, \tag{33}$$

$$\mathscr{G}(c, v, b) = \sum_{m=0}^{\infty} \frac{(-vb)^m}{m!b}(cb)^{-m/2} e^{-cb/2} \mathbf{W}_{-m/2,1-m/2}(cb), \tag{34}$$

$$\mathscr{K}(n, P_T) = \frac{e^{L/\eta_{TI}P_T M}}{\eta_{TI}} \mathscr{G}\left(\frac{\Upsilon_t \widehat{V}_I + L/M}{P_T}, \frac{n}{P_T M}, \frac{1}{\eta_{TI}}\right). \tag{35}$$

Proof. Please see Appendix B.

Inserting (25) and (29) into (24), one obtains the exact IOP formula for the proposed relay selection in EHCNs in a single-integral form as

$$\Theta = \mathscr{R} + \sum_{|\Delta|=1}^{N} \binom{N}{|\Delta|} \mathscr{W} \tag{36}$$

It is well-known that the single integral in (36) can be solved by numerical methods available in computational tools (e.g., Matlab, Mathematica). Accordingly, the accurate IOP formula in (36) for the proposed relay selection in EHCNs considering both the (peak transmit and interference) power confinements can be straightforwardly computed, which is useful to promptly measure the secrecy performance without time-consuming simulations. Relied on our understanding, this formula has not been published yet.

4. Results and Discussions

The IOP of the proposed relay selection in EHCNs is evaluated through critical system parameters. For illustration purposes, some specifications are selected as follows: T at (0.0, 0.0), I_r at (d, 0.0), D at (1.0, 0.0), E at (0.9, 0.5), R at (0.4, 0.6), C_t =0.1 bps/Hz, φ = 0.9, $V_E = V_I = \bar{V}_I = N_0$, ζ = 3. In the sequel, "The." means the theoretical result in (36) whereas "Sim." implies the simulated result.

Figure 3 shows the IOP w.r.t P_p/N_0 for ω =0.7, ε =0.6, d =0.4, Q_p/N_0 =15 dB. The results illustrate that the simulation coincides with the theory, verifying the preciseness of (36). Additionally, the IOP decreases with increasing P_p/N_0. This comes from the fact that increasing P_p/N_0 allows the relays to exactly restore the secondary message and to scavenge more radio frequency energy in signals of T, hence increasing the SNR at E in the Phase 2 and reducing the IOP. Nevertheless, the IOP bears the error floor at large P_p/N_0. This error floor is because of the power allocation for secondary transmitters (please recall (2) and (16)) where large values of P_p/N_0 make the transmit powers of T and I_r independent of P_p/N_0 (i.e., large P_p/N_0 neglects the peak transmit power confinement), inducing the constant IOP. Moreover, the IOP is proportional to the number of relays, confirming the effectiveness of the relay selection in improving the secrecy performance.

Figure 4 demonstrates the IOP w.r.t Q_p/N_0, with parameters of Figure 3, excepting P_p/N_0 =10 dB. The results expose that the theory coincides the simulation, again proving the
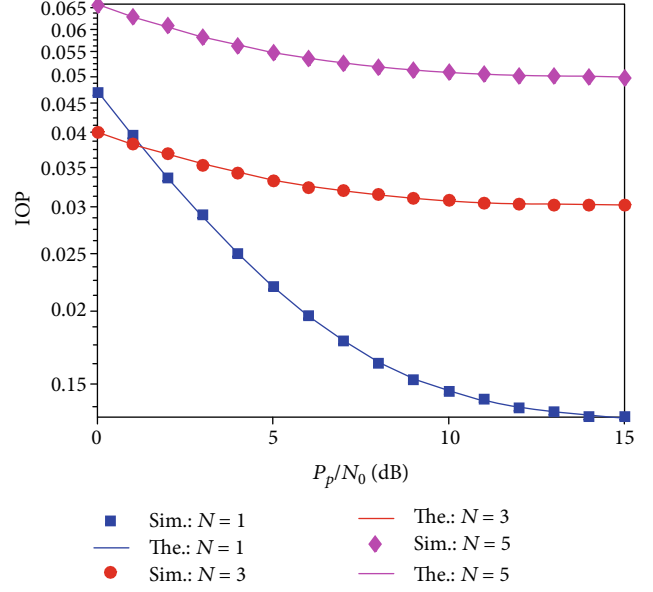
FIGURE 3: IOP w.r.t P_p/N_0.
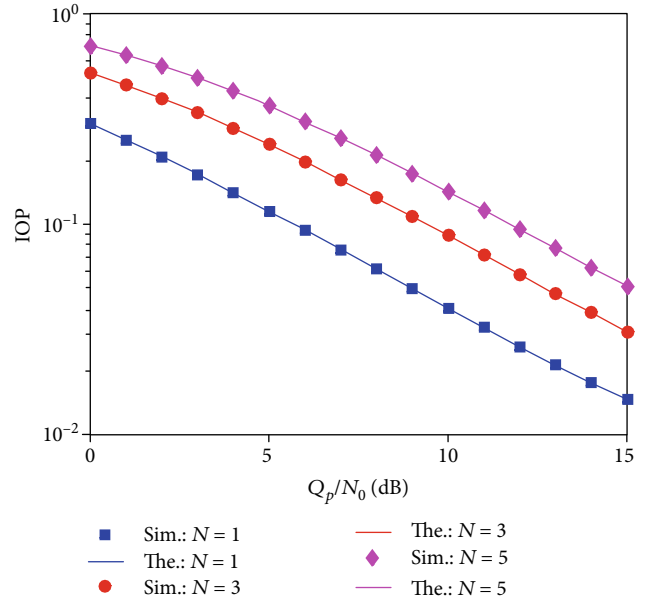
FIGURE 4: IOP w.r.t Q_p/N_0.

validity of (36). Additionally, the IOP declines with Q_p/N_0. This result is comprehended from the power distribution of T and I_r, similarly to Figure 3. Moreover, the IOP increases with the number of relays, showing the importance of the proposed relay selection method in preventing the wiretapper from overhearing the secondary message.

Figure 5 exposes the IOP w.r.t the distance from T to the relay group, with parameters of Figure 4, excepting P_p/N_0 =16 dB and Q_p/N_0 =12 dB. The results prove that the theory agrees with the simulation, again asserting the accuracy of (36). It should be reminded that the intercept outage event happens as the set Δ does not exist (i.e., the relay group is distant from T) or the selected relay I_s in the set Δ cannot

FIGURE 5: IOP w.r.t d.

FIGURE 6: IOP w.r.t ε.

FIGURE 7: IOP w.r.t ω.
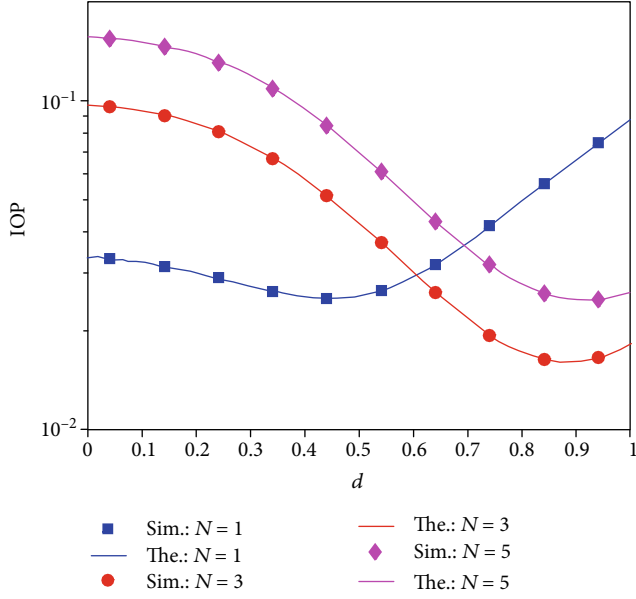
create the sufficient SNR at E (i.e., the relay group is distant from E). As such, the least secured information transmission (i.e., the IOP is minimum) happens when the relay group is located in a convenient position for E to eavesdrop the largest amount of information. This convenient position apparently represents the best compromise between the probability that the set Δ exists and the probability that E can achieve the highest SNR from the selected relay. Figure 5 shows that the least secure information transmission happens at d_{worst} =0.44, 0.88, 0.92 for N=1, 3, 5, respectively. That the d_{worst} is proportional to N can be interpreted as follows: i) The probability that the set Δ exists is higher for the larger value of N; hence, the relay group can be placed more distantly from T (i.e., increase d) as N increases; ii) That the relay group can be placed more distantly from T for the larger value of N induces the selected relay in Δ to be closer to E; hence, the SNR at E is improved and the IOP is reduced. Furthermore, Figure 5 apparently demonstrates the efficacy of the proposed relay selection (i.e., the IOP decreases with increasing N) in EHCNs.

Figure 6 plots the IOP w.r.t the time splitting ratio ε, with parameters of Figure 5, excepting d =0.4. The results expose that the theory coincides with the simulation, asserting the preciseness of (36). Moreover, the secrecy performance is better with the larger number of relays due to having more chances to select the optimum relay. Figure 6 exactly reflects this comment since increasing N induces an increase in the IOP. Furthermore, the time splitting ratio impacts the amount of the harvested energy and the relays' probability of successfully decoding the secondary message in the Phase 1 and the channel capacity at E in the Phase 2. More specifically, increasing ε prolongs the time of the Phase 1; therefore, the relays can scavenge more energy and accurately restore the secondary message with a larger probability. Nonetheless, increasing ε reduces the time of the Phase 2; hence, the channel capacity at E decreases and the IOP increases. Therefore,
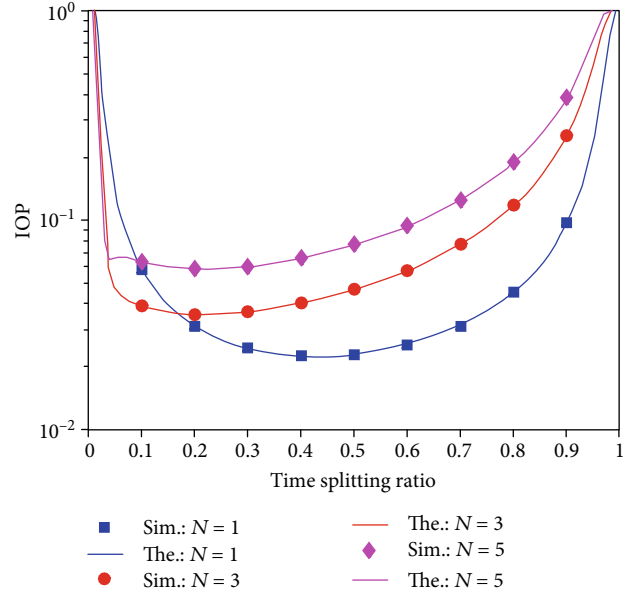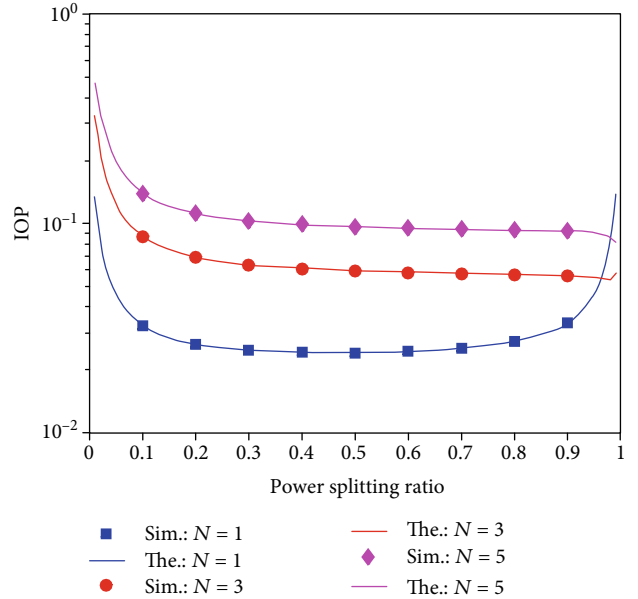
it is expected that there exists a certain value of ε that makes the IOP minimized (equivalently, the worst security performance). Figure 6 apparently illustrates this observation. To be more specific, the minimum IOPs happen at ε_{worst} =0.41, 0.22, 0.21 for N=1, 3, 5, respectively.

Figure 7 exposes the IOP w.r.t the power splitting ratio ω, with parameters of Figure 6, excepting ε =0.6. The results illustrate that the theory coincides the simulation, proving the preciseness of (36). Additionally, the larger number of relays drastically increases the IOP, demonstrating the efficacy of the suggested relay selection in reducing the information eavesdropping of E. Furthermore, turning appropriately the power splitting ratio can avoid the degradation of the

security performance. For example, ω should not be chosen in the range of [0.2, 0.7] for $N=1$ in which the IOP is small (i.e., bad security performance). This is because increasing ω enables the relays to harvest more energy; thus, the relays can produce high SNRs at E, eventually declining the IOP. Nonetheless, increasing ω also decreases the energy reserved for the message decoder, which consequently reduces the size of Δ (i.e., reducing the chance to adopt the optimum relay for minimizing the SNR at E) and increases the IOP. Therefore, appropriate selection of ω can avoid the least secure information transmission (i.e., smallest IOP). In Figure 7, the smallest IOP happens at $\omega = 0.41$ for $N=1$.

5. Conclusion

This paper proposes the relay selection method to improve the information security in energy harvesting cognitive networks against eavesdroppers. The relays are able to harvest radio frequency energy in the signals of the power-unconstrained secondary transmitter and the relay which creates the smallest SNR at the eavesdropper is adopted to decode and forward the secondary message to the secondary destination. The security performance of the proposed relay selection method considering both (peak transmit and interference) power confinements and Rayleigh distribution is quickly measured by the suggested precise IOP formula that is asserted by Monte-Carlo simulations. Multiple results indicate that the positions of the relays and the parameters (power and time splitting ratios) of the energy harvesting method can be properly adjusted to increase the IOP, eventually improving the security performance. Moreover, the IOP experiences the error floor as the transmit power is high.

Appendix

A. Proof of THEOREM 1

$\mathscr{R}$ in (23) is explicitly expressed as

$$\mathscr{R} = \Xi_{P_T} \left\{ \Pr \left\{ \Upsilon_{TI_1} \le \Upsilon_t, \Upsilon_{TI_2} \le \Upsilon_t, \cdots, \Upsilon_{TI_N} \le \Upsilon_t | P_T \right\} \right\}. \quad (A.1)$$

Conditioned on P_T, the events $\{ \Upsilon_{TI_r} \le \Upsilon_t \}$ with $r \in [1, N]$ are uncorrelated. Additionally, that relays are closely located induces $\Pr \{ \Upsilon_{TI_1} \le \Upsilon_t | P_T \} = \Pr \{ \Upsilon_{TI_2} \le \Upsilon_t | P_T \} = \cdots = \Pr \{ \Upsilon_{TI_N} \le \Upsilon_t | P_T \} = \mathscr{Z}$. Equivalently, $\Pr \{ \Upsilon_{TI_r} \le \Upsilon_t | P_T \}$ is the same for any relay I_r. Therefore, (A.1) is simplified as

$$\mathscr{R} = \Xi_{P_T} \left\{ \underbrace{\left(\Pr \left\{ \Upsilon_{TI_r} \le \Upsilon_t | P_T \right\} \right)}_{\mathscr{Z}}^N \right\}. \quad (A.2)$$

Using (9), one can rewrite $\mathscr{Z}$ as

$$\mathscr{Z} = \Pr \left\{ \frac{P_T g_{TI_r}}{\widehat{V}_I} \le \Upsilon_t \bigg| P_T \right\}. \quad (A.3)$$

It is recalled that $\eta_{TI_r} = \Xi_{g_{TI_r}} \{ g_{TI_r} \} = \eta_{TI}$. Therefore, (A.3) is further simplified as

$$\mathscr{Z} = \Pr \left\{ g_{TI_r} \le \frac{\Upsilon_t \widehat{V}_I}{P_T} \right\} = 1 - e^{-\Upsilon_t V \wedge_I / P_T \eta_{TI}}. \quad (A.4)$$

Inserting (A.4) into (A.2) and using $P_T = \min((Q_p / g_{TR}), P_p)$ in (2), the expectation with respect to P_T is solved as

$$\begin{aligned}
\mathscr{R} &= \Xi_{P_T} \left\{ \left(1 - e^{-\Upsilon_t V \wedge_I / P_T \eta_{TI}} \right)^N \right\} \\
&= \sum_{l=0}^{N} \binom{N}{l} (-1)^l \Xi_{P_T} \left\{ e^{-\Upsilon_t V \wedge_I l / P_T \eta_{TI}} \right\} \\
&= \sum_{l=0}^{N} \binom{N}{l} (-1)^l \left(\int_{Q_p / P_p}^{\infty} e^{-\Upsilon_t V \wedge_I l / \eta_{TI} Q_p x} \frac{1}{\eta_{TR}} e^{-x / \eta_{TR}} dx \right. \\
&\quad \left. + \int_0^{Q_p / P_p} e^{-\Upsilon_t V \wedge_I l / \eta_{TI} P_p} \frac{1}{\eta_{TR}} e^{-x / \eta_{TR}} dx \right)
\end{aligned} \quad (A.5)$$

The above integrals are straightforwardly computed; hence, $\mathscr{R}$ in (A.5) exactly matches (25) after using new notations in (26), (27), (28). This finishes the proof.

B. Proof of THEOREM 2

Conditioned on P_T, the event $\{ \min_{I_r \in \Delta} \Upsilon_{I,E} \le \Upsilon_e, \bigcap_{I_r \in \Delta} \{ \Upsilon_{TI_r} \ge \Upsilon_t \} \}$ is independent of the event $\{ \bigcap_{I_k \in \bar{\Delta}} \{ \Upsilon_{TI_k} < \Upsilon_t \} \}$. Therefore, the term $\mathscr{H}$ in $\mathscr{W}$ is decomposed as

$$\mathscr{H} = \underbrace{\Pr \left\{ \min \Upsilon_{I,E} \le \Upsilon_e, \cap \{ \Upsilon_{TI_r} \ge \Upsilon_t \} | P_T \right\}}_{\mathscr{H}_1} \underbrace{\Pr \left\{ \cap \{ \Upsilon_{TI_k} < \Upsilon_t \} | P_T \right\}}_{\mathscr{H}_2}. \quad (B.1)$$

The term $\mathscr{H}_2$ can be derived in the same way as $\mathscr{R}$, resulting in

$$\begin{aligned}
\mathscr{H}_2 &= \left(\underbrace{\Pr \left\{ \Upsilon_{TI_k} < \Upsilon_t | P_T \right\}}_{\mathscr{Z}} \right)^{|\bar{\Delta}|} \\
&= \left(1 - e^{-\Upsilon_t V \wedge_I / P_T \eta_{TI}} \right)^{|\bar{\Delta}|} = \left(1 - e^{-\Upsilon_t V \wedge_I / P_T \eta_{TI}} \right)^{N - |\Delta|}.
\end{aligned} \quad (B.2)$$

$\Upsilon_{I,E}$ correlates Υ_{TI_r} because g_{TI_r} is their common term. Therefore, the term $\mathscr{H}_1$ must be rewritten in terms of

conditional probabilities as

$$
\begin{aligned}
\mathcal{H}_1 &= \Xi_{\{g_{TI_r}\}_{I_r \in \Delta}} \left\{ \Pr\left\{ \min_{I_r \in \Delta} \Upsilon_{I,E} \leq \Upsilon_e, \bigcap_{I_r \in \Delta}\{\Upsilon_{TI_r} \geq \Upsilon_t\} \middle| P_T, \{g_{TI_r}\}_{I_r \in \Delta} \right\} \right\} \\
&= \Xi_{\{g_{TI_r}\}_{I_r \in \Delta}} \left\{ \Pr\left\{ \min_{I_r \in \Delta} \Upsilon_{I,E} \leq \Upsilon_e \middle| P_T, \left\{g_{TI_r} \geq \frac{\Upsilon_t \widehat{V}_I}{P_T}\right\}_{I_r \in \Delta} \right\} \right\} \\
&= \Xi_{\{g_{TI_r}\}_{I_r \in \Delta}} \left\{ 1 - \Pr\left\{ \min_{I_r \in \Delta} \Upsilon_{I,E} > \Upsilon_e \middle| P_T, \left\{g_{TI_r} \geq \frac{\Upsilon_t \widehat{V}_I}{P_T}\right\}_{I_r \in \Delta} \right\} \right\} \\
&= \Xi_{\{g_{TI_r}\}_{I_r \in \Delta}}\{1\} - \Xi_{\{g_{TI_r}\}_{I_r \in \Delta}} \left\{ \prod_{I_r \in \Delta} \Pr\left\{ \Upsilon_{I,E} > \Upsilon_e \middle| P_T, g_{TI_r} \geq \frac{\Upsilon_t \widehat{V}_I}{P_T} \right\} \right\} \\
&= \Xi_{\{g_{TI_r}\}_{I_r \in \Delta}}\{1\} - \prod_{I_r \in \Delta} \Xi_{g_{TI_r}} \left\{ \Pr\left\{ \Upsilon_{I,E} > \Upsilon_e \middle| P_T, g_{TI_r} \geq \frac{\Upsilon_t \widehat{V}_I}{P_T} \right\} \right\} \\
&= \underbrace{\Xi_{\{g_{TI_r}\}_{I_r \in \Delta}}\{1\}}_{\widetilde{\mathcal{H}}_1} - \left(\underbrace{\Xi_{g_{TI_r}} \left\{ \underbrace{\Pr\left\{ \Upsilon_{I,E} > \Upsilon_e \middle| P_T, g_{TI_r} \geq \frac{\Upsilon_t V \wedge_I}{P_T} \right\}}_{\mathcal{I}} \right\}}_{\bar{\mathcal{H}}_1} \right)^{|\Delta|}.
\end{aligned}
\tag{B.3}
$$

The term $\widetilde{\mathcal{H}}_1$ is straightforwardly inferred as

$$
\begin{aligned}
\widetilde{\mathcal{H}}_1 &= \prod_{I_r \in \Delta} \Xi_{g_{TI_r}} \left\{ 1 \middle| g_{TI_r} \geq \frac{\Upsilon_t \widehat{V}_I}{P_T} \right\} \\
&= \prod_{I_r \in \Delta} \int_{\Upsilon_t \widehat{V}_I/P_T}^{\infty} f_{g_{TI_r}}(x) dx = \left(e^{-\Upsilon_t V \wedge_I/P_T \eta_{TI}} \right)^{|\Delta|} \\
&= e^{-\Upsilon_t V \wedge_I |\Delta|/P_T \eta_{TI}}.
\end{aligned}
\tag{B.4}
$$

In order to compute $\bar{\mathcal{H}}_1$, the term $\mathcal{I}$ is firstly derived after inserting the explicit form of $\Upsilon_{I,E}$ in (15) into (B.3) as

$$
\begin{aligned}
\mathcal{I} &= \Pr\left\{ \Upsilon_{I,E} > \Upsilon_e \middle| P_T, g_{TI_r} \geq \frac{\Upsilon_t \widehat{V}_I}{P_T} \right\} \\
&= \Pr\left\{ \frac{g_{I_r E} \bar{P}_{I_r}}{V_E} > \Upsilon_e \middle| P_T, g_{TI_r} \geq \frac{\Upsilon_t \widehat{V}_I}{P_T} \right\} \\
&= \Xi_{\bar{P}_{I_r}} \left\{ e^{-\Upsilon_e V_E/\bar{P}_{I_r}\eta_{IE}} \middle| P_T, g_{TI_r} \geq \frac{\Upsilon_t \widehat{V}_I}{P_T} \right\}.
\end{aligned}
\tag{B.5}
$$

Plugging (16) into (B.5), the compact form of $\mathcal{I}$ is obtained as

$$
\begin{aligned}
\mathcal{I} &= \Xi_{g_{I_r R}} \left\{ e^{-\Upsilon_e V_E/\eta_{IE} \min\left(\frac{Q_p}{g_{I_r R}}, P_{I_r}\right)} \middle| P_T, g_{TI_r} \geq \frac{\Upsilon_t \widehat{V}_I}{P_T} \right\} \\
&= \int_{Q_p/P_{I_r}}^{\infty} e^{-\Upsilon_e V_E/\eta_{IE} Q_p x} \frac{1}{\eta_{IR}} e^{-x/\eta_{IR}} dx \\
&\quad + \int_0^{Q_p/P_{I_r}} e^{-\Upsilon_e V_E/\eta_{IE} P_{I_r}} \frac{1}{\eta_{IR}} e^{-x/\eta_{IR}} dx = (S-1) e^{-U/P_{I_r}} \\
&\quad + e^{-H/P_{I_r}},
\end{aligned}
\tag{B.6}
$$

where U, S, and H are given in (31), (32), and (33), correspondingly.

Inserting (B.6) into $\bar{\mathcal{H}}_1$ results in

$$
\begin{aligned}
\bar{\mathcal{H}}_1 &= (S-1) \underbrace{\Xi_{g_{TI_r}} \left\{ e^{-U/P_{I_r}} \middle| P_T, g_{TI_r} \geq \frac{\Upsilon_t \widehat{V}_I}{P_T} \right\}}_{\mathcal{K}(U, P_T)} \\
&\quad + \underbrace{\Xi_{g_{TI_r}} \left\{ e^{-H/P_{I_r}} \middle| P_T, g_{TI_r} \geq \frac{\Upsilon_t \widehat{V}_I}{P_T} \right\}}_{\mathcal{K}(U, P_T)}.
\end{aligned}
\tag{B.7}
$$

Given P_{I_r} in (4), the function $\mathcal{K}(n, P_T)$ is simplified as

$$
\begin{aligned}
\mathcal{K}(n, P_T) &= \Xi_{g_{TI_r}} \left\{ e^{-n/P_T g_{TI_r} M + L} \middle| P_T, g_{TI_r} \geq \frac{\Upsilon_t \widehat{V}_I}{P_T} \right\} \\
&= \int_{\Upsilon_t \widehat{V}_I/P_T}^{\infty} e^{-n/P_T M x + L} \frac{1}{\eta_{TI}} e^{-x/\eta_{TI}} dx.
\end{aligned}
\tag{B.8}
$$

By the variable change $y = x + (L/P_T M)$, one rewrites $\mathcal{K}(n, P_T)$ as

$$
\mathcal{K}(n, P_T) = \frac{e^{L/\eta_{TI} P_T M}}{\eta_{TI}} \int_{(\Upsilon_t \widehat{V}_I + L/M)/P_T}^{\infty} e^{-\frac{n}{P_T M}/y - y/\eta_{TI}} dy.
\tag{B.9}
$$

By defining

$$
\mathcal{G}(c, v, b) = \int_c^{\infty} e^{-v/y - by} dy,
\tag{B.10}
$$

it is apparent that (B.9) coincides (35). Accordingly, the proof continues with showing that the function $\mathcal{G}(c, v, b)$ is presented in the precise closed form as (34). Toward this end, one applies the series expansion to $e^{-b/y}$, which results in

$$
\mathcal{G}(c, v, b) = \int_c^{\infty} \left[\sum_{m=0}^{\infty} \frac{1}{m!} \left(-\frac{v}{y}\right)^m \right] e^{-by} dy = \sum_{m=0}^{\infty} \frac{(-v)^m}{m!} \int_c^{\infty} \frac{e^{-by}}{y^m} dy.
\tag{B.11}
$$

By the variable change $x = by$, one rewrites $\mathcal{G}(c, v, b)$ as

$$
\mathcal{G}(c, v, b) = \sum_{m=0}^{\infty} \frac{(-vb)^m}{m!b} \int_{cb}^{\infty} \frac{e^{-x}}{x^m} dx.
\tag{B.12}
$$

With the help of [63], eq. (3.381.6), the last integral in (B.12) is expressed in closed-form in terms of the Whittaker function; hence, (B.12) exactly matches (34).

Plugging (B.4) and (B.7) into (B.3) and then inserting the result together with (B.2) into (B.1), one achieves

$$
\begin{aligned}
\mathcal{H} &= \left[e^{-\Upsilon_t V \wedge_I |\Delta|/P_T \eta_{TI}} - \{(S-1)\mathcal{K}(U, P_T) + \mathcal{K}(H, P_T)\}^{|\Delta|} \right] \\
&\quad \cdot \left(1 - e^{-\Upsilon_t V \wedge_I/P_T \eta_{TI}} \right)^{N - |\Delta|}.
\end{aligned}
\tag{B.13}
$$

Because $\mathscr{W} = \Xi_{P_T}\{\mathscr{H}\}$ and $P_T = \min\left((Q_p/g_{TR}), P_p\right)$, by replacing P_T with $\min\left((Q_p/g_{TR}), P_p\right)$ in the formula of $\mathscr{H}$ and averaging $\mathscr{H}$ over the random variable g_{TR}, one obtains the single-integral formula of $\mathscr{W}$ as (29). As such, the proof is completed.

Data Availability

The authors declare that all data used to support the findings of this study are included within the article.

Conflicts of Interest

The authors declare that they have no conflicts of interest.

Acknowledgments

References

[1] W. S. H. M. W. Ahmad, N. A. M. Radzi, F. S. Samidi et al., "5G Technology: Towards Dynamic Spectrum Sharing Using Cognitive Radio Networks," *IEEE Access*, vol. 8, pp. 14460–14488, 2020.

[2] A. Alqasir and A. E. Kamal, "Cooperative Small Cell HetNets with Dynamic Sleeping and Energy Harvesting," *IEEE Transactions on Green Communications and Networking*, p. 1, 2020.

[3] K. Shafique, B. A. Khawaja, F. Sabir, S. Qazi, and M. Mustaqim, "Internet of things (IoT) for next-generation smart systems: a review of current challenges, future trends and prospects for emerging 5G-IoT scenarios," *IEEE Access*, vol. 8, pp. 23022–23040, 2020.

[4] M. J. Sobouti, Z. Rahimi, A. H. Mohajerzadeh et al., "Efficient deployment of small Cell Base stations mounted on unmanned aerial vehicles for the internet of things infrastructure," *IEEE Sensors Journal*, vol. 20, no. 13, pp. 7460–7471, 2020.

[5] Y. Dai and L. Lyu, "NOMA-Enabled CoMP clustering and power control for green internet of things networks," *IEEE Access*, vol. 8, pp. 90109–90117, 2020.

[6] F. Benkhelifa, H. ElSawy, J. A. Mccann, and M. Alouini, "Recycling cellular energy for self-sustainable IoT networks: a spatiotemporal study," *IEEE Transactions on Wireless Communications*, vol. 19, no. 4, pp. 2699–2712, 2020.

[7] FCC, *Spectrum policy task force report*, ET Docket 02–135, 2002.

[8] M. Polese, M. Giordani, T. Zugno et al., "Integrated access and backhaul in 5G mmWave networks: potential and challenges," *IEEE Communications Magazine*, vol. 58, no. 3, pp. 62–68, 2020.

[9] I. Dey, D. Ciuonzo, and P. S. Rossi, "Wideband Collaborative Spectrum Sensing using Massive MIMO Decision Fusion," *IEEE Transactions on Wireless Communications*, p. 1, 2020.

[10] L. Ge, G. Chen, Y. Zhang, J. Tang, J. Wang, and J. A. Chambers, "Performance analysis for multihop cognitive radio networks with energy harvesting by using stochastic geometry," *IEEE Internet of Things Journal*, vol. 7, no. 2, pp. 1154–1163, 2020.

[11] S. Buzzi, I. Chih-Lin, T. E. Klein, H. V. Poor, C. Yang, and A. Zappone, "A Survey of Energy-Efficient Techniques for 5G Networks and Challenges Ahead," *IEEE Journal on Selected Areas in Communications*, vol. 34, no. 4, pp. 697–709, 2016.

[12] D. Feng, C. Jiang, G. Lim, L. J. Cimini, G. Feng, and G. Y. Li, "A survey of energy-efficient wireless communications," *IEEE Communications Surveys & Tutorials*, vol. 15, no. 1, pp. 167–178, 2013.

[13] A. Celik, A. Alsharoa, and A. E. Kamal, "Hybrid Energy Harvesting Cooperative Spectrum Sensing in Heterogeneous CRNs," in *2016 IEEE Globecom Workshops (GC Wkshps)*, vol. 4–8, pp. 1–6, Washington DC, USA, 2017.

[14] X. Lu, P. Wang, D. Niyato, D. I. Kim, and Z. Han, "Wireless networks with RF energy harvesting: a contemporary survey," *IEEE Communications Surveys & Tutorials*, vol. 17, no. 2, pp. 757–789, 2015.

[15] L. Xu, W. Yin, X. Zhang, and Y. Yang, "Fairness-Aware Throughput Maximization over Cognitive Heterogeneous NOMA Networks for Industrial Cognitive IoT," *IEEE Transactions on Communications*, p. 1, 2020.

[16] G. Xu, C. Yang, J. Wu, and C. Chang, "Harvesting electromagnetic energy in air: a wireless energy harvester at 2.45 GHz using inexpensive materials," *IEEE Microwave Magazine*, vol. 21, no. 6, pp. 88–95, 2020.

[17] F. Zhou, Z. Li, J. Cheng, Q. Li, and J. Si, "Robust AN-aided Beamforming and power splitting Design for Secure MISO cognitive radio with SWIPT," *IEEE Transactions on Wireless Communications*, vol. 16, no. 4, pp. 2450–2464, 2017.

[18] G. Pan, H. Lei, Y. Yuan, and Z. Ding, "Performance analysis and optimization for SWIPT wireless sensor networks," *IEEE Transactions on Communications*, vol. 65, no. 5, pp. 2291–2302, 2017.

[19] T. Liu, X. Wang, and L. Zheng, "A cooperative SWIPT scheme for wirelessly powered sensor networks," *IEEE Transactions on Communications*, vol. 65, no. 6, pp. 2740–2752, 2017.

[20] H. Ding, D. B. da Costa, H. A. Suraweera, and J. Ge, "Role Selection Cooperative Systems With Energy Harvesting Relays," *IEEE Transactions on Wireless Communications*, vol. 15, no. 6, pp. 4218–4233, 2016.

[21] Y. Gu and S. Aissa, "RF-Based energy harvesting in decode-and-forward relaying systems: Ergodic and outage capacities," *IEEE Transactions on Wireless Communications*, vol. 14, no. 11, pp. 6425–6434, 2015.

[22] A. Rajaram, D. N. K. Jayakody, K. Srinivasan, B. Chen, and V. Sharma, "Opportunistic-Harvesting: RF wireless power transfer scheme for multiple access relays system," *IEEE Access*, vol. 5, pp. 16084–16099, 2017.

[23] A. Hamani, B. Allard, T.-P. Vuong, M. C. E. Yagoub, and R. Touhami, "Design of Rectenna Series-association Circuits for radio frequency energy harvesting in CMOS FD-SOI 28 nm," *IET Circuits, Devices & Systems*, vol. 12, no. 1, pp. 40–49, 2018.

[24] K. Janghel and S. Prakriya, "Performance of secondary network with primary Beamforming-assisted energy harvesting transmitters," *IEEE Transactions on Vehicular Technology*, vol. 66, no. 10, pp. 8895–8909, 2017.

[25] M. R. Amini and M. W. Baidas, "Availability-Reliability-Stability trade-offs in ultra-reliable energy-harvesting cognitive radio IoT networks," *IEEE Access*, vol. 8, pp. 82890–82916, 2020.

[26] M. Babaei, U. Aygolu, M. Basaran, and L. Durak-Ata, "BER Performance of Full-Duplex Cognitive Radio Network with

Nonlinear Energy Harvesting," *IEEE Transactions on Green Communications and Networking*, vol. 4, no. 2, pp. 448–460, 2020.

[27] A. Paul and S. P. Maity, "Outage analysis in cognitive radio networks with energy harvesting and Q-routing," *IEEE Transactions on Vehicular Technology*, vol. 69, no. 6, pp. 6755–6765, 2020.

[28] M. Hayashi and A. Vazquez-Castro, "Two-Way Physical Layer Security Protocol for Gaussian Channels," *IEEE Transactions on Communications*, vol. 68, no. 5, pp. 3068–3078, 2020.

[29] F. Zhu and M. Yao, "Improving Physical-Layer security for CRNs using SINR-based cooperative Beamforming," *IEEE Transactions on Vehicular Technology*, vol. 65, no. 3, pp. 1835–1841, 2016.

[30] I. Krikidis and B. Ottersten, "Secrecy sum-rate for orthogonal random Beamforming with opportunistic scheduling," *IEEE Signal Processing Letters*, vol. 20, no. 2, pp. 141–144, 2013.

[31] S. Yan, N. Yang, R. Malaney, and J. Yuan, "Transmit antenna selection with Alamouti coding and power allocation in MIMO wiretap channels," *IEEE Transactions on Wireless Communications*, vol. 13, no. 3, pp. 1656–1667, 2014.

[32] I. Krikidis, J. Thompson, and S. Mclaughlin, "Relay selection for secure cooperative networks with jamming," *IEEE Transactions on Wireless Communications*, vol. 8, no. 10, pp. 5003–5011, 2009.

[33] B. He and X. Zhou, "Secure on-off transmission design with channel estimation errors," *IEEE Transactions on Information Forensics and Security*, vol. 8, no. 12, pp. 1923–1936, 2013.

[34] J.-H. Lee, "Full-duplex relay for enhancing physical layer security in multi-hop relaying systems," *IEEE Communications Letters*, vol. 19, no. 4, pp. 525–528, 2015.

[35] K. Ho-Van, "Outage analysis in cooperative cognitive networks with opportunistic relay selection under Imperfect Channel information," *AEU - International Journal of Electronics and Communications*, vol. 69, no. 11, pp. 1700–1708, 2015.

[36] H. T. Nguyen, S. Q. Nguyen, and W.-J. Hwang, "Performance Analysis of Energy Harvesting Relay Systems under Unreliable Backhaul Connections," *IET Communications*, vol. 12, no. 15, pp. 1763–1770, 2018.

[37] C. Yin, H. T. Nguyen, C. Kundu, Z. Kaleem, E. Garcia-Palacios, and T. Q. Duong, "Secure Energy Harvesting Relay Networks with Unreliable Backhaul Connections," *IEEE Access*, vol. 6, pp. 12074–12084, 2018.

[38] H. T. Nguyen, J. Zhang, N. Yang, T. Q. Duong, and W.-J. Hwang, "Secure Cooperative Single Carrier Systems under Unreliable Backhaul and Dense Networks Impact," *IEEE Access*, vol. 5, pp. 18310–18324, 2017.

[39] K. Ho-Van and T. Do-Dac, "Analysis of security performance of relay selection in underlay cognitive networks," *IET Communications*, vol. 12, no. 1, pp. 102–108, 2018.

[40] K. Ho-Van, T. Do-Dac, N. Pham-Thi-Dan et al., "Improving Information Security in Cognitive Radio Networks with Relay Selection," in *Proc. ISEE*, vol. 29-30, pp. 274–279, HCM City, Vietnam, 2017.

[41] P. Maji, B. Prasad, S. D. Roy, and S. Kundu, "Secrecy outage of a cognitive radio network with selection of energy harvesting relay and imperfect CSI," *Wireless Personal Communications*, vol. 100, no. 2, pp. 571–586, 2018.

[42] F. Benkhelifa and M. S. Alouini, "A Thresholding-based Antenna Switching in MIMO Cognitive Radio Networks with SWIPT-enabled Secondary Receiver," in *2017 IEEE Interna-

tional Conference on Communications (ICC)*, vol. 21–25, pp. 1–6, Paris, France, May 2017.

[43] T. D. Hieu, T. T. Duy, and S. G. Choi, "Performance Enhancement for Harvest-to-Transmit Cognitive Multi-hop Networks with Best Path Selection Method under Presence of Eavesdropper," in *Proc. IEEE ICACT, GW*, vol. 11–14, pp. 323–328, Korea, February 2018.

[44] X. Zhang, J. Xing, Z. Yan, Y. Gao, and W. Wang, "Outage Performance Study of Cognitive Relay Networks with Imperfect Channel Knowledge," *IEEE Communications Letters*, vol. 17, no. 1, pp. 27–30, 2013.

[45] M. Seyfi, S. Muhaidat, and J. Liang, "Relay selection in cognitive radio networks with interference constraints," *IET Communications*, vol. 7, no. 10, pp. 922–930, 2013.

[46] K. Ho-Van, "Influence of channel information imperfection on outage probability of cooperative cognitive networks with partial relay selection," *Wireless Personal Communications*, vol. 94, no. 4, pp. 3285–3302, 2017.

[47] X. Zhou, R. Zhang, and C. K. Ho, "Wireless information and power transfer: architecture design and rate-energy tradeoff," *IEEE Transactions on Communications*, vol. 61, no. 11, pp. 4754–4767, 2013.

[48] A. A. Nasir, X. Zhou, S. Durrani, and R. A. Kennedy, "Relaying protocols for wireless energy harvesting and information processing," *IEEE Transactions on Wireless Communications*, vol. 12, no. 7, pp. 3622–3636, 2013.

[49] P. M. Quang, T. T. Duy, and V. N. Q. Bao, "Performance Evaluation of Underlay Cognitive Radio Networks over Nakagami-m fading Channels with Eenergy Harvesting," in *Proc. IEEE ATC*, vol. 10–12, pp. 108–113, HaNoi, Vietnam, October 2016.

[50] J. Zhang, G. Pan, and H. M. Wang, "On physical-layer security in underlay cognitive radio networks with full-duplex wireless-powered secondary system," *IEEE Access*, vol. 4, pp. 3887–3893, 2016.

[51] W. Mou, W. Yang, X. Xu, X. Li, and Y. Cai, "Secure Transmission in Spectrum-Sharing Cognitive Networks with Wireless Power Transfer," in *Proc. IEEE WCSP*, vol. 13–15, pp. 1–5, JiangSu, China, October 2016.

[52] H. Lei, M. Xu, H. Zhang, G. Pan, I. S. Ansari, and K. A. Qaraqe, "Secrecy Outage Performance for Underlay MIMO CRNs with Energy Harvesting and Transmit Antenna Selection," in *Proc. IEEE Globecom*, vol. 4–8, pp. 1–6, Washington DC, USA, December 2016.

[53] A. Singh, M. R. Bhatnagar, and R. K. Mallik, "Secrecy outage of a simultaneous wireless information and power transfer cognitive radio system," *IEEE Wireless Communications Letters*, vol. 5, no. 3, pp. 288–291, 2016.

[54] Y. Liu, L. Wang, S. A. R. Zaidi, M. Elkashlan, and T. Q. Duong, "Secure D2D communication in large-scale cognitive cellular networks: a wireless power transfer model," *IEEE Transactions on Communications*, vol. 64, no. 1, pp. 329–342, 2016.

[55] S. Raghuwanshi, P. Maji, S. D. Roy, and S. Kundu, "Secrecy Performance Of a Dual Hop Cognitive Relay Network with an Energy Harvesting Relay," in *Proc. IEEE ICACCI*, vol. 21–24, pp. 1622–1627, Jaipur, India, September 2016.

[56] R. Su, Y. Wang, and R. Sun, "Destination-Assisted Jamming for Physical-Layer Security in SWIPT Cognitive Radio Systems," in *Proc. IEEE WCNC*, vol. 15-18, pp. 1–6, Barcelona, Spain, April 2018.

[57] H. Lei, M. Xu, I. S. Ansari, G. Pan, K. A. Qaraqe, and M.-S. Alouini, "On secure underlay MIMO cognitive radio

networks with energy harvesting and transmit antenna selection," *IEEE Transactions on Green Communications and Networking,* vol. 1, no. 2, pp. 192–203, 2017.

[58] Z. Ning, L. Ning, C. Nan, J. W. Mark, and S. Xuemin, "Cooperative Networking towards Secure Communications for CRNs," in *Proc. IEEE WCNC,* vol. 7-10, pp. 1691–1696, Shanghai, China, April 2013.

[59] A. Bletsas, A. Khisti, D. P. Reed, and A. Lippman, "A simple cooperative diversity method based on network path selection," *IEEE Journal on Selected Areas in Communications*, vol. 24, no. 3, pp. 659–672, 2006.

[60] A. Mukherjee and A. L. Swindlehurst, "Detecting Passive Eavesdroppers in The MIMO Wiretap Channel," in *Proc. IEEE ICASSP*, pp. 2809–2812, Kyoto, Japan, 2012.

[61] M. Zhang, K. Cumanan, J. Thiyagalingam et al., "Energy efficiency optimization for secure transmission in MISO cognitive radio network with energy harvesting," *IEEE Access*, vol. 7, pp. 126234–126252, 2019.

[62] K. Ho-Van, "Exact outage probability analysis of proactive relay selection in cognitive radio networks with MRC receivers," *Journal of Communications and Networks*, vol. 18, pp. 288–298, 2016.

[63] I. S. Gradshteyn and I. M. Ryzhik, *Table of Integrals, Series and Products*, Academic, San Diego, CA, 6th edition, 2000.

WILEY | Hindawi

Research Article
Secrecy Wireless-Powered Sensor Networks for Internet of Things

Junxia Li,[1] **Hui Zhao** [iD]**,**[1] **Xueyan Chen,**[2] **Zheng Chu,**[3,4] **Li Zhen,**[4] **Jing Jiang,**[4]
and Haris Pervaiz[5]

[1]*College of Information Science and Engineering, Xinjiang University, Urumqi 830046, China*
[2]*Zhengzhou University of Light Industry, Zhengzhou 450002, China*
[3]*University of Surrey, Guildford GU2 7XH, UK*
[4]*College of Communication and Information Engineering, Xi'an University of Post and Telecommunications, Xi'an,*
 Shanxi 710061, China
[5]*School of Computing and Communications, Lancaster University, Lancaster LA1 4WA, UK*

Correspondence should be addressed to Hui Zhao; zhmerry@126.com

This paper investigates a secure wireless-powered sensor network (WPSN) with the aid of a cooperative jammer (CJ). A power station (PS) wirelessly charges for a user equipment (UE) and the CJ to securely transmit information to an access point (AP) in the presence of multiple eavesdroppers. Also, the CJ are deployed, which can introduce more interference to degrade the performance of the malicious eavesdroppers. In order to improve the secure performance, we formulate an optimization problem for maximizing the secrecy rate at the AP to jointly design the secure beamformer and the energy time allocation. Since the formulated problem is not convex, we first propose a global optimal solution which employs the semidefinite programming (SDP) relaxation. Also, the tightness of the SDP relaxed solution is evaluated. In addition, we investigate a worst-case scenario, where the energy time allocation is achieved in a closed form. Finally, numerical results are presented to confirm effectiveness of the proposed scheme in comparison to the benchmark scheme.

1. Introduction

Internet of things (IoT) has been considered one of the appealing paradigms for future wireless network which significantly improves massive connectivity for the sensor devices [1]. However, the IoT devices suffer from energy-constrained issues. In this case, the devices in an IoT network will disconnect the IoT server due to limited battery size in this low-energy consumption nature. In a variety of IoT applications, e.g., those enabling the smart manufactures, due to the life cycle of the IoT devices which is approximately 10 to 20 years or more, it has led to severely demanding battery life constraints. Therefore, energy efficiency has been one of the main challenges in IoT networks [2].

On the other hand, reliable data transmission for IoT networks has become increasingly important, especially in vari-ous civilian and military applications. For secured IoT networks, the IoT devices guarantee a reliable connection with the access point to safeguard the private information, such as credit card transaction, online personal data, and military intelligent transmissions [3]. As a matter of fact, information security has become an essential part of the IoT system. Conventionally, a reliable wireless network is guaranteed via conventional cryptographic techniques which are implemented in the network layer. Nevertheless, due to the inherent quality of wireless transmission, it will incur large overhead as well as various issues in the key distribution and management to build a reliable link [4, 5]. As an alternative approach, physical layer security has been developed to provide the secrecy capacity metric by exploiting information-theoretical fundamentals [3]. In recent years, a variety of resource allocation algorithms have been developed in physical layer security scenarios to improve

the secrecy performance of the wireless networks. Additionally, physical layer security has also been studied in the scenario of multiantenna [5–7]. In secure communications, the transmit power efficiency plays a key role to enhance the secrecy capacity. Ideally, the transmit power at the base station (BS) is minimized to satisfy the transmission requirement on achievable secrecy rate [8, 9]. Recently, the reliability and security of wireless system have been considered in [10, 11], which can be applied in IoT applications. In [10], cooperative dual-hop nonorthogonal multiple access (NOMA) was investigated, where the transceivers consider a detrimental factor of in-phase and quadrature-phase imbalance (IQI). A decode-and-forward (DF) relay was employed to assist the secure communication between the source and destination. To characterize the performance of this system, exact and asymptotic analytical expressions for the outage probability (OP) and intercept probability (IP) are derived in terms of the closed-form expression. Integrating ambient backscatter (AmBC) into the NOMA system has been investigated in [11], where the source is aimed at communicating with two NOMA users in the presence of an eavesdropper. A more practical case is that nodes and backscatter device (BD) suffer from IQI.

Wireless-powered communication networks (WPCNs), as an enabler of energy harvesting, have been considered one of the promising techniques to deal with the energy-constrained issue in the IoT system. In WPCNs, large amounts of IoT devices are deployed to collect the energy from dedicated energy sources to supply wireless charging services for the IoT sensor nodes via radio frequency (RF) wireless energy transfer (WET) [2]. In recent years, there has been a variety of existing literature focused on how to effectively use the harvested energy to improve system performance [12–16]. In [12], a generic transmission WPCN was proposed, where a "harvest-then-transmit" was investigated. In this WPCN, the devices first harvest energy via the RF signals broadcast by an AP in the downlink and then implement wireless information transfer (WIT) in the uplink. In response to the doubly near-far effect in [12], the proportional fairness is explored by jointly designing power and time allocation in [13]. In [14], the WPCN application in AmBC was investigated, where wireless-powered IoT devices can collect energy and transmit their own information using the primary signal. By exploiting the energy supply among devices, a new wireless-powered chain model was proposed in IoT networks, where the IoT devices not only transmit information to the AP but also extract the energy from the RF signal of others [15]. In addition, a nonlinear energy harvesting model was proposed to maximize sum throughput and the minimum individual throughput for all wireless-powered users [16]. Moreover, a group of power stations (PSs) are composed of a dedicated WET network which is deployed to coordinate WIT networks in the vicinity [17, 18]. Specifically, these IoT devices can achieve more energy benefits from these PSs to prolong their own battery life via wireless charging, which outperform the traditional battery-powered counterparts. The WPCN highlights its advantage to reduce the operational cost and improves the robustness of wireless communication networks, which is more suitable for the low energy use cases, named wireless-powered sensor networks (WPSNs) [1]. Recently, a worst-case secure WPCN has been considered, where the eavesdroppers intercept the legitimate information between a H-AP and the user, and the jammer node acts as an artificial noise to interfere eavesdroppers by utilizing its harvested energy [19]. Moreover, multiple-input single-output (MISO) simultaneous wireless information and power transfer (SWIPT) has been investigated to integrate the energy harvesting user with security requirement [20–22]. In [20], secrecy energy efficiency maximization was exploited with an energy harvesting receiver, where the formulated problem is fractional programming and can be reformulated into difference of concave (DC) functions. Thus, the successive convex approximation and Dinkelbach's algorithm are employed to iteratively solve this optimization problem. An artificial noise- (AN-) aided secure SWIPT was investigated to improve the secure performance and energy harvesting efficiency under channel certainty of the eavesdroppers [21]. In [22], the outage-constrained robust secure design was studied, where the energy receivers can overhear the desired information which can be treated as potential eavesdroppers. Although the abovementioned works have investigated the WPCN integrated with some promising techniques, the reliable information transfer supported by WPCN still remains a performance bottleneck. Thus, integration of WPCN with the secure communications is a promising solution to address the energy-constraint and reliable issues simultaneously. Also, it is noted that the secure transmission of the IoT devices can be guaranteed by the wireless charging service. To the best of our knowledge, there have been no published works that model and investigate this secure WPCN in IoT system, which motivates this work.

In this paper, we investigate a cooperative jamming- (CJ-) aided secure WPSN. In particular, a multiantenna PS employs an energy beamforming to offer wireless charging services for a user equipment (UE) (i.e., IoT device) as well as a CJ node, and then, the UE utilizes the harvested energy to build a secure communication link with the AP when there existed multiple eavesdroppers. Meanwhile, the CJ uses the harvested energy to introduce interference, so that the reception of the eavesdroppers can be degraded. For this communication model, the main contributions of this paper are summarized as follows:

(1) First, it is aimed at maximizing the achievable secrecy rate to jointly design the energy beamforming and time allocation. Due to the nonconvex property of the formulated problem, it cannot be solved directly. In order to circumvent this nonconvexity, we first analyze the feasibility of the optimal time allocation for the given energy beamforming. Next, we propose a global optimal scheme where the energy beamforming is optimally designed for a given time allocation. This reformulated problem is further divided into a two-level optimization problem via introducing an auxiliary variable. Specifically, this formulated optimization problem can be solved via a semidefinite

programming (SDP) relaxation and one-dimensional line search. In addition, the optimal time allocation can be achieved via numerical search

(2) Second, a novel low-complexity scheme is exploited, which is based on a worst-case scenario, i.e., eavesdroppers' noise-free signal. The time allocation can be derived in terms of closed-form expression via Lambert W function, while the energy beamforming can be achieved via similar relaxation with a global optimal scheme. Numerical results are demonstrated to validate the proposed scheme

The remainder of this paper is organized as follows. In Section 2, we introduce the system model and formulate the problem. In Section 3, we present the global optimal solution for the original problem. We propose the low-complexity scheme for the formulated problem in Section 4. In Section 5, we provide numerical results to evaluate the proposed scheme. Finally, the conclusions of this paper are presented in Section 6.

2. System Model

In this section, we investigate a CJ-aided secure WPSN as shown in Figure 1. Specifically, a power station (PS), powered by a stable energy supply (i.e., microgrid), wirelessly charges for a user equipment (UE), which utilizes its harvested energy to establish a secure transmission link with an access point (AP) overheard by multiple eavesdroppers (this system model practically fits within the civilian and military applications. Specifically, the UE is regarded as a smart sensor node embedded into the smart wearable devices, which harvests the energy to support monitor personal private information transmitted to the access point. Also, this UE acts as a low-power sensor node deployed in the battlefield which needs to collect the energy service from the PS to transmit the intelligence information monitored by the UE to the AP). In this paper, we assume that the UE employs the linear energy harvesting. This is due to the fact that this assumption practically holds when the harvested energy at the UE is relatively lower than its battery capacity. Meanwhile, a dedicated CJ is deployed to collect the energy from the PS to introduce addition interference to degrade the reception of the eavesdroppers. We consider the case that the PS is equipped with N_{PS} transmit antennas, while all the other nodes use a single antenna. In this paper, we consider quasistatic flat-fading channel model, where all channel gains remain constant during each time block. We assume that $\mathbf{h}$, $\mathbf{g}_J$, h_s, $h_{e,k}$, l_J, and $f_{J,k}$ are denoted as the channel coefficients between the PS and the UE, the PS and the jammer, the UE and the AP, the UE and the kth eavesdropper, the jammer and the AP, and the jammer and the kth eavesdropper, respectively. A well-known "harvesting-then-transmit" protocol is considered in downlink WPT phase and uplink WIT phase. We also assume that the whole transmission time block is T. In the WET phase, i.e., $\theta \in (0, 1)$, the PS wirelessly charges for the UE and the jammer; thus, the harvested energy at the UE

WET
WIT
CJ
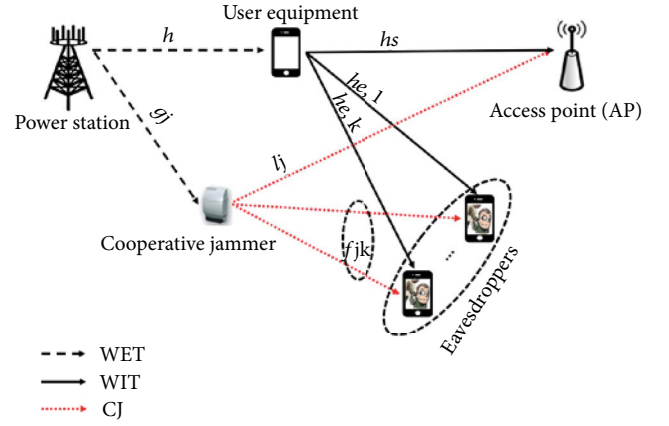
FIGURE 1: System model.

and the jammer can be written, respectively, as

$$
\begin{aligned}
E_{IT} &= \eta P_s \left| \mathbf{h}^H \mathbf{w} \right|^2 \theta, \\
E_J &= \eta P_s \left| \mathbf{g}_J \mathbf{w} \right|^2 \theta,
\end{aligned}
\tag{1}
$$

where $\eta \in (0, 1]$ accounts for the energy efficiency at the UE and the jammer, $\mathbf{w}$ denotes the normalized energy beamforming at the PS, and P_s is the transmit power at the PS. Accordingly, the transmit power at the UE and the jth jammer is given by, respectively,

$$
\begin{aligned}
P_{IT} &= \frac{\eta P_s \left| \mathbf{h}^H \mathbf{w} \right|^2 \theta}{T - \theta}, \\
P_J &= \frac{\eta P_s \left| \mathbf{g}_J \mathbf{w} \right|^2 \theta}{T - \theta}.
\end{aligned}
\tag{2}
$$

During the WIT phase, i.e., $T - \theta$, the UE and the jammer utilize the harvested energy to perform the information transfer. Specifically, the UE transmits the confidential information to the AP when there existed multiple eavesdroppers during the WIT phase; meanwhile, the CJ introduces the interference, so that the reception of the eavesdroppers is degraded. Noting that, the jammer guarantees that there is no interference leakage to the AP, i.e., the jammer is dedicated to help the UE to interfere with the eavesdropper, where there is a cooperation between the AP and the jammer such that the AP can decode the interference signal from the jammer. Thus, we write the mutual information at the AP and the kth eavesdropper, respectively, as follows:

$$
\begin{aligned}
R_u(\mathbf{w}, \theta) &= \log_2 \left(1 + \frac{\eta \theta P_s \left| \mathbf{h}^H \mathbf{w} \right|^2 |h_s|^2}{(T - \theta)\sigma_s^2} \right) \\
&= \log_2 \left(1 + \frac{\theta}{T - \theta} X_s(\mathbf{w}) \right),
\end{aligned}
\tag{3}
$$

$$
\begin{aligned}
R_{e,k}(\mathbf{w}, \theta) &= \log_2\left(1 + \frac{\left(\eta\theta P_s |\mathbf{h}^H\mathbf{w}|^2/T - \theta\right)|h_{e,k}|^2}{\left(\eta\theta P_s |\mathbf{g}_J^H\mathbf{w}|^2/T - \theta\right)|f_{J,k}|^2 + \sigma_e^2}\right) \\
&= \log_2\left(1 + \frac{\eta\theta P_s |\mathbf{h}^H\mathbf{w}|^2 |h_{e,k}|^2}{\theta\left(P_s\eta|\mathbf{g}_J^H\mathbf{w}|^2|f_{J,k}|^2 - \sigma_{e,k}^2\right) + T\sigma_e^2}\right) \\
&= \log_2\left(1 + \frac{\theta X_{e,k}(\mathbf{w})}{\theta(X_{J,k}(\mathbf{w}) - 1) + T}\right),
\end{aligned}
\tag{4}
$$

where

$$
\begin{aligned}
X_s(\mathbf{w}) &= \frac{\eta P_s |h_s|^2 |\mathbf{h}^H\mathbf{w}|^2}{\sigma_s^2}, \\
X_{e,k}(\mathbf{w}) &= \frac{\eta P_s |h_{e,k}|^2 |\mathbf{h}^H\mathbf{w}|^2}{\sigma_e^2}, \\
X_{j,k}(\mathbf{w}) &= \frac{\eta P_s |f_{J,k}|^2 |\mathbf{g}_J^H\mathbf{w}|^2}{\sigma_e^2}.
\end{aligned}
\tag{5}
$$

From (3), the achievable secrecy rate at the AP can be expressed as

$$
R_s(\mathbf{w}, \theta) = \left[R_u - \max_{k\in[1,K]} R_{e,k}\right]^+.
\tag{6}
$$

Thus, we formulate the secrecy throughput maximization subject to the energy beamformer and time allocation constraints, which is given by

$$
\max_{\theta,\mathbf{w}} \quad (T - \theta)R_s(\mathbf{w}, \theta)
\tag{7}
$$

$$
\text{s.t.} \quad \|\mathbf{w}\|^2 \le 1, \quad 0 < \theta < 1.
\tag{8}
$$

Problem (7) is nonconvex due to its objective function; thus, it cannot be solved directly. In order to address this problem, we employ a two-layer approach to globally obtain the optimal time allocation θ and energy beamformer $\mathbf{w}$. We further provide a worst-case scenario and obtain the closed-form expression of the optimal time allocation.

3. Global Optimal Solution to (7)

In this section, we propose a global optimal scheme to solve problem (7). Specifically, the energy beamforming can be optimally designed for given time allocation, which is reformulated into two level subproblems. The inner level problem can be solved by using an SDP, and the outer level problem is a single-variable optimization problem, which employs a one-dimensional line search to achieve the optimal energy beamforming. In addition, the time allocation can be optimally designed via numerical search.

3.1. Feasibility Analysis. In this subsection, we characterize the feasibility of time allocation of problem for the given energy beamforming $\mathbf{w}$. Thus, the following lemma is required to exploit the feasibility of problem (7).

Lemma 1. *For a given* $\mathbf{w}$, *problem (7) is feasible for* $\theta_{\min} < \theta < 1$, *where*

$$
\theta_{\min} = \arg\max_{k\in[1,K]} \frac{X_{e,k}(\mathbf{w}) - X_s(\mathbf{w})}{X_s(\mathbf{w})X_{J,k}(\mathbf{w}) - X_s(\mathbf{w}) + X_{e,k}(\mathbf{w})}.
\tag{9}
$$

Proof. In order to show the feasibility of (7), it is achieved from (6) that $R_s > 0$ such that we have $R_u - R_{e,k} > 0$, $\forall k$. Thus,

$$
\frac{\theta}{T - \theta} X_s(\mathbf{w}) > \frac{\theta X_{e,k}(\mathbf{w})}{\theta(X_{J,k}(\mathbf{w}) - 1) + T},
\tag{10}
$$

$$
\theta\left[\left(X_s(\mathbf{w})X_{J,k}(\mathbf{w}) - X_s(\mathbf{w}) + X_{e,k}(\mathbf{w})\right)\theta - T(X_{e,k}(\mathbf{w}) - X_s(\mathbf{w}))\right] > 0.
\tag{11}
$$

From (11), we have two cases, i.e., $X_s(\mathbf{w})X_{J,k}(\mathbf{w}) - X_s(\mathbf{w}) + X_{e,k}(\mathbf{w}) \le 0$ and $X_s(\mathbf{w})X_{J,k}(\mathbf{w}) - X_s(\mathbf{w}) + X_{e,k}(\mathbf{w}) > 0$. First, we discuss the case $X_s(\mathbf{w})X_{J,k}(\mathbf{w}) - X_s(\mathbf{w}) + X_{e,k}(\mathbf{w}) \le 0$, which results in $X_{e,k}(\mathbf{w}) - X_s(\mathbf{w}) < 0$ due to $X_s(\mathbf{w})X_{J,k}(\mathbf{w}) > 0$. In order to guarantee $R_u - R_{e,k} > 0$, one of the following inequalities should be satisfied:

$$
\begin{cases}
\theta > 0, \\
X_s(\mathbf{w})X_{J,k}(\mathbf{w}) - X_s(\mathbf{w}) + X_{e,k}(\mathbf{w}) = 0, \\
0 < \theta < 1 < \dfrac{X_{e,k}(\mathbf{w}) - X_s(\mathbf{w})}{X_s(\mathbf{w})X_{J,k}(\mathbf{w}) - X_s(\mathbf{w}) + X_{e,k}(\mathbf{w})}, \\
X_s(\mathbf{w})X_{J,k}(\mathbf{w}) - X_s(\mathbf{w}) + X_{e,k}(\mathbf{w}) < 0.
\end{cases}
\tag{12}
$$

Then, we discuss the second case $X_s(\mathbf{w})X_{J,k}(\mathbf{w}) - X_s(\mathbf{w}) + X_{e,k}(\mathbf{w}) > 0$. In order to guarantee $R_u - R_{e,k} > 0$, one of the following inequalities should hold:

$$
\forall k, \begin{cases}
\theta > 0, \\
X_{e,k}(\mathbf{w}) - X_s(\mathbf{w}) < 0, \\
\dfrac{X_{e,k}(\mathbf{w}) - X_s(\mathbf{w})}{X_s(\mathbf{w})X_{J,k}(\mathbf{w}) - X_s(\mathbf{w}) + X_{e,k}(\mathbf{w})} \le \theta < 1, \\
X_{e,k}(\mathbf{w}) - X_s(\mathbf{w}) \ge 0.
\end{cases}
\tag{13}
$$

From the abovementioned results, we obtain

$$
\theta_{\min} \le \theta < 1,
\tag{14}
$$

where

$$
\theta_{\min} = \arg\max_{k\in[1,K]} \frac{X_{e,k}(\mathbf{w}) - X_s(\mathbf{w})}{X_s(\mathbf{w})X_{J,k}(\mathbf{w}) - X_s(\mathbf{w}) + X_{e,k}(\mathbf{w})}.
\tag{15}
$$

By exploiting Lemma 1, we can derive the optimal time allocation through one-dimensional line search over $\theta \in (\theta_{\min}, 1)$.

3.2. Global Optimal Scheme. In the previous subsection, we characterize the feasibility condition for the formulated problem (7) to obtain optimal time allocation. To proceed, we optimize the energy beamformer $\mathbf{w}$ in (7) for a given time allocation θ, which is written as

$$\max_{\mathbf{w}} \quad R_s \tag{16}$$

$$\text{s.t.} \quad \|\mathbf{w}\|^2 \le 1. \tag{17}$$

Problem (16) is nonconvex in terms of $\mathbf{w}$ such that it cannot be solved directly. To tackle it, we propose a global optimal scheme via employing two-dimensional line search and SDP relaxation. First, we fix the time allocation θ and introduce an auxiliary variable t such that problem (16) can then be rewritten as

$$R_s^* = \max_{\mathbf{w},t} \log_2\left(1 + \frac{\theta}{T-\theta}X_s(\mathbf{w})\right) + \log_2(t)$$

$$\text{s.t.} \max_{k \in [1,K]} \log_2\left(1 + \frac{\theta X_{e,k}(\mathbf{w})}{\theta(X_{J,k}(\mathbf{w}) - 1) + T}\right) \le \log_2\left(\frac{1}{t}\right),$$

$$\|\mathbf{w}\|^2 \le 1. \tag{18}$$

Although we have introduced an auxiliary variable t to reformulate problem (16), it is still nonconvex and intractable. In order to circumvent this issue, problem (16) can be divided into two-level subproblems, which can be given by the following:

(1) Outer level: the outer level subproblem is given by

$$R_s^* = \max_t \log_2(1 + \Gamma(t)) + \log_2(t) \tag{19}$$

$$\text{s.t.} \quad t_{\min} \le t \le 1, \tag{20}$$

where $\Gamma(t) = (\theta/(T-\theta))X_s(\mathbf{w})$ and $t_{\min}$ denote the lower bound of variable t. Note that this lower bound can be easily derived as $t_{\min} = (1 + (\eta\theta P_s|h_s|^2\|\mathbf{h}\|^2)/((T-\theta)\sigma_s^2))^{-1}$ [23].

(2) Inner level: for a given t, the inner level subproblem is written as

$$\Gamma(t) = \max_{\mathbf{w}} \frac{\eta\theta P_s|h_s|^2|\mathbf{h}^H\mathbf{w}|^2}{(T-\theta)\sigma_s^2} \tag{21}$$

$$\text{s.t.} \max_{k \in [1,K]} \log_2\left(1 + \frac{\eta\theta P_s|\mathbf{h}^H\mathbf{w}|^2|h_{e,k}|^2}{\theta\left(P_s\eta|\mathbf{g}_J^H\mathbf{w}|^2|f_{J,k}|^2 - \sigma_e^2\right) + T\sigma_e^2}\right) \le \log_2\left(\frac{1}{t}\right),$$

$$\tag{22}$$

$$\|\mathbf{w}\|^2 \le 1. \tag{23}$$

From (19), the outer level subproblem is a single-variable optimization problem in terms of t with interval $t \in [t_{\min}, 1]$, which is tackled via one-dimensional line search, while the inner level subproblem (21) is still nonconvex due to its constraint with any feasible t. In the following, we will tackle the inner stage problem (21) to optimally design the energy beamforming $\mathbf{w}$.

3.3. Optimal Solution to (21). In this subsection, we consider a SDP relaxation to optimally solve the inner stage problem (21). First, let us denote $\mathbf{W} = \mathbf{w}\mathbf{w}^H$; problem (21) can be relaxed as

$$\Gamma(t) = \max_{\mathbf{W} \ge \mathbf{0}} \frac{\eta\theta P_s|h_s|^2\text{Tr}\left(\mathbf{h}\mathbf{h}^H\mathbf{W}\right)}{(T-\theta)\sigma_s^2}$$

$$\text{s.t.} \quad \log_2\left(1 + \frac{\eta\theta P_s|h_{e,k}|^2\text{Tr}\left(\mathbf{h}\mathbf{h}^H\mathbf{W}\right)}{\theta\left(P_s\eta|f_{J,k}|^2\text{Tr}\left(\mathbf{g}_J\mathbf{g}_J^H\mathbf{W}\right) - \sigma_e^2\right) + T\sigma_e^2}\right) \le \log_2\left(\frac{1}{t}\right),$$

$$\tag{24a}$$

$$\text{Tr}(\mathbf{W}) \le 1, \tag{24b}$$

$$\text{rank}(\mathbf{W}) \le 1. \tag{24c}$$

Problem (24) is intractable due to (24a) and (24c). To proceed, by exploiting a few of the mathematical manipulations to tackle (24a), (24) can be equivalently modified as

$$\widetilde{\Gamma}(t) = \max_{\mathbf{W} \ge \mathbf{0}} \text{Tr}\left(\mathbf{h}\mathbf{h}^H\mathbf{W}\right) \tag{25}$$

$$\text{s.t.} \quad \eta\theta P_s|h_{e,k}|^2\text{Tr}\left(\mathbf{h}\mathbf{h}^H\mathbf{W}\right)$$

$$- \theta\left(\frac{1}{t} - 1\right)\left(P_s\eta|f_{J,k}|^2\text{Tr}\left(\mathbf{g}_J\mathbf{g}_J^H\mathbf{W}\right) - \sigma_e^2\right) \tag{26}$$

$$- \left(\frac{1}{t} - 1\right)T\sigma_e^2 \le 0, \quad \forall k,$$

$$(17b), (17c). \tag{27}$$

Note that $\Gamma^* = (\eta\theta P_s|h_s|^2/(T-\theta)\sigma_s^2)\widetilde{\Gamma}^*$. Problem (25) is an SDP; by ignoring the nonconvex rank-one constraint, we adopt an interior-point approach to solve it [24]. To proceed, the condition of the optimality to the problem is characterized by showing that problem (24) yields a rank-one solution [25]. By exploiting the two-level-based SDP approach, we solve problem (16) for a given time allocation θ. Then, we consider the optimal solution of the time allocation θ, where problem (7) is equivalently formulated as

$$\max_\theta \quad (T-\theta)\left[\log_2\left(1 + \frac{\theta}{T-\theta}X_s\right) - \log_2\left(1 + \frac{\theta X_e}{\theta(X_J - 1) + T}\right)\right], \tag{28}$$

$$\text{s.t.} \quad \theta_{\min} < \theta < 1, \tag{29}$$

where $X_e = \text{argmax}_{k \in [1,K]} X_{e,k}$ and $X_J = \text{argmin}_{k \in [1,K]} X_{J,k}$. For

convenience and without loss of generality, we substitute X_l into $X_l(\mathbf{w})$, $l \in \{s, e, j\}$.

4. Low-Complexity Scheme

In the previous section, we exploited a global optimal scheme to solve problem (7) via the SDP approach and two-dimensional search. However, this scheme involves two-dimensional search for the slack variable t and time allocation θ, respectively, which introduces a higher computational complexity and is time-consuming. In order to tackle this issue, in this section, we propose a novel low-complexity approach to obtain the optimal time allocation θ in terms of a closed-form expression. This approach can effectively reduce the complexity, since it only involves one-dimensional line search for the slack variable t.

4.1. Optimal Solution to Low-Complexity Scheme. In this sub-section, we propose a novel low-complexity scheme to solve problem ((7)), which assumes that the noise-free signal is available at the eavesdroppers, i.e., $\sigma_{e,k}^2 = 0$, $\forall k$. In order to implement the low-complexity scheme, we first rewrite the worst-case secrecy rate as

$$R_{\mathrm{wc}} = \left[\log_2 \left(1 + \frac{\theta}{T-\theta} X_s(\mathbf{w}) \right) - \max_{k \in [1, K]} \log_2 \left(1 + \frac{\bar{X}_{e,k}(\mathbf{w})}{\bar{X}_{J,k}(\mathbf{w})} \right) \right]^+, \tag{30}$$

where $\bar{X}_{e,k} = \eta P_s |h_{e,k}|^2 |\mathbf{h}^H \mathbf{w}|^2$ and $\bar{X}_{J,k} = \eta P_s |f_{J,k}|^2 |\mathbf{g}_J^H \mathbf{w}|^2$. Thus, the worst-case secrecy rate maximization problem can be formulated as

$$\max_{\mathbf{w}, \theta} \quad (T-\theta) R_{\mathrm{wc}} \tag{31}$$

$$\text{s.t.} \quad \|\mathbf{w}\|^2 \leq 1, 0 < \theta < 1. \tag{32}$$

Problem (31) is not jointly convex for the coupled variables $\mathbf{w}$ and θ. Similar to Section 3, we first fix the time allocation to optimally design the energy beamforming $\mathbf{w}$, which is omitted here to conserve space. To proceed, we propose the optimal time allocation in a closed form for problem (31) with a given $\mathbf{w}$. Note that (30) provides a lower bound of the achievable secrecy rate R_s, i.e., $R_s \geq R_{\mathrm{wc}}$. By exploiting the SDP relaxation to design energy beamforming $\mathbf{w}$, the worst-case secrecy rate can be modified as

$$R_{\mathrm{wc}} = \left[\log_2 \left(1 + \frac{\theta}{T-\theta} X_s \right) - \log_2 \left(1 + \frac{\bar{X}_e}{\bar{X}_J} \right) \right], \tag{33}$$

where $\bar{X}_e = \mathrm{argmax}_{k \in [1, K]} \bar{X}_{e,k}(\mathbf{w})$ and $\bar{X}_J = \mathrm{argmin}_{k \in [1, K]} \bar{X}_{J,k}$

($\mathbf{w}$). And problem (31) can be rewritten for a given $\mathbf{w}$ as

$$\max_{\theta} \quad \hat{R}_{\mathrm{wc}}(\theta) = (T-\theta) \left[\log_2 \left(1 + \frac{\theta}{T-\theta} X_s \right) - \log_2 \left(1 + \frac{\bar{X}_e}{\bar{X}_J} \right) \right] \tag{34}$$

$$\text{s.t.} \quad \bar{\theta}_{\min} < \theta < 1, \tag{35}$$

where $\bar{\theta}_{\min} = \bar{X}_e / (X_S \bar{X}_J + \bar{X}_e)$. It is worth noting that problem ((34)) is a special case of ((28)) with the eavesdroppers' noise-free signal, which incurs an upper bound of the eavesdroppers' achievable rate. It is verified that problem (28) is convex in terms of time allocation θ. We first consider that the first-order derivative of the objective function in (28) equals to zero, which is given by

$$\frac{\partial \bar{R}_{\mathrm{wc}}}{\partial \theta} = -\left[\log_2 \left(1 + \frac{\theta}{T-\theta} X_s \right) - \log_2 \left(1 + \frac{\bar{X}_e}{\bar{X}_J} \right) \right] \\ - \frac{1}{\ln 2} \frac{T X_s}{(1 + (\theta/T-\theta) X_s)(T-\theta)} = 0, \tag{36}$$

$$\left(1 + \frac{\theta}{T-\theta} X_s \right) \ln \left(1 + \frac{\theta}{T-\theta} X_s \right) - \left(1 + \frac{\theta}{T-\theta} X_s \right) \\ \cdot \left[1 + \ln \left(1 + \frac{\bar{X}_e}{\bar{X}_J} \right) \right] = X_s - 1. \tag{37}$$

To proceed reformulation, let $z = 1 (+\theta/(T-\theta)) X_s$; (37) is equivalently modified as

$$z \ln z - z \left[1 + \ln \left(1 + \frac{\bar{X}_e}{\bar{X}_J} \right) \right] = X_s - 1. \tag{38}$$

The following equations can be derived via a few of the exponential transformations:

$$e^{z \left[\ln z - \ln \left(e \left(1 + (\bar{X}_e/\bar{X}_J) \right) \right) \right]} = e^{X_s - 1} \Rightarrow e^{z \ln \left(z/\left(e \left(1 + (\bar{X}_e/\bar{X}_J) \right) \right) \right)} = e^{X_s - 1}$$

$$\Rightarrow e^{\left(z/\left(e \left(1 + (\bar{X}_e/\bar{X}_J) \right) \right) \right) \ln \left(z/\left(e \left(1 + (\bar{X}_e/\bar{X}_J) \right) \right) \right)}$$

$$= e^{(X_s - 1)/e \left(1 + (\bar{X}_e/\bar{X}_J) \right)}$$

$$\Rightarrow e^{\ln \left(z/\left(e \left(1 + (\bar{X}_e/\bar{X}_J) \right) \right) \right)} \ln \left(\frac{z}{e \left(1 + (\bar{X}_e/\bar{X}_J) \right)} \right)$$

$$= \frac{X_s - 1}{e \left(1 + (\bar{X}_e/\bar{X}_J) \right)}. \tag{39}$$

By exploiting Lambert W function, (39) is equivalent

to the following equality:

$$\ln\left(\frac{z}{e\left(1 + \left(\bar{X}_e/\bar{X}_J\right)\right)}\right) = W\left(\frac{X_s - 1}{e\left(1 + \left(\bar{X}_e/\bar{X}_J\right)\right)}\right), \qquad (40)$$

where $W(\cdot)$ represents the Lambert W function. Thus, the optimal time allocation can be derived as

$$\theta^* = \frac{\left[e^{W\left((X_s-1)/\left(e\left(1+\left(\bar{X}_e/\bar{X}_J\right)\right)\right)\right)+1}\left(1 + \left(\bar{X}_e/\bar{X}_J\right)\right) - 1\right]T}{X_s - 1 + e^{W\left(\left((X_s-1)/\left(\left(e\left(1+\left(\bar{X}_e/\bar{X}_J\right)\right)\right)\right)\right)\right)+1}\left(1 + \left(\bar{X}_e/\bar{X}_J\right)\right)}. \qquad (41)$$

By exploiting the property of the Lambert W function $e^{W(x)} = x/W(x)$, (41) can be further equivalently simplified as

$$\theta^* = \frac{\left[1 - W\left[(X_s - 1)\left(\bar{X}_J/\left(\left(\bar{X}_e + \bar{X}_J\right)e\right)\right)\right]/(X_s - 1)\right]T}{W\left[(X_s - 1)\left(\bar{X}_J/\left(\left(\bar{X}_e + \bar{X}_J\right)e\right)\right) + 1\right]}. \qquad (42)$$

By exploiting (42), we derived the optimal time allocation in terms of a closed-form expression for given energy beamforming $\mathbf{w}$. Thus, in order to optimally obtain the worst-case achievable secrecy rate, we present an alternating optimization algorithm to iteratively design energy beamforming $\mathbf{w}$ and time allocation θ, respectively, which is guaranteed to converge to satisfy the Karush-Kuhn-Tucker (KKT) conditions of problem (31).

4.2. Special Case. In the previous subsection, we have optimally designed the time allocation in terms of a closed-form expression to propose the low-complexity schemes. This optimal time allocation fits within generic worst cases of the achievable secrecy rate. In this subsection, we characterize the optimal time allocation for two special cases in terms of signal-to-interference-plus-noise ratio (SINR) regions of the eavesdroppers. First, we derive the optimal time allocation in low-SINR region, e.g., $\bar{X}_e \ll \bar{X}_J$. Thus, according to (42), the optimal time allocation can be further approximated as

$$\theta_{\text{low}}^* = \frac{\left[1 - \left(W\left((X_s - 1)/e\right)/(X_s - 1)\right)\right]T}{W\left((X_s - 1)/e\right) + 1}. \qquad (43)$$

The optimal solution (43) releases a fact that secure WPSN system is degraded into the conventional WPSN-based rate maximization, where the jamming node introduces extra interference which has a prominent role to design the time allocation similar to the case that the reception of the eavesdroppers is too small to be ignored. In addition, the scenario of higher-SINR region at the eavesdroppers is characterized, where $\bar{X}e \gg \bar{X}_J$ holds. Thus, for the higher SINR
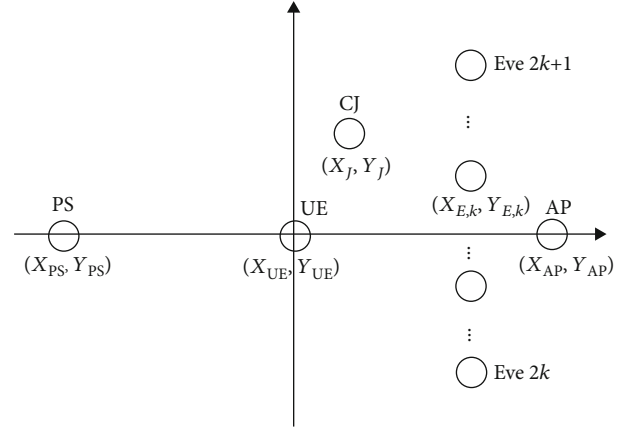
FIGURE 2: System deployment.

case, (42) can be further simplified as

$$\theta_{\text{high}}^* = \frac{\left[1 - W\left[(X_s - 1)\left(\bar{X}_J/e\bar{X}_e\right)\right]/(X_s - 1)\right]T}{W\left[(X_s - 1)\bar{X}_J/e\bar{X}_e + 1\right]}. \qquad (44)$$

This scenario unveils the fact that more energy time is allocated to the WPT phase for the UE while the jamming node also needs more sufficient energy collected from the PS to introduce extra interference to degrade the reception of the eavesdroppers.

5. Numerical Results

In this section, we present the numerical results to evaluate the performance of the proposed scheme in the secure WPSN system. In simulation, we take into consideration the system deployment as shown in Figure 2 to describe the system model, where the PS, the UE, the CJ, and the AP are located $(X_{PS}, Y_{PS}) = (-50, 0)$, $(X_{UE}, Y_{UE}) = (0, 0)$, and $(X_J, Y_J) = (20, 8)$, and $(X_{AP}, Y_{AP}) = (50, 0)$, respectively. Also, all of eavesdroppers are located at $(X_{E,k}, Y_{E,k}) = (30, n * l/2)$ when $n = 1, \cdots, 2 * k + 1$, or $(X_{E,k}, Y_{E,k}) = (30, -(n - 1) * k/2)$ when $n = 2, \cdots, 2 * k$, where l denotes the interval between two neighbouring eavesdroppers. The channel coefficient is composed of distance-dependent path loss model and small-scale fading, where the path loss model is set to $\text{PL} = Ad^{-\kappa}$, where $A = 10^{-3}$, κ is the path loss exponent, and d represents the distance between any two devices, i.e., the PS and UE, the PS and the CJ, the UE and the AP, the UE and the eavesdroppers, and the CJ and the eavesdroppers. All small-scale channel coefficients are generated to follow Rayleigh fading. Also, we set $P_s = 20$ dBm, $\eta = 0.8$, and $\sigma^2 = \sigma^2 = -150$ dBm unless otherwise stated. In order to highlight the proposed scheme, we evaluate the performance of the benchmark schemes in comparison to the proposed scheme. Specifically, we take into consideration two benchmark schemes: (1) maximum ratio transmission (MRT) scheme, in this way, the direction of the energy beamformer is consistent with channel $\mathbf{h}$; (2) equal time allocation (ET) scheme, where the transmission time is equally allocated for both WET and WIT durations.
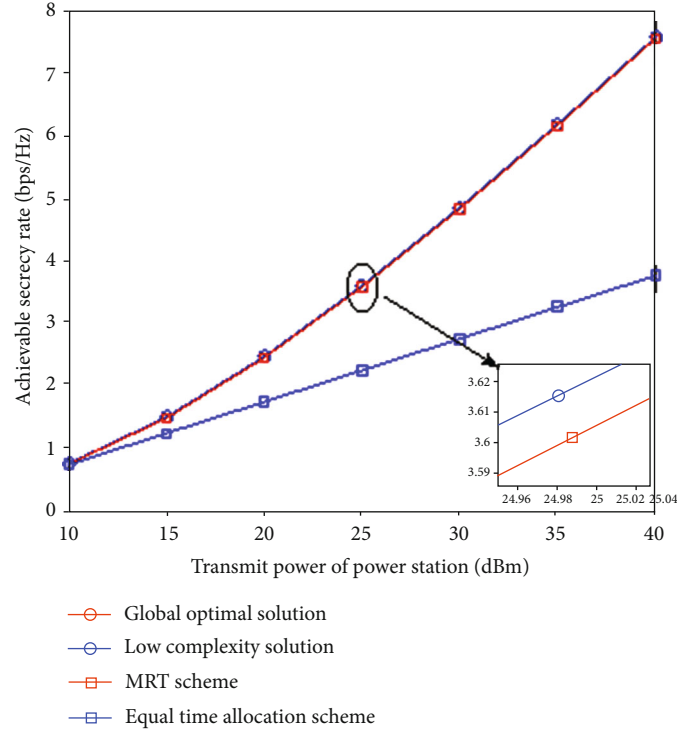
Figure 3: Achievable secrecy rate versus transmit power at PS.
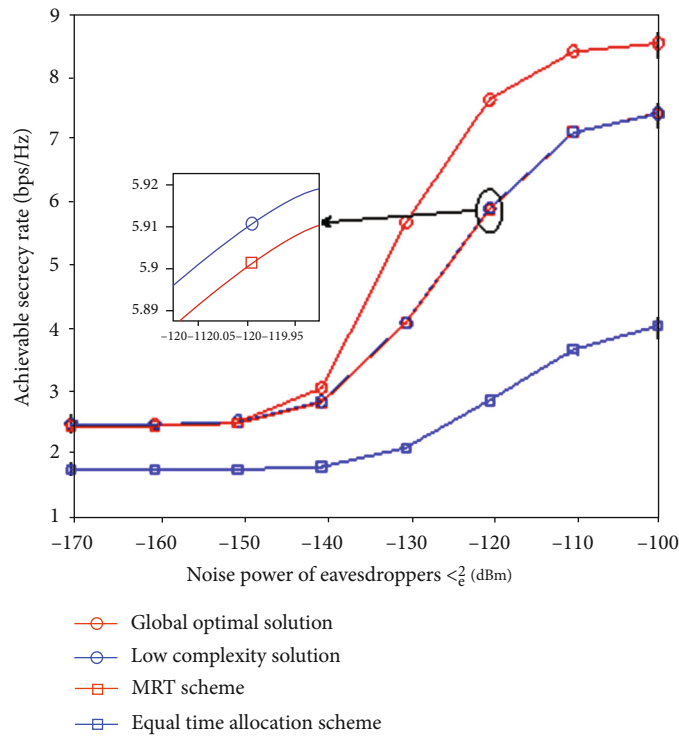
Figure 4: Achievable secrecy rate versus noise power.

First, Figure 3 presents the achievable secrecy rate versus transmit power at the PS P_s. From this figure, it can be seen that the achievable secrecy rate increases with P_s in terms of each scheme. This releases that larger transmit power at the PS can guarantee the reliability of the WIT. Also, the proposed low-complexity scheme can achieve the same
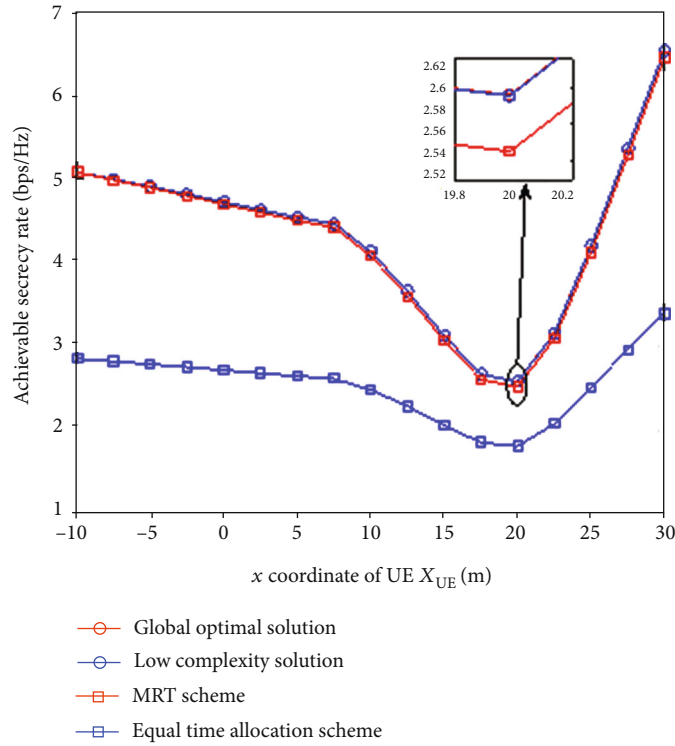
FIGURE 5: Achievable secrecy rate versus UE x-coordinate.
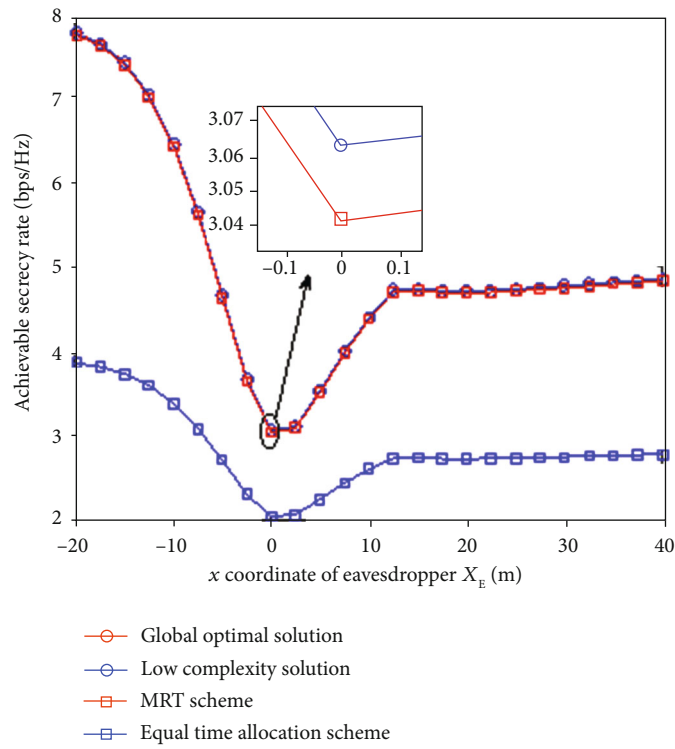
FIGURE 6: Achievable secrecy rate versus eavesdropper x-coordinate.

achievable secrecy rate as the global optimal scheme, which validates the correctness and effectiveness of the derivations in Section 4. In addition, we evaluate the performance of the proposed scheme against the benchmark schemes, it is shown that the proposed scheme is superior to the MRT scheme and outperforms the ET scheme in terms of the achievable secrecy rate. This effectively highlights the importance of the optimal time allocation in our proposed scheme.
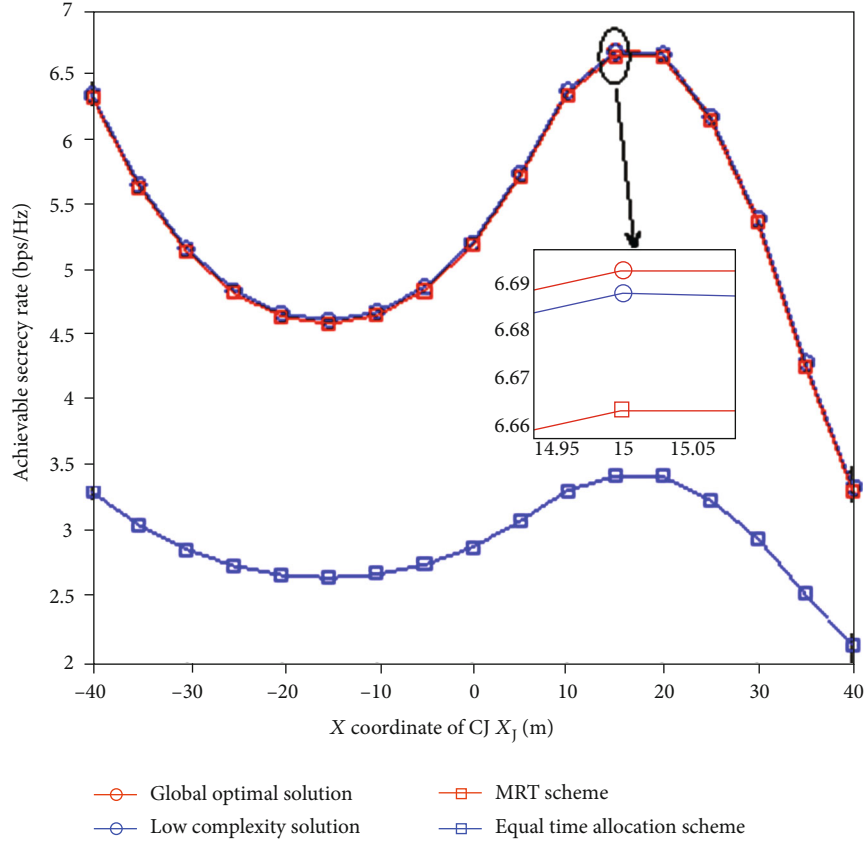
FIGURE 7: Achievable secrecy rate versus CJ x-coordinate.

Next, we evaluate the impact of the noise power of eavesdroppers σ_e^2 on the achievable secrecy rate in Figure 4. These results clearly show that, if the noise power σ_e^2 is relatively low, the proposed low-complexity scheme has the same performance with the global optimal scheme in terms of achievable secrecy rate. As σ_e^2 increases, the proposed low-complexity scheme shows a degradation in terms of the achievable secrecy rate in comparison to the global optimal scheme. This is due to the fact that the eavesdroppers are not able to decode the overheard signal in the high-noise power region σ_e^2, such that the low-complexity scheme can be considered in a low-noise power region to design a secure WPSN. Also, the low-complexity scheme slightly outperforms the MRT scheme and obtains higher achievable secrecy rate than the ET scheme.

Then, the impact of the deployment of the UE, the eavesdroppers, and the CJ on the achievable secrecy rate is evaluated. In Figure 5, the achievable secrecy rate versus the x-coordinate of the UE X_{UE} is presented, where the achievable secrecy rate first decreases and then has an increasing trend after $X_{UE} = 20$ m for each scheme. This confirms the optimal deployment of the UE, where the UE is deployed nearer to the AP or PS to gain a higher achievable secrecy rate. In Figure 6, we present that the achievable secrecy rate versus the x-coordinate of the eavesdroppers X_E, where the achievable secrecy rate has an obviously decreasing trend and then increases after $X_E = 0$ m for each scheme; also,

the achievable secrecy rate gradually achieves a stable trend after approximately $X_E = 12$ m. Similar arguments in Figures 5 and 6 can be justified with Figure 3, where the proposed low-complexity scheme achieves the same performance with the global optimal scheme and outperforms the MRT and ET schemes in terms of the achievable secrecy rate.

Finally, the impact of the deployment of the CJ has been evaluated. Specifically, Figure 7 shows that the achievable secrecy rate has a decreasing trend when the x-coordinate of the CJ X_J is small and increases as X_J is located from -15 m to 15 m and then will decline again after that. This confirms the optimal deployment of the CJ, where it is deployed nearer to the PS or in the vicinity of the UE to achieve a higher achievable secrecy rate. This is because this deployment enables the CJ to obtain a higher energy harvesting efficiency to introduce a higher interference to degrade the reception of the eavesdroppers. In addition, the proposed low-complexity scheme is matched with the global optimal scheme, as well as outperforms the MRT and the ET schemes in terms of the achievable secrecy rate.

6. Conclusion

This paper investigated a secure WPSN with the assistance of a CJ. The PS provides wireless energy for a UE and the CJ to secure information transfer to the AP and introduce

extra interference to the eavesdroppers, respectively. Our aim is to jointly design the secure beamformer and the energy time allocation via maximizing the secrecy throughput at the AP. Due to nonconvexity of the formulated problem, we first propose a global optimal solution which employs the semidefinite programming (SDP) relaxation. In addition, we investigate a worst-case scenario, where the closed-form expression of energy time allocation is derived. Finally, our proposed schemes have been validated through the numerical results, which highlight that the jammer plays an improving role in the secure WPSN.

Data Availability

The (Matlab) data used to support the findings of this study are available from the corresponding author upon request.

Conflicts of Interest

The authors declare that there is no conflict of interest regarding the publication of this paper.

Acknowledgments

References

[1] Z. Chu, F. Zhou, Z. Zhu, R. Q. Hu, and P. Xiao, "Wireless powered sensor networks for internet of things: maximum throughput and optimal power allocation," *IEEE Internet of Things Journal*, vol. 5, no. 1, pp. 310–321, 2018.

[2] S. Bi, C. K. Ho, and R. Zhang, "Wireless powered communication: opportunities and challenges," *IEEE Communications Magazine*, vol. 53, no. 4, pp. 117–125, 2015.

[3] Y. Wu, A. Khisti, C. Xiao, G. Caire, K.-K. Wong, and X. Gao, "A survey of physical layer security techniques for 5G wireless networks and challenges ahead," *IEEE Journal on Selected Areas in Communications*, vol. 36, no. 4, pp. 679–695, 2018.

[4] K. Cumanan, Z. Ding, B. Sharif, G. Y. Tian, and K. K. Leung, "Secrecy rate optimizations for a MIMO secrecy channel with a multiple-antenna eavesdropper," *IEEE Transactions on Vehicular Technology*, vol. 63, no. 4, pp. 1678–1690, 2014.

[5] Z. Chu, K. Cumanan, Z. Ding, M. Johnston, and S. Y. Le Goff, "Secrecy rate optimizations for a MIMO secrecy channel with a cooperative jammer," *IEEE Transactions on Vehicular Technology*, vol. 64, no. 5, pp. 1833–1847, 2015.

[6] Q. Li and W.-K. Ma, "Optimal and robust transmit designs for MISO channel secrecy by semidefinite programming," *IEEE Transactions on Signal Processing*, vol. 59, no. 8, pp. 3799–3812, 2011.

[7] F. Zhou, Z. Li, J. Cheng, Q. Li, and J. Si, "Robust AN-aided beamforming and power splitting design for secure MISO cognitive radio with SWIPT," *IEEE Transactions on Wireless Communications*, vol. 16, no. 4, pp. 2450–2464, 2017.

[8] D. W. K. Ng, E. S. Lo, and R. Schober, "Robust beamforming for secure communication in systems with wireless information and power transfer," *IEEE Transactions on Wireless Communications*, vol. 13, no. 8, pp. 4599–4615, 2014.

[9] D. W. K. Ng and R. Schober, "Secure and green SWIPT in distributed antenna networks with limited backhaul capacity," *IEEE Transactions on Wireless Communications*, vol. 14, no. 9, pp. 5082–5097, 2015.

[10] X. Li, M. Zhao, X.-C. Gao et al., "Physical layer security of cooperative NOMA for IoT networks under I/Q imbalance," *IEEE Access*, vol. 8, pp. 51189–51199, 2020.

[11] X. Li, M. Zhao, Y. Liu, L. Li, Z. Ding, and A. Nallanathan, "Secrecy analysis of ambient backscatter NOMA systems under I/Q imbalance," *IEEE Transactions on Vehicular Technology*, p. 1, 2020.

[12] H. Ju and R. Zhang, "Throughput maximization in wireless powered communication networks," *IEEE Transactions on Wireless Communications*, vol. 13, no. 1, pp. 418–428, 2014.

[13] Y. Cheng, P. Fu, Y. Chang, B. Li, and X. Yuan, "Joint power and time allocation in full-duplex wireless powered communication networks," *Mobile Information Systems*, vol. 2016, Article ID 4845865, 15 pages, 2016.

[14] X. Kang, Y.-C. Liang, and J. Yang, "Riding on the primary: a new spectrum sharing paradigm for wireless-powered IoT devices," *IEEE Transactions on Communications*, vol. 17, no. 9, pp. 6335–6347, 2018.

[15] J. Wang, X. Kang, Y. Liang, and S. Sun, "An energy harvesting chain model for wireless-powered IoT networks," in *2018 10th International Conference on Wireless Communications and Signal Processing (WCSP)*, pp. 1–6, Hangzhou, China, 2018.

[16] E. Boshkovska, D. W. K. Ng, N. Zlatanov, A. Koelpin, and R. Schober, "Robust resource allocation for MIMO wireless powered communication networks based on a non-linear EH model," *IEEE Transactions on Communications*, vol. 65, no. 5, pp. 1984–1999, 2017.

[17] K. Huang and X. Zhou, "Cutting the last wires for mobile communications by microwave power transfer," *IEEE Communications Magazine*, vol. 53, no. 6, pp. 86–93, 2015.

[18] K. Huang and V. K. N. Lau, "Enabling wireless power transfer in cellular networks: architecture, modeling and deployment," *IEEE Transactions on Wireless Communications*, vol. 13, no. 2, pp. 902–912, 2014.

[19] J. Moon, H. Lee, C. Song, and I. Lee, "Time allocation methods for secure wireless powered communication networks," in *2018 IEEE 88th Vehicular Technology Conference (VTC-Fall)*, pp. 1–5, Chicago, IL, USA, USA, 2018.

[20] M. Zhang, K. Cumanan, J. Thiyagalingam et al., "Energy efficiency optimization for secure transmission in MISO cognitive radio network with energy harvesting," *IEEE Access*, vol. 7, pp. 126234–126252, 2019.

[21] M. Zhang, K. Cumanan, L. Ni, H. Hu, A. G. Burr, and Z. Ding, "Robust beamforming for AN aided MISO SWIPT system with unknown eavesdroppers and non-linear eh model," in

2018 IEEE Globecom Workshops (GC Wkshps), pp. 1–7, Abu Dhabi, United Arab Emirates, United Arab Emirates, 2018.

[22] L. Ni, X. Da, H. Hu, M. Zhang, and K. Cumanan, "Outage constrained robust secrecy energy efficiency maximization for EH cognitive radio networks," *IEEE Wireless Communications Letters*, vol. 9, no. 3, pp. 363–366, 2020.

[23] Q. Li and W.-K. Ma, "Spatially selective artificial-noise aided transmit optimization for MISO multi-eves secrecy rate maximization," *IEEE Transactions on Signal Processing*, vol. 61, no. 10, pp. 2704–2717, 2013.

[24] S. Boyd and L. Vandenberghe, *Convex Optimization*, Cambridge University Press, Cambridge, UK, 2004.

[25] Z. Chu, Z. Zhu, M. Johnston, and S. Y. Le Goff, "Simultaneous wireless information power transfer for MISO secrecy channel," *IEEE Transactions on Vehicular Technology*, vol. 65, no. 9, pp. 6913–6925, 2016.

[26] Q. Li, M. Hong, H.-T. Wai, Y.-F. Liu, W.-K. Ma, and Z.-Q. Luo, "Transmit solutions for MIMO wiretap channels using alternating optimization," *IEEE Journal on Selected Areas in Communications*, vol. 31, no. 9, pp. 1714–1727, 2013.

WILEY | Hindawi

Research Article

Interference Minimization Resource Allocation for V2X Communication Underlaying 5G Cellular Networks

Xiaoqin Song,[1] Kuiyu Wang,[1] Lei Lei [ID],[1] Liping Zhao,[2] Yong Li,[2] and Jiankang Wang[3]

[1]*College of Electronic and Information Engineering, Nanjing University of Aeronautics and Astronautics, Nanjing, China*
[2]*The 63rd Research Institute of National University of Defense Technology, China*
[3]*Samsung Research China-Beijing (SRC-B), Beijing, China*

Correspondence should be addressed to Lei Lei; leilei@nuaa.edu.cn

In this paper, the resource allocation for vehicle-to-everything (V2X) underlaying 5G cellular mobile communication networks is considered. The optimization problem is modeled as a mixed binary integer nonlinear programming (MBINP), which minimizes the interference to 5G cellular users (CUs) subject to the quality of service (QoS), the total available power, the interference threshold, and the minimal transmission rate. To achieve that, the original MBINP is decomposed into three steps: transmission power initialization, subchannel assignment, and power allocation. Firstly, the minimum transmission power required by the V2X users (VUs) is set as the initial power value. Secondly, the Hungarian algorithm is used to obtain the appropriate subchannel. Finally, an optimization mechanism is proposed to the power allocation. Simulation results show that the proposed algorithm can not only ensure the minimal transmission rate of VUs but also further improve the CUs' channel capacity under the premise of guaranteeing the QoS of the CUs.

1. Introduction

Nowadays, vehicle-to-everything (V2X) communication [1], an important main area of Internet of things (IoT) in the intelligent transportation systems (ITS), has attracted considerable attention. It is anticipated that there will be 1.5 billion mobile-connected devices in 2020 [2], including a large number of IoT devices.

On the other hand, 3GPP is working with the cellular V2X based on the new radio (NR) of the fifth-generation (5G) cellular mobile communication networks in release 16 [3]. It is one of typical applications of ultrareliability low-latency communications (uRLLC) in 5G [4] and can extensively provide enhanced V2X scenarios, such as vehicle platform, advanced driving, extended sensors, and remote driving [5].

It is expected that the future V2X communication will offer a wide range of services, such as safety applications, road traffic management, mobile video streaming, and other entertainment applications. This poses a greater challenge to the reasonable allocation of radio resources for V2X communication, especially to improve the channel capacity on the premise of ensuring the communication quality of the cellular users (CUs) [6].

There are two main spectrum sharing modes, namely, the underlay and the overlay spectrum access [7]. In the underlay mode, the V2X users (VUs) and the CUs can use the same licensed spectrum at the same time, but due to simultaneous access, the VUs inevitably cause the cochannel interference to the CUs. Therefore, it is necessary to control the interference of the VUs to the CUs so that the VUs can access the licensed spectrum under the condition of guaranteeing the quality of service (QoS) of the CUs. However, in the overlay mode, the VUs and the CUs also share the licensed spectrum at the same time. Different from the underlay mode, the VUs need the relevant information of the CUs, so as to help the CUs to send some information to compensate for their interference to the CUs, and then use the remaining time slots to transmit their own data.

This paper focuses on the underlay mode. The V2X communication [8] underlaying 5G cellular network means that the closer VUs can bypass the 5G base station (gNB) and establish direct communication pairs to each other. The
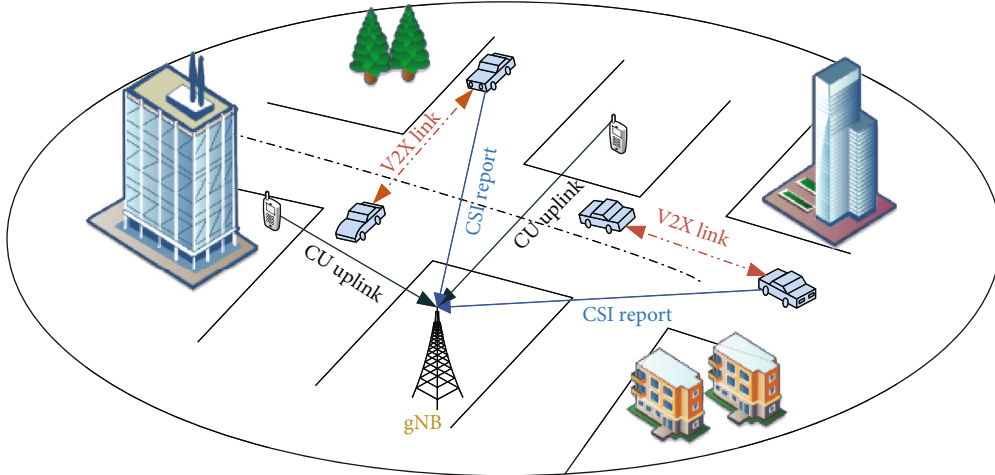
FIGURE 1: System model of underlaying V2X communication in 5G cellular network.

VUs can transmit on the cellular spectrum subject to the tolerable interference to the CUs. Therefore, the underlaying V2X communication can not only offload traffic from the 5G cellular infrastructure [9, 10] but also improve the spatial frequency reuse and energy efficiency.

To handle the ever-increasing demand of user associations, resource allocation for V2X communication underlaying 5G cellular networks [11] has attracted significant research and industry interests. In [12], a model for 5G virtualized networks in a heterogeneous cloud infrastructure is proposed, and resource allocation is formulated as a convex optimization problem, maximizing the overall system utility function. Halabian proposed a joint resource allocation solution that considers a double-sided auction-based distributed resource allocation (DS-ADRA) method [13]. Li et al. propose a method to maximize the sum of the proportional fairness functions of all users, while simultaneously taking into account factors such as the fairness, signal to interference plus noise ratio (SINR) requirements, and severe interference to ensure the QoS of users [14]. In [15], a resource allocation framework is presented for spectrum underlay in cognitive wireless networks and taking into account both interference constraints for primary users and quality of service (QoS) constraints for secondary users. In [16], a low-complexity algorithm is proposed to solve the nonconvex problem. Candidate D2D user equipment (DUE) sets are narrowed down according to required outage probability constraints, which are used to construct a simplified bipartite graph and then the Hungarian algorithm is used to determine the optimal pairing between D2D links and cellular user equipment (CUE). Zhang et al. propose a distance-based power control scheme for D2D communication underlaying uplink cellular network to achieve the expected performance gain without generating evident interference to primary CUE [17].

In this paper, our optimization objective is to minimize the interference to 5G CUs considering the SNR and rate requirements of VUs. The rest of the paper is organized as follows. The system model of underlay spectrum access is described in Section 2. We formulate the interference minimization underlay resource allocation problem of the described system in Section 3. Section 4 decomposes the proposed resource allocation scheme into subchannel assignment and power allocation and a suboptimal scheme is proposed. Finally, performance evaluation and conclusion are provided in Section 5 and Section 6, respectively.

2. System Model

We present the system model of V2X underlay 5G communication system, where multiple VUs coexist with multiple CUs in the same cell.

In our scheme, we only focus on the resource allocation for reusing the cellular uplink radio resources. A centralized resource allocation architecture is considered, where the gNB determines the radio resource allocation. As shown in Figure 1, if one VU (transmitter) has its designated VU (receiver) within its transmission range, the VU (transmitter) is allowed to bypass the gNB and communicates directly to the VU (receiver). This short-range, low-power V2X links coexist with the CU uplinks. The gNB has the capability of estimating the channel state information (CSI) of the cellular uplinks of CUs, whereas the CSI of the V2X links should be estimated at the VUs, then fed back to the gNB and use the uplink idle band to transmit the CSI report.

Each subchannel resource is assumed to be occupied by at most one VU link and one CU uplink. The total uplink system bandwidth B of CUs is divided into Z subchannels, and each VU link uses one subchannel. The index sets of subchannels are $\mathcal{Z} = \{1, 2, \cdots, Z\}$. The bandwidth of each subchannel is $B_0 = B/Z$. It is supposed that there are L CUs and K VUs, and the index sets of the CU uplinks and VU links are $\mathcal{L} = \{1, 2, \cdots, L\}$ and $K = \{1, 2, \cdots, K\}$, respectively.

3. Problem Formulation

The sum of the interference caused by VUs to CUs is expressed as

$$\sum_{l=1}^{L} I_l = \sum_{k=1}^{K} \sum_{z=1}^{Z} \rho_{k,z} I_{k,z}^S, \tag{1}$$

where $I_{k,z}^S$ denotes the interference power of the VU k to a certain CU uplink on the subchannel z. $\rho_{k,z}$ indicates whether a VU k occupies the subchannel z, and $\rho_{k,z} = 1$ indicates that the subchannel z is occupied by the VU k; $\rho_{k,z} = 0$ indicates that the subchannel z is not occupied by the VU k. Each subchannel can be occupied by only one VU at most.

The interference that the CUs can tolerate should satisfy

$$C1 : I_{k,z}^S \leq I^{\text{th}}, \quad \forall k \in \mathcal{K}, z \in \mathcal{Z}, \tag{2}$$

where I^{th} is the interference tolerance threshold of the CUs.

To verify the QoS of the VUs, the SINR should satisfy

$$C2 : \text{SINR}_{k,z}^S \geq \vartheta_k^{\text{th}}, \quad \forall k \in \mathcal{K}, z \in \mathcal{Z}, \tag{3}$$

where ϑ_k^{th} is the SINR threshold of the VU.

The transmission rate of each VU link should satisfy

$$C3 : R_k \geq R_{\min}, \quad \forall k \in \mathcal{K}, \tag{4}$$

where $R_{\min}$ is the minimum transmission rate of the VU.

The power constraint of the VU k should satisfy

$$C4 : \sum_{z=1}^{Z} \rho_{k,z} P_{k,z}^S \leq P_k, \quad \forall k \in \mathcal{K}, \tag{5}$$

where $\rho_{k,z}$ can be either 1 or 0 to represent whether the subchannel z is occupied by the kth VU or not; P_k is the maximum transmission power budgets of the VU k.

The optimization goal is to minimize the sum of the interference caused by the VUs to CUs. According to the above analysis, the objective function is expressed as

$$\min \sum_{k=1}^{K} \sum_{z=1}^{Z} \rho_{k,z} I_{k,z}^S$$

$$\text{s.t.C1} \sim C4$$

$$C5 : \rho_{k,z} \in \{0, 1\}, \quad \forall k \in \mathcal{K}, z \in \mathcal{Z} \tag{6}$$

$$C6 : \sum_{k=1}^{K} \rho_{k,z} \leq 1, \quad \forall z \in \mathcal{Z},$$

where C5 and C6 indicate that each subchannel is at most used by one VU.

4. The Proposed Allocation Algorithm

In order to facilitate the solution, we first transform the initial objective function (6) into an equivalent function. First, according to the SINR formula

$$\text{SINR}_{k,z}^S = \frac{P_{k,z}^S G_{k,z}^S}{I_{l,z}^O}, \tag{7}$$

where $P_{k,z}^S$ is the transmission power; $G_{k,z}^S$ is the channel power gain value; $I_{l,z}^O$ is the sum of interference and noise on subchannel z to the CU l.

Next, define Z' as the total number of subchannels actually allocated to K VUs; the index sets of which are $\mathcal{Z}' = \{1, 2, \cdots, Z'\}$. It is reasonable to assume that the number of subchannels that the network can provide is sufficient, that is, $Z' \leq Z$. Z' can be expressed as

$$Z' = \sum_{k=1}^{K} \frac{R_k}{B_0 \log_2 \left(1 + \text{SINR}_k^S\right)}, \tag{8}$$

where SINR_k^S is the minimum SINR among the subchannels actually used by the VU k.

We consider that the SINR of the CUs in the system must also be satisfied. If we let β^* as the minimum SINR threshold of the CU l, the maximum interference threshold I^{th} on the actually allocated subchannel z' of the CU receiver can be determined by

$$I^{\text{th}} = \frac{g_{l,z'}^P P_{l,z'}^P}{\beta^*} - N_0 B_0, \tag{9}$$

where N_0 is the noise power spectral density.

In order to minimize the interference caused by the VUs to the CUs, when the subchannel allocation is fixed, the SINR and data transmission rate of the VUs must be as low as possible. Therefore, the QoS of the VU resource allocation should take the minimum threshold, that is,

$$\text{SINR}_k^S = \vartheta_k^{\text{th}}, \tag{10}$$

$$R_k = R_{\min}. \tag{11}$$

When (10) and (11) are satisfied, the number of subchannels m_k allocated by the gNB to the VU k can be expressed as

$$m_k = \left\lceil \frac{R_{\min}}{B_0 \log_2 \left(1 + \vartheta_k^{\text{th}}\right)} \right\rceil. \tag{12}$$

And (8) can be rewritten as

$$Z' = \sum_{k=1}^{K} m_k = \sum_{k=1}^{K} \frac{R_{\min}}{B_0 \log_2 \left(1 + \vartheta_k^{\text{th}}\right)}. \tag{13}$$

The interference constraints and SINR constraints of the original optimization problem can be expressed as

$$C1' : \frac{I_{l,z'}^o \vartheta_k^{\text{th}}}{G_{k,z'}^S} \leq P_{k,z'}^S \leq \frac{g_{l,z'}^P P_{l,z'}^P}{g_{k,z'}^S \beta^*}. \tag{14}$$

The power and rate constraints in the original problem can be represented by C2$'$ and C3$'$, respectively.

$$C2' : \sum_{k=1}^{K} \sum_{z'=1}^{Z'} P_{k,z'}^{S} \leq P_{T},$$

$$C3' : \sum_{z'=1}^{Z'} \rho_{k,z'} = \frac{R_{\min}}{B_0 \log_2 \left(1 + \vartheta_k^{\mathrm{th}}\right)}. \tag{15}$$

According to the analysis above, the equivalent form of the original optimization problem in (6) is expressed as

$$\min \sum_{k=1}^{K} \sum_{z'=1}^{Z'} \rho_{k,z'} I_{k,z'}^{S}$$

$$\mathrm{s.t.} C1' \sim C3'$$

$$C4' : \boxtimes \rho_{k,z'} \in \{0, 1\}, \quad \forall k \in \mathcal{K}, z' \in \mathcal{Z}' \tag{16}$$

$$C5' : \boxtimes \sum_{k=1}^{K} \rho_{k,z'} \leq 1, \quad \forall z' \in \mathcal{Z}'.$$

Obviously, the optimization problem proposed in this paper is a mixed binary integer nonlinear programming (MBINP) problem. The variables to be solved are integer variable $\rho_{k,z'}$ and continuous variable $P_{k,z'}^{S}$, which are difficult to solve directly. Therefore, we use a stepwise algorithm for subchannel and power allocation. The main process of the algorithm includes three steps. First, the VU transmit power is initialized; then, when the power is determined, the Hungarian algorithm is used to complete the subchannel allocation; finally, power allocation is performed, and the initialization power of the subchannel allocated on the VU is limited according to the interference constraint condition and the power constraint condition. If these constraints are not satisfied, the VU on the subchannel refuses to share the frequency spectrum with the CU. The specific process of the algorithm is described as follows.

4.1. Transmit Power Initialization. Since the optimization goal is to minimize interference, according to equation $I_{k,z'}^{S} = g_{k,z'}^{S} P_{k,z'}^{S}$, interference is equal to the channel gain of the interfering link multiplied by the transmission power, so the transmission power of the VUs is also required to be minimal. Under constraint $C1'$, suppose

$$\frac{I_{l,z'}^{o} \vartheta_k^{\mathrm{th}}}{G_{k,z'}^{S}} \leq \frac{g_{l,z'}^{P} P_{l,z'}^{P}}{g_{k,z'}^{S} \beta^{*}}, \tag{17}$$

where $g_{k,z}^{S}$ is the power gain on the interference link from the cognitive base station to the receiving end of the CU, $g_{l,z'}^{P}$ is the power gain of the CU to the VU on the interference link, and $P_{l,z'}^{P}$ is the transmission power of the CU l on subchannel z'.

If (17) holds and constraint condition $C2'$ is satisfied, then the minimum transmission power required by the VU k on the subchannel z' is expressed as

TABLE 1: Simulation parameters.

Parameter	Value
gNB coverage radius (R)	500 m
Number of CUs (L)	4
Number of VUs (K)	2, 4, 8, 16, 32
Subchannel bandwidth (B_0)	0.3215 MHz
Pathloss factor (α)	4
Noise power spectral density (N_0)	4×10^{-20} W/Hz
Transmission power of CU ($P_{l,z}^{P}$)	100 mW
Total transmission power of gNB (P_{T})	2 W
SINR of CUs (β^{*})	20 dB
SINR of VUs ($\vartheta_k^{\mathrm{th}}$)	[-15 dB, 15 dB]

$$P_{k,z'}^{S} = \frac{I_{l,z'}^{o} \vartheta_k^{\mathrm{th}}}{G_{k,z'}^{S}}. \tag{18}$$

4.2. Subchannel Allocation. After completing the power initialization, the optimization problem can be expressed as

$$\min_{\rho_{k,z}} \sum_{k=1}^{K} \sum_{z'=1}^{Z'} \rho_{k,z'} \frac{g_{k,z'}^{S} I_{l,z'}^{o} \vartheta_k^{\mathrm{th}}}{G_{k,z'}^{S}}$$

$$\mathrm{s.t.} C3' : \sum_{z'=1}^{Z'} \rho_{k,z'} = \frac{R_{\min}}{B_0 \log_2 \left(1 + \vartheta_k^{\mathrm{th}}\right)} \tag{19}$$

$$C4' : \rho_{k,z'} \in \{0, 1\}, \quad \forall k \in \mathcal{K}, z' \in \mathcal{Z}'$$

$$C5' : \sum_{k=1}^{K} \rho_{k,z'} \leq 1, \quad \forall z' \in \mathcal{Z}'.$$

According to equation (19), it can be seen that the optimization problem is a 0-1 assignment integer linear programming problem about $\rho_{k,z}$. The Hungarian algorithm [18] is used here to solve the global optimal solution of the problem.

4.3. Power Allocation. The Hungarian algorithm is used to complete the subchannel allocation. However, in order to perform the optimal power allocation, both the constraint condition $C2'$ and condition (17) assumed when initializing the power need to be reconsidered based on the subchannel allocation results. Therefore, after each VU has assigned a subchannel, power detection needs to be performed according to the constraints. If the power allocated by the VU satisfies condition (17) and the total transmission power satisfies the constraint condition $C2'$, then the power allocation result is the optimal solution of the original optimization problem and completes resource allocation; otherwise, the following VU access control iterative algorithm will be used to reallocate power.

Step 1. If assumption (17) is not satisfied, it means that the VU cannot obtain enough transmission power to satisfy its
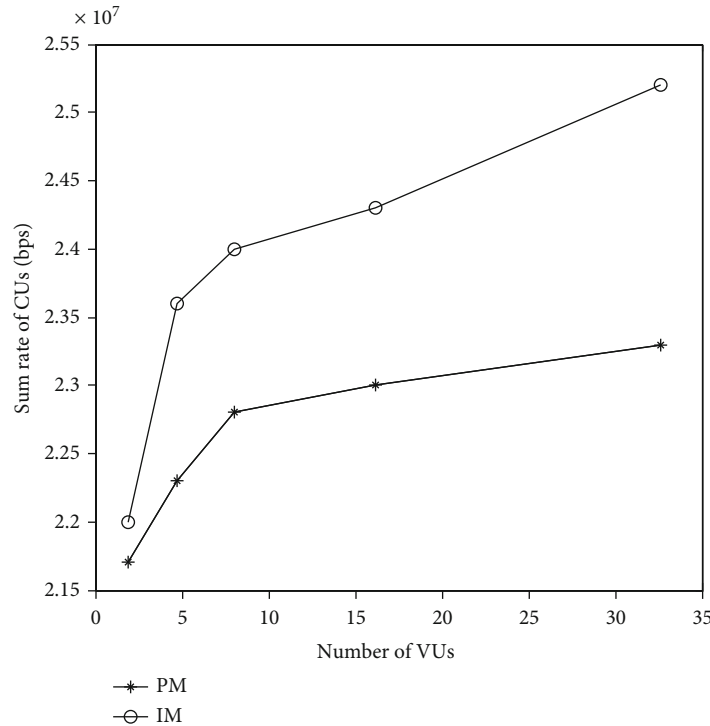
FIGURE 2: Performance of the number of VUs and the CU rate.

SINR requirements under the restriction of the CU interference threshold, so the VU must give up access to the shared spectrum opportunity.

Step 2. On the basis of Step 1, the VU does not give up the opportunity to access the spectrum, so the VU can choose to compromise on the data rate requirement and access the spectrum at a data rate lower than its own requirement.

Step 3. Next, considering constraint condition C2$'$, the total transmission power can be obtained based on the initialization power and subchannel allocation above. If the total power exceeds the power threshold in constraint condition C2$'$, the subchannel allocated to the maximum power is denied access to the VU. Then, recalculate the power until the constraint condition C2$'$ is satisfied, at which point the power allocation is completed.

5. Performance Evaluation

This section uses MATLAB to simulate and analyze the above resource allocation algorithms and compares them with traditional algorithms. The simulation results are the average of 1,000 Monte Carlo experiments. The simulation parameters are shown in Table 1. One gNB and multiple VUs are considered, and all users are randomly distributed in the covered cell. The slow fading in the system model is assumed to be multipath Rayleigh fading, pathloss factor α = 4, and shadow fading standard deviation σ_{XY} = 4 dB. It is also assumed that the angle between the movement direction of each VU and the horizontal axis of the coordinate system

is a random value uniformly distributed between 0 and 2π. Simultaneously, the location information and spectrum sensing results of the VUs can be transmitted to the gNB through dedicated channels. According to [19], the authors propose that in a mobile scenario and the VUs predict the channel state information, assuming that the time required for the VUs to sense once is 1 ms, then the time for the VUs to sense twice is 2 ms.

We first analyze the complexity of the algorithm. The complexity of the proposed resource allocation algorithm is determined by three steps in Section 3. Due to the small number of subchannels and VUs, compared with the integer programming problem in the second step, the complexity of the initialization power in the first step and the iterative power allocation in the third step is greatly reduced and can be ignored. So the complexity of the resource allocation algorithm mainly depends on the second step of the subchannel allocation process. According to [20], the complexity of the Hungarian subchannel allocation algorithm is $O(K^3 Z'^3)$.

In order to facilitate the analysis and ensure the fairness of the comparative analysis, first define the algorithm for comparison. For the comparison of power minimization algorithms, we consider the same constraints and solution algorithms, but change the optimization goal to minimize the transmission power of VUs, it is expressed as "PM." The complexity of PM is also $O(K^3 Z'^3)$. Meanwhile, the minimum interference we propose is expressed as "IM."

Figures 2 and 3 compare the two algorithms, showing the rate of the CUs, and the performance of the total power required by the VUs varies with the number of VUs.
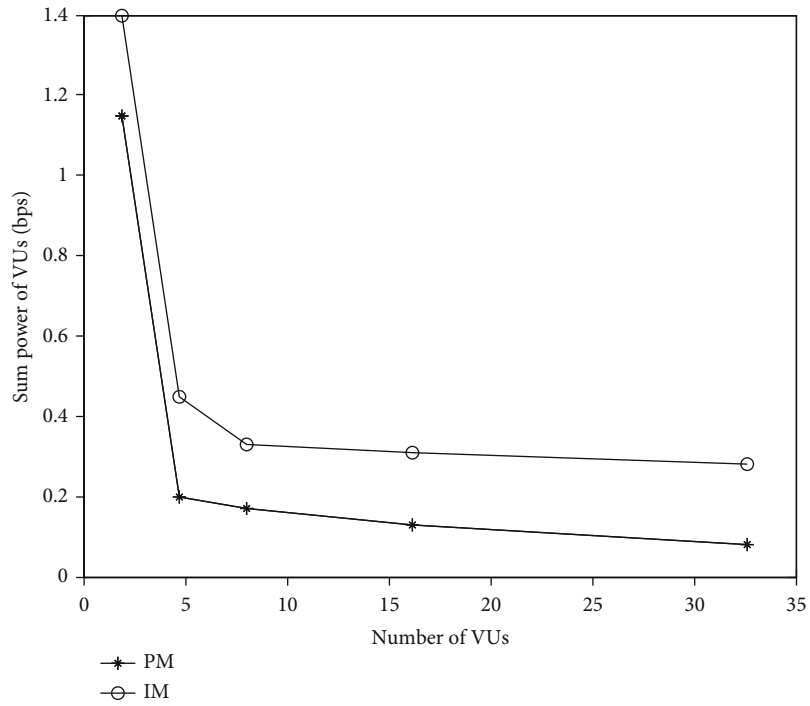
Figure 3: Performance of the number of VUs vs. the total power of VUs.
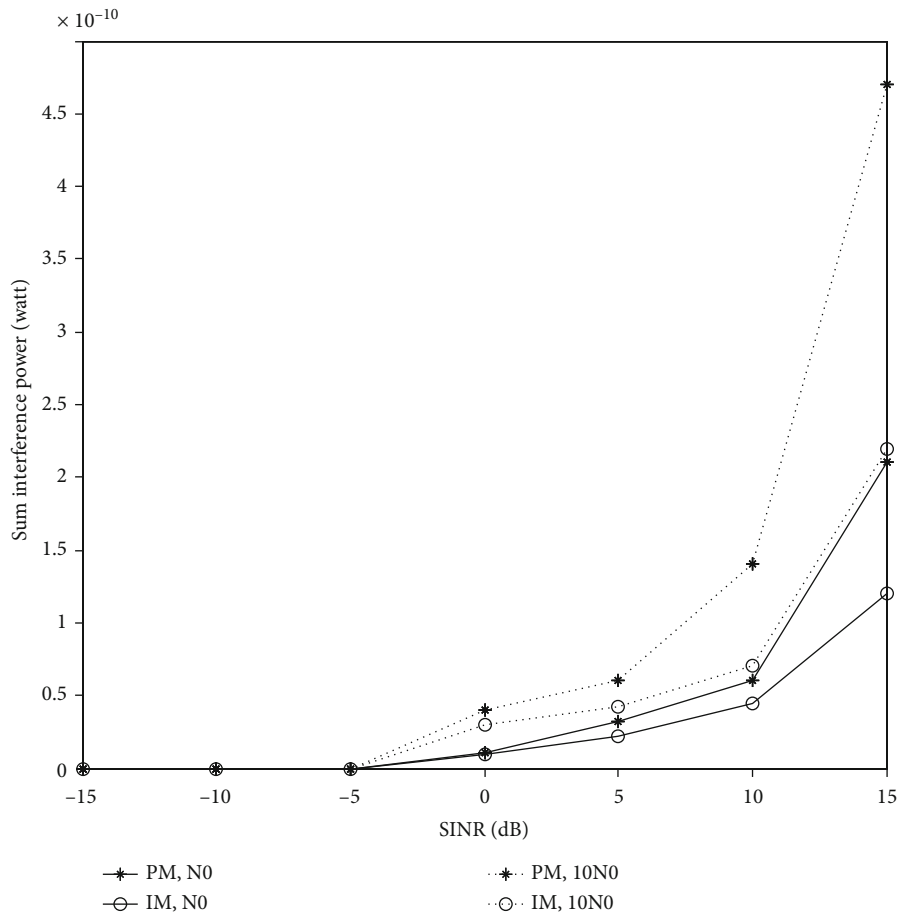
Figure 4: Performance of SINR, noise power, and interference of CUs.
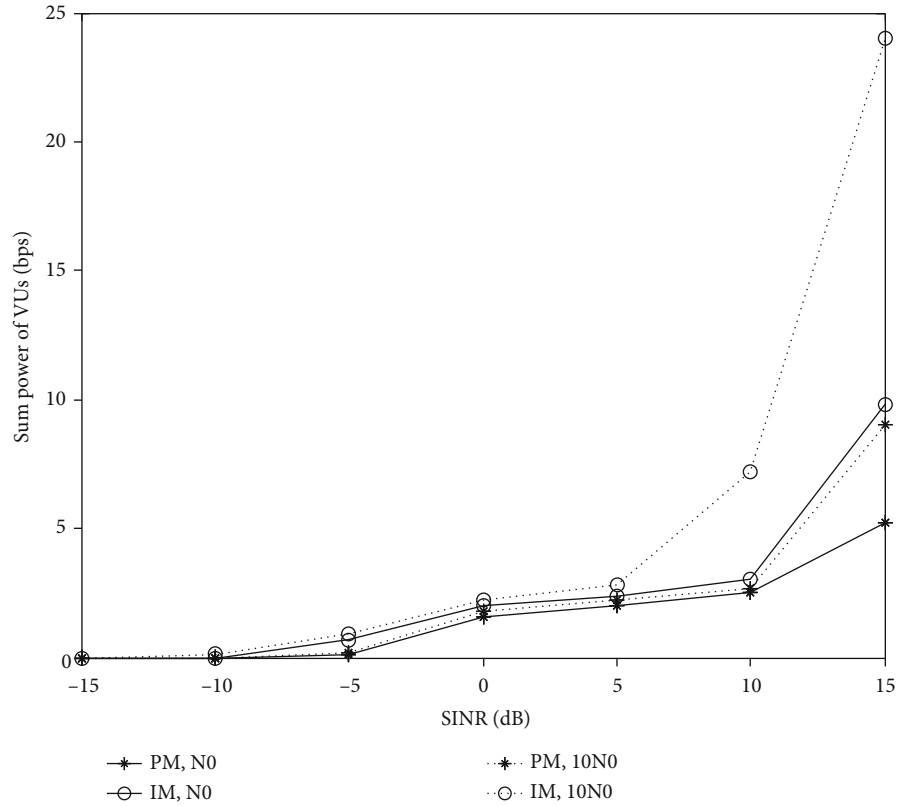
FIGURE 5: Performance of SINR, noise power, and total power of VUs.

The CU rate obtained by the PM and IM algorithms increases with the number of VUs, and under the same conditions, the IM algorithm can obtain a larger CU rate in Figure 2. This is also because when the number of VUs increases, the subchannels have more opportunities to be assigned to better channel states and VUs with less interference, and when the CUs suffer less interference, the CU rate will inevitably increase.

Total power of the VUs obtained by the IM and PM algorithms decreases as the number of VUs increases in Figure 3. When the number of VUs is small, the cognitive base station total power required by the VUs is large. However, as the number of VUs increases, subchannels can be allocated to more suitable VUs, so the required power is naturally reduced.

Considering Figures 2 and 3 together, it can be seen that the conclusions obtained by the two figures are basically the same: the proposed IM algorithm not only guarantees QoS, power, and interference of VUs but also reduces the interference to CUs, thus protecting the capacity of CUs and improving the adaptability of CUs to different business requirements.

Figures 4 and 5 compare and analyze the rules of the interference to the CUs and the performance of the total power required by the VUs with the change of the SINR of the VUs under two different noise power conditions.

As can be seen from Figure 4, the CU interference obtained by the IM and PM algorithms increases with the VU SINR. Compared with PM, IM has the least interference

to the CUs. From Figure 5, we can see the same trend. When the VU SINR is relatively small, the total power obtained by IM and PM is small. However, with the increase of the SINR of the VUs, the total power of IM and PM also increases. Combining the two graphs shows that when the SINR is relatively low, the performance of the IM and PM algorithms is better. As the SINR becomes larger, the VUs require more power, and the interference to the CUs will also increase. If the SINR continues to increase, the power required by the VUs and the interference caused to the CUs will exceed the threshold value. At the same time, it can be seen that the larger the noise power, the greater the power required by the system and the interference to the CUs, and the performance is far worse than under low noise power conditions.

Finally, Figure 6 compares the performance of the two algorithms with the change of SINR of VUs. It can be seen from Figure 6 that the CU rate obtained by the IM and PM algorithms decreases as the SINR increases, and the CU rate obtained by the PM algorithm is lower than that in the IM algorithm. At the same time, the rate of the CUs is kept at an acceptable low level due to the significant increase in the rate of the VUs. For the IM and PM algorithms, as the SINR increases, cognitive base stations need to allocate more power to VUs to satisfy their requirements. Therefore, the VUs will inevitably cause greater interference to the CUs. According to the Shannon channel capacity formula of the CUs, gradually increasing interference will cause the CU rate to decrease.
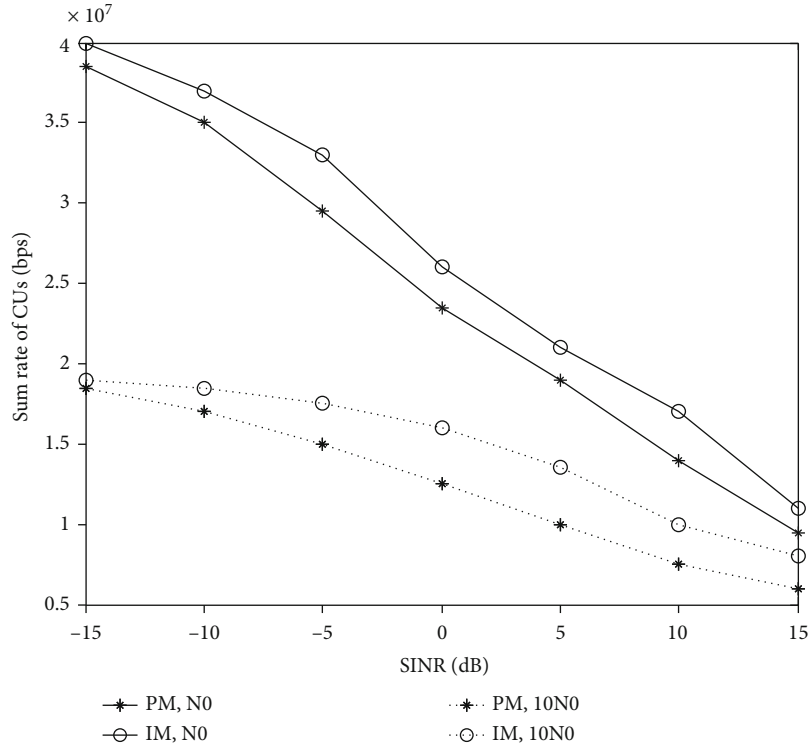
FIGURE 6: Performance of SINR vs. CU rate.

Combined with Figures 4–6, it can be seen that the performance of IM and PM algorithms is similar with the increase of SINR of VUs, but IM can have less interference, which further protects the channel capacity of CUs.

6. Conclusion

In this paper, we propose a resource allocation algorithm to V2X communication under 5G networks, where VUs and CUs coexist in 5G cellular networks. Considering the constraints of the SINR and the minimal rate and the interference threshold requirements of each VU, the power and subchannel allocation of the VUs is allocated according to the channel gain of the VUs and the interference of each VU link to the CUs. The objective function is established according to the goal of minimizing interference while satisfying multiple constraints. We use three stages to solve MBINP and propose an optimization power allocation mechanism. Simulation results demonstrate that, compared with PM and RM algorithms, the proposed resource allocation algorithm can satisfy the QoS of VUs while minimizing the interference to CUs and can further protect the channel capacity of the CUs.

Data Availability

The model data used to support the findings of this study are included within the article. The code data used to support the findings of this study have not been made available because the data also forms part of an ongoing study.

Conflicts of Interest

The authors declare that there is no conflict of interest regarding the publication of this paper.

Acknowledgments

References

[1] S. Chen, J. Hu, Y. Shi et al., "Vehicle-to-everything (v2x) services supported by LTE-based systems and 5G," *IEEE Communications Standards Magazine*, vol. 1, no. 2, pp. 70–76, 2017.

[2] M. Peng, Y. Sun, X. Li, Z. Mao, and C. Wang, "Recent advances in cloud radio access networks: system architectures, key techniques, and open issues," *IEEE Communications Surveys & Tutorials*, vol. 18, no. 3, pp. 2282–2308, 2016.

[3] *Study on NR Vehicle-to-Everything (V2X)*, Standard 3GPP TR 38.885, 2018.

[4] X. Li, J. Li, Y. Liu, Z. Ding, and A. Nallanathan, "Residual transceiver hardware impairments on cooperative NOMA networks," *IEEE Transactions on Wireless Communications*, vol. 19, no. 1, pp. 680–695, 2020.

[5] Y. Kim, F. Sun, Y. Wang et al., "New radio (NR) and its evolution toward 5G-advanced," *IEEE Wireless Communications*, vol. 26, no. 3, pp. 2–7, 2019.

[6] N. Cheng, H. Zhou, L. Lei et al., "Performance analysis of vehicular device-to-device underlay communication," *IEEE Transactions on Vehicular Technology*, vol. 66, no. 6, pp. 5409–5421, 2017.

[7] I. de la Iglesia, U. Hernandez-Jayo, E. Osaba, and R. Carballedo, "Smart bandwidth assignation in an underlay cellular network for internet of vehicles," *Sensors*, vol. 17, no. 10, p. 2217, 2017.

[8] A. Asadi, Q. Wang, and V. Mancuso, "A survey on device-to-device communication in cellular networks," *IEEE Communications Surveys & Tutorials*, vol. 16, no. 4, pp. 1801–1819, 2014.

[9] X. Li, J. Li, and L. Li, "Performance analysis of impaired SWIPT NOMA relaying networks over imperfect Weibull channels," *IEEE Systems Journal*, vol. 14, no. 1, pp. 669–672, 2020.

[10] X. Li, M. Liu, C. Deng, P. T. Mathiopoulos, Z. Ding, and Y. Liu, "Full-duplex cooperative NOMA relaying systems with I/Q imbalance and imperfect SIC," *IEEE Wireless Communications Letters*, vol. 9, no. 1, pp. 17–20, 2020.

[11] Q. Chen, H. Jiang, and G. Yu, "Service oriented resource management in spatial reuse-based C-V2X networks," *IEEE Wireless Communications Letters*, vol. 9, no. 1, pp. 91–94, 2020.

[12] L. Ferdouse, A. Anpalagan, and S. Erkucuk, "Joint communication and computing resource allocation in 5G cloud radio access networks," *IEEE Transactions on Vehicular Technology*, vol. 68, no. 9, pp. 9122–9135, 2019.

[13] H. Halabian, "Distributed resource allocation optimization in 5G virtualized networks," *IEEE Journal on Selected Areas in Communications*, vol. 37, no. 3, pp. 627–642, 2019.

[14] X. Li, R. Shankaran, M. A. Orgun, G. Fang, and Y. Xu, "Resource allocation for underlay D2D communication with proportional fairness," *IEEE Transactions on Vehicular Technology*, vol. 67, no. 7, pp. 6244–6258, 2018.

[15] L. Le and E. Hossain, "Resource allocation for spectrum underlay in cognitive radio networks," *IEEE Transactions on Wireless Communications*, vol. 7, no. 12, pp. 5306–5315, 2008.

[16] L. Wang, H. Tang, H. Wu, and G. L. Stüber, "Resource allocation for D2D communications underlay in Rayleigh fading channels," *IEEE Transactions on Vehicular Technology*, vol. 66, no. 2, pp. 1159–1170, 2017.

[17] Z. Zhang, R. Q. Hu, and Y. Qian, "D2D communication underlay in uplink cellular networks with distance based power control," in *2016 IEEE International Conference on Communications (ICC)*, pp. 1–6, Kuala Lumpur, December 2016.

[18] H. W. Kuhn, "The Hungarian method for the assignment problem," *Naval Research Logistics*, vol. 52, no. 1, pp. 7–21, 2005.

[19] D. W. K. Ng, E. S. Lo, and R. Schober, "Energy-efficient resource allocation in multi-cell OFDMA systems with limited backhaul capacity," *IEEE Transactions on Wireless Communications*, vol. 11, no. 10, pp. 3618–3631, 2012.

[20] L. Zhang, M. Xiao, G. Wu, S. Li, and Y.-C. Liang, "Energy-efficient cognitive transmission with imperfect spectrum sensing," *IEEE Journal on Selected Areas in Communications*, vol. 34, no. 5, pp. 1320–1335, 2016.

WILEY | Hindawi

Research Article

Real-Time Performance Evaluation of IEEE 802.11p EDCA Mechanism for IoV in a Highway Environment

Hong Li,[1] **Qiong Wu** ,[2,3] **Jing Fan** ,[1] **Qiang Fan,**[4] **Bo Chang,**[2] **and Guilu Wu**[3]

[1]*University Key Laboratory of Information and Communication on Security Backup and Recovery in Yunnan Province, Yunnan Minzu University, Kunming 650500, China*
[2]*Jiangsu Laboratory of Lake Environment Remote Sensing Technologies, Huaiyin Institute of Technology, Huaian 223003, China*
[3]*School of Internet of Things Engineering, Jiangnan University, Wuxi 214122, China*
[4]*Department of Electrical and Computer Engineering, New Jersey Institute of Technology, Newark, NJ 07102, USA*

Correspondence should be addressed to Qiong Wu; qiongwu@jiangnan.edu.cn and Jing Fan; fanjing9476@163.com

With the development of 5G, the Internet of Vehicles (IoV) evolves to be one important component of the Internet of Things (IoT), where vehicles and public infrastructure communicate with each other through a IEEE 802.11p EDCA mechanism to support four access categories (ACs) to access a channel. Due to the mobility of the vehicles, the network topology is time varying and thus incurs a dynamic network performance. There are many works on the stationary performance of 802.11p EDCA and some on real-time performance, but existing work does not consider real-time performance under extreme highway scenario. In this paper, we consider four ACs defined in the 802.11p EDCA mechanism to evaluate the limit of the real-time network performance in an extreme highway scenario, i.e., all vehicles keep the minimum safety distance between each other. The performance of the model has been demonstrated through simulations. It is found that some ACs can meet real-time requirements while others cannot in the extreme scenario.

1. Introduction

Nowadays, IoT networks are deployed to collect various information from surrounding systems through the real-time interaction with environment [1]. As one kind of IoT, Internet of Vehicles (IoV) enables vehicles and infrastructures to exchange data through the vehicle-to-vehicle (V2V) communications and vehicle-to-infrastructure (V2I) communications [2]. With the aid of the emerging 5G technologies, IOV will develop rapidly [3, 4]. There are many researches on 5G in the industry and academia [5]; 5G can be utilized to facilitate low latency, high reliability, and higher quality communication of IoV [6, 7]. It is promising to overcome some bottlenecks and thus significantly improve the network performance of IoV [8].

With the development of IoV, effectiveness and safety have become the key factors considered by an intelligent transportation system (ITS) [9]. In the network, each mobile vehicle is considered a node with a variety of secure/nonse-

cure applications. IEEE 802.11p is a physical layer and medium access control (MAC) layer standard and has been widely used in wireless access in vehicular environments (WAVE) [10]. It adopts an enhanced distributed channel access (EDCA) mechanism to access a channel. The IEEE 802.11p EDCA mechanism defines four ACs to provision services of different priorities through setting different parameters [11].

One of the characteristics of the IoV is dynamic topology changes. For example, when vehicles are moving on the highway, the movement of the vehicles and the drivers' decision will cause the network topology to change (not always in a stationary state). Some analytical models have been put forward in existing performance modeling studies of the 802.11p EDCA mechanism in IoV [12–14], In [12], Han et al. constructed models to analyze the stationary performance of the 802.11p EDCA mechanism. In [13], Zheng and Wu considered the factors including saturated condition (vehicles always have data to transmit) and nonsaturated

condition (vehicle do not always have data to transmit), standard parameters, backoff counter, internal collision, and computational complexity to analyze the performance of the IEEE 802.11p EDCA mechanism in the stationary state. In [14], Yao et al. used the probability generating function (PGF) approach to capture the nonstationary performance of IoV.

As far as we know, most existing works only studied the stationary performance of the 802.11p EDCA mechanism, but the vehicular network is in a high-speed environment, and thus the number of vehicles in the carrier sensing range of each vehicle is changing all the time, which cause the performance of the 802.11p EDCA mechanism to be changed in real time. Therefore, the traditional analysis methods were not suitable for the real situations. In [15], Xu et al. constructed models to study the time-varying behaviour of the 802.11p EDCA mechanism in a two-way highway scenario, but this work only considers two ACs, which does not consist of the definition of the 802.11p EDCA mechanism. According to the regulations in [16], the vehicles driving on the highway should follow the 4-second rule, i.e., the time interval between two contiguous vehicles on a common lane passing through a fixed reference object beside the highway should be larger in four seconds. Thus, there is a minimum safety distance between contiguous vehicles. To the best of our knowledge, there is no work analyzing the limit of the real-time performance of the 802.11p EDCA mechanism in the extreme highway scenario, i.e., all vehicles keep the minimum safety distance between each other, which motivates us to conduct this work. In this paper, we consider four ACs and conduct models to analyze the limit of the real-time performance of the 802.11p EDCA mechanism in IoV. Note that it is challenging to build a model in complex road conditions and to calculate the performance of the 802.11p EDCA mechanism considering four ACs.

The rest of this paper is organized as follows. In Section 2, a review of related work is presented. In Section 3, we describe the scenario and model IEEE 802.11p EDCA mechanism. The analytical model is provided in Section 4. In Section 5, numerical results are provided for performance evaluation and comparison. Finally, Section 6 concludes the paper.

2. Related Work

In this section, we first review the existing works for the performance analysis of the 802.11 distributed coordination function (DCF) mechanism, which is the basis of the 802.11p EDCA mechanism; next, we review the related works on the performance analysis of the 802.11p EDCA mechanism; and finally, the works about the real-time performance analysis of the 802.11p EDCA mechanism is reviewed.

There are lots of existing modeling approaches to analyze the performance of the 802.11 DCF mechanism. In [17], Bianchi proposed a simple two-dimensional Markov chain model under the assumption of an ideal channel and finite number terminals to describe the binary exponential backoff algorithm and computed the saturated throughput perfor-

mance based on the proposed model. In [18], Ni et al. proposed an analytical model to calculate the throughput under saturated conditions in both congested and error-prone channels. In [19], Malone et al. took the 802.11 DCF mechanism-based network and bursty data traffic into account to derive a carrier sense multiple access/collision avoidance (CSMA/CA) model in a nonsaturated environment and validated the accuracy of the derived model through simulation. Some works analyzed the broadcast performance of the DCF mechanism in IoV. In [20], Vinel et al. proposed an analytical D/M/1 queue model to calculate the message reception probability and mean packet delay in the 802.11 DCF mechanism-based vehicular networks. In [21], Ma et al. proposed a 1-D Markov chain model to analyze the broadcast performance of the 802.11a DCF mechanism and evaluate the packet reception rate (PRR) and packet delay (PD) of V2V safety-related broadcast services.

In addition to those works, there are some studies about the analysis of the 802.11p EDCA mechanism. In [12], Han et al. proposed a three-dimensional Markov chain analytical model to analyze the 802.11p EDCA mechanism under a saturated network condition. The proposed model is validated through simulations and is justified to be suitable for both basic access and the request to send/clear to send (RTS/CST) access mode, but it does not consider backoff freezing. In [22], Gallardo et al. proposed a Markovian model to analyze the performance of the 802.11p EDCA mechanism over the control channel (CCH) under both saturated and nonsaturated conditions. The model is composed by three Markov chains, and each chain describes the backoff procedure of an AC. It can be used to compute the throughput, frame error rate, and delay of the AC. In [23], Kaabi et al. only considered one AC and proposed an analytical model to investigate the performance of the IEEE 802.11p EDCA mechanism for safety messages in IoV, but they did not analyze the delay. In [13], Zheng and Wu considered the factors including saturated and nonsaturated condition, standard parameters, backoff counter, internal collision, and computational complexity and developed two Markov chains to analyze the performance of the IEEE 802.11p EDCA mechanism; the simulation experiments are conducted to verify the effectiveness of the derived performance models. However, these works focus on the stationary performance analysis of the 802.11p EDCA mechanism, which is not realistic in the dynamic IoV.

As described above, researches on stationary performance are mature. There are few works study on the real-time performance analysis of the IEEE 802.11p EDCA mechanism. In [24], Bilstrup et al. analyzed the channel delay of the 802.11p EDCA mechanism through simulations and compared with a self-organizing time division multiple address (TDMA). It is proven that TDMA is more suitable for the time-sensitive application in IoV. In [14], Xu et al. proposed a fluid-flow performance model to analyze the real-time performance of the 802.11p EDCA mechanism. The proposed model is computationally efficient, generalized and accurate to calculate the real-time performance of PD and packet delivery ratio (PDR). However, none of them considered four ACs to analyze the limit of the real-time
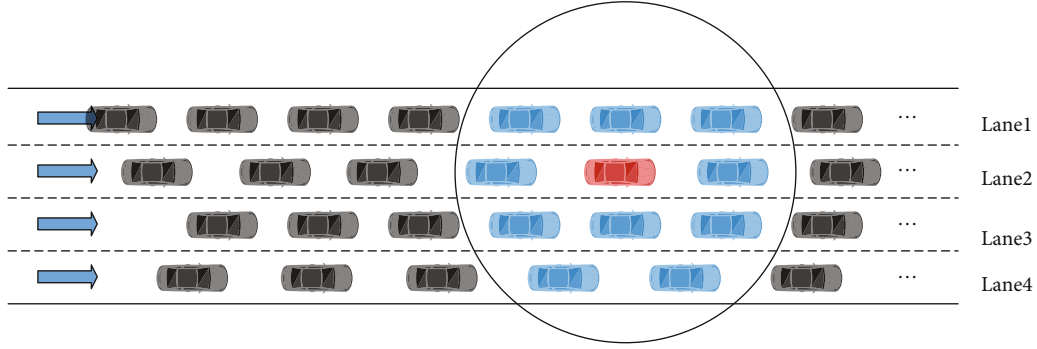
Figure 1: Network scenario in highway.

performance of 802.11p EDCA in the extreme highway scenario, which is the motivation of this work.

3. System Model

In this section, we first describe the extreme highway scenario; then, the 802.11p EDCA mechanism is reviewed briefly.

3.1. Extreme Highway Scenario. In order to find the performance limit of the network, we consider an extreme highway scenario as shown in Figure 1. Specifically, vehicles are driving on a one-way four-lane highway, where vehicles driving on the common lane with the same velocity and the velocities of the vehicles on the different lane are different. The distance between any of the contiguous vehicles on the common lane, i.e., intervehicle distance, is set to the minimum safety distance according to the 4-second rule. Since the minimum safety distance is determined by the velocity of vehicles, the intervehicle distances are different on different lanes. Each vehicle adopts the IEEE 802.11p protocol to exchange data packet through wireless communication. The channel access mechanism of the 802.11p protocol is the EDCA mechanism. Packets arrive at AC_m ($m = 0, 1, 2, 3$) of a vehicle according to the Poisson process with arrival rate $\lambda_m(t)$. In order to investigate the real-time performance of the 802.11p EDCA mechanism for each vehicle in the network, we denote the investigated vehicle as the target vehicle. As shown in Figure 1, the red vehicle is the tagged vehicle, and the blue vehicles are the vehicles within the carrier sensing range of the target vehicle which can successfully send or receive the packet from the tagged vehicle. Meanwhile, the black vehicles are not within the carrier sensing range of the target vehicle and they cannot communicate with the tagged vehicle. Next, we review the 802.11 EDCA mechanism briefly.

3.2. IEEE 802.11p EDCA Mechanism. The IEEE 802.11p EDCA mechanism defines four AC queues to support different priorities of services to access a channel [25], i.e., voice (VO), video (VI), best effort (BE), and background (BK) [26], where each AC queue has a specific parameter configuration, including the minimum backoff window $\mathrm{CW}_{\mathrm{min}}$, maximum backoff window $\mathrm{CW}_{\mathrm{max}}$, arbitration interframe space number AIFSN, and the retransmission limit. When

a packet arrives at the AC_m queue of a vehicle, it will be transmitted when the channel status is idle. If the channel is busy, the vehicle will continue to detect the channel until the channel keeps idle for AIFS[m], then start a backoff process, where AIFS[m] is calculated as

$$\mathrm{AIFS}[m] = \mathrm{AIFSN}[m] \times \sigma + \mathrm{SIFS}, \tag{1}$$

where SIFS is the short interframe space and σ is a slot time.

The backoff process is described as follows. The contention window size W_m^0 is first set to $\mathrm{CW}_m^{\mathrm{min}} + 1$ and a value is randomly selected from $[0, W_m^0]$ as the value of a backoff counter; then, it would be decreased by one after each idle slot [27]. If the channel is busy during the backoff process, the value of the backoff counter will be frozen until the channel becomes idle again [28]. When the backoff counter is decreased to 0, the packet will be transmitted. At this time, the transmission is successful if no AC of other vehicles and no higher priority AC of the vehicle are transmitting. Otherwise, a collision occurs. Specifically, an external collision occurs if at least one AC of other vehicles is transmitting, and an internal collision occurs if at least one other AC of this vehicle is transmitting. In the condition of a collision, the contention window size is doubled, and a new backoff process is initiated to retransmit the packet. The contention window would not be doubled after the number of retransmission reaches M_m. If the number of retransmission reaches the retransmission limit $M_m + f_m$, the packet would be dropped. The contention window of the AC_m queue under the number of retransmission i is given by

$$W_m^i = \begin{cases} \mathrm{CW}_m^{\mathrm{min}} + 1, & i = 0, \\ 2^i W_m^0, & 1 \leq i \leq M_m, \\ \mathrm{CW}_m^{\mathrm{max}} + 1, & M_m \leq i \leq M_m + f_m. \end{cases} \tag{2}$$

The access process of 802.11p is shown in Figure 2. Note that if an internal collision occurs, the packet with the highest priority will be transmitted, the contention window of the lower priority will be doubled, and then a backoff process is initiated.
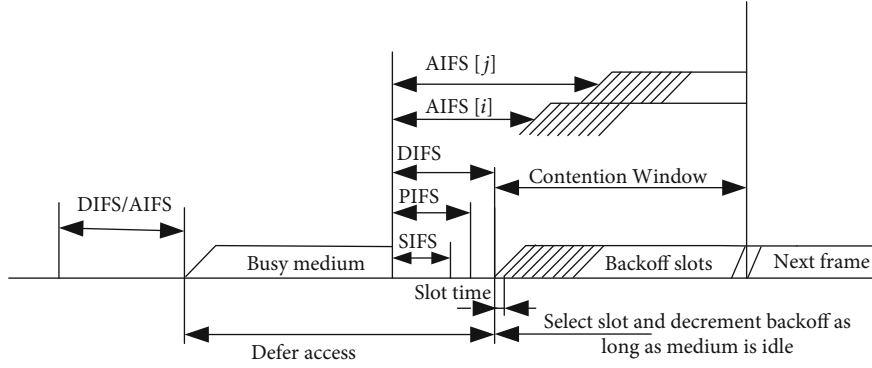
FIGURE 2: IEEE 802.11p EDCA process.

4. Analytical Model

In this section, we elaborate our model to analyze the real-time performance of the 802.11p EDCA mechanism. We first construct a connectivity metric to denote the connection of vehicles in the network, and then, we develop models to derive the real-time performance of the IEEE 802.11p EDCA mechanism including the mean service time and variance for the target vehicle. The notations used in this paper are summarized in Table 1.

4.1. Connectivity Metric. There are N vehicles in this scenario, the vehicles are numbered sequentially from lane 4 to lane 1, and on each lane vehicles are numbered from left to right, e.g., the number of the leftmost vehicle on lane 4 is 1 and the number of the rightmost vehicle on lane 1 is N. The coordinate of vehicle l is denoted as (s_{abs}^l, s_{ord}^l); here, we set that the coordinate of vehicle 1 as $(0,0)$. Each vehicle can acquire the coordination of other vehicles through communications; thus, each vehicle can acquire the matrix of the coordination of N vehicles at time t, i.e.,

$$S(t) = \left\{ \begin{array}{c} [s_{abs}^1(t), s_{ord}^1(t)] \\ [s_{abs}^2(t), s_{ord}^2(t)] \\ \vdots \\ [s_{abs}^N(t), s_{ord}^N(t)] \end{array} \right\}. \tag{3}$$

If the Euclidean distance of the two vehicles is less than the carrier sensing range, they are considered to be connected with each other, i.e., communicate with each other. Each vehicle can calculate a connectivity metric $H(t)$ according to $S(t)$ to denote the connectivity of the vehicles in the network at time t, i.e.,

$$H(t) = \begin{bmatrix} h_{1,1}(t) & h_{1,2}(t) & \cdots h_{1,N}(t) \\ h_{2,1}(t) & h_{2,2}(t) & \cdots & h_{2,N}(t) \\ \vdots & \vdots & \ddots & \vdots \\ h_{N,1}(t) & h_{N,2}(t) & \cdots & h_{N,N}(t) \end{bmatrix}, \tag{4}$$

where $h_{k,l}(t)$ denotes whether vehicle k can connect with vehicle l.

In our scenario, vehicles drive on the same lane with the same velocity and drive on different lanes with different velocities. Since the intervehicle distance is related with the velocity of vehicles, the intervehicle distances of vehicles are the same on the same lane and are different on different lanes. Therefore, the connection of the vehicles in the network is changed in real time due to the different velocities and intervehicle distances on different lanes, thus causing the matrix $H(t)$ to be time varying. Let vehicle k be the target vehicle in the network, the number of vehicles in the carrier sensing range of the tagged vehicle k can be calculated according to $H(t)$, i.e.,

$$N_{tr}^k(t) = \sum_{l=1}^{N} h_{k,l}(t). \tag{5}$$

4.2. Real-Time Mean Service Time and Variance. In this section, we regard access process of the 802.11p EDCA mechanism as the service process and derive the real-time performance of the IEEE 802.11p EDCA mechanism including the mean service time and variance for the target vehicle k. The mean service time and variance can be calculated according to the first and second moments of the probability generating function (PGF) of service time of AC_m for vehicle k, i.e.,

$$E_m^k = \left. \frac{dP_{Ts}^{k,m}(z)}{dz} \right|_{z=1}, \tag{6}$$

$$D_m^k = \left\{ \frac{d^2 P_{Ts}^{k,m}(z)}{dz^2} + \frac{dP_{Ts}^{k,m}(z)}{dz} - \left[\frac{dP_{Ts}^{k,m}(z)}{dz} \right]^2 \right\} \Bigg|_{z=1}, \tag{7}$$

where $P_{Ts}^{k,m}(z)$ is the PGF of service time and is calculated according the Markov chain in [29], which is shown as follows:

$$\begin{cases} P_{Ts}^{k,0}(z) = \dfrac{TR(z)}{W_0^0} \sum_{k=0}^{W_0^0-1} \left[H_m^k(z)\right]^k, \\ P_{Ts}^{k,m}(z) = \left[1 - p_c^{k,m}(t)\right] TR(z) \sum_{n=0}^{M_m+f_m} \left\{ \left[p_c^{k,m}(t)\right]^n \prod_{i=0}^{n} B_{m,i}^k(z) \right\} + p_c^{k,m}(t)^{M_m+f_m+1} \prod_{i=0}^{M_m+f_m} B_{m,i}^k(z), m = 1, 2, 3, \end{cases}$$ (8)

where $TR(z)$ is the PGF of transmission time, $B_{m,i}^k(z)$ is the PGF of stationary probability of AC_m at stage i for vehicle k, $H_m^k(z)$ is the PGF of the average duration that the backoff counter of AC_m for vehicle k is decremented by one, $p_c^{k,m}(t)$ is the internal collision probability of AC_m for vehicle k at time t. According to Equation (8), $P_{Ts}^{k,m}(z)$ depends on $TR(z)$, $B_{m,i}^k(z)$, $H_m^k(z)$, and $p_c^{k,m}(t)$, which need to be further derived.

We first derive $TR(z)$. Since the duration of a transmission is composed of the propagation delay and the duration occupied by the physical header, MAC header, and packet, the transmission time T_{tr} can be calculated as

$$T_{tr} = \frac{PHY_H}{R_b} + \frac{MAC_H + E[P]}{R_d} + \delta,$$ (9)

where δ is the propagation delay, PHY_H and MAC_H are the size of the physical and MAC header, respectively. Assuming each packet for all ACs has the same size, let $E[P]$ be the packet size. According to Equation (9), the transmission time T_{tr} is a constant; thus, the PGF of transmission time T_{tr} is expressed as

$$TR(z) = z^{T_{tr}}.$$ (10)

Next, we derive $B_{m,i}^k(z)$. According to the Markov chain model for backoff instance in [29], $B_{m,i}^k(z)$ can be calculated as

$$B_{m,i}^k(z) = \frac{1}{\min\left(W_m^i, M_m\right)} \sum_{i=0}^{\min\left(W_m^i, M_m\right)-1} \left[H_m^k(z)\right]^i,$$ (11)
$$i \in (0, M_m + f_m).$$

Since the channel may be idle or busy when the backoff counter is decremented by one, $H_m^k(z)$ can be calculated as

$$H_m^k(z) = \left[1 - p_{busy}^{k,m}(t)\right] z^\sigma + p_{busy}^{k,m}(t) z^{T_{tr}+AIFS[m]}.$$ (12)

The probability $p_{busy}^{k,m}$ is channel busy probability of AC_m for vehicle k at time t, i.e., the probability that at least one AC is transmitting in a time slot, including the probability that the other ACs of the vehicle k is transmitting and the probability that the ACs of another vehicle is transmitting. Considering the priority of different ACs, the channel busy probability of AC_m can be derived according to the following equation:

$$p_{busy}^{k,m}(t) = 1 - \left\{ \left[1 - \tau^k(t)\right]^{N_{tr}^k(t)-1} \prod_{\substack{j=0 \\ j \neq m}}^{3} \left(1 - \alpha_j^k(t)\right) \right\}^{A_m+1}.$$ (13)

The packet will be transmitted when the backoff counter becomes 0; the internal transmission probability for AC_m can be expressed by α_m^k,

$$\begin{cases} \alpha_0^k(t) = b_{0,0,0}^k(t), \\ \alpha_m^k(t) = \sum_{j=0}^{M_m+f_m} b_{m,j,0}^k(t) = \dfrac{1 - p_c^{k,m}(t)^{M_m+f_m+1}}{1 - p_c^{k,m}(t)} b_{m,0,0}^k(t), \end{cases}$$ (14)

where the probability of the highest priority AC is the probability of the backoff state 0; the internal transmission probability for other ACs is equal to the sum of all backoff states.

According to the transition probability of the Markov chain, the probability can be calculated as

$$\begin{cases} b_{0,0,0}^k(t) = \left\{ \dfrac{W_0^0 + 1}{2\left[1 - p_{busy}^{k,0}(t)\right]} + \dfrac{1 - \rho_0^k(t)}{p_a^0(t)} \right\}^{-1}, \\ b_{m,0,0}^k(t) = \left\{ \dfrac{1 - p_c^{k,m}(t)^{M_m+f_m+1}}{1 - p_c^{k,m}(t)} + \dfrac{W_m^0 - 1}{2\left[1 - p_{busy}^{k,m}(t)\right]} + \dfrac{W_m^0 p_c^{k,m}(t)\left[1 - \left(2p_c^{k,m}(t)\right)^{M_m}\right]}{\left[1 - p_{busy}^{k,m}(t)\right]\left[1 - mp_c^{k,m}(t)\right]} + \dfrac{m^{M_m-1} W_m^0 p_c^{k,m}(t)^{M_m+1}\left[1 - p_c^{k,m}(t)^{f_m}\right]}{\left[1 - p_{busy}^{k,m}(t)\right]\left[1 - p_c^{k,m}(t)\right]} + \dfrac{1 - \rho_m^k(t)}{p_a^m(t)} \right\}^{-1}, \end{cases}$$ (15)

Table 1: Notations used in the model.

Notation	Definition
s_{abs}^l	Abscissa of vehicle l
s_{ord}^l	Ordinate of vehicle l
$S(t)$	Location matrix at time t
$h_{k,l}(t)$	Connectivity between vehicle k and vehicle l
$H(t)$	Network hearing topology matrix at time t
$N_{\text{tr}}^k(t)$	Number of vehicles in the transmission range of vehicle k
N	Total number of vehicles
CW_m^{max}	Maximum contention window size of AC_m
CW_m^{min}	Minimum contention window size of AC_m
W_m^i	Contention window size of AC_m at stage i
$M_m + f_m$	Retransmission limit of AC_m
A_m	AIFS differentiation of AC_m
R_d	Date rate
R_b	Basic rate
δ	Propagation delay
T_{tr}	Average transmission time
$p_c^{k,m}(t)$	Internal collision probability of AC_m for vehicle k at time t
$\tau^k(t)$	Total transmission probability for vehicle k at time t
$p_a^m(t)$	Packet arrival probability of AC_m at time t
$p_{\text{busy}}^{k,m}(t)$	Channel busy probability at time of AC_m for vehicle k at time t
$b_{m,0,0}^k(t)$	Stationary probability of AC_m for vehicle k at time t
$\alpha_m^k(t)$	Internal transmission probability of AC_m for vehicle k at time t
$\text{TR}(z)$	PGF of transmission time
$H_m^k(z)$	PGF of the average duration that the backoff counter of AC_m for vehicle k is decremented by one
$B_{m,i}^k(z)$	PGF of stationary probability of AC_m at stage i for vehicle k
σ	Slot time
$P_{Ts}^{k,m}(z)$	PGF of service time of AC_m for vehicle k
E_m^k	Mean of service time
D_m^k	Variance of service time
λ_m	The arrival rate of AC_m

Table 2: Parameter values.

Parameters	Value
Highway length	3000 m
Lane width	3.5 m
Transmission range	300 m
Speed range	20 m/s~30 m/s
Vehicle length	3 m
Header length of physical layer (PHY_H)	48 bits
Header length of MAC layer (MAC_H)	112 bits
Packet length $E[P]$	200 bits
Basic rate (R_b)	1 Mbps
Date rate (R_d)	6 Mbps
Propagation delay (δ)	2 μs
SIFS	32 μs
Slot time σ	13 μs
CW_0^{min}	3
CW_1^{min}	7
CW_2^{min}	15
CW_3^{min}	15
CW_0^{max}	7
CW_1^{max}	15
CW_2^{max}	1023
CW_3^{max}	1023
AIFSN[0]	2
AIFSN[1]	3
AIFSN[2]	6
AIFSN[3]	9
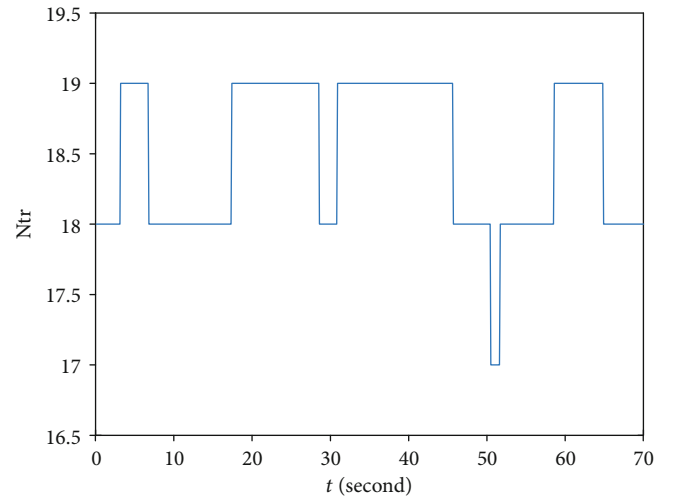
Figure 3: Number of vehicles.

Denote $p_a^m(t)$ as the packet arrival probability of AC_m at time t. Due to the packet arrival process of AC_m is a Poisson process with arrival rate $\lambda_m(t)$, thus $p_a^m(t)$ is calculated as

$$p_a^m(t) = \sum_{i=1}^{\infty} \frac{[\lambda_m(t)\sigma]^i}{K!} e^{-\lambda_m(t)\sigma} = 1 - e^{-\lambda_m(t)\sigma}. \quad (16)$$

As mentioned in the system model, an internal collision occurs when there are more than two ACs in a vehicle trans-

mitting at the same time. In this case, the AC with the highest priority is transmitted successfully. Let $\alpha_m^k(t)$ be the transmission probability and $p_c^{k,m}(t)$ be the internal collision probability of AC_m for vehicle k at time t, we have
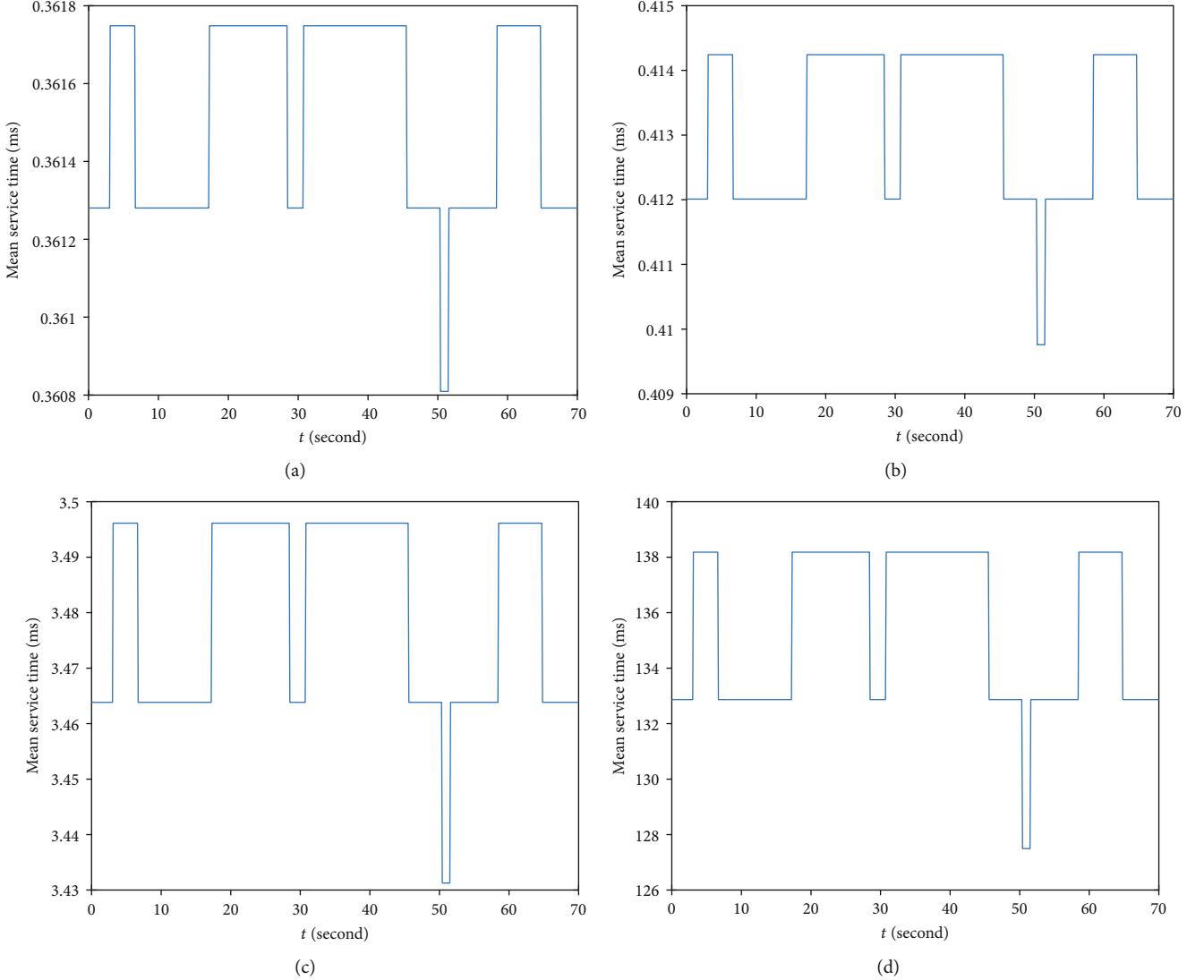
FIGURE 4: Mean of service time. (a) Mean of service time of AC_0. (b) Mean of service time of AC_1. (c) Mean of service time of AC_2. (d) Mean of service time of AC_3.

$$\begin{cases} p_c^{k,0}(t) = 0, \\ p_c^{k,1}(t) = \alpha_0^k(t), \\ p_c^{k,2}(t) = 1 - \left(1 - \alpha_0^k(t)\right)\left(1 - \alpha_1^k(t)\right), \\ p_c^{k,3}(t) = 1 - \left(1 - \alpha_0^k(t)\right)\left(1 - \alpha_1^k(t)\right)\left(1 - \alpha_2^k(t)\right). \end{cases} \tag{17}$$

Since the packet transmission is considered to be successful only when there is no internal collision, and the transmission probability of a vehicle is the sum of four ACs, the transmission probability of a vehicle is calculated as

$$\tau^k(t) = \alpha_0^k(t)\left(1 - p_c^{k,0}(t)\right) + \alpha_1^k(t)\left(1 - p_c^{k,1}(t)\right) \\ + \alpha_2^k(t)\left(1 - p_c^{k,2}(t)\right) + \alpha_3^k(t)\left(1 - p_c^{k,3}(t)\right). \tag{18}$$

By now, we have found all the relationships between ρ_m^k, $p_{busy}^{k,m}$, α_m^k, $b_{m,0,0}^k$, p_a^m, $p_c^{k,m}$, and τ^k in Equations (13), (14), (15), (16), (17) and (18). Since the number of variables is more than that of the equations, iterative method is used to solve the system, and thus we can further calculate the mean and variance of the service time.

(1) Assign initial values to four ρ_m^k

(2) Bring ρ_m^k into Equations (13), (14), (15), (16), (17) and (18) and solve the other 21 variables

(3) Combining relations Equations (6), (7), (8), (9),(10), (11) and (12), we obtain the average service time E_m^k and then calculate $\rho_m^k = \min\left(\lambda_m E_m^k, 1\right)$

(4) Setting an error bound ε, compare the error of the actual ρ_m^k with ε, if it is less than the error, the iteration is completed, otherwise, go to step (2)
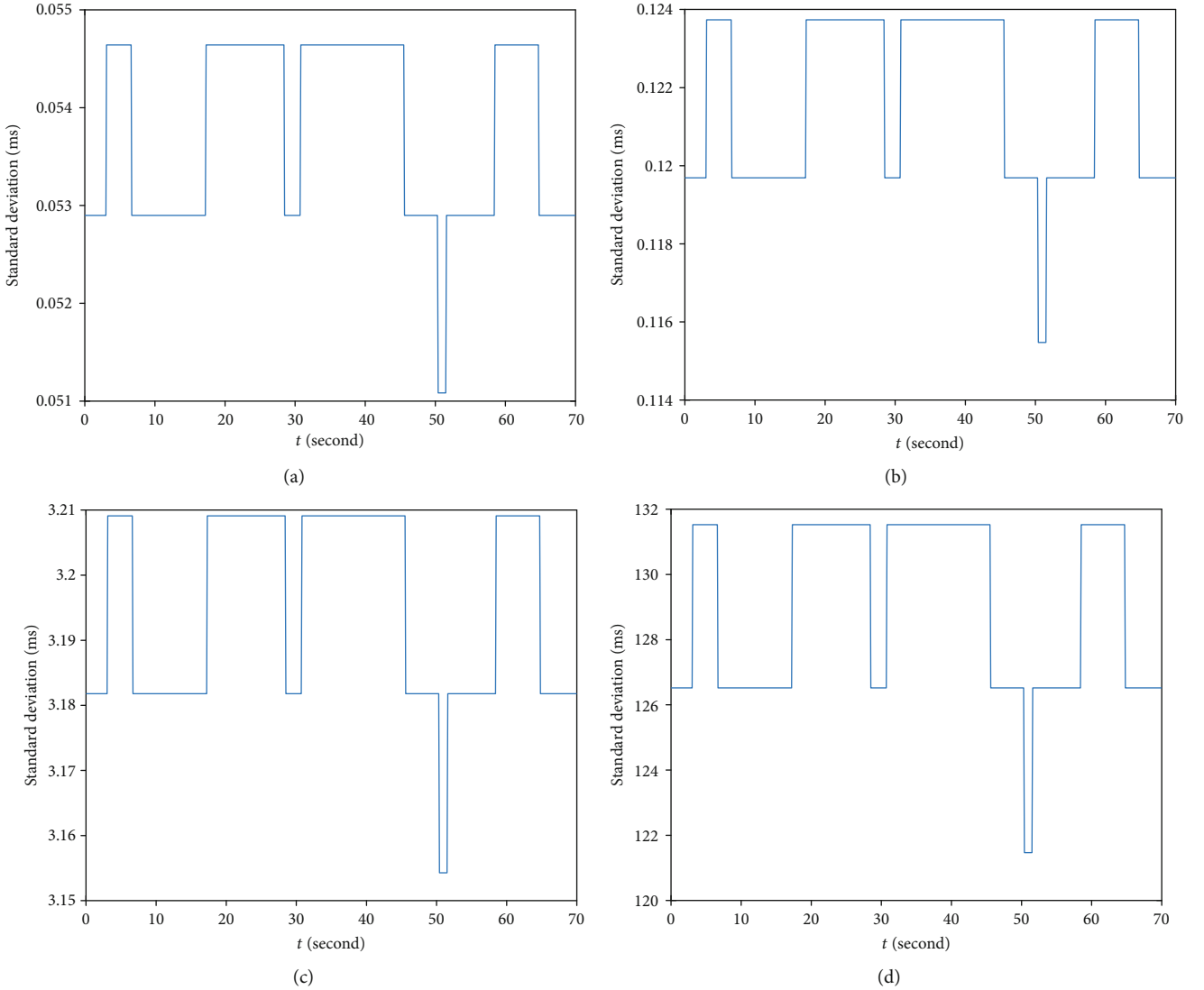
FIGURE 5: Standard deviation of service time. (a) Standard deviation of AC_0. (b) Standard deviation of AC_1. (c) Standard deviation AC_2. (d) Standard deviation AC_3.

(5) Calculating the mean and variance of service time according to Equations (6) and (7).

5. Results and Discussion

In this section, we evaluate the network performance in the extreme highway scenario with four lanes. The simulation is conducted on MATLAB R2018a. The distance between contiguous vehicles is set to be the minimum distance according to the 4-second rule. As the speed range of the American highway is from 20 m/s to 30 m/s, we set the speeds of the four lanes to be 20 m/s, 23 m/s, 20 m/s, and 30 m/s, respectively. The total length of the highway is 3000 m and the transmission range is 300 m, the values of 802.11p parameters and scenario description are shown in Table 2.

In order to ensure that the target vehicle is always within the scope of the scenario, we take the fifth vehicle in the second lane as the target vehicle. Each vehicle has four ACs to broadcast packets. Since the vehicle speed of each lane is different, the relative position of the vehicle is time varying, thus causing other vehicles to move in/out of the transmission range of the target vehicle. In this case, the number of vehicles in the carrier sensing range of the target vehicle may change in real time.

As shown in Figure 3, at first, the number of vehicles in the transmission range of the target vehicle is 18. About three seconds later, vehicles in the fast lane which were previously out of the range move into the transmission range of the target vehicle, which causes the total number of vehicles increasing immediately. The total number of vehicles keeps for about four seconds; then, vehicles in the slow lane that were previously in the transmission range of the target vehicle move out the transmission range and the number of vehicles decreases immediately. As described above, the number of vehicles is changed due to different vehicle speeds in different lanes and is fluctuated repeatedly according to Equations (3), (4) and (5).

Figures 4 and 5 show the real-time mean and standard deviation of service time, which is the value calculated by Equations (6) and (7). The trend of the mean and standard deviation of service time keeps consistent with the change of the number of vehicles. The number of vehicles will impact the probability of backoff block p_{busy}^m, which will further affect the state probability $b_{m,0,0}^k$, resulting in the change of the mean and standard deviation of service time. Therefore, the mean and standard deviation increase with the number of vehicles increasing. From Figure 4, we can find that the higher priority AC has less average service time delay than low priority AC. Moreover, we can see that as the average delay of AC_0, AC_1, and AC_2 is less than 0.01 s, which is the minimum delay to ensure safety in IoV [7]. Therefore, AC_0, AC_1, and AC_2 can meet the real-time requirements, while AC_3 cannot meet the requirements.

6. Conclusion

In this paper, we considered four ACs and proposed models to investigate the limit of the real-time performance of the 802.11p EDCA mechanism in the extreme highway scenario. Specifically, we model the real-time network between vehicles, study the connection between vehicles, calculate the real-time number of vehicles within the carrier sensing range, and then calculate the real-time performance metrics of the 802.11p EDCA mechanism including mean and variance of service time. The simulation result is employed to demonstrate that AC_0, AC_1, and AC_2 are able to meet the real-time requirement in the extreme highway scenario but AC_3 cannot. In the future work, we will study the real-time performance modeling of the 802.11p EDCA mechanism in other scenarios.

Data Availability

The data used to support the findings of this study are included within the article.

Conflicts of Interest

The authors declare no conflicts of interest.

Acknowledgments

References

[1] B. Mohammed and D. Naouel, "An efficient greedy traffic aware routing scheme for internet of vehicles," *Computers, Materials & Continua*, vol. 60, no. 3, pp. 959–972, 2019.

[2] D. Zhang, Y. Liu, L. Dai, A. K. Bashir, A. Nallanathan, and B. Shim, "Performance analysis of FD-NOMA-based decentralized V2X systems," *IEEE Transactions on Communications*, vol. 67, no. 7, pp. 5024–5036, 2019.

[3] Y. Fan, L. Yang, D. Zhang, G. Han, and D. Zhang, "An angle rotate-QAM aided differential spatial modulation for 5G ubiquitous mobile networks," *Mobile Networks and Applications*, vol. 1, pp. 1–13, 2019.

[4] H. Zhang, Y. Dong, J. Cheng, M. J. Hossain, and V. C. M. Leung, "Fronthauling for 5G LTE-U ultra dense cloud small cell networks," *IEEE Wireless Communications*, vol. 23, no. 6, pp. 48–53, 2016.

[5] Y. Dong, A. El Shafie, M. J. Hossain, J. Cheng, N. Al-Dhahir, and V. C. M. Leung, "Secure beamforming in full-duplex MISO-SWIPT systems with multiple eavesdroppers," *IEEE Transactions on Wireless Communications*, vol. 17, no. 10, pp. 6559–6574, 2018.

[6] N. Lu, N. Cheng, N. Zhang, X. Shen, and J. W. Mark, "Connected vehicles: solutions and challenges," *IEEE Internet of Things Journal*, vol. 1, no. 4, pp. 289–299, 2014.

[7] S. Chen, J. Hu, Y. Shi, and L. Zhao, "LTE-V: a TD-LTE-based V2X solution for future vehicular network," *IEEE Internet of Things Journal*, vol. 3, no. 6, pp. 997–1005, 2016.

[8] M. R. Palattella, M. Dohler, A. Grieco et al., "Internet of things in the 5G era: enablers, architecture, and business models," *IEEE Journal on Selected Areas in Communications*, vol. 34, no. 3, pp. 510–527, 2016.

[9] W. Xu, H. Zhou, N. Cheng et al., "Internet of vehicles in big data era," *IEEE/CAA Journal of Automatica Sinica*, vol. 5, no. 1, pp. 19–35, 2018.

[10] J. B. Kenney, "Dedicated short-range communications (DSRC) standards in the United States," *Proceedings of the IEEE*, vol. 99, no. 7, pp. 1162–1182, 2011.

[11] C. Shao, S. Leng, Y. Zhang, and H. Fu, "A multi-priority supported p-persistent MAC protocol for vehicular ad hoc networks," in *2012 IEEE Wireless Communications and Networking Conference (WCNC)*, pp. 2532–2537, Paris, France, 2012.

[12] C. Han, M. Dianati, R. Tafazolli, R. Kernchen, and X. Shen, "Analytical study of the IEEE 802.11p MAC sublayer in vehicular networks," *IEEE Transactions on Intelligent Transportation Systems*, vol. 13, no. 2, pp. 873–886, 2012.

[13] J. Zheng and Q. Wu, "Performance modeling and analysis of the IEEE 802.11p EDCA mechanism for VANET," *IEEE Transactions on Vehicular Technology*, vol. 65, no. 4, pp. 2673–2687, 2016.

[14] Y. Yao, L. Rao, X. Liu, and X. Zhou, "Delay analysis and study of IEEE 802.11p based DSRC safety communication in a highway environment," in *2013 Proceedings IEEE INFOCOM*, pp. 1591–1599, Turin, Italy, 2013.

[15] K. Xu, D. Tipper, Y. Qian, and P. Krishnamurthy, "Time-dependent performance analysis of IEEE 802.11p vehicular networks," *IEEE Transactions on Vehicular Technology*, vol. 65, no. 7, pp. 5637–5651, 2016.

[16] Q. Wu, S. Xia, P. Fan, Q. Fan, and Z. Li, "Velocity-adaptive V2I fair-access scheme based on IEEE 802.11 DCF for platooning vehicles," *Sensors*, vol. 18, no. 12, p. 4198, 2018.

[17] G. Bianchi, "Performance analysis of the IEEE 802.11 distributed coordination function," *IEEE Journal on Selected Areas in Communications*, vol. 18, no. 3, pp. 535–547, 2000.

[18] Q. Ni, T. Li, T. Turletti, and Y. Xiao, "Saturation throughput analysis of error-prone 802.11 wireless networks," *Wireless Communications and Mobile Computing*, vol. 5, no. 8, pp. 945–956, 2005.

[19] D. Malone, K. Duffy, and D. Leith, "Modeling the 802.11 distributed coordination function in nonsaturated heterogeneous conditions," *IEEE/ACM Transactions on Networking*, vol. 15, no. 1, pp. 159–172, 2007.

[20] A. Vinel, V. Vishnevsky, and Y. Koucheryavy, "A simple analytical model for the periodic broadcasting in vehicular ad-hoc networks," in *2008 IEEE Globecom Workshops*, pp. 1–5, New Orleans, LA, USA, 2008.

[21] X. Ma, X. Chen, and H. H. Refai, "Performance and reliability of DSRC vehicular safety communication: a formal analysis," *EURASIP Journal on Wireless Communications and Networking*, vol. 2009, no. 1, 2009.

[22] J. R. Gallardo, D. Makrakis, and H. T. Mouftah, "Performance analysis of the EDCA medium access mechanism over the control channel of an IEEE 802.11p WAVE vehicular network," in *2009 IEEE International Conference on Communications*, pp. 1–6, Dresden, Germany, 2009.

[23] F. Kaabi, P. Cataldi, F. Filali, and C. Bonnet, "Performance analysis of IEEE 802.11p control channel," in *2010 Sixth International Conference on Mobile Ad-hoc and Sensor Networks*, pp. 211–214, Hangzhou, China, 2010.

[24] K. Bilstrup, E. Uhlemann, E. G. Ström, and U. Bilstrup, "Evaluation of the IEEE 802.11p MAC method for vehicle-to-vehicle communication," in *2008 IEEE 68th Vehicular Technology Conference*, pp. 1–5, Calgary, BC, Canada, 2008.

[25] Q. Wu, S. Xia, Q. Fan, and Z. Li, "Performance analysis of IEEE 802.11p for continuous backoff freezing in IoV," *Electronics*, vol. 8, no. 12, p. 1404, 2019.

[26] Q. Wu and J. Zheng, "Performance modeling of the IEEE 802.11p EDCA mechanism for VANET," in *2014 IEEE Global Communications Conference*, pp. 57–63, Austin, TX, USA, December 2014.

[27] Q. Wu and J. Zheng, "Performance modeling and analysis of the ADHOC MAC protocol for vehicular networks," *Wireless Networks*, vol. 22, no. 3, pp. 799–812, 2016.

[28] Q. Wu, H. Zhang, Z. Li, Y. Liu, and C. Zhang, "Performance evaluation of the V2I fair access with a finite retry limit," *EURASIP Journal on Wireless Communications and Networking*, vol. 2018, no. 1, 2018.

[29] Y. Yao, L. Rao, and X. Liu, "Performance and reliability analysis of IEEE 802.11p safety communication in a highway environment," *IEEE Transactions on Vehicular Technology*, vol. 62, no. 9, pp. 4198–4212, 2013.

WILEY | Hindawi

Research Article

SIC-Coding Schemes for Underlay Two-Way Relaying Cognitive Networks

Pham Ngoc Son [ID],[1] **Tran Trung Duy,**[2] **and Khuong Ho-Van**[3,4]

[1]*Ho Chi Minh City University of Technology and Education, Ho Chi Minh City, Vietnam*
[2]*Posts and Telecommunications Institute of Technology, Ho Chi Minh City, Vietnam*
[3]*Ho Chi Minh City University of Technology (HCMUT), Ho Chi Minh City, Vietnam*
[4]*Vietnam National University Ho Chi Minh City, Ho Chi Minh City, Vietnam*

Correspondence should be addressed to Pham Ngoc Son; sonpndtvt@hcmute.edu.vn

In this paper, we propose an underlay two-way relaying scheme with the successive interference cancellation (SIC) solution in which two secondary sources transmit simultaneously their data to each other through secondary relays. The proposed scheme is operated in only two time slots and under an interference constraint of a primary receiver, denoted as the UTW-2TS scheme. In the UTW-2TS scheme, the secondary relays employ the SIC operation to decode successively the data from received broadcast signals and then encode these data by two techniques: digital network coding (DNC) enforced by XOR operations (denoted as the UTW-2TS-DNC protocol) and superposition coding (SC) enforced by power domain additions (denoted as the UTW-2TS-SC protocol). A selected secondary relay which subjects to maximize decoding capacities and to minimize collection time of channel state information in two protocols UTW-2TS-DNC and UTW-2TS-SC experiences residual interferences from imperfect SIC operations. Outage probabilities and throughputs are solved in terms of exact closed-form expressions to evaluate the system performance of the proposed protocols. Simulation and analysis results provide performance enhancement of the proposed protocols UTW-2TS-DNC and UTW-2TS-SC owing to increase the number of the cooperative secondary relays, the interference constraints, and the distances from the secondary network to the primary receiver. The best throughputs are pointed at optimal interference power allocation coefficients and optimal locations of the selected secondary relay. Considering the same power consumption, the UTW-2TS-DNC protocol outperforms the UTW-2TS-SC protocol. Finally, the simulation results are collected to confirm the exact analysis values of the outage probabilities and throughputs.

1. Introduction

In recent years, the radio spectrum has become scarce due to the increasing bandwidth demand for mobile multimedia services and the explosive development of next-generation wireless networks such as wireless sensor networks, Internet of Things (IoT), and fifth-generation (5G) networks. On the other hand, the utilization of the licensed frequency spectrum versus time and space is low [1]. In this context, cognitive radio was proposed as an effective spectrum sharing solution in which secondary users (SUs) coexist with primary users (PUs) [2]. The SUs can operate flexibly and intelligently in (interweave, overlay, and underlay) protocols to access the licensed frequency spectra of the PUs as long as quality of

service (QoS) of the primary network is maintained [3, 4]. In the interweave cognitive radio [5], the SUs use spectrum sensing methods to detect the unoccupied spectra to avoid interference to the PUs. In an opposite way, the SUs in the overlay and underlay methods can access the licensed bands at the same time with the PUs [6–9]. The overlay approach requires the cooperation between the SUs and the PUs; i.e., the secondary transmitters have to combine the data of the SUs and the PUs and then send the combined data to the intended secondary and primary receivers [6]. The SUs in the underlay approach can access the spectra at any time provided that the interferences affected on the PUs must be below a tolerable interference level [7–9]. Based on the required QoS, the PUs can calculate the tolerable interference

level and send it to the secondary network so that the SUs can appropriately adjust their transmit powers.

Two-way communication networks have been much interested in switching data between interactive users in which many research studies have been launched to enhance performance [10]. Two-way cooperation solutions investigated in [10] have great attractions owing to increase significantly spectrum utilization efficiency. The operation of two-way relaying is to exchange data between users with the help of other intermediate users as amplify-and-forward (AF) and decode-and-forward (DF) devices, denoted as relays. In [11], an optimum relay is selected to decode received signals from the transmit users, mix these data by XOR operation, and then broadcast back to both users. The operation of the optimum relay in [11] is named as digital network coding (DNC).

1.1. Related Work and Motivation. Proposals for increasing performance in the underlay two-way relaying networks have been studied in [12–18]. The authors in [12] combined DNC and opportunistic relay selection (ORS) to decrease the outage performance of the secondary two-way relaying network under the interference constraint required by the primary receiver. Moreover, the best relay selection strategy in the third time slot, which follows a max-min criterion, was proposed in [12] to significantly decrease the system outage probabilities, as compared with the traditional DNC approach [12]. By expanding the published work [12], Toan et al. in [13, 14] analyzed the performance of the underlay two-way relaying communication systems with the presence of multiple primary receivers. The authors in [15] evaluated the outage probabilities and symbol error probabilities of many primary one-way networks and a secondary two-way network operating on both the independent and identically distributed (i.i.d.) and independent but nonidentically distributed (i.n.i.d.) Nakagami-m fading channels. Imperfect channel state information (CSI) from the SUs to the PUs have been included in probability analyses [16]. The authors exploited both the direct and relaying links with appropriate diversity combinations in an underlay three-phase two-way scheme [17]. In [18], the authors considered an underlay wiretap cognitive two-way relaying network in which two SUs exchange their messages via multiple secondary DF relays in the presence of an eavesdropper. In [18], DNC, ORS, and artificial noises were used to mitigate eavesdropping attacks. However, above investigations perform on three orthogonal time slots, and hence, the bandwidth utilization efficiency is only 2/3 (two data per three time slots). This motivates us to propose new two-way relaying approaches for the underlay cognitive radio network, where only two time slots are used to obtain the data rate of 2/2.

In [19], the authors applied successive interference cancellation (SIC) technique to sequentially decode signals received from multiple sources. With SIC, the spectral efficiency of the two-way relaying systems is improved because the number of time slots decreases. Indeed, SIC is one of the core technologies in nonorthogonal multiple access (NOMA) systems which can assign nonorthogonal resources such as power, time, and code to different users [20]. For the NOMA systems operating in the power domain, multiple transmit signals that are allocated with different transmit powers are merged by the superposition coding (SC) before they are sent to intended receivers. At each receiver, the signal with higher transmit power is first decoded, and it is then removed from the received signal. This process, named SIC, is repeated until the receiver obtains the desired signal [21]. The authors in [19] pointed out some implementation problems of the SIC utilization such as complexity and residual interference after performing interference cancellations. These issues will lead to lower decoding capacities than expected ones. In [22], the authors evaluated two-way relaying NOMA systems fully in terms of the outage probability, outage floor, ergodic capacity, and power allocation. The system performance of the proposed protocol in [22] outperforms that of three-time slot two-way relaying systems with orthogonal multiple access. In addition, we have applied the SIC scheme with DNC and ORS at the last time slot (the second time slot) for traditional two-way relaying networks in [23]. The results obtained in [23] presented improvements of the system performances as well as bandwidth utilization efficiencies, as compared with the corresponding scenarios without using SIC. However, the previous published works [19, 22, 23] only considered the conventional wireless networks; i.e., the underlay cognitive network was not studied.

1.2. Contributions. Motivated by above issues, in this paper, we propose an underlay two-way relaying scheme with the SIC solution in which two secondary sources send concurrently their data to each other through multiple secondary relays under an interference constraint of a primary receiver. The proposed scheme is operated in two time slots, denoted as the UTW-2TS scheme. In the UTW-2TS scheme, the secondary relays employ the SIC operation to decode successively the data from received broadcast signals. The data carried by the stronger channel gains is decoded firstly and will be subtracted to detect the remaining data. These decoded data are encoded by two techniques: the DNC enforced by XOR operations (denoted as the UTW-2TS-DNC protocol) and the SC enforced by power domain additions (denoted as the UTW-2TS-SC protocol). In addition, because of imperfect operations of the SIC, the secondary relays experience residual interferences. A secondary relay is selected in two protocols UTW-2TS-DNC and UTW-2TS-SC which subjects to maximize decoding capacities and to minimize collection time of CSI. Outage probabilities and throughputs are solved in terms of exact closed-form expressions to evaluate the system performance of the proposed UTW-2TS-DNC and UTW-2TS-SC protocols. These outage probability and throughput expressions are proved by doing the Monte Carlo simulations. The contributions of this paper are cataloged as follows:

(1) Proposing SIC-based underlay two-way relaying cognitive protocols which enhance the data rate, as compared with the corresponding ones without using the SIC

(2) Exactly analyzing the outage probabilities and throughputs of two secondary sources in two operation protocols UTW-2TS-DNC and UTW-2TS-SC with the same two-way relaying model in which the SIC solution in the selected secondary relay is practically considered in the perfect and imperfect cases

(3) The UTW-2TS-DNC protocol outperforms the UTW-2TS-SC protocol with the same power consumption

(4) The proposed UTW-2TS-DNC and UTW-2TS-SC protocols can achieve the best throughputs at optimal interference power allocation coefficients and optimal locations of the selected secondary relay. In addition, we examine the throughputs of the UTW-2TS-SC protocol versus the changes of the power allocation coefficients

(5) The system performances in terms of the outage probabilities and throughputs are improved when the number of the cooperative secondary relays, the interference constraints, and the distances from the secondary nodes to the primary receiver are increased as well as when the residual interference powers decrease

1.3. Paper Organization and Notations. This paper is organized into sections as follows. Section 2 presents a system model of an underlay two-way relaying scheme with multiple secondary relays. Section 3 analyzes outage probabilities and throughputs of the proposed protocols UTW-2TS-DNC and UTW-2TS-SC. Results and discussions are shown in Section 4. Lastly, Section 5 summarizes contributions.

The notations used in this paper are denoted as follows: $f_\Upsilon(\cdot)$ and $F_\Upsilon(\cdot)$ denote, respectively, the probability density function (PDF) and the cumulative distribution function (CDF) of a random variable (RV) Υ; $\Pr\{\Xi\}$ denotes the probability operation of an event Ξ; $E\{\cdot\}$ denotes the expectation operator; $\begin{pmatrix} p \\ M \end{pmatrix}$ denotes the binomial coefficient ($\begin{pmatrix} p \\ M \end{pmatrix} = M!/p!(M-p)!$); $\oplus$ denotes XOR math operation; and $\Gamma[u, v]$ is the upper incomplete Gamma function.

2. System Model

Figure 1 presents a system model of an underlay two-way relaying scheme. In this scheme, secondary sources S_1 and S_2 own data x_1 and x_2 ($x_1 \in S_1$ and $x_2 \in S_2$), respectively. The exchange of information is achieved between the S_1 and the S_2 through a cluster of M intermediate secondary relays R_i, where $i = \{1, 2, \cdots, M\}$ [12]. More specifically, the data x_1 of S_1 is exchanged with the data x_2 of S_2. The secondary network including S_1, S_2, and R_i suffers an interference constraint of a primary receiver (PR), denoted as I. The secondary relays can perform the SIC technique to decode the
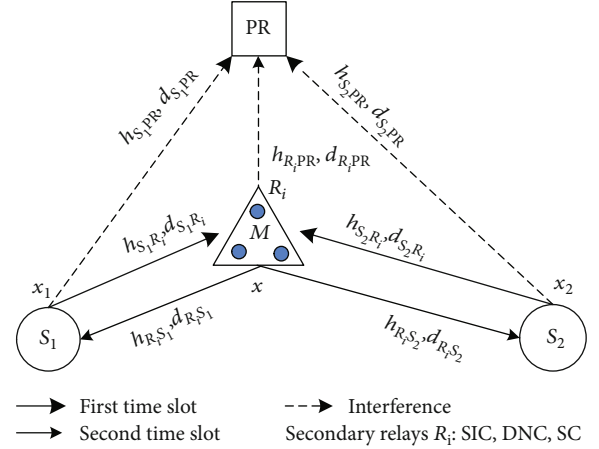
FIGURE 1: System model of an underlay two-way relaying scheme.

received data-carried signals successively in an interval of a time slot.

We assume that a direct link between the secondary sources S_1 and S_2 does not exist due to the far distance or deep shadow fading [18, 23, 24]. It is also assumed that the secondary and primary nodes are installed with a single antenna, and additive noises at all the receivers are zero-mean Gaussian random variables (RVs) whose mean is zero, and variance is σ^2.

In Figure 1, h_{XY} and d_{XY} denote the flat-block Rayleigh fading channel coefficient and the normalized link distance of link X-Y, respectively, where $X, Y \in \{S_1, S_2, R_i, \text{PR}\}$. Because the secondary relays R_i are located in the cluster, where the secondary relays R_i are close to each other, the normalized distances can be assumed to be identical, i.e., $d_{S_1 R_i} = d_{R_i S_1} = d_1$, $d_{S_2 R_i} = d_{R_i S_2} = d_2$, $d_{R_i \text{PR}} = d_3$, $d_{S_1 \text{PR}} = d_4$, and $d_{S_2 \text{PR}} = d_5$ [25, 26]. Because $|h_{XY}|$ have Rayleigh distributions, the channel gains $g_{XY} = |h_{XY}|^2$ are exponential RVs with the PDFs $f_{g_{XY}}(y) = \lambda_{XY} e^{-\lambda_{XY} y}$ and the CDFs $F_{g_{XY}}(y) = 1 - e^{-\lambda_{XY} y}$, where $\lambda_{XY} = d_{XY}^\eta$, and η is a path loss exponent (see [23, 27, 28]). Moreover, we have $\lambda_{S_1 R_i} = \lambda_{R_i S_1} = \lambda_1$, $\lambda_{S_2 R_i} = \lambda_{R_i S_2} = \lambda_2$, $\lambda_{R_i \text{PR}} = \lambda_3$, $\lambda_{S_1 \text{PR}} = \lambda_4$, and $\lambda_{S_2 \text{PR}} = \lambda_5$.

In the underlay cognitive radio network, the secondary network coexisted in the same frequency with the primary network and satisfies that the interference power at the primary receiver (PR) is less than or equal the constraint I [29, 30]. We have the inequality

$$\begin{cases} P_{S_1} g_{S_1 \text{PR}} + P_{S_2} g_{S_2 \text{PR}} \leq I, \\ P_{R_i} g_{R_i \text{PR}} \leq I, \quad i = \{1, 2, \cdots, M\}, \end{cases} \tag{1}$$

where P_{S_1}, P_{S_2}, and P_{R_i} are transmit powers of the secondary source S_1, the secondary source S_2, and the secondary relays R_i, respectively.

From (1), the transmit powers of the secondary transmitters can be set as $P_{S_1} = \alpha_1 I/g_{S_1 \text{PR}}$, $P_{S_2} = \alpha_2 I/g_{S_2 \text{PR}}$, and $P_{R_i} = I/g_{R_i \text{PR}}$, where α_1 and α_2 are interference power allocation coefficients, $0 < \alpha_1, \alpha_2 < 1$, and $\alpha_1 + \alpha_2 = 1$.

Comment 1. In practice, the transmit powers P_X must be below a maximum power (denoted by $P_{X,\max}$), where $X \in \{S_1, S_2, R_i\}$. Therefore, P_X should be formulated as $P_X = \min(P_{X,\max}, uI/g_{XPR})$, where $u \in \{\alpha_1, \alpha_2, 1\}$. Suppose that $P_{X,\max} \gg I$ (e.g., the X nodes are near the PR node); hence, we can approximate P_X by $P_X \approx uI/g_{XPR}$. It is worth noting that this assumption is used in many published literatures, i.e., [12, 26, 30–36].

The operation principle of the UTW-2TS schemes happens in two time slots as follows. In the first time slot, secondary sources S_1 and S_2 transmit simultaneously the data-carried signals x_1 and x_2, respectively, to all secondary relays under interference constraint of the primary receiver (PR). A selected secondary relay, denoted as R_m, where $m = \{1, 2, \cdots, M\}$, decodes the desired data by applying the SIC process. In the second time slot (last time slot), the R_m creates the new data x by the DNC technique, denoted as the UTW-2TS-DNC protocol, or by the SC technique, denoted as the UTW-2TS-SC protocol. The new data will be transmitted back to two secondary sources S_1 and S_2. Collection of CSI and system parameters for decoding data, cancelling interferences, subtracting self-interference components, and selecting the cooperative relay are performed by the medium access control (MAC) protocol as specified in [37].

The secondary sources S_1 and S_2 transmit simultaneously the data x_1 and x_2, respectively, to the secondary relays R_i at the same time (the first time slot) and the same frequency as the uplink NOMA operation, where $i = \{1, 2, \cdots, M\}$. The received signal at the R_i is expressed as

$$y_{R_i} = \sqrt{P_{S_1}} x_1 h_{S_1 R_i} + \sqrt{P_{S_2}} x_2 h_{S_2 R_i} + n_{R_i}, \qquad (2)$$

where $E\{|x_1|^2\} = E\{|x_2|^2\} = 1$, and n_{R_i} presents the Gaussian noises at the secondary relays R_i with the same variance σ^2.

The secondary relays R_i can compute the distances $d_{S_1 R_i}$ and $d_{S_2 R_i}$ by taking coordinate parameters in received request-to-send (RTS) messages of the secondary sources S_1 and S_2 in the setup phase [37]. Coordinates of the nodes can be received from the navigation systems. Hence, the secondary relays R_i can make decoding decisions of the signals x_1 and x_2 in (2) by the SIC technique as follows.

Case 1. ($d_{S_1 R_i} \leq d_{S_2 R_i}$ or $E\{g_{S_1 R_i}\} \geq E\{g_{S_2 R_i}\}$ (R_i is closer S_1 than S_2)).

In this case, the data x_1 in (2) is decoded by the secondary relay R_i firstly whereas a signal $\sqrt{P_{S_2}} x_2 h_{S_2 R_i}$ containing x_2 is treated as interference. The received signal-to-interference-plus-noise ratios (SINRs) at the R_i to decode x_1 are obtained from (2) as

$$\gamma^{(1)}_{R_i \to x_1} = \frac{P_{S_1} g_{S_1 R_i}}{P_{S_2} g_{S_2 R_i} + \sigma^2} = \frac{\alpha_1 Q g_{S_1 R_i} g_{S_2 PR}}{\alpha_2 Q g_{S_2 R_i} g_{S_1 PR} + g_{S_1 PR} g_{S_2 PR}}, \qquad (3)$$

where $Q = I/\sigma^2$.

In (3), to increase the decoding capacity for the data x_1, decrease the collection of the CSI, and minimize help of the cooperative secondary relays, we only select one secondary relay among M secondary relays. Indeed, the selected secondary relay R_m is obtained as $R_m = \arg \max_{i=1,2,\cdots,M} g_{S_1 R_i}$. Then, the CDF and PDF of the RV $g_{S_1 R_m}$ are correspondingly expressed as ([28], eqs. 7–14)

$$F_{g_{S_1 R_m}}(y) = \left(1 - e^{-\lambda_1 y}\right)^M = \sum_{p=0}^{M} \binom{p}{M} (-1)^p e^{-p \lambda_1 y}, \qquad (4)$$

$$f_{g_{S_1 R_m}}(y) = M \lambda_1 e^{-\lambda_1 y} \left(1 - e^{-\lambda_1 y}\right)^{M-1}. \qquad (5)$$

After decoding x_1 successfully, the inference component $\sqrt{P_{S_1}} x_1 h_{S_1 R_m}$ in (2) can be cancelled completely or partly by the SIC technique in which the transmit power P_{S_1} and the channel coefficient $h_{S_1 R_m}$ were known in the setup phase [37]. The remaining received SINR at the selected secondary relay R_m to decode x_2 is inferred as

$$\gamma^{(1)}_{R_m \to x_2} = \frac{P_{S_2} g_{S_2 R_m}}{\varepsilon I |r_m|^2 + \sigma^2}, \qquad (6)$$

where r_m is a residual interference part at the secondary relay R_m due to the imperfect SIC operations and can be modeled as an identical complex normal distribution $r_m \sim CN(0, \Psi)$ [19] with zero mean and same variance Ψ (Ψ is also the power of the residual interference part), and hence, $g_m = |r_m|^2$ are also exponentially distributed RVs with the PDF as $f_{g_m}(y) = \Omega e^{-\Omega y}$ and the CDF as $F_{g_m}(y) = 1 - e^{-\Omega y}$ ([28], eqs. 6–68), where $\Omega = 1/\Psi$; $\varepsilon = 0$ and $\varepsilon = 1$ denote perfect and imperfect interference cancellation at the secondary relay R_m, respectively.

Substituting $P_{S_2} = \alpha_2 I/g_{S_2 PR}$ into (6), $\gamma^{(1)}_{R_m \to x_2}$ is expressed as

$$\gamma^{(1)}_{R_m \to x_2} = \frac{\alpha_2 Q g_{S_2 R_m}}{g_{S_2 PR} (\varepsilon Q g_m + 1)}. \qquad (7)$$

Case 2. ($d_{S_1 R_i} > d_{S_2 R_i}$ or $E\{g_{S_1 R_i}\} < E\{g_{S_2 R_i}\}$ (R_i is closer S_2 than S_1)).

Similarly, the secondary relay R_i decodes the data x_2 firstly with the interference signal $\sqrt{P_{S_1}} x_1 h_{S_1 R_i}$, where $i = \{1, 2, \cdots, M\}$. The SINRs at the R_i for decoding x_2 and x_1 are expressed, respectively, as

$$\gamma^{(2)}_{R_i \to x_2} = \frac{P_{S_2} g_{S_2 R_i}}{P_{S_1} g_{S_1 R_i} + \sigma^2} = \frac{\alpha_2 Q g_{S_2 R_i} g_{S_1 PR}}{\alpha_1 Q g_{S_1 R_i} g_{S_2 PR} + g_{S_1 PR} g_{S_2 PR}}, \qquad (8)$$

$$\gamma^{(2)}_{R_i \to x_1} = \frac{P_{S_1} g_{S_1 R_i}}{\varepsilon I g_i + \sigma^2} = \frac{\alpha_1 Q g_{S_1 R_i}}{g_{S_1 PR} (\varepsilon Q g_i + 1)}. \qquad (9)$$

In the second time slot, if the selected secondary relay R_m decodes successfully both data x_1 and x_2 in the first time slot, the R_m creates a new data x as

$$x = \begin{cases} x_1 \oplus x_2, & \text{digital network coding (the UTW-2TS-DNC protocol)}, \\ \sqrt{\beta_1}x_1 + \sqrt{\beta_2}x_2, & \text{superposition coding (the UTW-2TS-SC protocol)}, \end{cases} \tag{10}$$

where β_1 and β_2 are power allocation coefficients to data x_1 and x_2, respectively, and satisfy conditions as [21]

$$\begin{cases} \beta_1 + \beta_2 = 1, & 0 \leq \beta_1 \leq 1, \ 0 \leq \beta_2 \leq 1, \\ \beta_1 \geq \beta_2, & d_{S_1 R_m} \leq d_{S_2 R_m} \text{(Case 1)}, \\ \beta_1 < \beta_2, & d_{S_1 R_m} > d_{S_2 R_m} \text{(Case 2)}. \end{cases} \tag{11}$$

We remark that for the UTW-2TS-SC protocol as in (10) and (11), the selected secondary relay R_m performs the downlink NOMA operation to allocate powers to data x_1 and x_2 as $x = \sqrt{\beta_1}x_1 + \sqrt{\beta_2}x_2$ in which x_1 and x_2 are the desired data of the secondary sources S_2 and S_1, respectively [21]. If the S_k is closer to the R_m, the R_m will allocate the lower power for the data x_l, where $k, l = \{1, 2\}$ and $l \neq k$ and vice versa. More specifically, in Case 1 ($d_{S_1 R_m} \leq d_{S_2 R_m}$), the S_1 is the nearby user and the S_2 is the distant user. Hence, the R_m uses the lower power allocation coefficient β_2 ($\beta_2 \leq \beta_1$) to transmit the data x_2 to the S_1 and the higher power allocation coefficient β_1 to transmit the data x_1 to the S_2. In addition, we note that the secondary relay R_m in Case 2 is selected by $R_m = \arg \max_{i=1,2,\cdots,M} g_{S_2 R_i}$.

The coded data x in (10) will be broadcasted back to two secondary sources S_1 and S_2, and then the received signals at the secondary sources S_k are expressed as

$$y_{S_k} = \sqrt{P_{R_m}} x h_{R_m S_k} + n_{S_k}$$
$$= \begin{cases} \sqrt{P_{R_m}} h_{R_m S_k}(x_1 \oplus x_2) + n_{S_k} \text{ (the UTW-2TS-DNC protocol)} \\ \sqrt{P_{R_m}} h_{R_m S_k}\left(\sqrt{\beta_1}x_1 + \sqrt{\beta_2}x_2\right) + n_{S_k} \text{ (the UTW-2TS-SC protocol)} \end{cases}$$
$$= \begin{cases} \sqrt{P_{R_m}} h_{R_m S_k}(x_1 \oplus x_2) + n_{S_k} \text{ (the UTW-2TS-DNC protocol)} \\ \sqrt{\beta_l P_{R_m}} h_{R_m S_k} x_l + \sqrt{\beta_k P_{R_m}} h_{R_m S_k} x_k + n_{S_k} \text{ (the UTW-2TS-SC protocol)}. \end{cases} \tag{12}$$

where n_{S_k} presents the Gaussian noises at the secondary sources S_k with the same variance σ^2.

For the UTW-2TS-DNC protocol with $x = x_1 \oplus x_2$ in (12), the received SINRs at the secondary sources S_k can be obtained from (12) to take x as

$$\gamma_{S_k \to x}^{\text{UTW-2TS-DNC}} = \frac{P_{R_m} |h_{R_m S_k}|^2}{\sigma^2} = \frac{Q g_{R_m S_k}}{g_{R_m PR}}. \tag{13}$$

The decoding method of the secondary sources S_k to take the desired data is performed by decoding operations of the network coding; i.e., the S_1 takes the data x_2 by XOR opera-

tions of its data x_1 with the compressed data x as $x_1 \oplus x = x_1 \oplus x_1 \oplus x_2 = x_2$.

For the UTW-2TS-SC protocol, the received signals at the secondary sources S_k are shown more clearly as

$$y_{S_k} = \underbrace{\sqrt{\beta_l P_{R_m}} h_{R_m S_k} x_l}_{\text{desired component}} + \underbrace{\sqrt{\beta_k P_{R_m}} h_{R_m S_k} x_k}_{\text{self-interference component}} + n_{S_k}. \tag{14}$$

In (14), the secondary source S_k owns the data x_k and does not decode this data. In addition, the S_k can estimate the fading channel coefficient $h_{R_m S_k}$ from receiving the setup messages of the selected secondary relay R_m and takes the system parameters as the transmit power P_{R_m} and the power allocation coefficient β_k during the setup time, where $k = \{1, 2\}$, [37]. Hence, the S_k knows the parameters x_k, $h_{R_m S_k}$, P_{R_m}, and β_k, which then can cancel out the self-interference component $\sqrt{\beta_k P_{R_m}} h_{R_m S_k} x_k$ in (14) [38, 39]. The received signals at the S_k after subtracting the known self-interference components are obtained as

$$\widehat{y_{S_k}} = \underbrace{\sqrt{\beta_l P_{R_m}} h_{R_m S_k} x_l}_{\text{desired component}} + n_{S_k}. \tag{15}$$

The received SINRs at the secondary sources S_k can be computed to take the desired data x_l as

$$\gamma_{S_k \to x_l}^{\text{UTW-2TS-SC}} = \frac{P_{R_m} \beta_l |h_{R_m S_k}|^2}{\sigma^2} = \frac{Q \beta_l g_{R_m S_k}}{g_{R_m PR}}. \tag{16}$$

3. Outage Probability and Throughput Analyses

In this paper, it is assumed that an outage event occurs when the received SINR is less than a threshold SINR γ_{th} [30, 40]. In addition, the data transmission in the secondary network is fixed to the delay-limited mode in which the secondary receivers such as the selected secondary relay R_m and the secondary sources S_1 and S_2 decode the desired data block by block without using buffers [30, 40]. Throughput has been considered to characterize the spectrum utilization of the communication systems [30, 40, 41] (known as the mean spectral efficiency) and is related to outage analyses as

$$\begin{aligned} \text{TP}_Z^{(l)} &= \frac{1}{2}\left(1 - \text{OP}_{Z-S_1}^{(l)}\right)R_{\text{th}} + \frac{1}{2}\left(1 - \text{OP}_{Z-S_2}^{(l)}\right)R_{\text{th}} \\ &= \frac{1}{2}\left(2 - \text{OP}_{Z-S_1}^{(l)} - \text{OP}_{Z-S_2}^{(l)}\right)R_{\text{th}}, \end{aligned} \tag{17}$$

where 1/2 denotes that the Z protocol operates in the two time slots, $Z \in \{\text{UTW-2TS-DNC}, \text{UTW-2TS-SC}\}$; R_{th} is the threshold data rate and is given by $R_{\text{th}} = \log_2(1 + \gamma_{\text{th}})$ (bits/s/Hz) [30, 38, 40, 41]; $\text{OP}_{Z-S_k}^{(l)}$ is the outage probability at the secondary source S_k in the case l ($l, k = \{1, 2\}$) and is defined as probability that the secondary source S_k cannot decode successfully the desired data.

3.1. The UTW-2TS-DNC Protocol

3.1.1. Case 1: $d_{S_1 R_i} \leq d_{S_2 R_i}$, $i = \{1, 2, \cdots, M\}$. The outage probability of the secondary source S_1 occurs when the secondary source S_1 cannot successfully decode the data x_2 of the opposite secondary source S_2. Due to the exploitation of the SIC technique at the selected secondary relay R_m which was set up in the initial phase, the outage probability of the secondary source S_1 happens when (1) the R_m fails to decode the data x_1; or (2) the R_m decodes the data x_1 successfully but does not decode the data x_2; or (3) the R_m decodes both x_1 and x_2 successfully, but the S_1 cannot decode the DNC-coded data x to get the desired data x_2 in the second time slot. We express the outage probability of the secondary source S_1 by the mathematical expression

$$
\begin{aligned}
OP^{(1)}_{\text{UTW-2TS-DNC-}S_1} = &\underbrace{\Pr\left\{\gamma^{(1)}_{R_m \to x_1} < \gamma_{\text{th}}\right\}}_{\Phi_1} \\
&+ \underbrace{\Pr\left\{\left(\gamma^{(1)}_{R_m \to x_1} \geq \gamma_{\text{th}}\right) \cap \left(\gamma^{(1)}_{R_m \to x_2} < \gamma_{\text{th}}\right)\right\}}_{\Phi_2} \\
&+ \Pr\left\{\left(\gamma^{(1)}_{R_m \to x_1} \geq \gamma_{\text{th}}\right) \cap \left(\gamma^{(1)}_{R_m \to x_2} \geq \gamma_{\text{th}}\right)\right. \\
&\left. \cdot \cap \left(\gamma^{\text{UTW-2TS-DNC}}_{S_1 \to x} < \gamma_{\text{th}}\right)\right\}.
\end{aligned}
\tag{18}
$$

In (18), the probability $\Phi_1 = \Pr\{\gamma^{(1)}_{R_m \to x_1} < \gamma_{\text{th}}\}$ is considered when the secondary relay R_m fails to decode the data x_1 while applying the SIC technique. The probability $\Phi_2 = \Pr\{(\gamma^{(1)}_{R_m \to x_1} \geq \gamma_{\text{th}}) \cap (\gamma^{(1)}_{R_m \to x_2} < \gamma_{\text{th}})\}$ is the decoding error of the data x_2 at the secondary relay R_m. Finally, the probability $\Pr\{(\gamma^{(1)}_{R_m \to x_1} \geq \gamma_{\text{th}}) \cap (\gamma^{(1)}_{R_m \to x_2} \geq \gamma_{\text{th}}) \cap (\gamma^{\text{UTW-2TS-DNC}}_{S_1 \to x} < \gamma_{\text{th}})\}$ measures the decoding error of the coded data x at the secondary source S_1. The event $\gamma^{\text{SIC-DNC}}_{S_1 \to x} < \gamma_{\text{th}}$ occurs independently with the events $\gamma^{(1)}_{R_m \to x_1} \geq \gamma_{\text{th}}$ and $\gamma^{(1)}_{R_m \to x_2} \geq \gamma_{\text{th}}$; thus, we have an equivalent representation of (18) as

$$
\begin{aligned}
OP^{(1)}_{\text{UTW-2TS-DNC-}S_1} = &\Phi_1 + \Phi_2 + \Pr\left\{\left(\gamma^{(1)}_{R_m \to x_1} \geq \gamma_{\text{th}}\right) \cap \left(\gamma^{(1)}_{R_m \to x_2} \geq \gamma_{\text{th}}\right)\right\} \\
&\times \Pr\left\{\gamma^{\text{UTW-2TS-DNC}}_{S_1 \to x} < \gamma_{\text{th}}\right\} \\
= &\Phi_1 + \Phi_2 + \left(\Pr\left\{\gamma^{(1)}_{R_m \to x_1} \geq \gamma_{\text{th}}\right\} - \Pr\left\{\left(\gamma^{(1)}_{R_m \to x_1} \geq \gamma_{\text{th}}\right)\right.\right. \\
&\left.\left. \cdot \cap \left(\gamma^{(1)}_{R_m \to x_2} < \gamma_{\text{th}}\right)\right\}\right) \times \Pr\left\{\gamma^{\text{UTW-2TS-DNC}}_{S_1 \to x} < \gamma_{\text{th}}\right\} \\
= &\Phi_1 + \Phi_2 + \left(1 - \Pr\left\{\gamma^{(1)}_{R_m \to x_1} < \gamma_{\text{th}}\right\}\right. \\
&\left. - \Pr\left\{\left(\gamma^{(1)}_{R_m \to x_1} \geq \gamma_{\text{th}}\right) \cap \left(\gamma^{(1)}_{R_m \to x_2} < \gamma_{\text{th}}\right)\right\}\right) \\
&\times \Pr\left\{\gamma^{\text{UTW-2TS-DNC}}_{S_1 \to x} < \gamma_{\text{th}}\right\} \\
= &\left(\Phi_1 + \Phi_2\right)\left(1 - \Pr\left\{\gamma^{\text{UTW-2TS-DNC}}_{S_1 \to x} < \gamma_{\text{th}}\right\}\right) \\
&+ \Pr\left\{\gamma^{\text{UTW-2TS-DNC}}_{S_1 \to x} < \gamma_{\text{th}}\right\}.
\end{aligned}
\tag{19}
$$

To analyze the probabilities Φ_1, Φ_2, and $\Pr\{\gamma^{\text{UTW-2TS-DNC}}_{S_1 \to x} < \gamma_{\text{th}}\}$, we define $G_{X_1 Y_1 / X_2 Y_2} = g_{X_1 Y_1} / g_{X_2 Y_2}$, where $X_1, X_2, Y_1, Y_2 \in \{S_1, S_2, R_i, \text{PR}\}$, $g_{X_1 Y_1} \neq g_{X_2 Y_2}$, and $i = \{1, 2, \cdots, M\}$; then, by referring from [30] (eqs. 24–25), the CDF and PDF of the RV $G_{X_1 Y_1 / X_2 Y_2}$ are obtained as

$$
F_{G_{X_1 Y_1 / X_2 Y_2}}(z) = \frac{\lambda_{X_1 Y_1} z}{\lambda_{X_2 Y_2} + \lambda_{X_1 Y_1} z},
\tag{20}
$$

$$
f_{G_{X_1 Y_1 / X_2 Y_2}}(x) = \frac{dF_{G_{X_1 Y_1 / X_2 Y_2}}(x)}{dx} = \frac{\lambda_{X_1 Y_1} \lambda_{X_2 Y_2}}{\left(\lambda_{X_2 Y_2} + \lambda_{X_1 Y_1} x\right)^2}.
\tag{21}
$$

For the selected secondary relay R_m from the S_1-R_i links ($m, i = \{1, 2, \cdots, M\}$), the CDF of the RV $G_{S_1 R_m / S_1 \text{PR}}$ is given as

$$
\begin{aligned}
F_{G_{S_1 R_m / S_1 \text{PR}}}(z) &= \Pr\left\{G_{S_1 R_m / S_1 \text{PR}} < z\right\} = \Pr\left\{\frac{g_{S_1 R_m}}{g_{S_1 \text{PR}}} < z\right\} \\
&= \Pr\left\{g_{S_1 R_m} < z g_{S_1 \text{PR}}\right\} \\
&= \int_0^\infty f_{g_{S_1 \text{PR}}}(t) \times F_{g_{S_1 R_m}}(zt) dt.
\end{aligned}
\tag{22}
$$

Substituting the CDF of the RV $g_{S_1 R_m}$ in (4) and the PDF of the RV $g_{S_1 \text{PR}}$ into (22), we have a final result as

$$
\begin{aligned}
F_{G_{S_1 R_m / S_1 \text{PR}}}(z) &= \int_0^\infty \lambda_4 e^{-\lambda_4 t} \sum_{p=0}^M \binom{p}{M} (-1)^p e^{-p\lambda_1 z t} dt \\
&= \lambda_4 \sum_{p=0}^M \binom{p}{M} (-1)^p \int_0^\infty e^{-t(\lambda_4 + p\lambda_1 z)} dt \\
&= \lambda_4 \sum_{p=0}^M \binom{p}{M} \frac{(-1)^p}{\lambda_4 + p\lambda_1 z}.
\end{aligned}
\tag{23}
$$

The probabilities Φ_1 and Φ_2 are solved by Lemmas 1 and 2 as follows.

Lemma 1. *The probability Φ_1 is solved as*

$$
\begin{aligned}
\Phi_1 = 1 + \lambda_2 \lambda_4 \lambda_5 \sum_{p=1}^M \binom{p}{M} \frac{(-1)^p}{\lambda_2 v_3(p) - \lambda_5 v_4(p)} \\
\cdot \left(\frac{1}{\lambda_5} - \frac{v_4(p)}{\lambda_2 v_3(p) - \lambda_5 v_4(p)} \ln\left(\frac{\lambda_2 v_3(p)}{\lambda_5 v_4(p)}\right)\right),
\end{aligned}
\tag{24}
$$

where $v_1 = \gamma_{th} \alpha_2 / \alpha_1$, $v_2 = \gamma_{th} / \alpha_1 Q$, $v_3(p)$, and $v_4(p)$ are functions versus count variable p and are defined, respectively, as $v_3(p) = \lambda_4 + p\lambda_1 v_2$ and $v_4(p) = p\lambda_1 v_1$.

Proof. (proven in Appendix A).

Lemma 2. *The probability Φ_2 is given in two cases of ε as follows:*

Case $\varepsilon = 0$ (perfect SICs):

$$\Phi_2 = \frac{\lambda_2 v_5}{\lambda_5 + \lambda_2 v_5} - \lambda_2 \lambda_4 \lambda_5 \sum_{p=0}^{M} \binom{p}{M} \frac{(-1)^p}{\lambda_2 v_3(p) - \lambda_5 v_4(p)}$$
$$\times \left(\frac{\lambda_2 v_5}{\lambda_5(\lambda_5 + \lambda_2 v_5)} - \frac{v_4(p)}{\lambda_2 v_3(p) - \lambda_5 v_4(p)} \ln \left(\frac{(\lambda_5 + \lambda_2 v_5) \times v_3(p)}{\lambda_5 \times (v_3(p) + v_5 v_4(p))} \right) \right). \tag{25}$$

Cas $\varepsilon = 1$ (imperfect SICs):

$$\Phi_2 = 1 - \lambda_5 e^{(\lambda_5 + \lambda_2 v_5)\Omega/\lambda_2 v_6} \Gamma\left(0, \frac{(\lambda_5 + \lambda_2 v_5)\Omega}{\lambda_2 v_6} \right) \left\{ \frac{\Omega}{\lambda_2 v_6} \right.$$
$$- \sum_{p=0}^{M} \binom{p}{M} \frac{(-1)^p}{\lambda_2 v_3(p) - \lambda_5 v_4(p)} \left(\frac{\Omega \lambda_4}{v_6} + \frac{\lambda_2 \lambda_4 v_4(p)}{\lambda_2 v_3(p) - \lambda_5 v_4(p)} \right) \right\}$$
$$- \lambda_2 \lambda_4 \sum_{p=0}^{M} \binom{p}{M} \frac{(-1)^p}{\lambda_2 v_3(p) - \lambda_5 v_4(p)} \left\{ 1 - \frac{\lambda_5 v_4(p)}{\lambda_2 v_3(p) - \lambda_5 v_4(p)} \right.$$
$$\times \left(\ln \left(\frac{(\lambda_5 + \lambda_2 v_5) v_3(p)}{\lambda_5 (v_3(p) + v_5 v_4(p))} \right) \right.$$
$$\left. \left. - e^{(v_3(p) + v_5 v_4(p))\Omega/v_6 v_4(p)} \Gamma\left(0, \frac{(v_3(p) + v_5 v_4(p))\Omega}{v_6 v_4(p)} \right) \right) \right\}, \tag{26}$$

where $\Gamma(u, v)$ is the upper incomplete Gamma function ($\Gamma(u, v) = \int_v^\infty e^{-t} t^{u-1} dt$) ([42], eq. 8.350.2).

Proof. (see the proof and notations in Appendix B).

The last probability $\Pr\{\gamma_{S_1 \to x}^{\text{UTW-2TS-DNC}} < \gamma_{\text{th}}\}$ in (19) is obtained by using formula (13) with $k = 1$ as

$$\Pr\left\{ \gamma_{S_1 \to x}^{\text{UTW-2TS-DNC}} < \gamma_{\text{th}} \right\} = \Pr\left\{ \frac{Q g_{R_m S_1}}{g_{R_m \text{PR}}} < \gamma_{\text{th}} \right\}$$
$$= \Pr\left\{ G_{R_m S_1 / R_m \text{PR}} < \frac{\gamma_{\text{th}}}{Q} \right\}$$
$$= F_{G_{R_m S_1 / R_m \text{PR}}} \left(\frac{\gamma_{\text{th}}}{Q} \right) \tag{27}$$
$$= \frac{\lambda_1(\gamma_{\text{th}}/Q)}{\lambda_3 + \lambda_1(\gamma_{\text{th}}/Q)}$$
$$= \frac{\lambda_1 \gamma_{\text{th}}}{\lambda_3 Q + \lambda_1 \gamma_{\text{th}}}.$$

Substituting (27) into (19), the outage probability of the secondary source S_1 is obtained by the closed-form expression

$$\text{OP}_{\text{UTW-2TS-DNC-}S_1}^{(1)} = \frac{(\Phi_1 + \Phi_2)\lambda_3 Q + \lambda_1 \gamma_{\text{th}}}{\lambda_3 Q + \lambda_1 \gamma_{\text{th}}}, \tag{28}$$

where Φ_1 and Φ_2 are given by closed-form expressions in Lemmas 1 and 2, respectively.

The secondary source S_2 expects to receive the desired data x_1 of the secondary source S_1. Hence, the outage probability of the secondary source S_2 occurs when (1) the selected secondary relay R_m cannot decode the data x_1 or (2) the S_2 fails to decode the data transmitted by the R_m after the data x_1 is decoded successfully. We formulate the outage probability of the secondary source S_1 as

$$\text{OP}_{\text{UTW-2TS-DNC-}S_2}^{(1)} = \Pr\left\{ \gamma_{R_m \to x_1}^{(1)} < \gamma_{\text{th}} \right\} + \Pr\left\{ \left(\gamma_{R_m \to x_1}^{(1)} \geq \gamma_{\text{th}} \right) \right.$$
$$\left. \cap \left(\gamma_{S_2 \to x}^{\text{UTW-2TS-DNC}} < \gamma_{\text{th}} \right) \right\}. \tag{29}$$

In (29), the probability part $\Pr\{(\gamma_{R_m \to x_1}^{(1)} \geq \gamma_{\text{th}}) \cap (\gamma_{S_2 \to x}^{\text{UTW-2TS-DNC}} < \gamma_{\text{th}})\}$ shows transmission errors of the data x_1 from the selected secondary relay R_m to the desired secondary source S_2. Because the event $\gamma_{S_2 \to x}^{\text{UTW-2TS-DNC}} < \gamma_{\text{th}}$ occurs independently, and with the help of (13) with $k = 1$, the outage probability of the secondary source S_2 is manipulated and solved as

$$\text{OP}_{\text{UTW-2TS-DNC-}S_2}^{(1)} = \Phi_1 + \Pr\left\{ \gamma_{R_m \to x_1}^{(1)} \geq \gamma_{\text{th}} \right\}$$
$$\times \Pr\left\{ \gamma_{S_2 \to x}^{\text{UTW-2TS-DNC}} < \gamma_{\text{th}} \right\}$$
$$= \Phi_1 + (1 - \Phi_1) \times \Pr\left\{ \frac{Q g_{R_m S_2}}{g_{R_m \text{PR}}} < \gamma_{\text{th}} \right\}$$
$$= \Phi_1 + (1 - \Phi_1) \times F_{G_{R_m S_2 / R_m \text{PR}}} \left(\frac{\gamma_{\text{th}}}{Q} \right)$$
$$= \Phi_1 + (1 - \Phi_1) \times \left(\frac{\lambda_2 \gamma_{\text{th}}}{\lambda_3 Q + \lambda_2 \gamma_{\text{th}}} \right), \tag{30}$$

where Φ_1 is given exactly by Lemma 1.

Next, the throughput of the UTW-2TS-DNC protocol as in (17) is solved in Case 1 ($d_{S_1 R_i} \leq d_{S_2 R_i}$) by

$$\text{TP}_{\text{UTW-2TS-DNC}}^{(1)} = \frac{1}{2} \left(2 - \text{OP}_{\text{UTW-2TS-DNC-}S_1}^{(1)} - \text{OP}_{\text{UTW-2TS-DNC-}S_2}^{(1)} \right)$$
$$\cdot \log_2(1 + \gamma_{\text{th}})$$
$$= \frac{\log_2(1 + \gamma_{\text{th}})}{2} \left\{ 2 - 2\Phi_1 - (1 - \Phi_1) \right.$$
$$\cdot \left(\frac{\lambda_1 \gamma_{\text{th}}}{\lambda_3 Q + \lambda_1 \gamma_{\text{th}}} + \frac{\lambda_2 \gamma_{\text{th}}}{\lambda_3 Q + \lambda_2 \gamma_{\text{th}}} \right)$$
$$\left. - \frac{\lambda_3 Q \Phi_2}{\lambda_3 Q + \lambda_1 \gamma_{\text{th}}} \right\}, \tag{31}$$

where Φ_1 and Φ_2 are taken from Lemmas 1 and 2, respectively.

3.1.2. Case 2: $d_{S_1 R_i} > d_{S_2 R_i}$. In this case, a selected secondary relay R_m must decode the data x_2 firstly. Because the system model of the UTW-2TS-DNC protocol in Figure 1 is

symmetric, we can model the outage probabilities in Case 1 as functions versus symmetric parameters as $\mathrm{OP}^{(1)}_{\text{UTW-2TS-DNC-}S_1} \equiv \mathrm{OP}^{(1)}_{\text{UTW-2TS-DNC-}S_1}(\lambda_1, \alpha_1, \lambda_2, \alpha_2)$ and $\mathrm{OP}^{(1)}_{\text{UTW-2TS-DNC-}S_2} \equiv \mathrm{OP}^{(1)}_{\text{UTW-2TS-DNC-}S_2}(\lambda_1, \alpha_1, \lambda_2, \alpha_2)$. Hence, in Case 2 ($d_{S_1 R_i} > d_{S_2 R_i}$), the outage probability of the secondary sources S_1 and S_2 can be inferred from Case 1 as follows:

$$\mathrm{OP}^{(2)}_{\text{UTW-2TS-DNC-}S_1} = \mathrm{OP}^{(1)}_{\text{UTW-2TS-DNC-}S_2}(\lambda_2, \alpha_2, \lambda_1, \alpha_1), \quad (32)$$

$$\mathrm{OP}^{(2)}_{\text{UTW-2TS-DNC-}S_2} = \mathrm{OP}^{(1)}_{\text{UTW-2TS-DNC-}S_1}(\lambda_2, \alpha_2, \lambda_1, \alpha_1), \quad (33)$$

where $\mathrm{OP}^{(1)}_{\text{UTW-2TS-DNC-}S_2}(\lambda_2, \alpha_2, \lambda_1, \alpha_1)$ and $\mathrm{OP}^{(1)}_{\text{UTW-2TS-DNC-}S_1}(\lambda_2, \alpha_2, \lambda_1, \alpha_1)$ are closed-form outage probability expressions of the secondary sources S_2 and S_1 in Case 1 with replacing $\lambda_1 \leftrightarrow \lambda_2$ and $\alpha_1 \leftrightarrow \alpha_2$.

The throughput of the UTW-2TS-DNC protocol as in (17) is obtained in Case 2 by

$$\mathrm{TP}^{(2)}_{\text{UTW-2TS-DNC}} = \frac{\log_2(1 + \gamma_{\text{th}})}{2} \cdot \left(2 - \mathrm{OP}^{(2)}_{\text{UTW-2TS-DNC-}S_1} - \mathrm{OP}^{(2)}_{\text{UTW-2TS-DNC-}S_2}\right), \quad (34)$$

where $\mathrm{OP}^{(2)}_{\text{UTW-2TS-DNC-}S_1}$ and $\mathrm{OP}^{(2)}_{\text{UTW-2TS-DNC-}S_2}$ are presented in (32) and (33), respectively.

3.2. The UTW-2TS-SC Protocol. Operation of the UTW-2TS-SC protocol is different to the UTW-2TS-DNC protocol in the time slot 2 (the last time slot) with power allocation coefficients β_1 and β_2 to decoded data x_1 and x_2. Similar to the UTW-2TS-DNC protocol for Case 1 ($d_{S_1 R_i} \leq d_{S_2 R_i}$) and Case 2 ($d_{S_1 R_i} > d_{S_2 R_i}$), the outage probability and corresponding throughput of the secondary sources S_1 and S_2 will be obtained briefly in the next subsections.

3.2.1. Case 1: $d_{S_1 R_i} \leq d_{S_2 R_i}$. The decoding operation of the UTW-2TS-SC protocol is similar to that of the UTW-2TS-DNC protocol. One difference is that the secondary source S_1 expects to decode the desired data x_2 directly from the received signal y_{S_1} as in (14) where $k = 1$ and $l = 2$. Hence, the outage probability of the secondary source S_1 (denoted as $\mathrm{OP}^{(1)}_{\text{UTW-2TS-SC-}S_1}$) is expressed in Case 1 ($d_{S_1 R_i} \leq d_{S_2 R_i}$) as

$$\begin{aligned} \mathrm{OP}^{(1)}_{\text{UTW-2TS-SC-}S_1} &= \Pr\left\{\gamma^{(1)}_{R_m \to x_1} < \gamma_{\text{th}}\right\} \\ &+ \Pr\left\{\left(\gamma^{(1)}_{R_m \to x_1} \geq \gamma_{\text{th}}\right) \cap \left(\gamma^{(1)}_{R_m \to x_2} < \gamma_{\text{th}}\right)\right\} \\ &+ \Pr\left\{\left(\gamma^{(1)}_{R_m \to x_1} \geq \gamma_{\text{th}}\right) \cap \left(\gamma^{(1)}_{R_m \to x_2} \geq \gamma_{\text{th}}\right) \right. \\ &\left. \cap \left(\gamma^{\text{UTW-2TS-SC}}_{S_1 \to x_2} < \gamma_{\text{th}}\right)\right\} \\ &= (\Phi_1 + \Phi_2) \times \left(1 - \Pr\left\{\gamma^{\text{UTW-2TS-SC}}_{S_1 \to x_2} < \gamma_{\text{th}}\right\}\right) \\ &+ \Pr\left\{\gamma^{\text{UTW-2TS-SC}}_{S_1 \to x_2} < \gamma_{\text{th}}\right\}, \end{aligned}$$

(35)

where Φ_1 and Φ_2 are obtained from Lemmas 1 and 2.

In (35), the probability $\Pr\left\{(\gamma^{(1)}_{R_m \to x_1} \geq \gamma_{\text{th}}) \cap (\gamma^{(1)}_{R_m \to x_2} \geq \gamma_{\text{th}}) \cap (\gamma^{\text{UTW-2TS-SC}}_{S_1 \to x_2} < \gamma_{\text{th}})\right\}$ directly calculates the decoding error of the data x_2 at the secondary source S_1.

Substituting (16) with $k = 1$ and $l = 2$ into the probability $\Pr\left\{\gamma^{\text{UTW-2TS-SC}}_{S_1 \to x_2} < \gamma_{\text{th}}\right\}$ in (35) and performing similarly as (27), we have a result as

$$\begin{aligned} \Pr\left\{\gamma^{\text{UTW-2TS-SC}}_{S_1 \to x_2} < \gamma_{\text{th}}\right\} &= \Pr\left\{\frac{Q\beta_2 g_{R_m S_1}}{g_{R_m \text{PR}}} < \gamma_{\text{th}}\right\} \\ &= \Pr\left\{G_{R_m S_1 / R_m \text{PR}} < \frac{\gamma_{\text{th}}}{\beta_2 Q}\right\} \\ &= F_{G_{R_m S_1 / R_m \text{PR}}}\left(\frac{\gamma_{\text{th}}}{\beta_2 Q}\right) \\ &= \frac{\lambda_1(\gamma_{\text{th}}/(\beta_2 Q))}{\lambda_3 + \lambda_1(\gamma_{\text{th}}/(\beta_2 Q))} \\ &= \frac{\lambda_1 \gamma_{\text{th}}}{\lambda_3 \beta_2 Q + \lambda_1 \gamma_{\text{th}}}. \end{aligned} \quad (36)$$

Hence, the outage probability $\mathrm{OP}^{(1)}_{\text{UTW-2TS-SC-}S_1}$ is solved in a closed-form expression with Φ_1, Φ_2, and $\Pr\{\gamma^{\text{UTW-2TS-SC}}_{S_1 \to x_2} < \gamma_{\text{th}}\}$ from Lemmas 1 and 2 and (36).

We see that because $\beta_2 \leq 1$, then $\Pr\{\gamma^{\text{UTW-2TS-SC}}_{S_1 \to x_2} < \gamma_{\text{th}}\} \geq \Pr\{\gamma^{\text{UTW-2TS-DNC}}_{S_1 \to x} < \gamma_{\text{th}}\}$ which leads to $\mathrm{OP}^{(1)}_{\text{UTW-2TS-SC-}S_1} \geq \mathrm{OP}^{(1)}_{\text{UTW-2TS-DNC-}S_1}$.

Similarly, the remaining outage probability of the secondary source S_2 is obtained as

$$\begin{aligned} \mathrm{OP}^{(1)}_{\text{UTW-2TS-SC-}S_2} &= \Pr\left\{\gamma^{(1)}_{R_m \to x_1} < \gamma_{\text{th}}\right\} + \Pr\left\{\left(\gamma^{(1)}_{R_m \to x_1} \geq \gamma_{\text{th}}\right) \right. \\ &\left. \cap \left(\gamma^{\text{UTW-2TS-SC}}_{S_2 \to x_1} < \gamma_{\text{th}}\right)\right\} \\ &= \Phi_1 + (1 - \Phi_1) \times \left(\frac{\lambda_2 \gamma_{\text{th}}}{\lambda_3 \beta_1 Q + \lambda_2 \gamma_{\text{th}}}\right). \end{aligned} \quad (37)$$

Then, the throughput of the UTW-2TS-SC protocol is solved in Case 1 ($d_{S_1 R_i} \leq d_{S_2 R_i}$) by

$$\begin{aligned} \mathrm{TP}^{(1)}_{\text{UTW-2TS-SC}} &= \frac{1}{2}\left(2 - \mathrm{OP}^{(1)}_{\text{UTW-2TS-SC-}S_1} - \mathrm{OP}^{(1)}_{\text{UTW-2TS-SC-}S_2}\right) \\ &\cdot \log_2(1 + \gamma_{\text{th}}) \\ &= \frac{\log_2(1 + \gamma_{\text{th}})}{2}\left\{2 - 2\Phi_1 - (1 - \Phi_1) \right. \\ &\cdot \left(\frac{\lambda_1 \gamma_{\text{th}}}{\lambda_3 \beta_2 Q + \lambda_1 \gamma_{\text{th}}} + \frac{\lambda_2 \gamma_{\text{th}}}{\lambda_3 \beta_2 Q + \lambda_2 \gamma_{\text{th}}}\right) \\ &\left. - \frac{\lambda_3 \beta_2 Q \Phi_2}{\lambda_3 \beta_2 Q + \lambda_1 \gamma_{\text{th}}}\right\}. \end{aligned} \quad (38)$$

3.2.2. Case 2: $d_{S_1 R_i} > d_{S_2 R_i}$. We can also model the outage probabilities in Case 1 as functions versus parameters as
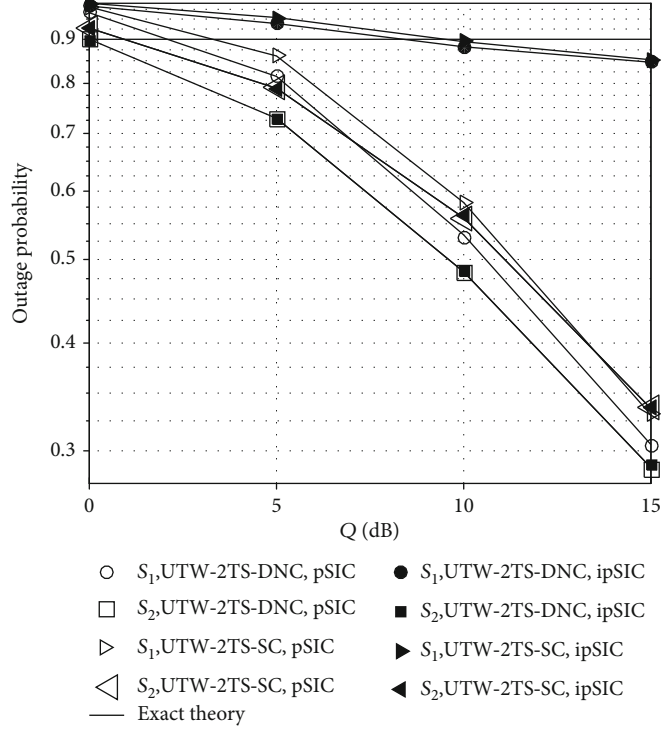
FIGURE 2: Outage probabilities of the secondary sources S_1 and S_2 versus Q (dB) when $\alpha_1 = \alpha_2 = 0.5$, $\beta_1 = 0.7$, $\beta_2 = 1 - \beta_1 = 0.3$, $\Psi = 0$ (dB), $x_R = 0.3$, $y_R = 0$, $x_{PR} = y_{PR} = 0.5$, and $M = 3$.

$\mathrm{OP}^{(1)}_{\mathrm{UTW\text{-}2TS\text{-}SC\text{-}}S_1}(\lambda_1, \alpha_1, \beta_1, \lambda_2, \alpha_2, \beta_2)$ and $\mathrm{OP}^{(1)}_{\mathrm{UTW\text{-}2TS\text{-}SC\text{-}}S_2}($ $\lambda_1, \alpha_1, \beta_1, \lambda_2, \alpha_2, \beta_2)$. Because of the symmetry model of the UTW-2TS-SC protocol in Figure 1, the outage probability of the secondary sources S_1 and S_2 in Case 2 can be concluded from Case 1 as follows:

$$\mathrm{OP}^{(2)}_{\mathrm{UTW\text{-}2TS\text{-}SC\text{-}}S_1} = \mathrm{OP}^{(1)}_{\mathrm{UTW\text{-}2TS\text{-}SC\text{-}}S_2}(\lambda_2, \alpha_2, \beta_2, \lambda_1, \alpha_1, \beta_1),$$
(39)

$$\mathrm{OP}^{(2)}_{\mathrm{UTW\text{-}2TS\text{-}SC\text{-}}S_2} = \mathrm{OP}^{(1)}_{\mathrm{UTW\text{-}2TS\text{-}SC\text{-}}S_1}(\lambda_2, \alpha_2, \beta_2, \lambda_1, \alpha_1, \beta_1),$$
(40)

where $\mathrm{OP}^{(1)}_{\mathrm{UTW\text{-}2TS\text{-}SC\text{-}}S_2}(\lambda_2, \alpha_2, \beta_2, \lambda_1, \alpha_1, \beta_1)$ and $\mathrm{OP}^{(1)}_{\mathrm{UTW\text{-}2TS\text{-}SC\text{-}}S_1}(\lambda_2, \alpha_2, \beta_2, \lambda_1, \alpha_1, \beta_1)$ are closed-form outage probability expressions of the secondary sources S_2 and S_1 in Case 1 with replacing $\lambda_1 \leftrightarrow \lambda_2$, $\alpha_1 \leftrightarrow \alpha_2$, and $\beta_1 \leftrightarrow \beta_2$.

The corresponding throughput of the UTW-2TS-SC protocol is obtained in Case 2 as

$$\mathrm{TP}^{(2)}_{\mathrm{UTW\text{-}2TS\text{-}SC}} = \frac{\log_2(1 + \gamma_{\mathrm{th}})}{2}$$
$$\cdot \left(2 - \mathrm{OP}^{(2)}_{\mathrm{UTW\text{-}2TS\text{-}SC\text{-}}S_1} - \mathrm{OP}^{(2)}_{\mathrm{UTW\text{-}2TS\text{-}SC\text{-}}S_2}\right),$$
(41)

where $\mathrm{OP}^{(2)}_{\mathrm{UTW\text{-}2TS\text{-}SC\text{-}}S_1}$ and $\mathrm{OP}^{(2)}_{\mathrm{UTW\text{-}2TS\text{-}SC\text{-}}S_2}$ are given in (39) and (40), respectively.

4. Results and Discussions

This section presents analysis and simulation results in terms of outage probabilities and throughputs of the protocols UTW-2TS-DNC and UTW-2TS-SC in the two-dimensional plane. These proposed protocols are considered in two cases of perfect SICs ($\varepsilon = 0$, denoted by pSIC) and imperfect SICs ($\varepsilon = 1$, denoted by ipSIC). The simulation results are performed by the Monte Carlo method to validate the analysis ones which are shown from exact closed-form expressions. Coordinates of the nodes S_1, S_2, PR, and the cluster with M secondary relay R_i are set as $S_1(0,0)$, $S_2(1,0)$, $\mathrm{PR}(x_{PR}, y_{PR})$, and $R_i(x_R, y_R)$, where $0 < x_R < 1$ and $i = \{1, 2, \cdots, M\}$. The normalized distances are calculated from the coordinates as $d_1 = \sqrt{x_R^2 + y_R^2}$, $d_2 = \sqrt{(1 - x_R)^2 + y_R^2}$, $d_3 = \sqrt{(x_{PR} - x_R)^2 + (y_{PR} - y_R)^2}$, $d_4 = \sqrt{x_{PR}^2 + y_{PR}^2}$, and $d_5 = \sqrt{(1 - x_{PR})^2 + y_{PR}^2}$. It is assumed that the threshold SINR and the path loss exponent are fixed by $\gamma_{\mathrm{th}} = 3$ and $\eta = 3$, and Q (dB) on the x-axis is defined as $Q = 10 \times \log_{10}(I/\sigma^2)$ (dB). Markers denote simulated results, and solid lines present analyzed ones.

Figure 2 shows the outage probabilities of the secondary sources S_1 and S_2 in the protocols UTW-2TS-DNC and UTW-2TS-SC versus Q (dB) when $x_R = 0.3$, $y_R = 0$, $x_{PR} = y_{PR} = 0.5$, $\Psi = 0$ (dB), $M = 3$, and interference allocation coefficients $\alpha_1 = \alpha_2 = 0.5$ [19, 30]. The normalized distances are calculated as $d_1 = 0.3$, $d_2 = 0.7$, $d_3 = 0.54$, $d_4 = 0.71$, and $d_5 = 0.71$; hence, the results are presented following Case 1

Figure 3: Throughputs of the protocols UTW-2TS-DNC and UTW-2TS-SC versus Q (dB) when $\alpha_1 = \alpha_2 = 0.5$, $\beta_1 = 0.7$, $\beta_2 = 1 - \beta_1 = 0.3$, $\Psi = 0$ (dB), $x_R = 0.3$, $y_R = 0$, $x_{PR} = y_{PR} = 0.5$, and $M = \{3, 12\}$.

($d_{S_1 R_i} \leq d_{S_2 R_i}$). The power allocation coefficients β_1 and β_2 at the selected secondary relay are suitably set as $\beta_1 = 0.7$ and $\beta_2 = 1 - \beta_1 = 0.3$. We note that the power allocation coefficients β_1 and β_2 to carry the desired data x_1 and x_2 from the selected relay to the S_2 and S_1, respectively. Simulated results are performed from equations (18) and (29) by making RVs in (3), (7), and (13), whereas exact theory values are calculated by closed-form expressions in (28) and (30) for the secondary sources S_1 and S_2, respectively. From Figure 2, some findings are watched as follows. Firstly, the outage probabilities of the secondary source S_1 and S_2 in both protocols with the perfect SICs and imperfect SICs decrease when the interference constraint parameters Q increase. Secondly, the system performances of the secondary source S_1 with the perfect SICs are always better than those with the imperfect SICs. We note that the outage probabilities of the secondary source S_2 in both protocols are not affected by SIC operations, and thus, the system performances of the secondary source S_2 with the perfect SICs and the imperfect SICs are identical (markers and solid line are merged in Figure 2). Thirdly, in this case, the outage probabilities of the secondary source S_2 are almost smaller than those of the secondary source S_1. Finally, the results (solid lines) from the theory expressions of the outage probabilities are exact to the Monte Carlo simulations. These findings can be reasoned that the received SINRs in (3) and (7) to decode the data x_1 and x_2 declined by more interferences from transmittance of the data-carried signal x_2, affecting of the residual interference signal and interference constraints as in (1). In addition, with

large values of Q, the transmit powers of the nodes S_1, S_2, and R_m increase as in (1) which correspond to large SINRs to decode the data x_1, x_2, and x as in (3), (7), (13), and (16), where $m = \{1, 2, \cdots, M\}$.

Figure 3 compares the throughputs of the UTW-2TS-DNC and UTW-2TS-SC protocols versus Q (dB) when $x_R = 0.3$, $y_R = 0$, $x_{PR} = y_{PR} = 0.5$, $\Psi = 0$ (dB), $\alpha_1 = \alpha_2 = 0.5$, $\beta_1 = 0.7$, $\beta_2 = 1 - \beta_1 = 0.3$, and the number of intermediate secondary relays is set as $M \in \{3, 12\}$. Exact throughput curves of the UTW-2TS-DNC and UTW-2TS-SC protocols are obtained by theoretic analyses in (31) and (38). Simulation markers are carried out by (17) with separate outage probabilities for each protocol. From Figure 3, the throughputs of the UTW-2TS-DNC protocol are larger than those of the UTW-2TS-SC protocol with all the cases of SICs and M. In addition, the throughputs of both protocols increase when the UTW-2TS systems use more secondary relays (M is increased). These contributions are based on observations from SINRs (13) and (16). With $0 \leq \beta_1$ and $\beta_2 \leq 1$, the SINRs in (13) of the UTW-2TW-DNC protocol are always larger than those in (16) of the UTW-2TW-SC protocol. Furthermore, with more cooperative secondary relays, the diversity capacity of both protocols will be increased by the relay selection methods.

Figure 4 presents the throughputs of the protocols UTW-2TS-DNC and UTW-2TS-SC versus α_1 when $Q = 10$ (dB), $\beta_1 = 0.7$, $\beta_2 = 1 - \beta_1 = 0.3$, $\Psi = -5$ (dB), $x_R = 0.3$, $y_R = 0$, $x_{PR} = y_{PR} = 0.5$, $M = 3$, and α_2 can be set as $\alpha_2 = 1 - \alpha_1$. In Figure 4, the throughputs of the protocols UTW-2TS-DNC
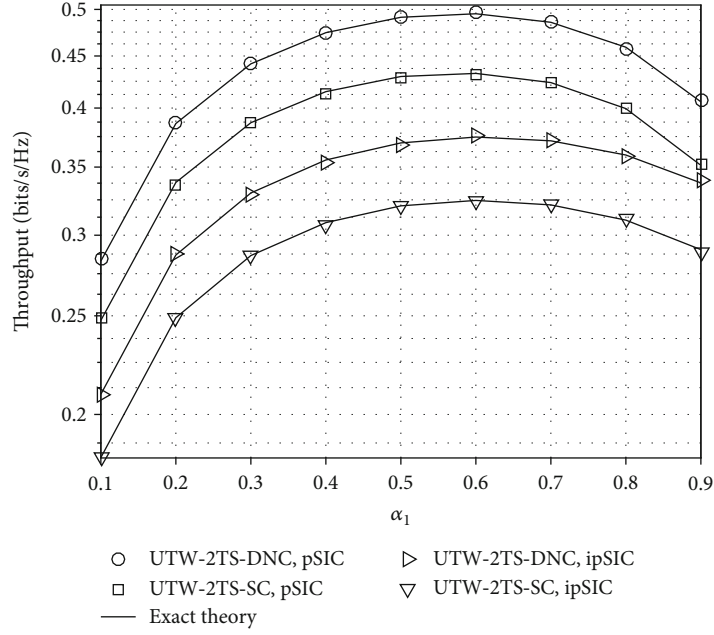
FIGURE 4: Throughputs of the protocols UTW-2TS-DNC and UTW-2TS-SC versus α_1 when $Q = 10$ (dB), $\beta_1 = 0.7$, $\beta_2 = 1 - \beta_1 = 0.3$, $\Psi = -5$ (dB), $x_R = 0.3$, $y_R = 0$, $x_{PR} = y_{PR} = 0.5$, $M = 3$, and $\alpha_2 = 1 - \alpha_1$.
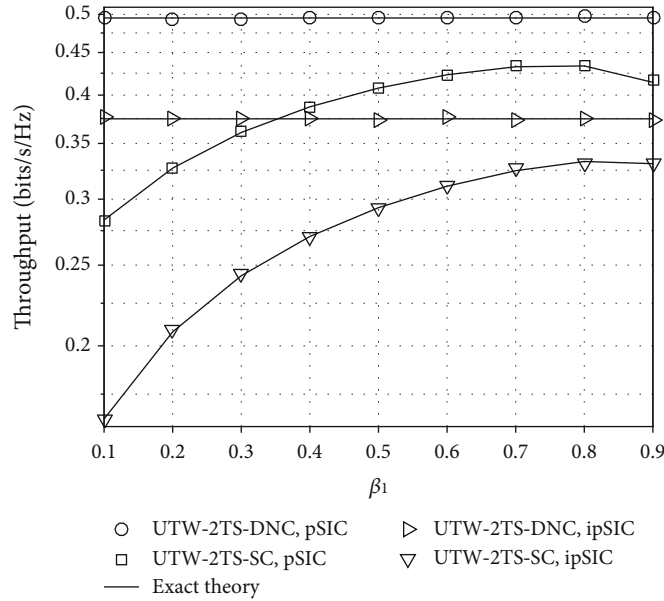
FIGURE 5: Throughputs of the protocols UTW-2TS-DNC and UTW-2TS-SC versus β_1 when $Q = 10$ (dB), $\alpha_1 = 0.6$, $\alpha_2 = 1 - \alpha_1 = 0.4$, $\Psi = -5$ (dB), $x_R = 0.3$, $y_R = 0$, $x_{PR} = y_{PR} = 0.5$, $M = 3$, and $\beta_2 = 1 - \beta_1$.

and UTW-2TS-SC achieve the large values at an approximate interference power allocation coefficient $\alpha_1 \approx 0.6$ for both cases (perfect SICs and imperfect SICs). The value $\alpha_1 \approx 0.6$ is to balance constraints such as interferences from the secondary network to the primary network, locations of the secondary relays, and perfect/imperfect SIC operations.

Figure 5 shows the throughputs of the protocols UTW-2TS-DNC and UTW-2TS-SC versus β_1 when $Q = 10$ (dB), $\alpha_1 = 0.6$, $\alpha_2 = 1 - \alpha_1 = 0.4$, $\Psi = -5$ (dB), $x_R = 0.3$, $y_R = 0$, $x_{PR} = y_{PR} = 0.5$, $M = 3$, and β_2 is changed as $\beta_2 = 1 - \beta_1$. As observed from Figure 5, the UTW-2TS-DNC protocol is not affected by the power allocation coefficients β_1 and β_2, and the UTW-2TS-SC protocol reaches the largest throughputs at approximate values $\beta_1 = 0.7$ and $\beta_1 = 0.8$ corresponding to perfect SICs and imperfect SICs, respectively. These values $\beta_1 = 0.7$ and $\beta_1 = 0.8$ are to equalize the SINR qualities between two hops from the selected secondary relay to the secondary sources.

Figure 6 shows the throughputs of the protocols UTW-2TS-DNC and UTW-2TS-SC versus α_1 and β_1 in the three-
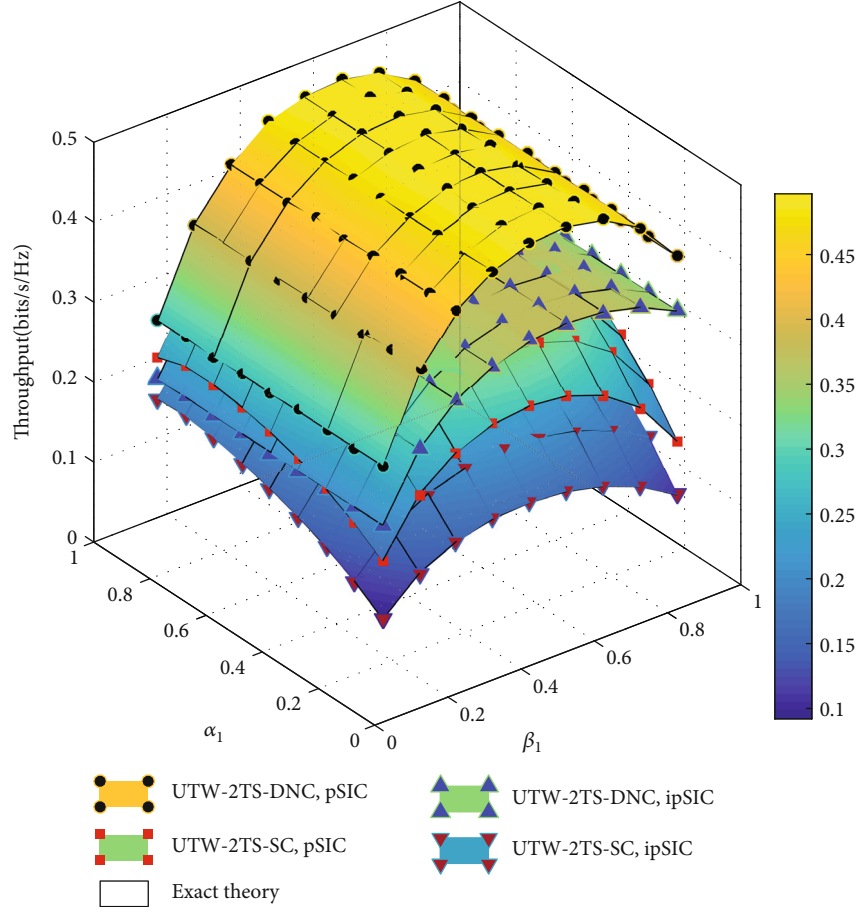
FIGURE 6: Throughputs of the protocols UTW-2TS-DNC and UTW-2TS-SC versus α_1 and β_1 when $Q = 10$ (dB), $\Psi = -5$ (dB), $x_R = 0.3$, $y_R = 0$, $x_{PR} = y_{PR} = 0.5$, $M = 3$, $\alpha_2 = 1 - \alpha_1$, and $\beta_2 = 1 - \beta_1$.
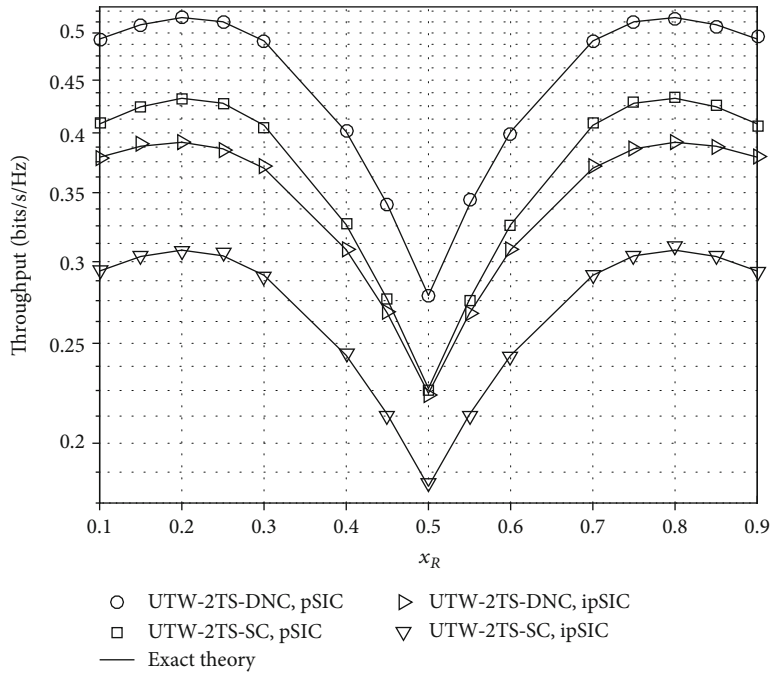
FIGURE 7: Throughputs of the protocols UTW-2TS-DNC and UTW-2TS-SC versus x_R when $Q = 10$ (dB), $\alpha_1 = \alpha_2 = 0.5$, $\beta_1 = \beta_2 = 0.5$, $\Psi = -5$ (dB), $x_{PR} = y_{PR} = 0.5$, $M = 3$, and $y_R = 0$.
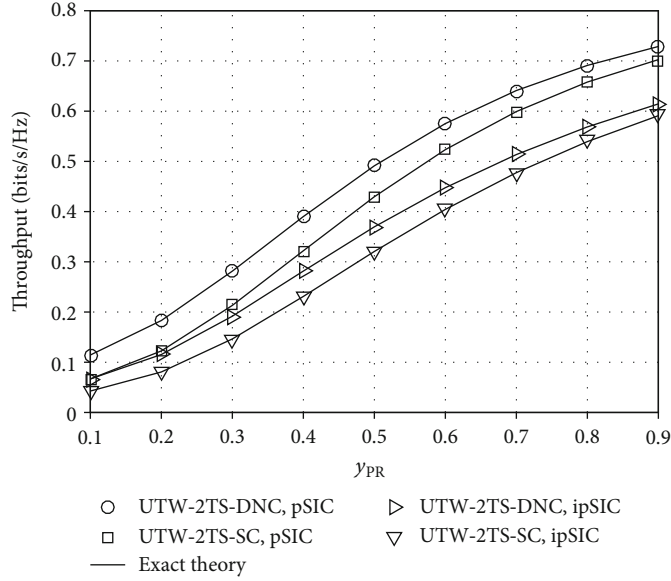
Figure 8: Throughputs of the protocols UTW-2TS-DNC and UTW-2TS-SC versus y_{PR} when $Q = 10$ (dB), $\alpha_1 = \alpha_2 = 0.5$, $\beta_1 = 0.7$, $\beta_2 = 1 - \beta_1 = 0.3$, $\Psi = -5$ (dB), $x_R = 0.3$, $y_R = 0$, $M = 3$, and $x_{PR} = 0.5$.

dimensional plane when $Q = 10$ (dB), $\Psi = -5$ (dB), $x_R = 0.3$, $y_R = 0$, $x_{PR} = y_{PR} = 0.5$, $M = 3$, and α_2 and β_2 are set as $\alpha_2 = 1 - \alpha_1$ and $\beta_2 = 1 - \beta_1$. The value ranges of α_1 and β_1 are established between 0.1 and 0.9. The results from Figure 6 confirm the contributions from Figures 4 and 5.

Figure 7 presents the throughputs of the protocols UTW-2TS-DNC and UTW-2TS-SC versus x_R when $Q = 10$ (dB), $\alpha_1 = \alpha_2 = 0.5$, $\beta_1 = \beta_2 = 0.5$, $\Psi = -5$ (dB), $x_{PR} = y_{PR} = 0.5$, $M = 3$, and y_R is fixed as $y_R = 0$. In this simulation, the normalized distances d_4 and d_5 are fixed at the same value 0.7 and the remaining normalized distances d_1, d_2, and d_3 are changed from 0.1 to 0.9 for d_1, 0.9 to 0.1 for d_2 (the distance d_2 has a reverse change versus the distance d_1), and 0.64 to 0.5 and back to 0.64 for d_3. From Figure 7, these proposed protocols UTW-2TS-DNC and UTW-2TS-SC achieve the largest throughputs at asymmetric locations of the selected secondary relay as $x_R \approx 0.2$ ($d_1 = 0.2, d_2 = 0.8$) and $x_R \approx 0.8$ ($d_1 = 0.8, d_2 = 0.2$) because of decoding the received data sequentially (SIC operations). In addition, at the symmetric location $x_R = 0.5$ ($d_1 = d_2 = 0.5$), the throughputs of both protocols again have the lowest values.

Figure 8 presents the throughputs of the protocols UTW-2TS-DNC and UTW-2TS-SC versus y_{PR} when $Q = 10$ (dB), $\alpha_1 = \alpha_2 = 0.5$, $\beta_1 = 0.7$, $\beta_2 = 1 - \beta_1 = 0.3$, $\Psi = -5$ (dB), $x_R = 0.3$, $y_R = 0$, $M = 3$, and x_{PR} is fixed at $x_{PR} = 0.5$. In this case, the normalized distances d_1 and d_2 are fixed to 0.3 and 0.7, respectively, and the primary receiver (PR) is moving farther the secondary network characterized by changing the normalized distances d_3, d_4, and d_5 from 0.22 to 0.92 for d_3 and from 0.51 to 1.03 for d_4 and d_5. As shown in Figure 8, the throughputs of the protocols UTW-2TS-DNC and UTW-2TS-SC are enhanced when the value of y_{PR} increases because of low influence of the interference constraint to the sources and relays in the secondary network. Therefore, the secondary sources and relays can transmit with the maxi-
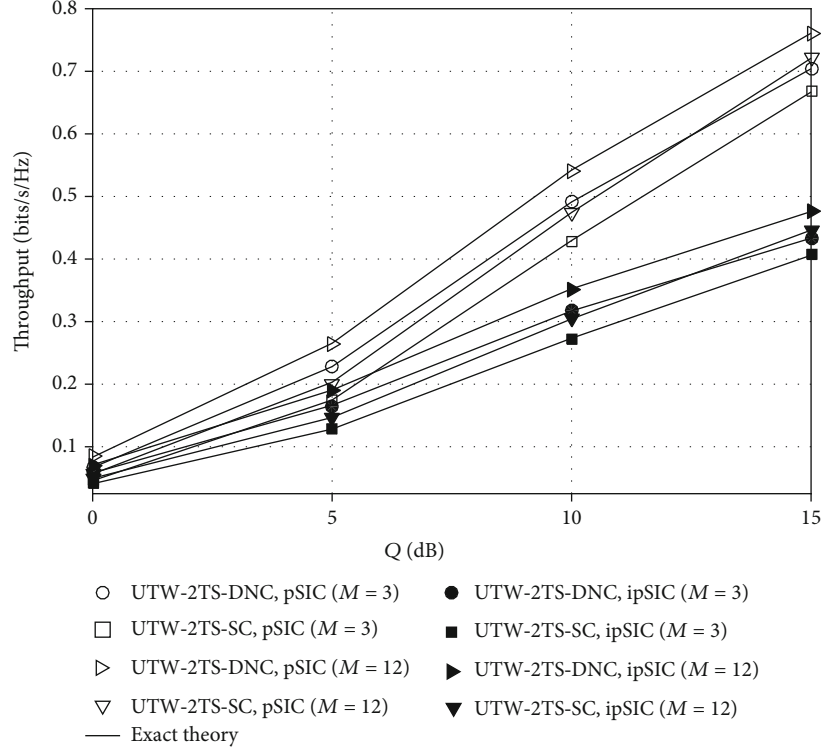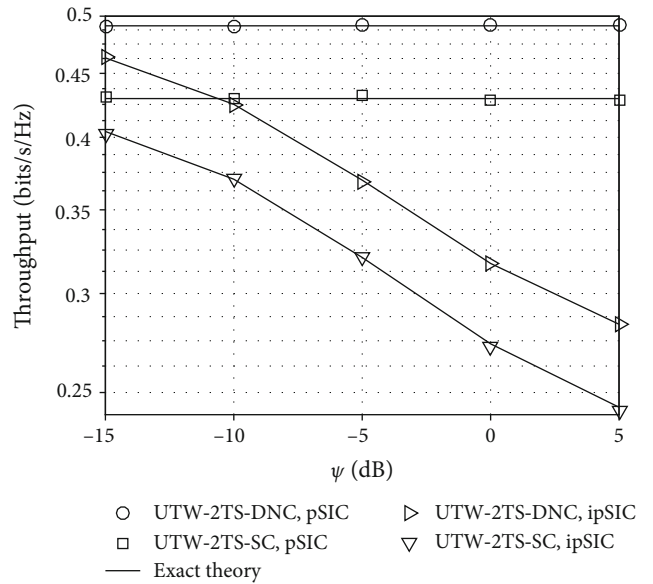

Figure 9: Throughputs of the protocols UTW-2TS-DNC and UTW-2TS-SC versus Ψ when $Q = 10$ (dB), $\alpha_1 = \alpha_2 = 0.5$, $\beta_1 = 0.7$, $\beta_2 = 1 - \beta_1 = 0.3$, $x_R = 0.3$, $y_R = 0$, $x_{PR} = y_{PR} = 0.5$, and $M = 3$.

mum power, and interference cancelling and decoding capacity at the secondary relays and the secondary sources increase.

Figure 9 presents the throughputs of the protocols UTW-2TS-DNC and UTW-2TS-SC versus the residual interference powers Ψ when $Q = 10$ (dB), $\alpha_1 = \alpha_2 = 0.5$, $\beta_1 = 0.7$, $\beta_2 = 1 - \beta_1 = 0.3$, $x_R = 0.3$, $y_R = 0$, $x_{PR} = y_{PR} = 0.5$, and $M = 3$. Considering the case of the imperfect SICs for both protocols, the throughput performances decrease when the residual interference powers increase. Furthermore, the throughputs of the protocols UTW-2TS-DNC and UTW-2TS-SC in the

perfect SICs are upper limitations (expectations) of the ones in the imperfect SICs when $\Psi \to -\infty$ (dB).

5. Conclusions

In this paper, we proposed and analyzed the underlay two-way relaying scheme with two secondary sources and multiple secondary relays, known as the UTW-2TS scheme. The UTW-2TS scheme with the SIC solution operated in only two time slots and under an interference constraint of the primary receiver. The secondary relays decode successively the data transmitted by two secondary sources and then encode these data by two techniques: the DNC enforced by XOR operations (known as the UTW-2TS-DNC protocol) and the SC enforced by power domain additions (known as the UTW-2TS-SC protocol). A selected secondary relay which subjects to maximize the decoding capacities and to minimize the collection time of CSI in the proposed protocols UTW-2TS-DNC and UTW-2TS-SC suffered the residual interferences from the imperfect SIC operations. Exact outage probabilities and throughputs were derived to evaluate the system performance of the proposed UTW-2TS-DNC and UTW-2TS-SC protocols. Simulation and analysis results provided discoveries of the performance improvements by increasing of the number of the cooperative secondary relays, the interference constraints, and the distances from the secondary network to the primary receiver. In addition, the proposed UTW-2TS-DNC and UTW-2TS-SC protocols achieved the best throughputs at optimal interference power allocation coefficients and optimal locations of the selected secondary relay. Considering the same power consumption, the UTW-2TS-DNC protocol performed better than the UTW-2TS-SC protocol. Finally, the analysis results of the outage probabilities and throughputs were validated by the Monte Carlo simulations.

Appendix

A. Proof of Lemma 1

Substituting (3) into the formula of Φ_1 as in (18), we have the expression

$$
\begin{aligned}
\Phi_1 &= \Pr\left\{ \frac{\alpha_1 Q g_{S_1 R_m} g_{S_2 \mathrm{PR}}}{\alpha_2 Q g_{S_2 R_m} g_{S_1 \mathrm{PR}} + g_{S_1 \mathrm{PR}} g_{S_2 \mathrm{PR}}} < \gamma_{\mathrm{th}} \right\} \\
&= \Pr\left\{ \frac{g_{S_1 R_m}}{g_{S_1 \mathrm{PR}}} < \frac{\gamma_{\mathrm{th}} \left(\alpha_2 Q g_{S_2 R_m} + g_{S_2 \mathrm{PR}} \right)}{\alpha_1 Q g_{S_2 \mathrm{PR}}} \right\} \\
&= \Pr\left\{ G_{S_1 R_m/S_1 \mathrm{PR}} < \underbrace{\frac{\gamma_{\mathrm{th}} \alpha_2}{\alpha_1}}_{v_1} G_{S_2 R_m/S_2 \mathrm{PR}} + \underbrace{\frac{\gamma_{\mathrm{th}}}{\alpha_1 Q}}_{v_2} \right\} \\
&= \int_0^\infty f_{G_{S_2 R_m/S_2 \mathrm{PR}}}(y) \times F_{G_{S_1 R_m/S_1 \mathrm{PR}}}(v_1 y + v_2) dy.
\end{aligned}
$$

(A.1)

From (23), we infer the CDF and the corresponding PDF of the RV $G_{S_2 R_m/S_2 \mathrm{PR}}$ as

$$
\begin{aligned}
F_{G_{S_2 R_m/S_2 \mathrm{PR}}}(z) &= \lambda_5 \sum_{p=0}^{1} \binom{0}{1} \frac{(-1)^p}{\lambda_5 + p \lambda_2 z} = \lambda_5 - \frac{1}{\lambda_5 + \lambda_2 z} \\
&= \frac{\lambda_2 z}{\lambda_5 + \lambda_2 z},
\end{aligned}
$$

(A.2)

$$
f_{G_{S_2 R_m/S_2 \mathrm{PR}}}(z) = \frac{\partial F_{G_{S_2 R_m/S_2 \mathrm{PR}}}(z)}{\partial z} = \frac{\lambda_2 \lambda_5}{(\lambda_5 + \lambda_2 z)^2}.
$$

(A.3)

Substituting (23) and (A.3) into (A.1), we have the equivalent formula:

$$
\begin{aligned}
\Phi_1 &= \int_0^\infty \frac{\lambda_2 \lambda_5}{(\lambda_5 + \lambda_2 y)^2} \lambda_4 \sum_{p=0}^{M} \binom{p}{M} \frac{(-1)^p}{\lambda_4 + p \lambda_1 (v_1 y + v_2)} dy \\
&= \lambda_2 \lambda_4 \lambda_5 \sum_{p=0}^{M} \binom{p}{M} (-1)^p \int_0^\infty \frac{dy}{(\lambda_4 + p \lambda_1 v_2 + p \lambda_1 v_1 y)(\lambda_5 + \lambda_2 y)^2}.
\end{aligned}
$$

(A.4)

By performing variable transformations for the integral in (A.4) as $t = 1/(\lambda_5 + \lambda_2 y)$ and $y = v_4(p) + (\lambda_2 v_3(p) - \lambda_5 v_4(p))t$, where $v_3(p) = \lambda_4 + p \lambda_1 v_2$ and $v_4(p) = p \lambda_1 v_1$, Lemma 1 is proven completely.

B. Proof of Lemma 2

Substituting (3) and (6) into the formula of Φ_2 as in (18), the probability Φ_2 is expressed as

$$
\begin{aligned}
\Phi_2 &= \Pr\left\{ \left(\frac{\alpha_1 Q g_{S_1 R_m} g_{S_2 \mathrm{PR}}}{\alpha_2 Q g_{S_2 R_m} g_{S_1 \mathrm{PR}} + g_{S_1 \mathrm{PR}} g_{S_2 \mathrm{PR}}} \geq \gamma_{\mathrm{th}} \right) \cap \left(\frac{P_{S_2} g_{S_2 R_m}}{\varepsilon I |r_m|^2 + \sigma^2} < \gamma_{\mathrm{th}} \right) \right\} \\
&= \Pr\left\{ \left(G_{S_1 R_m/S_1 \mathrm{PR}} \geq v_1 G_{S_2 R_m/S_2 \mathrm{PR}} + v_2 \right) \cap \left(G_{S_2 R_m/S_2 \mathrm{PR}} < \underbrace{\frac{\gamma_{\mathrm{th}}}{\alpha_2 Q}}_{v_5} + \varepsilon \underbrace{\frac{\gamma_{\mathrm{th}}}{\alpha_2}}_{v_6} g_m \right) \right\}.
\end{aligned}
$$

(B.1)

In (B.1), we consider two cases of perfect SICs ($\varepsilon = 0$) and imperfect SICs ($\varepsilon = 1$) to solve the following:

Case $\varepsilon = 0$: formula (B.1) is expressed and manipulated as

$$
\begin{aligned}
\Phi_2 &= \Pr\left\{ \left(G_{S_1 R_m/S_1 \mathrm{PR}} \geq v_1 G_{S_2 R_m/S_2 \mathrm{PR}} + v_2 \right) \cap \left(G_{S_2 R_m/S_2 \mathrm{PR}} < v_5 \right) \right\} \\
&= \int_0^{v_5} f_{G_{S_2 R_m/S_2 \mathrm{PR}}}(y) \times \left(1 - F_{G_{S_1 R_m/S_1 \mathrm{PR}}}(v_1 y + v_2) \right) dy \\
&= F_{G_{S_2 R_m/S_2 \mathrm{PR}}}(v_5) - \int_0^{v_5} f_{G_{S_2 R_m/S_2 \mathrm{PR}}}(y) \times F_{G_{S_1 R_m/S_1 \mathrm{PR}}}(v_1 y + v_2) dy,
\end{aligned}
$$

(B.2)

where $F_{G_{S_2 R_m/S_2 \mathrm{PR}}}(v_5)$ is the CDF of the RV $G_{S_2 R_m/S_2 \mathrm{PR}}$ at a value $v_5 = \gamma_{\mathrm{th}}/(\alpha_2 Q)$ (see (A.2)).

By using the PDF of the RV $G_{S_2R_m/S_2\text{PR}}$ as in (A.3) and the CDF of the RV $G_{S_1R_m/S_1\text{PR}}$ as in (23), formula (B.2) is rewritten as

$$\Phi_2 = F_{G_{S_2R_m/S_2\text{PR}}}(v_5) - \lambda_2\lambda_4\lambda_5 \sum_{p=0}^{M} \binom{p}{M}(-1)^p \int_0^{v_5}$$
$$\cdot \frac{dy}{(\lambda_4 + p\lambda_1 v_2 + p\lambda_1 v_1 y)(\lambda_5 + \lambda_2 y)^2}. \quad \text{(B.3)}$$

Solving (B.3) also by variable transformations as in (A.4), Φ_2 is presented as (25) in Lemma 2.

Case $\varepsilon = 1$: formula (B.1) is performed as

$$\Phi_2 = \Pr\left\{\left(G_{S_1R_m/S_1\text{PR}} \geq v_1 G_{S_2R_m/S_2\text{PR}} + v_2\right) \cap \left(G_{S_2R_m/S_2\text{PR}} < v_5 + v_6 g_m\right)\right\}$$
$$= \int_0^{\infty} f_{g_m}(t) \int_0^{v_5 + v_6 t} \left(1 - F_{G_{S_1R_m/S_1\text{PR}}}(v_1 y + v_2)\right) \times f_{G_{S_2R_m/S_2\text{PR}}}(y) dy dt. \quad \text{(B.4)}$$

Using the result of (B.2) for the inner integral of (B.4) and the PDF of RV g_m, we have the next result:

$$\Phi_2 = \int_0^{\infty} \Omega e^{-\Omega t}\left\{\frac{\lambda_2(v_5 + v_6 t)}{\lambda_5 + \lambda_2(v_5 + v_6 t)} - \lambda_2\lambda_4\lambda_5 \sum_{p=0}^{M}\binom{p}{M}\frac{(-1)^p}{\lambda_2 v_3(p) - \lambda_5 v_4(p)}\right.$$
$$\times \left.\left(\frac{\lambda_2(v_5 + v_6 t)}{\lambda_5(\lambda_5 + \lambda_2(v_5 + v_6 t))} - \frac{v_4(p)}{\lambda_2 v_3(p) - \lambda_5 v_4(p)}\ln\left(\frac{(\lambda_5 + \lambda_2(v_5 + v_6 t))v_3(p)}{\lambda_5(v_3(p) + (v_5 + v_6 t)v_4(p))}\right)\right)\right\}dt$$
$$= \underbrace{\Omega\lambda_2 \int_0^{\infty} \frac{(v_5 + v_6 t)e^{-\Omega t}}{\lambda_5 + \lambda_2(v_5 + v_6 t)}dt}_{I_1} - \underbrace{\Omega\lambda_2^2\lambda_4 \sum_{p=0}^{M}\binom{p}{M}\frac{(-1)^p}{\lambda_2 v_3(p) - \lambda_5 v_4(p)} \int_0^{\infty} \frac{(v_5 + v_6 t)e^{-\Omega t}}{\lambda_5 + \lambda_2(v_5 + v_6 t)}dt}_{I_2}$$
$$+ \underbrace{\Omega\lambda_2\lambda_4\lambda_5 \sum_{p=0}^{M}\binom{p}{M}\frac{(-1)^p v_4(p)}{(\lambda_2 v_3(p) - \lambda_5 v_4(p))^2} \int_0^{\infty} e^{-\Omega t}\ln\left(\frac{(\lambda_5 + \lambda_2(v_5 + v_6 t))v_3(p)}{\lambda_5 \times (v_3(p) + (v_5 + v_6 t)v_4(p))}\right)dt}_{I_3}. \quad \text{(B.5)}$$

We solve sequentially the integrals I_1, I_2, and I_3 in (B.5) as

$$I_1 = 1 - \frac{\Omega\lambda_5}{\lambda_2 v_6}e^{(\lambda_5 + \lambda_2 v_5)\Omega/(\lambda_2 v_6)}\Gamma\left(0, \frac{(\lambda_5 + \lambda_2 v_5)\Omega}{\lambda_2 v_6}\right), \quad \text{(B.6)}$$

$$I_2 = \lambda_2\lambda_4 \sum_{p=0}^{M}\binom{p}{M}\frac{(-1)^p}{\lambda_2 v_3(p) - \lambda_5 v_4(p)} - \Omega\lambda_2\lambda_4\lambda_5 \sum_{p=0}^{M}\binom{p}{M}$$
$$\cdot \frac{(-1)^p}{\lambda_2 v_3(p) - \lambda_5 v_4(p)} \int_0^{\infty} \frac{e^{-\Omega t}}{\lambda_5 + \lambda_2 v_5 + \lambda_2 v_6 t}dt$$
$$= \lambda_2\lambda_4 \sum_{p=0}^{M}\binom{p}{M}\frac{(-1)^p}{\lambda_2 v_3(p) - \lambda_5 v_4(p)} - \frac{\Omega\lambda_4\lambda_5}{v_6}\sum_{p=0}^{M}\binom{p}{M}$$
$$\cdot \frac{(-1)^p e^{(\lambda_5 + \lambda_2 v_5)\Omega/(\lambda_2 v_6)}}{\lambda_2 v_3(p) - \lambda_5 v_4(p)}\Gamma\left(0, \frac{(\lambda_5 + \lambda_2 v_5)\Omega}{\lambda_2 v_6}\right), \quad \text{(B.7)}$$

$$I_3 = \lambda_2\lambda_4\lambda_5 \sum_{p=0}^{M}\binom{p}{M}\frac{(-1)^p v_4(p)}{(\lambda_2 v_3(p) - \lambda_5 v_4(p))^2}$$
$$\cdot \left\{\ln\left(\frac{v_3(p)}{\lambda_5}\right) + \Omega\int_0^{\infty} e^{-\Omega t}\ln\left(\frac{\lambda_5 + \lambda_2(v_5 + v_6 t)}{v_3(p) + (v_5 + v_6 t)v_4(p)}\right)dt\right\}$$
$$= \lambda_2\lambda_4\lambda_5 \sum_{p=0}^{M}\binom{p}{M}\frac{(-1)^p v_4(p)}{(\lambda_2 v_3(p) - \lambda_5 v_4(p))^2}$$
$$\cdot \left\{\ln\left(\frac{v_3(p)}{\lambda_5}\right) + \Omega\int_0^{\infty} e^{-\Omega t}\ln\left(\lambda_5 + \lambda_2 v_5 + \lambda_2 v_6 t\right)dt\right.$$
$$\left. - \Omega\int_0^{\infty} e^{-\Omega t}\ln\left(v_3(p) + v_5 v_4(p) + v_6 v_4(p)t\right)dt\right\}$$
$$= \lambda_2\lambda_4\lambda_5 \sum_{p=0}^{M}\binom{p}{M}\frac{(-1)^p v_4(p)}{(\lambda_2 v_3(p) - \lambda_5 v_4(p))^2}$$
$$\cdot \left\{\ln\left(\frac{(\lambda_5 + \lambda_2 v_5)v_3(p)}{\lambda_5(v_3(p) + v_5 v_4(p))}\right) + e^{(\lambda_5 + \lambda_2 v_5)\Omega/\lambda_2 v_6}\Gamma\right.$$
$$\cdot \left(0, \frac{(\lambda_5 + \lambda_2 v_5)\Omega}{\lambda_2 v_6}\right) - e^{(v_3(p) + v_5 v_4(p))\Omega/v_6 v_4(p)}\Gamma$$
$$\left.\cdot \left(0, \frac{(v_3(p) + v_5 v_4(p))\Omega}{v_6 v_4(p)}\right)\right\}, \quad \text{(B.8)}$$

where $\Gamma(u, v)$ is the upper incomplete Gamma function ([42], eq. 8.350.2).

Substituting (B.6), (B.7), and (B.8) into (B.5), the probability Φ_2 is analyzed for the case $\varepsilon = 1$ as (26) in Lemma 2. Hence, the lemma is proven completely.

Data Availability

The data used to support the findings of this study are included within the article.

Conflicts of Interest

The authors declare that there is no conflict of interest regarding the publication of this paper.

Acknowledgments

References

[1] I. F. Akyildiz, W.-Y. Lee, M. C. Vuran, and S. Mohanty, "NeXt generation/dynamic spectrum access/cognitive radio wireless networks: a survey," *Computer Networks*, vol. 50, no. 13, pp. 2127–2159, 2006.

[2] J. Mitola and G. Q. Maguire, "Cognitive radio: making software radios more personal," *IEEE Personal Communications*, vol. 6, no. 4, pp. 13–18, 1999.

[3] A. Goldsmith, S. A. Jafar, I. Maric, and S. Srinivasa, "Breaking spectrum gridlock with cognitive radios: an information theoretic perspective," *Proceedings of the IEEE*, vol. 97, no. 5, pp. 894–914, 2009.

[4] H. B. Ahmad, "Ensemble classifier based spectrum sensing in cognitive radio networks," *Wireless Communications and Mobile Computing*, vol. 2019, Article ID 9250562, 16 pages, 2019.

[5] Y. J. Chun, M. O. Hasna, and A. Ghrayeb, "Adaptive network coding for spectrum sharing systems," *IEEE Transactions on Wireless Communications*, vol. 14, no. 2, pp. 639–654, 2014.

[6] Y. He, J. Evans, and S. Dey, "Secrecy rate maximization for cooperative overlay cognitive radio networks with artificial noise," in *2014 IEEE International Conference on Communications (ICC)*, pp. 1663–1668, Sydney, NSW, Australia, June 2014.

[7] P. N. Son, "Joint impacts of hardware impairments, imperfect CSIs, and interference constraints on underlay cooperative cognitive networks with reactive relay selection," *Telecommunication Systems*, vol. 71, no. 1, pp. 65–76, 2019.

[8] T. M. C. Chu and H. J. Zepernick, "Performance optimization for hybrid two-way cognitive cooperative radio networks with imperfect spectrum sensing," *IEEE Access*, vol. 6, pp. 70582–70596, 2018.

[9] K. Ho-Van and T. Do-Dac, "Security analysis for underlay cognitive network with energy-scavenging capable relay over Nakagami-*M* fading channels," *Wireless Communications and Mobile Computing*, vol. 2019, Article ID 5080952, 16 pages, 2019.

[10] P. Popovski and H. Yomo, "Physical network coding in two-way wireless relay channels," in *2007 IEEE International Conference on Communications*, Glasgow, UK, June 2007.

[11] Y. Li, R. H. Y. Louie, and B. Vucetic, "Relay selection with network coding in two-way relay channels," *IEEE Transactions on Vehicular Technology*, vol. 59, no. 9, pp. 4489–4499, 2010.

[12] T. T. Duy and H. Y. Kong, "Exact outage probability of cognitive two-way relaying scheme with opportunistic relay selection under interference constraint," *IET Communications*, vol. 6, no. 16, pp. 2750–2759, 2012.

[13] H. V. Toan and V. N. Q. Bao, "Opportunistic relaying for cognitive two-way network with multiple primary receivers over Nakagami-m fading," in *2016 International Conference on Advanced Technologies for Communications (ATC)*, Hanoi, Vietnam, October 2016.

[14] H. V. Toan, V. N. Quoc Bao, and H. Nguyen-le, "Cognitive two-way relay systems with multiple primary receivers: exact and asymptotic outage formulation," *IET Communications*, vol. 11, no. 16, pp. 2490–2497, 2017.

[15] S. Hatamnia, S. Vahidian, S. Aïssa, B. Champagne, and M. Ahmadian-Attari, "Network-coded two-way relaying in spectrum-sharing systems with quality-of-service requirements," *IEEE Transactions on Vehicular Technology*, vol. 66, no. 2, pp. 1299–1312, 2017.

[16] H. V. Toan, V. N. Q. Bao, and K. N. Le, "Performance analysis of cognitive underlay two-way relay networks with interference and imperfect channel state information," *EURASIP Journal on Wireless Communications and Networking*, vol. 2018, no. 1, 2018.

[17] S. Solanki, P. K. Sharma, and P. K. Upadhyay, "Adaptive link utilization in two-way spectrum sharing relay systems under average interference-constraints," *IEEE Systems Journal*, vol. 12, no. 4, pp. 3461–3472, 2018.

[18] Z. Cao, X. Ji, J. Wang, S. Zhang, Y. Ji, and J. Wang, "Security-reliability tradeoff analysis for underlay cognitive two-way relay networks," *IEEE Transactions on Wireless Communications*, vol. 18, no. 12, pp. 6030–6042, 2019.

[19] X. Yue, Y. Liu, S. Kang, A. Nallanathan, and Y. Chen, "Modeling and analysis of two-way relay non-orthogonal multiple access systems," *IEEE Transactions on Communications*, vol. 66, no. 9, pp. 3784–3796, 2018.

[20] X. Zou, B. He, and H. Jafarkhani, "An analysis of two-user uplink asynchronous non-orthogonal multiple access systems," *IEEE Transactions on Wireless Communications*, vol. 18, no. 2, pp. 1404–1418, 2019.

[21] Z. Yang, Z. Ding, P. Fan, and N. Al-Dhahir, "The impact of power allocation on cooperative non-orthogonal multiple access networks with SWIPT," *IEEE Transactions on Wireless Communications*, vol. 16, no. 7, pp. 4332–4343, 2017.

[22] A. Agarwal and A. K. Jagannatham, "Performance analysis for non-orthogonal multiple access (NOMA)-based two-way relay communication," *IET Communications*, vol. 13, no. 4, pp. 363–370, 2019.

[23] P. N. Son and T. T. Duy, "A new approach for two-way relaying networks: improving performance by successive interference cancellation, digital network coding and opportunistic relay selection," *Wireless Networks*, vol. 26, no. 2, pp. 1315–1329, 2020.

[24] X. Ding, T. Song, Y. Zou, X. Chen, and L. Hanzo, "Security-reliability tradeoff analysis of artificial noise aided two-way opportunistic relay selection," *IEEE Transactions on Vehicular Technology*, vol. 66, no. 5, pp. 3930–3941, 2017.

[25] P. N. Son and H. Y. Kong, "Exact outage analysis of energy harvesting underlay cooperative cognitive networks," *IEICE Transactions on Communications*, vol. E98.B, no. 4, pp. 661–672, 2015.

[26] K. Tourki, K. A. Qaraqe, and M. S. Alouini, "Outage analysis for underlay cognitive networks using incremental regenerative relaying," *IEEE Transactions on Vehicular Technology*, vol. 62, no. 2, pp. 721–734, 2013.

[27] J. N. Laneman, D. N. C. Tse, and G. W. Wornell, "Cooperative diversity in wireless networks: efficient protocols and outage behavior," *IEEE Transactions on Information Theory*, vol. 50, no. 12, pp. 3062–3080, 2004.

[28] A. Papoulis and S. U. Pillai, *Probability, Random Variables and Stochastic Processes*, McGraw-Hill, New York, NY, USA, 4th edition, 2002.

[29] H. Kim, S. Lim, H. Wang, and D. Hong, "Optimal power allocation and outage analysis for cognitive full duplex relay systems," *IEEE Transactions on Wireless Communications*, vol. 11, no. 10, pp. 3754–3765, 2012.

[30] P. N. Son and T. T. Duy, "Performance analysis of underlay cooperative cognitive full-duplex networks with energy-harvesting relay," *Computer Communications*, vol. 122, pp. 9–19, 2018.

[31] T. V. Nguyen, T. N. Do, V. N. Q. Bao, D. B. . Costa, and B. An, "On the performance of multihop cognitive wireless powered D2D communications in WSNs," *IEEE Transactions on Vehicular Technology*, vol. 69, no. 3, pp. 2684–2699, 2020.

[32] Y. Ruan, Y. Li, C. X. Wang, R. Zhang, and H. Zhang, "Energy efficient power allocation for delay constrained cognitive satellite terrestrial networks under interference constraints," *IEEE Transactions on Wireless Communications*, vol. 18, no. 10, pp. 4957–4969, 2019.

[33] T. V. Nguyen and B. An, "Cognitive multihop wireless powered relaying networks over Nakagami-m fading channels," *IEEE Access*, vol. 7, pp. 154600–154616, 2019.

[34] P. Chakraborty and S. Prakriya, "Securing primary downlink transmissions from untrusted receivers of co-existing underlay cognitive networks," *IEEE Transactions on Cognitive Communications and Networking*, vol. 5, no. 3, pp. 491–503, 2019.

[35] H. Arezumand, H. Zamiri-Jafarian, and E. Soleimani-Nasab, "Exact and asymptotic analysis of partial relay selection for cognitive RF-FSO systems with non-zero boresight pointing errors," *IEEE Access*, vol. 7, pp. 58611–58625, 2019.

[36] H. Gao, S. Zhang, Y. Su, M. Diao, and M. Jo, "Joint multiple relay selection and time slot allocation algorithm for the EH-abled cognitive multi-user relay networks," *IEEE Access*, vol. 7, pp. 111993–112007, 2019.

[37] L. Pei, T. Zhifeng, L. Zinan, E. Erkip, and S. Panwar, "Cooperative wireless communications: a cross-layer approach," *IEEE Wireless Communications*, vol. 13, no. 4, pp. 84–92, 2006.

[38] M. Matthaiou, A. Papadogiannis, E. Bjornson, and M. Debbah, "Two-way relaying under the presence of relay transceiver hardware impairments," *IEEE Communications Letters*, vol. 17, no. 6, pp. 1136–1139, 2013.

[39] P. N. Son, D. Har, and H. Y. Kong, "Smart power allocation for secrecy transmission in reciprocally cooperative spectrum sharing," *IEEE Transactions on Vehicular Technology*, vol. 64, no. 11, pp. 5395–5400, 2015.

[40] A. A. Nasir, X. Zhou, S. Durrani, and R. A. Kennedy, "Relaying protocols for wireless energy harvesting and information processing," *IEEE Transactions on Wireless Communications*, vol. 12, no. 7, pp. 3622–3636, 2013.

[41] P. K. Sharma and P. K. Upadhyay, "Performance analysis of cooperative spectrum sharing with multiuser two-way relaying over fading channels," *IEEE Transactions on Vehicular Technology*, vol. 66, no. 2, pp. 1324–1333, 2017.

[42] R. I. Gradshteyn, I. S. Jeffrey, and A. D. Zwillinger, *Table of Integral, Series and Products*, Elsevier, Amsterdam, 7th edition, 2007.

WILEY | Hindawi

Research Article

Performance Analysis of IQI Impaired Cooperative NOMA for 5G-Enabled Internet of Things

Hui Guo,[1] Xuejiao Guo,[1] Chao Deng [1], and Shangqing Zhao[2]

[1]*School of Physics and Electronic Information Engineering, Henan Polytechnic University, Jiaozuo 454000, China*
[2]*Department of Electrical Engineering, University of South Florida, Tampa, FL 33620, USA*

Correspondence should be addressed to Chao Deng; super@hpu.edu.cn

This paper investigates the joint effects of in-phase and quadrature-phase imbalance (IQI) and imperfect successive interference cancellation (ipSIC) on the cooperative Internet of Things (IoT) nonorthogonal multiple access (NOMA) networks where the Nakagami-m fading channel is taken into account. The closed-form expressions of outage probability for the far and near IoT devices are derived to evaluate the outage behaviors. For deeper insights of the performance of the considered system, the approximate outage probability and diversity order in high signal-to-noise ratio (SNR) regime are obtained. In addition, we also analyze the throughput and energy efficiency to characterize the performance of the considered system. The simulation results demonstrate that, compared with IQI, ipSIC has a greater impact on the outage performance for the near-IoT-device of the considered system. Furthermore, we also find that the outage probabilities of IoT devices can be minimized by selecting a specific power allocation scheme.

1. Introduction

With the development of Internet of Things (IoT), traditional orthogonal multiple access (OMA) can no longer afford massive connections due to its low spectrum utilization [1]. The proposals of massive multiple-input multiple-output (MIMO) [2], small cell networks (SCNs) [3], millimeter wave (mmWave) [4], nonorthogonal multiple access (NOMA) [5], and some other 5G-related technologies have made it possible to implement the IoT [6]. Among these technologies, NOMA has been accepted by the Third Generation Partnership Project (3GPP) due to the fact that it can serve multiple devices simultaneously without neglecting fairness [7]. Traditional OMA is required to use orthogonal resources to support multiple devices, while relying on the power multiplexing of NOMA IoT can serve a large number of various devices in the same time/frequency domain [8, 9]. Furthermore, the physical layer security performance of NOMA systems outperforms the OMA system and improves the security rate of the system greatly [10]. In addition, to ensure the fairness among devices, different power signals

are transmitted according to the channel state information (CSI) between the transmitter (TX) and receiver (RX), and the successive interference cancellation (SIC) is adopted at the RX to eliminate interdevice interference [11, 12].

To further enhance the robustness and expand coverage, cooperative relay communication has been introduced into NOMA systems [13–17]. In [13], cooperative relay was taken into account in the NOMA systems, and it has been proved that the proposed scheme can reduce the outage probability and increase the diversity gain of the systems. In order to improve the spectral efficiency, the authors of [14] proposed a new cooperative NOMA transmission scheme in the cognitive radio systems and derived the exact closed-form expressions for outage probability. The outage performance of cooperative NOMA amplify-and-forward (AF) and decode-and-forward (DF) system with a single user was studied in [15], and the results showed that the relay in AF protocol outperforms the relay in DF protocol. In [16], the outage probability of cooperative NOMA system over Rayleigh channels was analyzed where the near user acted as a DF relay. Particularly, the cooperative NOMA network in the

IoT was proposed in [17]; the average throughput and the diversity order were analyzed to characterize the system. In [18], the authors proposed a cooperative NOMA scheme in which the near user acts as a DF relay and the analytical expression of intercept probability was derived to evaluate the system. All of the above studies showed that the cooperative NOMA can improve the system performance. As the core technology of NOMA, SIC has well performance on signal detection, while at the expense of the complexity of RX [19]. To this end, a host of works has drawn attention to imperfect SIC (ipSIC) ([20–23] and references therein). Authors in [20] proposed a more practical network in which ipSIC was considered in the cooperative NOMA system, and the closed-form expressions of the outage probability were derived. In [21], the authors presented the closed-form expressions of outage probability and ergodic sum rate of the cooperative AF NOMA over Nakagami-m channels by considering ipSIC in the network. In addition, the effects of ipSIC on the two-way and cognitive radio NOMA system were studied in [22, 23], respectively. All of these articles are instructive for the practical NOMA systems.

The aforementioned works mainly focused on the perfect radio frequency (RF) which is overidealistic. In practice, in-phase and quadrature-phase imbalance (IQI) inevitably occurs due to component mismatch or manufacturing process problems [24]. Although the influence of IQI can be mitigated by compensation algorithms and correction algorithms, it cannot be completely eliminated due to the different forms of noise [25–28]. The authors in [29] have demonstrated that IQI has negative effects on the NOMA systems and cannot be ignored. To solve this problem, authors in [30] studied the impact of IQI on the two-way cooperative AF relay systems and derived the closed-form and asymptotic expressions for the outage probability. The effects of TX IQI, RX IQI, and joint TX/RX IQI on the outage performance of the single-hop NOMA system were compared in [31]. The performance of cooperative NOMA system with IQI at the relay was analyzed by deriving closed-form expressions for the outage probability [32]. Recently, the impact of IQI on the cooperative NOMA DF network over Rayleigh channels has been considered in [33], while the influence of IQI on the source node was not taken into account. Moreover, the direct link between the source and the far user was not considered in [33].

Motivated by the previous discussion, in this paper, we discuss the effect of IQI on the cooperative IoT NOMA AF relaying system over Nakagami-m fading channels, and ipSIC is taken into account as well. In the considered system, the source node can communicate with the destination nodes with the aid of an AF relay or directly. To demonstrate the performance of the considered system, the exact analytical expressions of the outage probability are derived. In order to gain more insights, asymptotic analyses and diversity orders are calculated. Finally, the throughput and energy efficiency are also performed. The main contributions of this paper are summarized as follows:

(i) The exact outage probability expressions of the near-IoT-device and far-IoT-device of the considered sys-
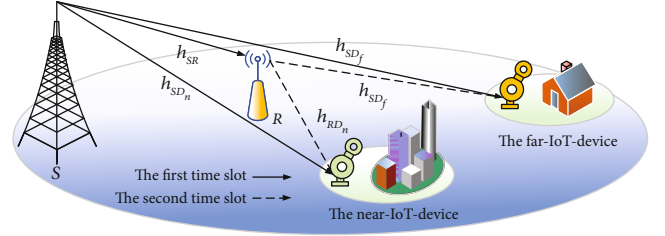
Figure 1: System model of cooperative IoT NOMA networks.

tem are derived by considering IQI at source, relay, and IoT devices; meanwhile, ipSIC is taken into account

(ii) In order to obtain more insights, the asymptotic outage performance is analyzed. For more intuitive evaluation of the considered system performance, the diversity order is further obtained

(iii) Finally, we deduce the throughput and energy efficiency of the considered network. The results confirm that (1) the system throughput will increase when the signal-to-noise ratio (SNR) is increasing, while approaches to a fixed value in the high SNR regime; (2) the energy efficiency will increase all the time in the ideal conditions, while in the nonideal conditions, the energy efficiency will reach the upper bound due to the existence of IQI and ipSIC

The rest of this paper is organized as follows. Section 2 describes the cooperative IoT NOMA systems with IQI and ipSIC; Section 3 discusses the exact and asymptotic outage performance, the diversity order, the system throughput, and the energy efficiency. The numerical results are presented in Section 4 before we conclude the paper in Section 5.

1.1. Notation. In this paper, $E[\cdot]$ denotes the expectation operator; $f_X(\cdot)$ and $F_X(\cdot)$ are the probability density function (PDF) and the cumulative distribution function (CDF) of a random variable X, respectively; $\Gamma(\cdot)$ is the Gamma function; $\Pr(\cdot)$ represents the probability of a random variable; $K_v(\cdot)$ symbolizes the vth-order modified Bessel function of the second kind, and $\triangleq$ stands for the definition operator.

2. System Model

As can be seen from Figure 1, we consider a single-carrier cooperative IoT NOMA network, which consists of one source S, one AF relay R, and multiple IoT devices. In the considered system, it is infeasible to study all devices due to the extremely high complexity. Therefore, under normal circumstances, all devices are divided into multiple clusters and OMA is used for the intercluster while NOMA is utilized within clusters (In this paper, we only study the devices in the same cluster.). In one cluster, the devices are classified into two groups, namely, the far-IoT -device D_f and the near-IoT-device D_n (The near-IoT-device and the far-IoT-device are distinguished by the geographic locations of the devices away from the source node, and this case of the

two-user downlink NOMA system has been widely considered in existing works, e.g., see Ref. [34–36].). It is assumed that all nodes are equipped with a single antenna and work in the half-duplex mode. The channel coefficients and channel gains between source and relay, source and destinations, and relay and destinations are denoted as h_{SR}, h_{SD_n}, h_{SD_f}, h_{RD_f}, h_{RD_n} and ρ_{SR}, ρ_{SD_n}, ρ_{SD_f}, ρ_{RD_f}, ρ_{RD_n}, respectively. Without loss of generality, the channel gains between source and M destinations are sorted as $\rho_{SD_1} \leq \rho_{SD_2} \leq \cdots \leq \rho_{SD_M}$.

2.1. Signal Transmission.

The communication procedure is divided into two time slots. In the first time slot, S transmits signals $y_S = \sqrt{a_1 P_S} x_1 + \sqrt{a_2 P_S} x_2$ to R, D_f, and D_n, where P_S is the transmit power of S, x_1 and x_2 are the desired signals of D_f and D_n, satisfying with $E[|x_1|^2] = E[|x_2|^2] = 1$, and a_1 and a_2 are the power allocation coefficients with $a_1 + a_2 = 1$ and $a_1 > a_2$. Thus, in the first time slot, the received signals at R, D_f, and D_n can be expressed as (The subscripts S, R, D_f, and D_n in μ_t, ν_t, μ_r, and ν_r represent IQIs caused by source, relay, the far-IoT-device, and the near-IoT-device, respectively.)

$$
\begin{aligned}
y_{SR} &= \mu_{r_R} \left[h_{SR} \left(\mu_{t_S} y_S + \nu_{t_S} y_S^* \right) + n_0 \right] \\
&\quad + \nu_{r_R} \times \left[h_{SR} \left(\mu_{t_S} y_S + \nu_{t_S} y_S^* \right) + n_0 \right]^*, \\
y_{SD_f} &= \mu_{r_{D_f}} \left[h_{SD_f} \left(\mu_{t_S} y_S + \nu_{t_S} y_S^* \right) + n_0 \right] \\
&\quad + \nu_{r_{D_f}} \times \left[h_{SD_f} \left(\mu_{t_S} y_S + \nu_{t_S} y_S^* \right) + n_0 \right]^*, \\
y_{SD_n} &= \mu_{r_{D_n}} \left[h_{SD_n} \left(\mu_{t_S} y_S + \nu_{t_S} y_S^* \right) + n_0 \right] \\
&\quad + \nu_{r_{D_n}} \times \left[h_{SD_n} \left(\mu_{t_S} y_S + \nu_{t_S} y_S^* \right) + n_0 \right]^*,
\end{aligned}
\tag{1}
$$

where $n_0 \sim \mathcal{CN}(0, N_0)$ denotes the additive white Gaussian noise (AWGN), μ_r, ν_r and μ_t, ν_t are the IQI coefficients caused by the RX and TX which can be expressed as

$$
\begin{aligned}
\mu_t &= \frac{1}{2} (1 + \zeta_t \exp(j\phi_t)), \\
\nu_t &= \frac{1}{2} (1 - \zeta_t \exp(-j\phi_t)), \\
\mu_r &= \frac{1}{2} (1 + \zeta_r \exp(-j\phi_r)), \\
\nu_r &= \frac{1}{2} (1 - \zeta_r \exp(j\phi_r)),
\end{aligned}
\tag{2}
$$

where ζ_t and ζ_r are the amplitude mismatch levels caused by TX and RX, while ϕ_t and ϕ_r are the phase mismatch levels and $j = \sqrt{-1}$ denotes the unit of imaginary. Furthermore, the TX/RX image rejection ratio (IRR) is expressed as

$$
\mathrm{IRR}_{t/r} = \frac{|\mu_{t/r}|^2}{|\nu_{t/r}|^2}.
\tag{3}
$$

According to the NOMA protocol, the received signal-to-interference-plus-noise ratio (SINR) for D_f and D_n to decoded x_1 is expressed as

$$
\gamma_{SD_f} = \frac{A_f \rho_{SD_f} a_1 \gamma_1}{a_2 \rho_{SD_f} A_f \gamma_1 + \rho_{SD_f} B_f \gamma_1 + C_f},
\tag{4}
$$

$$
\gamma_{SD_{n \to f}} = \frac{A_n \rho_{SD_n} a_1 \gamma_1}{a_2 \rho_{SD_n} A_n \gamma_1 + \rho_{SD_n} B_n \gamma_1 + C_n},
\tag{5}
$$

where $A_f = \mu_{r_{D_f}}^2 \mu_{t_S}^2 + \nu_{r_{D_f}}^2 \nu_{t_S}^2$, $A_n = \mu_{r_{D_n}}^2 \mu_{t_S}^2 + \nu_{r_{D_n}}^2 \nu_{t_S}^2$, $B_f = \mu_{r_{D_f}}^2 \nu_{t_S}^2 + \nu_{r_{D_f}}^2 \mu_{t_S}^2$, $B_n = \mu_{r_{D_n}}^2 \nu_{t_S}^2 + \nu_{r_{D_n}}^2 \mu_{t_S}^2$, $C_f = \mu_{r_{D_f}}^2 + \nu_{r_{D_f}}^2$, $C_n = \mu_{r_{D_n}}^2 + \nu_{r_{D_n}}^2$, and $\gamma_1 = P_S/N_0$ denotes the transmit SNR caused by S. Based on the ipSIC, the received SINR of D_n to decoded x_2 can be expressed as

$$
\gamma_{SD_n} = \frac{a_2 A_n \rho_{SD_n} \gamma_1}{a_2 B_n \rho_{SD_n} \gamma_1 + a_1 g_{SD_n} A_n \gamma_1 + C_n},
\tag{6}
$$

where $g_{SD_n} \sim \mathcal{CN}(0, \varepsilon \rho_{SD_n})$ and $\varepsilon \in (0, 1]$ is the parameter of ipSIC which follows the Gaussian distribution [37]. Note that in this system the value of ε cannot take the value of 1, because the network is completely out of the NOMA scheme when $\varepsilon = 1$, which is clearly contradictory to the considered system.

In the second time slot, the relay amplifies and forwards the received signals to the IoT devices. Thus, the received signals at D_f and D_n can be expressed as

$$
\begin{aligned}
y_{RD_f} &= \mu_{r_{D_f}} \left[h_{RD_f} \left(\mu_{t_R} (G y_{SR}) + \nu_{t_R} (G y_{SR}^*) \right) + n_0 \right] \\
&\quad + \nu_{r_{D_f}} \left[h_{RD_f} \left(\mu_{t_R} (G y_{SR}) + \nu_{t_R} (G y_{SR}^*) \right) + n_0 \right]^*, \\
y_{RD_n} &= \mu_{r_{D_n}} \left[h_{RD_n} \left(\mu_{t_R} (G y_{SR}) + \nu_{t_R} (G y_{SR}^*) \right) + n_0 \right] \\
&\quad + \nu_{r_{D_n}} \left[h_{RD_n} \left(\mu_{t_R} (G y_{SR}) + \nu_{t_R} (G y_{SR}^*) \right) + n_0 \right]^*,
\end{aligned}
\tag{7}
$$

where $G = \sqrt{P_R / (Q(P_S \rho_{SR} + N_0))}$ represents the amplifying gain factor and P_R is the transmit power by R and $Q = (|\mu_{t_R}|^2 + |\nu_{t_R}|^2)(|\mu_{r_R}|^2 + |\nu_{r_R}|^2)$. The received SINRs for D_f to decode x_1 and for D_n to decode x_1 and x_2 are expressed as

$$
\gamma_{RD_f} = \frac{a_1 E_f \rho_{SR} \rho_{RD_f} \gamma_1 \gamma_2}{(a_2 E_f + J_f) \rho_{SR} \rho_{RD_f} \gamma_1 \gamma_2 + T_f \rho_{SR} \gamma_1 + L_f \rho_{RD_f} \gamma_2 + T_f},
\tag{8}
$$

$$
\gamma_{RD_{n \to f}} = \frac{a_1 E_n \rho_{SR} \rho_{RD_n} \gamma_1 \gamma_2}{(a_2 E_n + J_n) \rho_{SR} \rho_{RD_n} \gamma_1 \gamma_2 + T_n \rho_{SR} \gamma_1 + L_n \rho_{RD_n} \gamma_2 + T_n},
\tag{9}
$$

$$\gamma_{RD_n} = \frac{a_2 E_n \rho_{SR} \rho_{RD_n} \gamma_1 \gamma_2}{(a_2 J_n + a_1 \varepsilon E_n) \rho_{SR} \rho_{RD_n} \gamma_1 \gamma_2 + L_n \rho_{RD_n} \gamma_2 + T_n \rho_{SR} \gamma_1 + T_n},$$

(10)

where $\gamma_1 = P_R/N_0$ represents the transmit SNR caused by R, $E_f = (\mu_{r_R}^2 \mu_{t_S}^2 + \nu_{r_R}^2 \nu_{t_S}^2)(\mu_{r_{D_f}}^2 \mu_{t_R}^2 + \nu_{r_{D_f}}^2 \nu_{t_R}^2) + (\mu_{r_R}^2 \nu_{t_S}^2 + \mu_{t_S}^2 \nu_{r_R}^2)$ $(\mu_{r_{D_f}}^2 \nu_{t_R}^2 + \mu_{t_R}^2 \nu_{r_{D_f}}^2)$, $E_n = (\mu_{r_R}^2 \mu_{t_S}^2 + \nu_{r_R}^2 \nu_{t_S}^2)(\mu_{r_{D_n}}^2 \mu_{t_R}^2 + \nu_{r_{D_n}}^2 \nu_{t_R}^2)$ $+ (\mu_{r_R}^2 \nu_{t_S}^2 + \mu_{t_S}^2 \nu_{r_R}^2)(\mu_{r_{D_n}}^2 \nu_{t_R}^2 + \mu_{t_R}^2 \nu_{r_{D_n}}^2)$, $J_f = (\mu_{r_R}^2 \nu_{t_S}^2 + \mu_{t_S}^2 \times \nu_{r_R}^2)$ $(\mu_{r_{D_f}}^2 \mu_{t_R}^2 + \nu_{r_{D_f}}^2 \nu_{t_R}^2) + (\mu_{r_{D_f}}^2 \nu_{t_R}^2 + \mu_{t_R}^2 \nu_{r_{D_f}}^2)(\mu_{r_R}^2 \mu_{t_S}^2 + \nu_{r_R}^2 \nu_{t_S}^2)$, $J_n = (\mu_{r_R}^2 \nu_{t_S}^2 + \mu_{t_S}^2 \nu_{r_R}^2)(\mu_{r_{D_n}}^2 \mu_{t_R}^2 + \nu_{r_{D_n}}^2 \times \nu_{t_R}^2) + (\mu_{r_{D_n}}^2 \nu_{t_R}^2 + \mu_{t_R}^2 \nu_{r_{D_n}}^2)$ $(\mu_{r_R}^2 \mu_{t_S}^2 + \nu_{r_R}^2 \nu_{t_S}^2)$, $L_f = 2\mu_{r_{D_f}}^2 \mu_{t_R}^2 + 2\mu_{r_{D_f}}^2 \nu_{t_R}^2 + 2\nu_{r_{D_f}}^2 \mu_{t_R}^2 + 2\nu_{r_{D_f}}^2 \nu_{t_R}^2$, $L_n = 2\mu_{r_{D_n}}^2 \mu_{t_R}^2 + 2\mu_{r_{D_n}}^2 \nu_{t_R}^2 + 2\nu_{r_{D_n}}^2 \mu_{t_R}^2 + 2\nu_{r_{D_n}}^2 \nu_{t_R}^2$, $T_f = QC_f$, and $T_f = C_n Q$.

2.2. Fading Channels.

Assume that all the channel gains follow Nakagami-m distribution; thus, the PDF and CDF of ρ_i can be expressed as [38]

$$f_{\rho_i}(x) = \frac{x^{\alpha_i - 1}}{\Gamma(\alpha_i)\beta_i^{\alpha_i}} e^{-x/\beta_i},$$

(11)

$$F_{\rho_i}(x) = 1 - \sum_{g_i=0}^{\alpha_i - 1} \frac{e^{-x/\beta_i}}{g_i!} \left(\frac{x}{\beta_i}\right)^{g_i},$$

(12)

where α_i denotes the multipath fading parameter while β_i represents the control spread parameter. By utilizing the order statistics, the PDF and CDF of the m-th devices' channel gain ρ_m can be expressed as

$$f_{\rho_m}(x) = \frac{M!}{(m-1)!(M-m)!} \left[F_{\rho_i}(x)\right]^{m-1} \times f_{\rho_i}(x) \left[1 - F_{\rho_i}(x)\right]^{M-m},$$

(13)

$$F_{\rho_m}(x) = \frac{M!}{(m-1)!(M-m)!} \sum_{z=0}^{M-m} \binom{M-m}{z} \times \frac{(-1)^z}{m+z} \left[F_{\rho_i}(x)\right]^{m+z},$$

(14)

where M denotes the total numbers of IoT devices.

3. Outage Probability Analysis

In this section, the outage performances of D_f and D_n are discussed. We first analyze the considered system by deriving the exact expressions of the outage probability and then formulate the asymptotic analysis in the high SNR. In addition, the throughput of the considered system is also explored.

3.1. Exact Outage Probability.

For D_f, the outage event will occur when D_f fails to decode the expected signal x_1 trans-

mitted from S and R. Therefore, the outage probability of D_f can be expressed as

$$P_{out}^{D_f} = \Pr\left(\gamma_{SD_f} < \gamma_{thf}\right) \Pr\left(\gamma_{RD_f} < \gamma_{thf}\right),$$

(15)

where γ_{thf} is the target threshold at D_f. The closed-form expression of outage probability of D_f under IQI and ipSIC is provided in the following theorem.

Theorem 1. *The exact outage probability expression of D_f in the presence of IQI and ipSIC is expressed as*

$$P_{out}^{D_f} = b_f \sum_{z=0}^{M-f} \binom{M-f}{z} \frac{(-1)^z}{f+z}$$

$$\cdot \left[1 - e^{-\theta/\beta_{SD_f}} \sum_{g_5=0}^{\alpha_{SD_f}-1} \frac{1}{g_5} \times \left(\frac{\theta}{\beta_{SD_f}}\right)^{g_5}\right]^{f+z}$$

$$\cdot \left[1 - \frac{2}{\Gamma\left(\alpha_{RD_f}\right)\beta_{RD_f}^{\alpha_{RD_f}}} \sum_{g_1=0}^{\alpha_{SR}-1} \sum_{t_1=0}^{\alpha_{RD_f}-1} \sum_{t_2=0}^{g_1} \frac{1}{g_1!}\right.$$

$$\times \binom{g_1}{g_2}\binom{\alpha_{RD_f}-1}{t_1}$$

$$\cdot \left(\beta_{SR}\gamma_1 T_f\right)^{-g_1-(t_1-t_2+1/2)} \varphi^{g_1+\alpha_{RD_f}-(t_1+t_2+1/2)}$$

$$\times \left(T_f + L_f \gamma_2 \varphi\right)^{((t_1+t_2+1)/2)} \beta_{RD_f}^{(t_1-t_2+1)/2} \left(L_f \gamma_2\right)^{g_1-t_2}$$

$$\times e^{-\left(\varphi/\beta_{RD_f}\right) - \left(L_f \gamma_2 \varphi/\beta_{SR} T_f \gamma_1\right)}$$

$$\left. \cdot K_{t_1-t_2+1}\left(2\sqrt{\frac{(T_f + L_f \gamma_2 \varphi)\varphi}{\beta_{SR}\beta_{RD_f} T_f \gamma_1}}\right)\right],$$

(16)

where f denotes the f-th device (the far device), $b_f \triangleq M!/(f - 1)!(M-f)!$, $\theta \triangleq C_f \gamma_{thf}/[a_1 A_f \gamma_1 - (a_1 A_f + B_f)\gamma_1 \gamma_{thf}]$ with $A_f a_1 > (a_1 A_f + B_f)\gamma_{thf}$, and $\varphi \triangleq T_f \gamma_{thf}/[a_1 E_f \gamma_2 - (a_2 E_f + J_f)\gamma_2 \gamma_{thf}]$ with $a_1 E_f > (a_2 E_f + J_f)\gamma_{thf}$.

Proof. See Appendix A.

For D_n, the outage event will occur when D_n fails to decode either the signals x_1 or x_2 transmitted from S or R. Therefore, the outage probability of D_n can be expressed as

$$P_{out}^{D_n} = \left[1 - \Pr\left(\gamma_{SD_{n\to f}} > \gamma_{thf}, \gamma_{SD_n} > \gamma_{thn}\right)\right] s$$
$$\times \left[1 - \Pr\left(\gamma_{RD_{n\to f}} > \gamma_{thf}, \gamma_{RD_n} > \gamma_{thn}\right)\right],$$

(17)

where γ_{thn} is the target threshold at D_n. The closed-form expression of outage probability of D_n under IQI and ipSIC is provided in the following theorem.

Theorem 2. *The exact outage probability expression of D_n in the presence of IQI and ipSIC is expressed as*

$$
P_{out}^{D_n} = b_n \sum_{z=0}^{M-n} \binom{M-n}{z} \frac{(-1)^z}{n+z}
$$
$$
\cdot \left[1 - \sum_{g_4=0}^{\alpha_{SD_n}-1} \frac{1}{g_4!} e^{-\xi/\beta_{SD_n}} \times \left(\frac{\xi}{\beta_{SD_n}} \right)^{g_4} \right]^{n+z}
$$
$$
\cdot \left[1 - \frac{2}{\alpha_{RD_n}\beta_{RD_n}^{\alpha_{RD_n}}} \sum_{g_1=0}^{\alpha_{SR}-1} \sum_{q_1=0}^{\alpha_{RD_n}-1} \sum_{q_2=0}^{g_1} \frac{1}{g_1!} \right.
$$
$$
\times \binom{g_1}{q_2} \binom{\alpha_{RD_n}-1}{q_1}
$$
$$
\cdot (\beta_{SR}\gamma_1 T_n)^{-g_1-((q_1-q_2+1)/2)} \tau^{g_1+\alpha_{RD_n}-((q_1+q_2+1)/2)}
$$
$$
\times (T_n + L_n\gamma_2\tau)^{(q_1+q_2+1)/2} \beta_{RD_n}^{(q_1-q_2+1)/2} (L_n\gamma_2)^{g_1-q_2}
$$
$$
\times e^{-(\tau/\beta_{RD_n})-(L_n\gamma_2\tau/\beta_{SR}T_n\gamma_1)}
$$
$$
\left. \cdot K_{q_1-q_2+1}\left(2\sqrt{\frac{(T_n+L_n\gamma_2\tau)\tau}{\beta_{SR}\beta_{RD_n}T_f\gamma_1}} \right) \right],
$$

$$(18)$$

where n denotes the n-th device (the near device) and $b_n \triangleq M!/(n-1)!(M-n)!$, $\xi \triangleq \max(\xi_1, \xi_2)$, $\xi_1 \triangleq C_f\gamma_{thf}/[a_1 A_n\gamma_1 - (a_1 A_n + B_n)\gamma_1\gamma_{thf}]$, $\xi_2 \triangleq C_n\gamma_{thn}/[a_2 A_n\gamma_1 - \gamma_1\gamma_{thn}(a_2 B_n + a_1\varepsilon A_n)]B_n + a_1\varepsilon A_n)]$, $\tau = \max(\tau_1, \tau_2)$, $\tau_1 \triangleq T_n\gamma_1\gamma_{thf}/[a_1 E_n\gamma_2 - (a_2 E_n + J_n)\gamma_2\gamma_{thf}]$, and $\tau_2 \triangleq T_n\gamma_{thn}/[a_2 E_n\gamma_2 - (a_2 J_n + a_1\varepsilon E_n)\gamma_2\gamma_{thn}]$.

Proof. See Appendix B.

Remark 3. From Theorems 1 and 2, we can observe that the outage probabilities of D_f and D_n are determined by IQI parameters, the performance of SIC, fading parameters, and distortion noise. Meanwhile, it is worth noting that when $\varsigma_t = \varsigma_r = 1$, $\phi_t = \phi_r = 0°$, and $\varepsilon = 0$ are all satisfied, the considered system reduces to ideal conditions.

3.2. Asymptotic Outage Probability. In this subsection, the asymptotic outage probabilities of D_f and D_n are analyzed to obtain more insights on the outage behavior of the considered system. The asymptotic CDF of the channel gain ρ_i in the case of ordering and nonordering can be expressed as [39]

$$
f_{\rho_i}^{\infty}(x) = \frac{x^{\alpha_i}}{\alpha_i!\beta_i^{\alpha_i}}, \tag{19}
$$

$$
F_{\rho_i}^{\infty}(x) = \frac{M!}{(M-m)!m!} \left(\frac{1}{\alpha_i} \right)^m \left(\frac{x}{\beta_i} \right)^{m\alpha_i}. \tag{20}
$$

The asymptotic expressions of outage probabilities of D_f and D_n are described in the following corollaries.

Corollary 4. *The asymptotic closed form of outage probability of D_f in the high SNR regime is expressed as*

$$
P_{out}^{D_f,\infty} = b_f^{\infty} \left(\frac{1}{\alpha_{SD_f}!} \right)^f \left(\frac{\theta}{\beta_{SD_f}} \right)^{\alpha_{SD_f}f}
$$
$$
\times \left(\frac{\varphi'^{\alpha_{SR}}}{\alpha_{SR}!\beta_{SR}^{\alpha_{SR}}} + \frac{\varphi''^{\alpha_{RD_f}}}{\alpha_{RD_f}!\beta_{RD_f}^{\alpha_{RD_f}}} \right), \tag{21}
$$

where $b_f^{\infty} = M!/[f!(M-f)!]$, $\varphi' = L_f\gamma_{thf}/[a_1 E_f\gamma_1 - (a_2 E_f + J_f)\gamma_1\gamma_{thf}]E_f\gamma_1 - (a_2 E_f + J_f)\gamma_1\gamma_{thf}]$, and $\varphi'' = T_f\gamma_{thf}/[a_1\gamma_2 E_f - (a_2 E_f + J_f)\gamma_2\gamma_{thf}]$.

Proof. See Appendix C.

Corollary 5. *The asymptotic closed form of outage probability of D_n in the high SNR regime is expressed as*

$$
P_{out}^{D_n,\infty} = b_n^{\infty} \left(\frac{1}{\alpha_{RD_n}!} \right)^n \left(\frac{\xi}{\beta_{RD_n}} \right)^{n\alpha_{SD_n}}
$$
$$
\times \left(\frac{\tau'^{\alpha_{SR}}}{\alpha_{SR}!\beta_{SR}^{\alpha_{SR}}} + \frac{\tau''^{\alpha_{RD_n}}}{\alpha_{RD_n}!\beta_{RD_n}^{\alpha_{RD_n}}} \right), \tag{22}
$$

where $b_n^{\infty} = M!/[n!(M-n)!]$, $\tau' = \max(\tau'_1, \tau'_2)$, $\tau'' = \max(\tau''_1, \tau''_2)$, $\tau'_1 \triangleq L_n\gamma_{thf}/[a_1 E_n\gamma_1 - \gamma_1\gamma_{thf}(a_2 E_n + J_n)]$, $\tau''_1 \triangleq T_n\gamma_{thf}/[a_1 E_n\gamma_2 - \gamma_2\gamma_{thf}(a_2 E_n + J_n)]$, $\tau'_2 \triangleq L_n\gamma_{thn}/[a_2 E_n\gamma_1 - a_2 J_n\gamma_{thn}\gamma_1]$, and $\tau''_2 \triangleq T_n\gamma_{thn}/[a_2 E_n\gamma_2 - a_2 J_n\gamma_{thn}\gamma_2]$.

Proof. See Appendix D.

Remark 6. The results of Corollaries 4 and 5 show the effects of channel fading parameters, IQI parameters, the performance of SIC, and distortion noise on asymptotic outage performances of D_f and D_n. In addition, we can also observe that the asymptotic outage probability is related to the order of user arrangement directly.

3.3. Diversity Order. The diversity order can reflect the trend of the outage probability intuitively. To this end, the diversity order of the considered system is explored in this subsection. The diversity order is defined as [40]

$$
d = -\lim_{\gamma \to \infty} \frac{\log\left(P_{out}^{D_m,\infty} \right)}{\log \gamma}, \tag{23}
$$

where $P_{out}^{D_m,\infty}$ denotes asymptotic outage probability of m-th device and $\gamma \in [\gamma_1, \gamma_2]$ represents the transmitted SNR.

Corollary 7. *Based on (23), the diversity orders of D_f and D_n in ideal conditions ($\varsigma_t = \varsigma_r = 1$, $\phi_t = \phi_r = 0°$, and $\varepsilon = 0$) and*

nonideal conditions ($\varsigma_t, \varsigma_r \neq 1$, $\phi_t, \phi_r \neq 0°$, and $\varepsilon \neq 0$) can be written as

$$d_f^{id} = d_f^{nid} = \min\left(f\alpha_{SD_f}\alpha_{SR}, f\alpha_{SD_f}\alpha_{RD_f}\right),$$
$$d_n^{id} = d_n^{nid} = \min\left(n\alpha_{SD_n}\alpha_{SR}, n\alpha_{SD_n}\alpha_{RD_n}\right). \tag{24}$$

Remark 8. The results show that the diversity order of D_f is the minimum of $f\alpha_{SD_f}\alpha_{SR}$ and $f\alpha_{SD_f}\alpha_{RD_f}$, which indicates that the diversity order of D_f is relative to α_{SD_f}, α_{SR}, α_{RD_f}, and f, while the value is affected by the multipath fading parameters α_{SR} and α_{RD_f} of $S \longrightarrow R$ and $R \longrightarrow D_f$. Similarly, the diversity order of D_n is the minimum of $n\alpha_{SD_n}\alpha_{SR}$ and $n\alpha_{SD_n}\alpha_{RD_n}$, which is related to α_{SD_n}, α_{SR}, α_{RD_n}, and n, and the final value is jointly determined by α_{SR} and α_{RD_n}. The results also show that the outage probabilities of D_f and D_n of the considered system will always decrease with the increase of SNR. In addition, we can also observe that although the outage probabilities of IoT devices in ideal and nonideal conditions are different, the trends are the same due to the diversity orders.

3.4. Throughput Analysis. The system throughput is another measure of system performance, which is the number of signals transmitted per unit of time successfully. Thus, the system throughput is formulated as [41]

$$T = \sum_{m=1}^{M}\left(1 - P_{out}^{D_m}\right)R_{thm}, \tag{25}$$

where $P_{out}^{D_m}$ is the outage probability of D_m which can be obtained from (16) and (18), $R_{thm} = (1/2)\log(1 + \gamma_{thm})$ denotes the target rate of D_m, and $1/2$ represents that the communication transmit process is divided into two time slots.

3.5. Energy Efficiency. To further evaluate the performance of the considered system, the energy efficiency is analyzed in this subsection. Energy efficiency refers to the useful signals that IoT devices received for each unit of energy consumed by S. Hence, the energy efficiency of the considered system can be expressed as [42]

$$\eta_{ee} = \frac{T}{P_{EE}}, \tag{26}$$

where $P_{EE} = P_S + P_R + P_C$ denotes total energy consumption and P_C is the fixed energy consumption which is caused by transmitter and the IoT devices and T is the system throughput which can be obtained from (25).

4. Numerical Results

In this section, the correctness of analytical results in Section 3 is demonstrated by some computer simulations. Unless otherwise noted, the simulation parameters are provided in Table 1.

TABLE 1: Simulation parameters.

Parameters	Value	Parameters	Value
α_i	2	β_i	1
n	2	f	1
γ_{thf}	1.5	γ_{thn}	3
M	2	N_0	1
P_C	0.1 W		
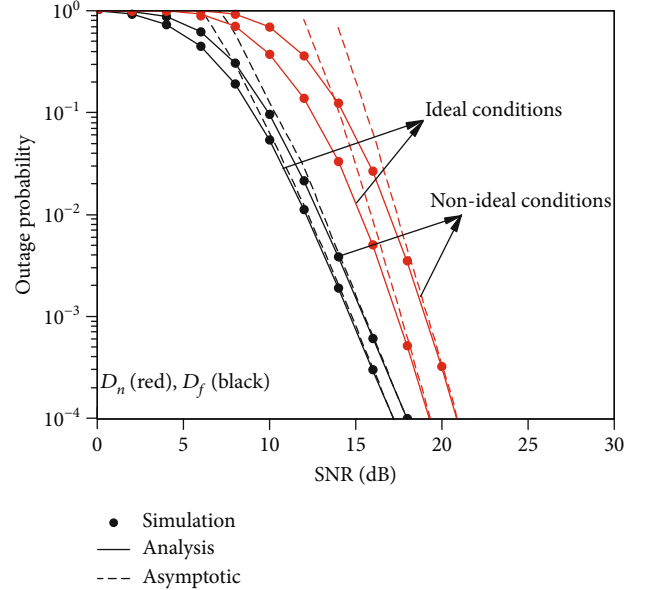
FIGURE 2: Outage probability of IoT devices versus transmit SNR in different conditions.

Figure 2 shows the outage probabilities of IoT devices versus transmit SNR in ideal conditions ($\varsigma_t = \varsigma_r = 1$, $\phi_t = \phi_r = 0°$, and $\varepsilon = 0$) and nonideal conditions ($\varsigma_t = \varsigma_r = 1.2$, $\phi_t = \phi_r = 10°$, and $\varepsilon = 0.01$) with $a_1 = 0.8$ and $a_2 = 0.2$. The perfect coincidence of the theoretical analysis value and the Monte Carlo simulation value curves in Figure 2 verifies our derivations in (16), (18), (21), and (22). From Figure 2, we can observe that the gaps caused by ideal and nonideal conditions of D_n are larger than those of D_f. The reason for this phenomenon can be explained by the fact that ipSIC has no impact on D_f. As can also be seen from Figure 2, the curves of different IoT devices are almost parallel in the high SNR region. Meanwhile, we also notice that the outage probability of the far-IoT-device outperforms that of the near-IoT-device, because of the large power allocation factor. Additionally, the results also show that the outage performance of the considered system can be greatly prompted by improving the transmitting SNR.

Figure 3 illustrates the outage probabilities of the IoT devices versus IRR in perfect I/Q and IQI conditions with $IRR_t = IRR_r$, SNR = 15 dB, $\varepsilon = 0.01$, and $a_1 = 0.8$ and $a_2 = 0.2$ for power allocation. As can be seen from Figure 3, with the increase of IRR, the outage performances of devices D_f and D_n improve continuously, and when IRR > 32 dB, the
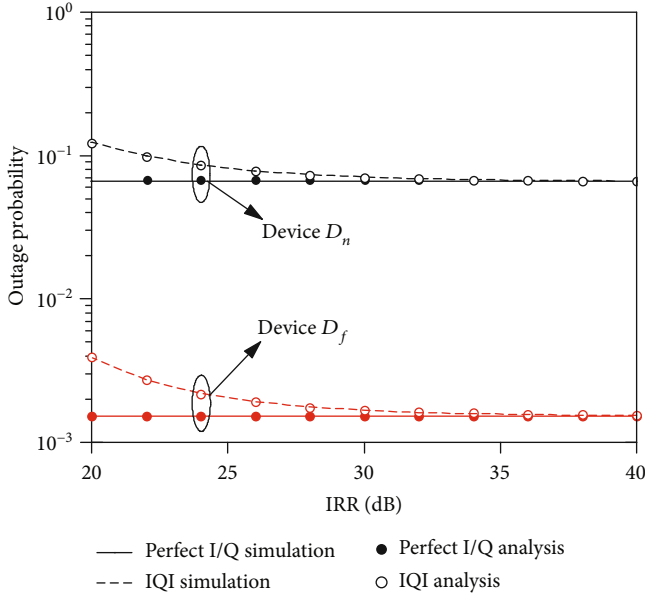
FIGURE 3: Outage probability of IoT devices versus IRR in different conditions.

FIGURE 5: Outage probability of IoT devices versus ε in different conditions.

FIGURE 4: Outage probability of IoT devices versus SNR under different nonideal factors.
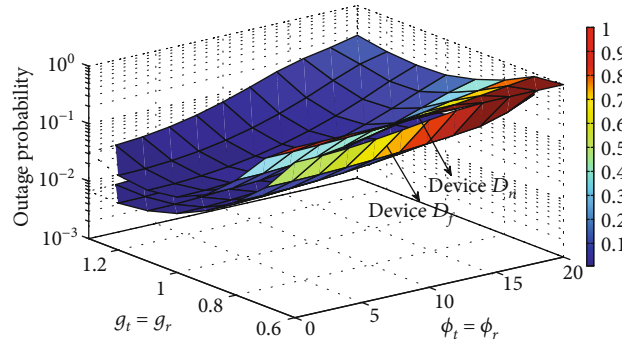
FIGURE 6: Outage probability of IoT devices versus g and ϕ.

outage probabilities of the devices almost coincide with those of the ideal IQ matching. In addition, in terms of the gaps between the perfect IQ matching and IQI curves in the figure, IQI has different effects on the outage performances of different IoT devices in the considered NOMA system. Furthermore, we can also observe that the outage performance of the far-IoT-device is better than that of the near device, which is due to the more power allocation obtained by the far device.

Figure 4 plots the variations of outage probabilities of the IoT devices with the increase of SNR in the presence of different nonideal factors with $a_1 = 0.8$ and $a_2 = 0.2$. In the simula-

tion, we assume three cases: (1) only IQI ($\varsigma_t = \varsigma_r \neq 1.05$, $\phi_t = \phi_r \neq 9°$, and $\varepsilon = 0$), (2) only ipSIC ($\varsigma_t = \varsigma_r = 1$, $\phi_t = \phi_r = 0°$, and $\varepsilon = 0.05$), and (3) both IQI and ipSIC ($\varsigma_t = \varsigma_r = 1.05$, $\varepsilon = 0.05$, and $\phi_t = \phi_r = 9°$). The reason for setting the nonideal factors in this way is to ensure that the level of IQ mismatch is at the same extent as the level of ipSIC. For the near-IoT-device D_n, the case of only IQI outperforms the case of only ipSIC in the outage performance which indicates that ipSIC has a severe negative impact on the considered system. Interestingly, the curves of only IQI and both ipSIC and IQI are coincident, since in the NOMA system, the outage performance of D_f is not affected by SIC.

As a further development, Figure 5 presents the outage performances of IoT devices versus ε with SNR = 15 dB. For nonideal conditions, we set $\varsigma_t = \varsigma_r = 1.2$ and $\phi_t = \phi_r = 10°$. It can be observed from Figure 5 that, for the far-IoT-device D_f, the outage probabilities in either ideal or nonideal conditions will not change with the variation of ε, which is due to the fact that the outage performance of D_f is independent of the performance of SIC, while for D_n the outage probability almost increases linearly with the increase of ε. This indicates
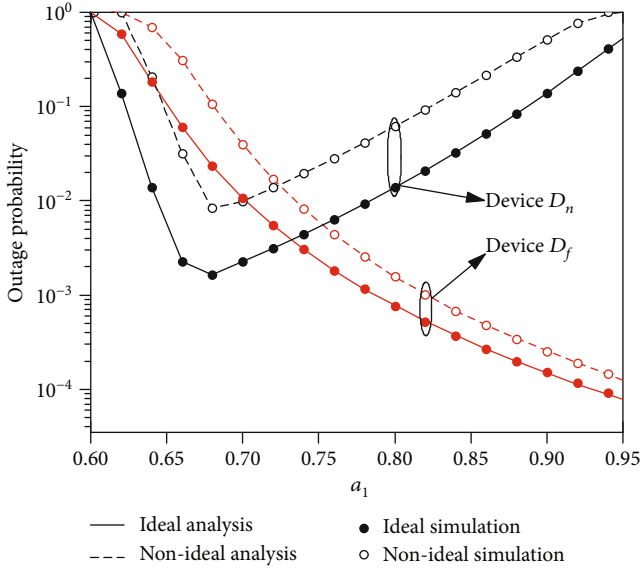
FIGURE 7: Outage probability of IoT devices versus a_1 in different conditions.
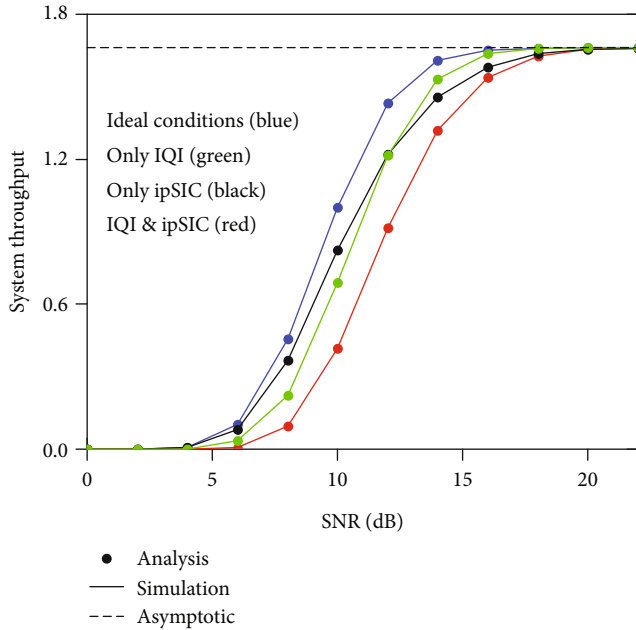
FIGURE 8: System throughput versus SNR in different conditions.

FIGURE 9: Energy efficiency versus SNR under different nonideal factors.

that SIC is vital in the outage performance of D_n. From Figure 5, we can also see that when $\varepsilon = 0$, there are gaps between the outage probabilities of ideal and nonideal conditions, which is due to the existence of IQI in the considered system. It is worth noting that although we have mentioned $\varepsilon \in [0, 1)$ in Section 2, the maximum value of ε here is taken as 0.1. The reason is that $a_2 A_n > (a_2 B_n + a_1 \varepsilon A_n)\gamma_{thn}$ and $a_2 E_n > (a_2 J_n + a_1 \varepsilon E_n)\gamma_{thn}$ are all needed to be satisfied from (18). Thus, when $\varepsilon = 0.1$, the outage probability of D_n is almost 1.

Figure 6 analyzes the impact of amplitude and phase mismatch levels on the outage probabilities versus SNR for dif-

ferent IoT devices with SNR = 15 dB, $\varepsilon = 0.01$, and $a_1 = 0.7$ and $a_2 = 0.3$ for power allocation. For simplicity, in this simulation, we set $g_{t_S} = g_{t_R} = g_{r_R} = g_{r_D}$ and $\phi_{t_S} = \phi_{t_R} = \phi_{r_R} = \phi_{r_D}$. As can be seen from Figure 6, when $0.6 < g < 1$, the outage probabilities decrease with the increase of g; however, when $1 < g < 1.3$, the opposite phenomenon appears. This can be explained that when the amplitude mismatch levels are closer to 1, the system is closer to the ideal conditions. Another observation is that the outage performances of IoT devices deteriorate with the increase of ϕ, and when the phase mismatch levels reach to about 20°, the considered system turns meaningless due to the high outage probability.

Figure 7 investigates the outage probabilities of IoT devices versus power allocation a_1 with SNR = 15 dB in ideal conditions and nonideal conditions for $\varsigma_t = \varsigma_r = 1.2$, $\phi_t = \phi_r = 10°$, and $\varepsilon = 0.01$. The outage probability of D_n first decreases and then increases with the increase of a_1, and when a_1 is about 0.68, the outage probability of D_n reaches the minimum. This can be deciphered that when $0.5 < a_1 < 0.6$, the considered network is always in an off-line state due to the insufficient power level for D_f, and when $0.6 < a_1 < 0.68$, the considered system begins to perform NOMA; after that, the outage performance of D_n begins to deteriorate as the power allocation to D_n decreases. Unlike D_n, the outage probability of D_f keeps decreasing as the power allocated to it increases.

Figure 8 shows the exact and asymptotic system throughput versus SNR. In this simulation, we set $\varsigma_t = \varsigma_r = 1.3$, $\phi_t = \phi_r = 15°$, and $\varepsilon = 0.05$ for nonideal factors and $a_1 = 0.7$ and $a_2 = 0.3$ for power allocation. When the SNR is lower than 5 dB, the throughput of the considered system is almost 0 due to the high outage probability. And the system throughput tends to be a fixed value in the high SNR regime. This is because when the SNR is large enough, the outage probabilities of IoT devices are almost close to 0. It is worth

mentioning that there exists an intersection between the green curve (only IQI in the considered system) and the black curve (only ipSIC in the considered system), which indicates that in the case of low SNR, IQI has a greater impact on the system throughput, while ipSIC will have a more severe impact on the considered system in the moderate and high SNR region. From Figure 8, we can also find that these nonideal factors play a negative role in the considered system.

In Figure 9, the energy efficiency of the considered system versus SNR is plotted. From the figure, we can see that in both ideal and nonideal conditions, the energy efficiency of the considered system first increases and then decreases, which is due to the fact that when the SNR is low, most of the transmission power is used for signal transmission. From the figure, we can also observe that the energy efficiency of the system which is only affected by IQI is higher than that only affected by ipSIC. This indicates that compared with IQI, the energy efficiency of the considered system is more dependent on the performance of SIC. In addition, we can also observe that when $\text{SNR} > 20\,\text{dB}$, the energy efficiencies of the considered system in the four cases are almost identical. Finally, we can also conclude that the overall performance of the system cannot be improved by simply increasing the SNR in practical communication networks.

5. Conclusion

In this paper, the performance of cooperative AF IoT NOMA system in the presence of IQI and ipSIC is studied. The exact and asymptotic outage probability expressions are derived to evaluate the considered system. Furthermore, the diversity order in the high SNR region, the system throughput, and the energy efficiency are also presented. The results show that IQI and ipSIC play negative roles in the considered system performance and the outage performance of the considered system will be greatly improved with the increase of SNR. Compared with IQI, identical degree of ipSIC plays a greater impact on the outage performance. Particularly, tuning the power allocation scheme properly can improve the outage performances of the IoT devices. The results also show that, according to the inherent characteristics of the NOMA scheme, the outage probability of the far-IoT-device is independent of the SIC performance. In addition, the simulation results of the system throughput and the energy efficiency show that the system performance cannot be improved by simply improving the SNR.

Appendix

A. Proof of Theorem 1

By substituting (4) and (8) into (15), the outage probability of D_f is rewritten as

$$P_{\text{out}}^{D_f} = \underbrace{\Pr\left(\frac{a_1 A_f \rho_{SD_f} \gamma_1}{a_2 \rho_{SD_f} A_f \gamma_1 + \rho_{SD_f} B_f \gamma_1 + C_f} < \gamma_{thf}\right)}_{I_1} \times \underbrace{\Pr\left(\frac{a_1 E_f \rho_{SR} \rho_{RD_f} \gamma_1 \gamma_2}{(a_2 E_f + J_f)\rho_{SR}\rho_{RD_f}\gamma_1\gamma_2 + T_f \rho_{SR}\gamma_1 + L_f \rho_{RD_f}\gamma_2 + T_f} < \gamma_{thf}\right)}_{I_2}.$$

$$(A.1)$$

Utilizing the PDF and CDF in (11)–(14), I_1 and I_2 can be further expressed as

$$I_1 = \Pr\left(\rho_{SD_f} < \theta\right) = b_f \sum_{z=0}^{M-f} \binom{M-f}{z} \frac{(-1)^z}{f+z}$$
$$\cdot \left[1 - \sum_{g_5=0}^{\alpha_{SD_f}-1} \frac{1}{g_5} e^{-\theta/\beta_{SD_f}} \left(\frac{\theta}{\beta_{SD_f}}\right)^{g_5}\right]^{f+z},$$

$$(A.2)$$

$$I_2 = 1 - \Pr\left(\rho_{RD_f} > \varphi, \rho_{SR} > \frac{(T_f + L_f \gamma_2 \rho_2)\varphi}{(\rho_2 - \varphi)T_f \gamma_1}\right)$$
$$= \int_\varphi^\infty f_{\rho_{RD_f}}(y)dy \int_{(T_f+L_f\gamma_2\rho_2)\varphi/(y-\varphi)T_f\gamma_1}^\infty f_{\rho_{SR}}(x)dx$$

$$= 1 - \frac{2}{\Gamma\left(\alpha_{RD_f}\right)\beta_{RD_f}^{\alpha_{RD_f}}} \sum_{g_1=0}^{\alpha_{SR}-1} \sum_{t_1=0}^{\alpha_{RD_f}-1} \sum_{t_2=0}^{g_1} \frac{1}{g_1!} \binom{\alpha_{RD_f}-1}{t_1}$$
$$\times \binom{g_1}{g_2} \left(\frac{1}{\beta_{SR}\gamma_1 T_f}\right)^{g_1+((t_1-t_2+1)/2)}$$
$$\cdot \varphi^{g_1+\alpha_{RD_f}-(t_1+t_2+1)/2} \left(L_f\gamma_2\right)^{g_1-t_2}$$
$$\times \left(T_f + L_f\gamma_2\varphi\right)^{(t_1+t_2+1)/2} \beta_{RD_f}^{(t_1-t_2+1)/2} e^{-\left(\varphi/\beta_{RD_f}\right)-\left(L_f\gamma_2\varphi/\beta_{SR}T_f\gamma_1\right)}$$
$$\times K_{t_1-t_2+1}\left(2\sqrt{\frac{(T_f+L_f\gamma_2\varphi)\varphi}{\beta_{SR}\beta_{RD_f}T_f\gamma_1}}\right).$$

$$(A.3)$$

Combining (A.2) and (A.3) with (A.1), the outage probability of D_f can be obtained.

B. Proof of Theorem 2

By substituting (5), (6), (9), and (10) into (17), the outage probability of D_n is rewritten as

$$
\begin{aligned}
P_{\text{out}}^{D_f} &= \left[1 - \Pr\left(\gamma_{SD_{n\to f}} > \gamma_{thf}, \gamma_{SD_n} > \gamma_{thn}\right)\right]\left[1 - \Pr\left(\gamma_{RD_{n\to f}} > \gamma_{thf}, \gamma_{RD_n} > \gamma_{thn}\right)\right] \\
&= \underbrace{\left[1 - \Pr\left(\frac{A_n \rho_{SD_n} a_1 \gamma_1}{(a_2 A_n + B_n)\rho_{SD_n}\gamma_1 + C_n} > \gamma_{thf}, \frac{a_2 A_n \rho_{SD_n}\gamma_1}{(a_2 B_n + a_1 \varepsilon A_n)\rho_{SD_n}\gamma_1 + C_n} > \gamma_{thn}\right)\right]}_{I_3} \\
&\quad \times \underbrace{\left[1 - \Pr\left(\frac{a_1 E_n \rho_{SR}\rho_{RD_n}\gamma_1\gamma_2}{(a_2 E_n + J_n)\rho_{SR}\rho_{RD_n}\gamma_1\gamma_2 + T_n\rho_{SR}\gamma_1 + L_n\rho_{RD_n}\gamma_2 + T_n} > \gamma_{thf}, \frac{a_2 E_n \rho_{SR}\rho_{RD_n}\gamma_1\gamma_2}{(a_2 J_n + a_1 \varepsilon E_n)\rho_{SR}\rho_{RD_n}\gamma_1\gamma_2 + L_n\rho_{RD_n}\gamma_2 + T_n\rho_{SR}\gamma_1 + T_n} > \gamma_{thn}\right)\right]}_{I_4}.
\end{aligned}
\tag{B.1}
$$

Utilizing the PDF and CDF in (11)–(14), I_3 and I_4 can be further expressed as

$$
\begin{aligned}
I_3 &= 1 - \Pr\left(\rho_{SD_n} < \xi\right) = b_n \sum_{z=0}^{M-n}\binom{M-n}{z}\frac{(-1)^z}{n+z} \\
&\quad \cdot \left[1 - \sum_{g_4=0}^{\alpha_{SD_n}-1}\frac{1}{g_4!}e^{-\xi/\beta_{SD_n}}\left(\frac{\xi}{\beta_{SD_n}}\right)^{g_4}\right]^{n+z},
\end{aligned}
\tag{B.2}
$$

$$
\begin{aligned}
I_4 &= 1 - \Pr\left(\rho_{RD_n} > \tau, \rho_{SR} > \frac{\left(T_n + L_n\gamma_2\rho_{RD_n}\right)\tau}{\left(\rho_{RD_n} - \tau\right)T_n\gamma_1}\right) \\
&= \int_\tau^\infty f_{\rho_{RD_n}}(y)\,dy \int_{(T_n+L_n\gamma_2 y)\tau/(y-\tau)T_n\gamma}^\infty f_{\rho_{SR}}(x)\,dx \\
&= 1 - \frac{2}{\alpha_{RD_n}\beta_{RD_n}^{\alpha_{RD_n}}}\sum_{g_1=0}^{\alpha_{SR}-1}\sum_{q_1=0}^{\alpha_{RD_n}-1}\sum_{q_2=0}^{g_1}\frac{1}{g_1!}\binom{\alpha_{RD_n}-1}{q_1}\binom{g_1}{q_2} \\
&\quad \times \left(\frac{1}{\beta_{SR}\gamma_1 T_n}\right)^{g_1+(q_1-q_2+1)/2}\tau^{g_1+\alpha_{RD_n}-(q_1+q_2+1)/2}\beta_{RD_n}^{(q_1-q_2+1)/2} \\
&\quad \times (T_n + L_n\gamma_2\tau)^{(q_1+q_2+1)/2}(L_n\gamma_2)^{g_1-q_2}e^{-\left(\tau/\beta_{RD_n}\right)-(L_n\gamma_2\tau/\beta_{SR}T_n\gamma_1)} \\
&\quad \times K_{q_1-q_2+1}\left(2\sqrt{\frac{(T_n+L_n\gamma_2\tau)\tau}{\beta_{SR}\beta_{RD_n}T_f\gamma_1}}\right).
\end{aligned}
\tag{B.3}
$$

Combining (B.2) and (B.3) with (B.1), the outage probability of D_n can be obtained.

C. Proof of Corollary 1

Based on (A.1), the asymptotic outage probability of D_f can be expressed as

$$
P_{\text{out}}^{D_f,\infty} = I_1^\infty I_2^\infty.
\tag{C.1}
$$

Utilizing the asymptotic CDF in (19), I_1^∞ can be further expressed as

$$
I_1^\infty = \Pr\left(\rho_{SD_n} < \theta\right) \approx b_f^\infty\left(\frac{1}{\alpha_{SD_f}!}\right)^f\left(\frac{\theta}{\beta_{SD_f}}\right)^{\alpha_{SD_f}f}.
\tag{C.2}
$$

Using the inequality $xy/(x+y+1) < \min(x,y)$ [43] and the asymptotic CDF in (20), I_2^∞ can be further expressed as

$$
\begin{aligned}
I_2^\infty &= 1 - \Pr\left(\frac{\rho_{SR}\gamma_1\left(L_f\rho_{RD_f}\gamma_2/T_f\right)}{\rho_{SR}\gamma_1 + \left(L_f\rho_{RD_f}\gamma_2/T_f\right) + 1}\right. \\
&\quad \left. > \frac{L_f\gamma_{thf}}{a_1 E_f - \left(a_2 E_f + J_f\right)\gamma_{thf}}\right) \\
&\approx 1 - \Pr\left(\rho_{SR} > \varphi', \rho_{RD_f} > \varphi''\right) \\
&\approx F_{\rho_{SR}}\left(\varphi'\right) + F_{\rho_{RD_f}}\left(\varphi''\right) \\
&\approx \frac{\varphi'^{\alpha_{SR}}}{\alpha_{SR}!\beta_{SR}^{\alpha_{SR}}} + \frac{\varphi''^{\alpha_{RD_f}}}{\alpha_{RD_f}!\beta_{RD_f}^{\alpha_{RD_f}}}.
\end{aligned}
\tag{C.3}
$$

Substituting (C.2) and (C.3) into (C.1), the asymptotic outage probability of D_f can be obtained.

D. Proof of Corollary 2

Based on (B.1), the asymptotic outage probability of D_n can be expressed as

$$
P_{\text{out}}^{D_{n,\infty}} = I_3^\infty I_4^\infty.
\tag{D.1}
$$

Similar to (C.2) and (C.3), I_3^∞ and I_4^∞ can be further expressed as

$$I_3^\infty = \Pr\left(\rho_{RD_n} < \xi\right) \approx b_n^\infty \left(\frac{1}{\alpha_{RD_n}!}\right)^n \left(\frac{\xi}{\beta_{RD_n}}\right)^{n\alpha_{RD_n}}, \quad \text{(D.2)}$$

$$
\begin{aligned}
I_4^\infty &= 1 - \Pr\left(\frac{\rho_{SR}\gamma_1\left(L_n\rho_{RD_n}\gamma_2/T_n\right)}{\rho_{SR}\gamma_1 + \left(L_f\rho_{RD_n}\gamma_2/T_n\right) + 1}\right. \\
&\quad > \frac{L_n\gamma_{thf}}{a_1E_n - (a_2E_n + J_n)\gamma_{thf}}, \frac{\rho_{SR}\gamma_1\left(L_n\rho_{RD_n}\gamma_2/T_n\right)}{\rho_{SR}\gamma_1 + \left(L_f\rho_{RD_n}\gamma_2/T_n\right) + 1} \\
&\quad > \left.\frac{L_n\gamma_{thn}}{a_2E_n - (a_2J_n + a_1\varepsilon E_n)\gamma_{thn}}\right) \\
&\approx 1 - \Pr\left(\rho_{SR} > \tau', \rho_{RD_n} > \tau''\right) \\
&\approx F_{\rho_{SR}}\left(\tau'\right) + F_{\rho_{RD_n}}\left(\tau''\right) \approx \frac{\tau'^{\alpha_{SR}}}{\alpha_{SR}!\beta_{SR}^{\alpha_{SR}}} + \frac{\tau''^{\alpha_{RD_n}}}{\alpha_{RD_n}!\beta_{RD_n}^{\alpha_{RD_n}}}.
\end{aligned}
$$
$$\text{(D.3)}$$

Substituting (D.2) and (D.3) into (D.1), the asymptotic outage probability of D_n can be obtained.

Data Availability

All data generated or analyzed during this study are owned by all the authors and will be used to our further research. The data used to support the findings of this study are available from the corresponding author upon request.

Conflicts of Interest

The authors declare that they have no conflicts of interest.

Acknowledgments

References

[1] D. Zhang, Z. Zhou, S. Mumtaz, J. Rodriguez, and T. Sato, "One integrated energy efficiency proposal for 5G IoT communications," *IEEE Internet of Things Journal*, vol. 3, no. 6, pp. 1346–1354, 2016.

[2] K. N. R. S. V. Prasad, E. Hossain, and V. K. Bhargava, "Energy efficiency in massive MIMO-based 5G networks: opportunities and challenges," *IEEE Wireless Communications*, vol. 24, no. 3, pp. 86–94, 2017.

[3] X. Li, J. Li, L. Li, L. Du, J. Jin, and D. Zhang, "Performance analysis of cooperative small cell systems under correlated rician/gamma fading channels," *IET Signal Process*, vol. 12, no. 1, pp. 64–73, 2018.

[4] S. M. R. Islam, N. Avazov, O. A. Dobre, and K. Kwak, "Power-domain non-orthogonal multiple access (NOMA) in 5G systems: potentials and challenges," *IEEE Communication Surveys Tutorials*, vol. 19, no. 2, pp. 721–742, 2017.

[5] D. Wang, D. Chen, B. Song, N. Guizani, X. Yu, and X. Du, "From IoT to 5G I-IoT: the next generation IoT-based intelligent algorithms and 5G technologies," *IEEE Communications Magazine*, vol. 56, no. 10, pp. 114–120, 2018.

[6] 3GPP TR 38.812, "Study on Non-Orthogonal Multiple Access (NOMA) for NR, TSG RAN Meeting 67," 2018, https://www .3gpp.org/DynaReport/TDocExMtg–R1-95–18807.htm.

[7] R. Abozariba, M. K. Naeem, M. Patwary, M. Eyedebrahimi, P. Bull, and A. Aneiba, "NOMA-based resource allocation and mobility enhancement framework for IoT in next generation cellular networks," *IEEE Access*, vol. 7, pp. 29158–29172, 2019.

[8] W. U. Khan, F. Jameel, T. Ristaniemi, B. M. Elhalawany, and J. Liu, "Efficient power allocation for multi-cell uplink NOMA network," in *2019 IEEE 89th Vehicular Technology Conference (VTC2019-Spring)*, pp. 1–5, Kuala Lumpur, Malaysia, Malaysia, April 2019.

[9] L. Dai, B. Wang, Z. Ding, Z. Wang, S. Chen, and L. Hanzo, "A survey of non-orthogonal multiple access for 5G," *IEEE Communications Surveys & Tutorials*, vol. 20, no. 3, pp. 2294–2323, 2018.

[10] W. U. Khan, "Maximizing physical layer security in relay-assisted multicarrier nonorthogonal multiple access transmission," *Internet Technology Letters*, vol. 2, no. 2, 2019.

[11] X. Liu, Y. Wang, S. Liu, and J. Meng, "Spectrum resource optimization for NOMA-based cognitive radio in 5G communications," *IEEE Access*, vol. 6, pp. 24904–24911, 2018.

[12] D. Zhang, Y. Liu, Z. Ding, Z. Zhou, A. Nallanathan, and T. Sato, "Performance analysis of non-regenerative massive-MIMO-NOMA relay systems for 5G," *IEEE Transactions on Communications*, vol. 65, no. 11, pp. 4777–4790, 2017.

[13] Z. Ding, M. Peng, and H. V. Poor, "Cooperative non-orthogonal multiple access in 5G systems," *IEEE Communications Letters*, vol. 19, no. 8, pp. 1462–1465, 2015.

[14] L. Lv, J. Chen, and Q. Ni, "Cooperative non-orthogonal multiple access in cognitive radio," *IEEE Communications Letters*, vol. 20, no. 10, pp. 2059–2062, 2016.

[15] O. Abbasi, A. Ebrahimi, and N. Mokari, "NOMA inspired cooperative relaying system using an AF relay," *IEEE Wireless Communications Letters*, vol. 8, no. 1, pp. 261–264, 2019.

[16] L. Zhang, J. Liu, M. Xiao, G. Wu, Y. Liang, and S. Li, "Performance analysis and optimization in downlink NOMA systems with cooperative full-duplex relaying," *IEEE Journal on Selected Areas in Communications*, vol. 35, no. 10, pp. 2398–2412, 2017.

[17] M. Alkhawatrah, Y. Gong, G. Chen, S. Lambotharan, and J. A. Chambers, "Buffer-aided relay selection for cooperative NOMA in the internet of things," *IEEE Internet of Things Journal*, vol. 6, no. 3, pp. 5722–5731, 2019.

[18] F. Jameel, W. U. Khan, Z. Chang, T. Ristaniemi, and J. Liu, "Secrecy analysis and learning-based optimization of cooperative NOMA SWIPT systems," in *2019 IEEE International Conference on Communications Workshops (ICC Workshops)*, pp. 1–6, Shanghai, China, China, May 2019.

[19] L. P. Qian, A. Feng, Y. Huang, Y. Wu, B. Ji, and Z. Shi, "Optimal SIC ordering and computation resource allocation in MEC-Aware NOMA NB-IoT networks," *IEEE Internet of Things Journal*, vol. 6, no. 2, pp. 2806–2816, 2019.

[20] X. Yan, J. Ge, Y. Zhang, and L. Gou, "NOMA-based multiple-antenna and multiple-relay networks over Nakagami-*m* fading channels with imperfect CSI and SIC error," *IET Communications*, vol. 12, no. 17, pp. 2087–2098, 2018.

[21] X. Li, M. Liu, C. Deng et al., "Joint effects of residual hardware impairments and channel estimation errors on SWIPT assisted cooperative NOMA networks," *IEEE Access*, vol. 7, pp. 135499–135513, 2019.

[22] X. Yue, Z. Qin, Y. Liu, S. Kang, and Y. Chen, "A unified framework for non-orthogonal multiple access," *IEEE Transactions on Communications*, vol. 66, no. 11, pp. 5346–5359, 2018.

[23] G. Im and J. H. Lee, "Outage probability for cooperative NOMA systems with imperfect SIC in cognitive radio networks," *IEEE Communications Letters*, vol. 23, no. 4, pp. 692–695, 2019.

[24] T. Schenk, *RF Imperfections in High-Rate Wireless Systems: Impact and Digital Compensation*, Springer, Netherlands, 2018.

[25] X. Li, J. Li, Y. Liu, Z. Ding, and A. Nallanathan, "Outage performance of cooperative NOMA networks with hardware impairments," in *2018 IEEE Global Communications Conference (GLOBECOM)*, pp. 1–6, Abu Dhabi, United Arab Emirates, December 2018.

[26] A. Gomaa and L. M. A. Jalloul, "Data-aided I/Q imbalance estimation and compensation in OFDM systems," *IEEE Communications Letters*, vol. 18, no. 3, pp. 459–462, 2014.

[27] M. Mokhtar, A. A. Boulogeorgos, G. K. Karagiannidis, and N. Al-Dhahir, "OFDM opportunistic relaying under joint transmit/receive I/Q imbalance," *IEEE Transactions on Communications*, vol. 62, no. 5, pp. 1458–1468, 2014.

[28] A. Gouissem, R. Hamila, and M. O. Hasna, "Outage performance of cooperative systems under IQ imbalance," *IEEE Transactions on Communications*, vol. 62, no. 5, pp. 1480–1489, 2014.

[29] B. Selim, S. Muhaidat, P. C. Sofotasios, A. Al-Dweik, B. S. Sharif, and T. Stouraitis, "Radio-frequency front-end impairments: performance degradation in nonorthogonal multiple access communication systems," *IEEE Vehicular Technology Magazine*, vol. 14, no. 1, pp. 89–97, 2019.

[30] J. Li, M. Matthaiou, and T. Svensson, "I/Q imbalance in two-way AF relaying," *IEEE Transactions on Communications*, vol. 62, no. 7, pp. 2271–2285, 2014.

[31] B. Selim, S. Muhaidat, P. C. Sofotasios et al., "Performance analysis of nonorthogonal multiple access under I/Q imbalance," *IEEE Access*, vol. 6, pp. 18453–18468, 2018.

[32] J. Li, M. Matthaiou, and T. Svensson, "I/Q imbalance in AF dual-hop relaying: performance analysis in Nakagami-*m* fading," *IEEE Transactions on Communications*, vol. 62, no. 3, pp. 836–847, 2014.

[33] X. Li, M. Liu, C. Deng, P. T. Mathiopoulos, Z. Ding, and Y. Liu, "Fullduplex cooperative NOMA relaying systems with I/Q imbalance and imperfect SIC," *IEEE Wireless Communications Letters*, vol. 9, no. 1, pp. 17–20, 2020.

[34] X. Li, Q. Wang, H. Peng et al., "A unified framework for HS-UAV NOMA networks: performance analysis and location optimization," *IEEE Access*, vol. 8, pp. 13329–13340, 2020.

[35] M. Chraiti, A. Ghrayeb, and C. Assi, "A NOMA scheme for a two-user MISO downlink channel with unknown CSIT," *IEEE Transactions on Wireless Communications*, vol. 17, no. 10, pp. 6775–6789, 2018.

[36] X. Li, J. Li, Y. Liu, Z. Ding, and A. Nallanathan, "Residual transceiver hardware impairments on cooperative NOMA networks," *IEEE Transactions on Wireless Communications*, vol. 19, no. 1, pp. 680–695, 2020.

[37] H. Haci, H. Zhu, and J. Wang, "Performance of non-orthogonal multiple access with a novel asynchronous interference cancellation technique," *IEEE Transactions on Communications*, vol. 65, no. 3, pp. 1319–1335, 2017.

[38] X. Yue, Y. Liu, S. Kang, and A. Nallanathan, "Performance analysis of NOMA with fixed gain relaying over Nakagami-*m* fading channels," *IEEE Access*, vol. 5, pp. 5445–5454, 2017.

[39] J. Men, J. Ge, and C. Zhang, "Performance analysis for downlink relaying aided non-orthogonal multiple access networks with imperfect CSI over Nakagami-*m* fading," *IEEE Access*, vol. 5, pp. 998–1004, 2017.

[40] X. Li, M. Liu, D. Deng, J. Li, C. Deng, and Q. Yu, "Power beacon assisted wireless power cooperative relaying using Noma with hardware impairments and imperfect CSI," *AEU - International Journal of Electronics and Communications*, vol. 108, pp. 275–286, 2019.

[41] X. Li, J. Li, and L. Li, "Smart home monitoring system via footstep-induced vibrations," *IEEE Systems Journal*, vol. 2019, pp. 1–7, 2019.

[42] Z. Zhou, C. Gao, C. Xu, T. Chen, D. Zhang, and S. Mumtaz, "Energy efficient stable matching for resource allocation in energy harvesting based device-to-device communications," *IEEE Access*, vol. 5, pp. 15184–15196, 2017.

[43] P. A. Anghel and M. Kaveh, "Exact symbol error probability of a cooperative network in a rayleigh-fading environment," *IEEE Transactions on Wireless Communications*, vol. 3, no. 5, pp. 1416–1421, 2004.

WILEY | Hindawi

Research Article

Adaptive Double-Threshold Cooperative Spectrum Sensing Algorithm Based on History Energy Detection

Shanshan Yu [iD],[1] **Ju Liu** [iD],[1] **Jing Wang,**[1] **and Inam Ullah** [iD][2]

[1]*School of Information Science and Engineering, Shandong University, Qingdao, China*
[2]*College of Internet of Things Engineering, Hohai University, Changzhou, China*

Correspondence should be addressed to Ju Liu; juliu@sdu.edu.cn

Spectrum sensing is one of the key technologies in the field of cognitive radio, which has been widely studied. Among all the sensing methods, energy detection is the most popular because of its simplicity and no requirement of any prior knowledge of the signal. In the case of low signal-to-noise ratio (SNR), the traditional double-threshold energy detection method employs fixed thresholds and there is no detection result when the energy is between high and low thresholds, which leads to poor detection performance such as lower detection probability and longer spectrum sensing time. To address these problems, we proposed an adaptive double-threshold cooperative spectrum sensing algorithm based on history energy detection. In each sensing period, we calculate the weighting coefficient of thresholds according to the SNR of all cognitive nodes; thus, the upper and lower thresholds can be adjusted adaptively. Furthermore, in a single cognitive node, once the current energy is within the high and low thresholds, we utilize the average energy of history sensing times to rejudge. To ensure the real-time performance, if the average history energy is still between two thresholds, the single-threshold method will be used for the end decision. Finally, the fusion center aggregates the detection results of each node and obtains the final cooperative conclusion through "or" criteria. Theoretical analysis and simulation results show that the algorithm proposed in this paper improved detection performance significantly compared with the other four different double-threshold algorithms.

1. Introduction

With the popularization of mobile Internet and the Internet of things, the demand for spectrum resources increases dramatically. The spectrum fragmentation and existing fixed allocation strategies result in low utilization of available spectrum resources [1]. Therefore, a new communication paradigm is required to exploit the available wireless spectrum opportunistically. The cognitive radio technology is an effective solution to improve the utilization of spectrum resources, and the spectrum sensing is the core technology of cognitive radio [2]. In the cognitive radio network, the second user (SU) actively detects whether a primary user (PU) exists in the licensed spectrum; if a PU does not exist in a specific frequency band, then the SU can utilize these spectrum holes. As long as a PU appears, the SU should free up the spectrum immediately to reduce the interference to the PU. Therefore, the spectrum sensing algorithm should

be reliable and fast [3]. Among the common spectrum sensing techniques, energy detection is widely used due to its flexibility and low complexity. It is a blind detection method that belongs to noncoherent detection of signals with the advantage that the detection process does not acquire the prior information of the signal, and there is no limitation on the signal type [4]. Nevertheless, its performance is easily affected by the uncertainty of the noise power. In the case of relatively low SNR, when the difference between noise and signal energy is not distinct, single-threshold detection methods are easy to cause SUs to perceive the existence of a PU incorrectly, which will reduce the detection probability of the entire system. There are some methods [5, 6] that optimized the single threshold and history-based method as [7] named three-event ED (3EED), which decides in one sensing event, considering also the event immediately before and the one immediately after it, which all lead to improving the energy detection performance-based single threshold.

Furthermore, to overcome the weakness of single-threshold detection, a lot of double-threshold detection schemes [8–19] are proposed to improve the performance of the system to a certain extent. Nowadays, many new methods are continuously proposed for energy detection in spectrum sensing. For example, in [20, 21], a triple-threshold energy detection method is proposed to improve the spectrum sensing efficiency as well as addressing the small-scale primary users which are unreliable in cognitive radio systems. Under the framework of random matrix theory, Zhao et al. [22] firstly proposed two enhanced detection algorithms based on the maximum eigenvalue and energy of the signal to achieve performance improvement. In [23], a dynamic matching-based spectrum detection scheme is proposed, which can detect sensing data, reduce the impact of malicious data, and make final sensing results more accurate with dynamic threshold setting and data matching, especially in the mobile scenario. Utilizing kennel function-based support vector machine (SVM), a spectrum mapping scheme is proposed in [24] and a boundary CR user searching algorithm is adopted to improve the performance of this scheme. The machine learning methods are all utilized in [25, 26] to improve the spectrum sensing performance. Article [27] is aimed at improving CR spectrum sensing by utilizing techniques such as real-valued FFT, Sparse Fast Fourier Transform, and collaborative spectrum sensing. Similar works can be found in the domain of nonorthogonal multiple access for cooperative and noncooperative wireless networks [28–32].

1.1. Related Works.

In this paper, we focus on the double-threshold energy detection methods. The traditional double-threshold spectrum sensing method compares the energy value with two fixed decision thresholds. If the energy is greater than the higher threshold, it indicates that the PU exists. If it is less than the lower threshold, it is determined that the PU does not exist. And if it is within the high and low thresholds, the decision is not made temporarily. A weighted-cooperative double-threshold spectrum sensing scheme and two adaptive double-threshold energy methods are proposed in [10–12], respectively, to improve the performance of energy detection. However, the double-threshold methods mentioned above are all no-decision when the energy is between the high and low thresholds. To address this problem, a memory-based energy detection method is presented in [13] by using memory sticks to improve the performance with the cost of delay in secondary devices' communication. Moreover, in [14–16], the correlation coefficient of received signals, the two-state Markov chain model, and the historical sensing data are employed, respectively, to determine a result in case the energy lies between the two thresholds. In [17], when the energy is between two thresholds, the result of the previous sensing time is used as the result of this time, and if there is also no result in the previous time, then wait for the result of the next sensing time to update the current time until generating a result. Considering the cooperation of multiple SUs, in [18], the fusion center receives relevant information of all nodes and makes a global decision based on "OR" rules. Cooperative spectrum sensing along with a double-threshold detection method is also proposed in [19], which utilized the history test statistic to compare with the high and low thresholds. If the test statistic is still within two thresholds, then increase the number of history energy to compare again until a result can be generated. It deserves to be mentioned that not all history-based methods can cope with this problem.

To sum up, the threshold value of many double-threshold detection algorithms is fixed and inflexible, and there is usually no decision when the detected energy is between the upper and lower thresholds. Moreover, methods based on historical energy information often have higher complexity and poor real-time performance. According to the above shortcomings, we propose an adaptive double-threshold cooperative spectrum sensing algorithm based on history energy detection.

1.2. Main Contributions.

The main contributions of this paper are as follows:

(1) We proposed an adaptive double-threshold cooperative spectrum sensing algorithm based on history energy detection, which excellent performance is verified by simulation especially in the case of low SNR

(2) Based on the traditional double-threshold detection, plus in the weighted coefficient obtaining from SNR values of SUs, the two decision thresholds are adjusted adaptively to improve the performance of energy detection

(3) To ensure the real-time performance, utilizing the average energy of history sensing times to complete subsequent judgment when the detected energy is between the high and the low threshold, and if the average history energy is still between two thresholds, the single-threshold method will be utilized as the end decision to guarantee that there will be at most only two rounds of detection, thereby enhancing the low complexity

(4) We derivated the exact closed-form expressions of the detection probability, the false alarm probability, and the missed detection probability base on the proposed scheme, respectively

The remainder of the paper is organized as follows. In Section 2, we briefly review the principle of energy detection and describe the traditional double-threshold method in the AWGN model. Moreover, the cooperative spectrum sensing method applied in this paper is introduced. In Section 3, we propose a novel adaptive double-threshold cooperative spectrum sensing algorithm based on history energy detection and present the scheme in detail. In Section 4, we derive the exact closed-form expressions of the detection probability, the false alarm probability, and the missed detection probability in our proposed scheme. In Section 5, the performances of the proposed method are shown with the
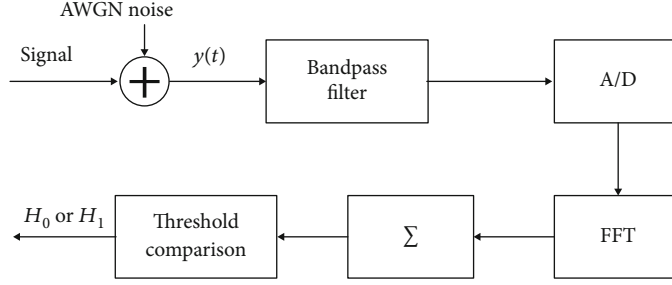
FIGURE 1: System model.

simulation and analysis. Finally, the conclusion of this paper is given in Section 6.

2. System Model

2.1. Principle of Energy Detection. The principle of energy detection technology is to determine whether a signal exists based on the power of the received signal. The specific method is to sum the energy of the signal after a series of changes in a certain range to obtain the power of the signal and then compare the obtained power value with the decision threshold to determine whether there is a user.

At present, although energy detection through the frequency domain will add additional calculation time due to FFT, nowadays FFT is widely used, its overhead on the detection time can be ignored, and it does not need to provide corresponding detection channels for each high-performance filter, so the implementation is more flexible, and it is more widely used in energy detection algorithms. The schematic diagram of energy detection based on the frequency domain is shown in Figure 1.

The radio frequency signal enters the receiving end of the energy detection, and after filtering, A/D conversion, and FFT conversion, the square sum is determined as the decision statistics and then sent to the threshold mechanism for judgment.

The energy detection algorithm establishes a model based on the statistical value of the signal energy received by the cognitive user, which can be represented by

$$Y(n) = \begin{cases} \omega(n), & \mathscr{H}_0, \\ s(n) + \omega(n), & \mathscr{H}_1, \end{cases} \tag{1}$$

where $s(n)$ is the PU signal, $\omega(n)$ is the channel noise, $Y(n)$ is the signal received by the cognitive node, $\mathscr{H}_0$ indicates that the channel is idle, and $\mathscr{H}_1$ indicates that the channel is occupied by the PU. Then, the energy statistics value E can be expressed as

$$E = \frac{1}{N} \sum_{i=1}^{n} [Y(n)]^2, \tag{2}$$

where N presents the number of detection sampling points.

2.2. Traditional Double-Threshold Energy Detection Method. The basic idea of the double-threshold energy detection

method is to make a decision by comparing the statistical energy value of the sampled signal with the decision threshold value, assuming λ_H and λ_L as the high and low decision thresholds, respectively. The decision rules are as follows:

$$\begin{cases} \mathscr{H}_0, & E \le \lambda_L, \\ \mathscr{H}_1, & E \ge \lambda_H, \\ \text{No decison,} & \text{else.} \end{cases} \tag{3}$$

Assuming that the channel environment is AWGN, when the number of sampling points is large, the energy statistics can approximately obey the Gaussian distribution [33] shown in

$$\begin{cases} \mathscr{H}_0 : E \sim \mathscr{N}\left(N\sigma_\omega^2, 2N\sigma_\omega^4\right), \\ \mathscr{H}_1 : E \sim \mathscr{N}\left(N\left(\sigma_s^2 + \sigma_\omega^2\right), 2N\left(\sigma_s^2 + \sigma_\omega^2\right)^2\right), \end{cases} \tag{4}$$

where σ_ω^2 is the noise variance and σ_s^2 is the average power of the main user signal, and the corresponding detection probability $\mathscr{P}_d$, the false alarm probability $\mathscr{P}_f$, and the missed detection probability $\mathscr{P}_m$ can be obtained from equation (4), respectively:

$$\mathscr{P}_d = \mathscr{P}\{E > \lambda_H | \mathscr{H}_1\} = Q\left(\frac{\lambda_H - N\left(\sigma_s^2 + \sigma_\omega^2\right)}{\sqrt{2N}\left(\sigma_s^2 + \sigma_\omega^2\right)}\right), \tag{5}$$

$$\mathscr{P}_f = \mathscr{P}\{E > \lambda_H | \mathscr{H}_0\} = Q\left(\frac{\lambda_H - N\sigma_\omega^2}{\sqrt{2N}\sigma_\omega^2}\right), \tag{6}$$

$$\mathscr{P}_m = \mathscr{P}\{E < \lambda_L | \mathscr{H}_1\} = 1 - Q\left(\frac{\lambda_L - N\left(\sigma_s^2 + \sigma_\omega^2\right)}{\sqrt{2N}\left(\sigma_s^2 + \sigma_\omega^2\right)}\right). \tag{7}$$

In formulas (5), (6), and (7), Q is the standard Gauss complementary cumulative distribution function. The detection probability $\mathscr{P}_d$ is the probability of correct decision when a PU exists, i.e., the state $\mathscr{H}_1$. And the false alarm probability $\mathscr{P}_f$ is the probability of determining PU existence when the channel is idle actually, i.e., the state $\mathscr{H}_0$ when the channel is idle, while the missed probability $\mathscr{P}_m$ is the probability of wrong decision when a PU exists, i.e., the state $\mathscr{H}_1$.

In the case of low SNR, when the false alarm probability $\mathscr{P}_f$ and the missed detection probability $\mathscr{P}_m$ are determined, from (6) and (7), the double threshold can be expressed in the following form:

$$\lambda_H = \left[\sqrt{2N} Q^{-1}(\mathscr{P}_f) + N \right] \sigma_\omega^2, \tag{8}$$

$$\lambda_L = \left[N - \sqrt{2N} Q^{-1}(\mathscr{P}_m) \right] (\sigma_s^2 + \sigma_\omega^2). \tag{9}$$

2.3. Cooperative Spectrum Sensing. In the actual communication environment, factors such as multipath fading and shadowing of buildings are inevitable, which will lead to a high probability of misjudgment of the licensed frequency band in a specific area for a single node. In this case, utilizing cooperative spectrum sensing technology can minimize the effects of multipath and shadow fading, thereby improving the detection performance of the algorithm. The centralized cooperative network coordinates the information of cognitive users through a control center, which is called a fusion center. First, each cognitive user employs the single-node spectrum sensing method to perform local spectrum sensing and then sends the results to the fusion center. Finally, the fusion center analyzes the aggregated information and makes a decision based on certain judgment criteria to complete a spectrum sensing process.

Different from the distributed cooperative scheme, which requires users to communicate with each other, the centralized cooperative scheme mainly utilizes the fusion center to make decisions, and each cognitive user is independent of each other. For the entire system, adding a new cognitive user requires only adding one communication link from the user to the fusion center, which is more flexible and simple. Therefore, the centralized cooperative scheme is the most suitable for cooperative spectrum sensing. Furthermore, the quality of its decision result is closely related to the fusion algorithm of the fusion center. But this is not the focus of this study. We employ a simple "or" criterion for multiuser cooperation in the fusion center, that is, the fusion center performs an "or" operation on all the received decision results from SUs. As long as the cognitive result of a cognitive SU is 1, the channel is determined to be occupied. Only when all the sensing results are 0, the fusion center determines the channel is idle and available.

3. Proposed Energy Detection Algorithm

The traditional double-threshold detection algorithm can solve the problem that the single-threshold detection algorithm is easily affected by noise and also can reduce the false alarm probability and the missed alarm probability. However, when the energy value is between the high and low thresholds, this sensing time is invalid, and the existence of the PU cannot be determined. Many methods improve the detection accuracy by optimizing the high and low thresholds, such as weighted double-threshold methods and adaptive double-threshold methods, but the case of no decision result during one sensing period still exists. To solve this problem, another type of method performs spectrum sensing

multiple times until a decision can be made, which can make every sensing period have a decision. However, these methods increase the length of one spectrum sensing period, which further reduces the opportunity for SU to access idle frequency bands.

In this case, we proposed a new spectrum sensing algorithm based on historical energy to solve the problem that there is no detection result when the energy statistic value is in the middle threshold. At the same time, our scheme can reduce detection time relatively and improve detection accuracy effectively by adjusting the double-threshold adaptively.

Figure 2 is the proposed algorithm detection flowchart of a single node at one sensing period. Considering the energy of the signal will not change too much in a short period, we calculate the average energy value in the recent limited sensing periods as the history energy. So we set a queue with the length of M to save the history energy of past M sensing periods. In one sensing period at the single cognitive node, if the current energy is between the double thresholds, we will calculate the average energy of past M sensing periods from the history queue to substitute the current energy value and start the second round detection. Furthermore, if the average energy is still between two thresholds, we will calculate the single threshold and make the final decision by comparing the average energy with it. Therefore, there would be a decision at every sensing period in our scheme.

The pseudocode for our proposed algorithm has been described in Algorithm 1. To eliminate the differences between cognitive SUs, it is assumed that the parameters of each cognitive node are the same within a certain period.

(1) According to formulas (8) and (9), the high and low threshold of single SU is calculated by the false alarm probability, the missed detection probability, the variance of noise, and the received signal. At this time, the decision threshold of each user is the same. Next, each cognitive SU sends the SNR value of the received signal to the fusion center to calculate the weight factor of each user, as shown in formula (10):

$$\xi_i = \frac{\text{SNR}_i}{1/L \sum_{i=1}^{L} \text{SNR}_i}, \tag{10}$$

where ξ_i is the weight factor of the i-th cognitive user, L is the number of cognitive SUs, and SNR_i is the signal-to-noise ratio of each cognitive user's received signal. Thus, every cognitive SU can adaptively adjust their own decision threshold through the weight factor calculated by formula (10) to improve the credibility, namely,

$$\lambda_{L_i} = \frac{\lambda_L}{\xi_i}, \tag{11}$$

$$\lambda_{H_i} = \frac{\lambda_H}{\xi_i} \tag{12}$$
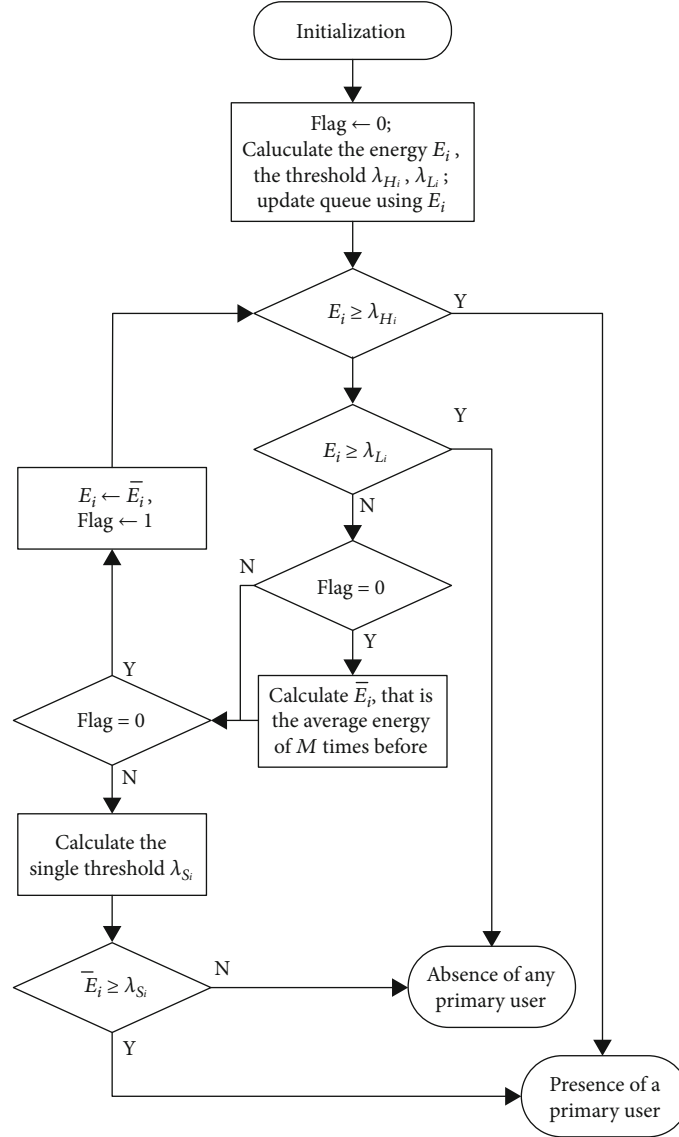
FIGURE 2: Flow chart of energy detection algorithm.

(2) Each cognitive SU obtains the energy statistical value E through formula (2) and updates the history energy queue simultaneously. Then, the SU compares the current energy E with its decision threshold. If it is higher than λ_{H_i}, it is determined that there is a primary user. And if it is lower than λ_{L_i}, it is determined that the channel is idle. In case it is between λ_{L_i} and λ_{H_i}, the average value of the history energy queue is taken as the current energy and start the next round of detection. Meanwhile, the "Flag" is set to 1, it means the first round of detection is over

(3) Next, in the second round, which is identified by the value of "Flag" being equal to 1, if the average history energy is also between λ_{L_i} and λ_{H_i}, then calculate the single threshold λ_{S_i}, which is used to

compare with the average energy to make the final decision

(4) At last, each cognitive SU sends its own decision result to the fusion center which would use the "or" criterion to make the final decision, that is, as long as one cognitive node detects a signal, it is determined that there is a PU. Therefore, we can get the detection probability $\mathscr{P}_d$ and false alarm probability $\mathscr{P}_f$ as follows:

$$\mathscr{P}_d = 1 - \prod_{i=1}^{L} (1 - \mathscr{P}_{di}), \qquad (13)$$

$$\mathscr{P}_f = 1 - \prod_{i=1}^{L} (1 - \mathscr{P}_{fi}), \qquad (14)$$

Input: $\mathscr{P}_f$, *Queue*, $\mathscr{P}_f$
Output: $R_i \in \{\mathscr{H}_0, \mathscr{H}_1\}$
1: **procedure** SINGLE NODE ENERGY DETECTION
2:     *Flag* ⟵ 0
3:     Calculate $E_i, \lambda_{H_i}, \lambda_{L_i}$
4:     *Queue* (*M*) ⟵ E_i
5: *top*:
6:     **if** $E_i \geq \lambda_{H_i}$ **then**
7:         $R_i \longleftarrow \mathscr{H}_1$
8:     **else**
9:         **if** $E_i \leq \lambda_{L_i}$ **then**
10:            $R_i \longleftarrow \mathscr{H}_0$
11:        **else**
12:            **if** *Flag* = 0 **then**
13:                Calculate $\bar{E}_i$
14:            **end if**
15:            **if** *Flag* = 0 **then**
16:                *Flag* ⟵ 1, $E_i \longleftarrow \bar{E}_i$
17:                **goto** *top*
18:            **else**
19:                Calculate λ_{S_i}
20:                **if** $\bar{E}_i \geq \lambda_{S_i}$ **then**
21:                    $R_i \longleftarrow \mathscr{H}_1$
22:                **else**
23:                    $R_i \longleftarrow \mathscr{H}_0$
24:                **end if**
25:            **end if**
26:        **end if**
27:    **end if**
28:    **return** R_i
29: **end procedure**

ALGORITHM 1: Adaptive double-threshold spectrum sensing algorithm of single node *i* based on history energy detection.

where $\mathscr{P}_{di}$ and $\mathscr{P}_{fi}$ is the detection probability and false alarm probability of the *i*-th cognitive SU, respectively

4. Theory Performance of the Algorithm

In this section, we derive the probability of detection, false alarm, and missed detection in the proposed algorithm, respectively.

According to the flow description in Section 3, there are three situations to determine the existence of the primary user:

(1) The current energy value is greater than λ_{H_i} in the first round of detection procedure

(2) When the current energy in the first round is between λ_{L_i} and λ_{H_i}, the average history energy calculated in the second round exceeds the upper threshold

(3) When the current energy of the first round and the average history energy of the second round are both within λ_{L_i} and λ_{H_i}, the average history energy is greater than the calculated single threshold λ_{S_i}

Hence, the detection alarm probability of single node is given by

$$
\begin{aligned}
\mathscr{P}_{di} = {} & P\{E_i \geq \lambda_{H_i}|H_1\} + P\{\lambda_{Li} < E_i < \lambda_{Hi}|H_1\} \\
& * \left(P\{\bar{E}_i \geq \lambda_{Hi}|H_1\} + P\{\lambda_{Li} < \bar{E}_i < \lambda_{Hi}|H_1\}\right) \\
& * P\{\bar{E}_i \geq \lambda_{Si}|H_1\}),
\end{aligned}
\tag{15}
$$

where λ_{Si} is the single threshold, which can be expressed as

$$
\lambda_{Si} = \left[\sqrt{2N}Q^{-1}(\mathscr{P}_f) + N\right]\sigma_\omega^2.
\tag{16}
$$

Then, every part of formula (15) is derivated as follows. From (6), we can get

$$
\mathscr{P}\{E_i \geq \lambda_{Hi}|\mathscr{H}_1\} = Q\left(\frac{\lambda_{Hi} - N\left(\sigma_{s_i}^2 + \sigma_{\omega_i}^2\right)}{\sqrt{2N}\left(\sigma_{s_i}^2 + \sigma_{\omega_i}^2\right)}\right),
\tag{17}
$$

$$
\mathscr{P}\{E_i \geq \lambda_{Li}|\mathscr{H}_1\} = Q\left(\frac{\lambda_{Li} - N\left(\sigma_{s_i}^2 + \sigma_{\omega_i}^2\right)}{\sqrt{2N}\left(\sigma_{s_i}^2 + \sigma_{\omega_i}^2\right)}\right),
\tag{18}
$$

$$
\begin{aligned}
\mathscr{P}\{\lambda_{Li} < E_i < \lambda_{Hi}|\mathscr{H}_1\} = {} & 1 - \mathscr{P}\{E_i \geq \lambda_{Hi}|\mathscr{H}_1\} \\
& - \mathscr{P}\{E_i < \lambda_{Li}|\mathscr{H}_1\} \\
= {} & 1 - \mathscr{P}\{E_i \geq \lambda_{Hi}|\mathscr{H}_1\} \\
& - (1 - \mathscr{P}\{E_i \geq \lambda_{Li}|\mathscr{H}_1\}) \\
= {} & Q\left(\frac{\lambda_{Li} - N\left(\sigma_{s_i}^2 + \sigma_{\omega_i}^2\right)}{\sqrt{2N}\left(\sigma_{s_i}^2 + \sigma_{\omega_i}^2\right)}\right) \\
& - Q\left(\frac{\lambda_{Hi} - N\left(\sigma_{s_i}^2 + \sigma_{\omega_i}^2\right)}{\sqrt{2N}\left(\sigma_{s_i}^2 + \sigma_{\omega_i}^2\right)}\right).
\end{aligned}
\tag{19}
$$

Similar to (4), according to the properties of the Gaussian distribution, once the number of sampling points is sufficient, the mean value of the past *M* sensing history energy also obeys the Gaussian distribution, which is expressed exactly as follows:

$$
\begin{cases}
\mathscr{H}_0 : \bar{E} \sim \mathscr{N}\left(\frac{N}{M}\sum_{j=0}^{M-1}\sigma_{\omega_j}^2, \left(\frac{\sqrt{2N}}{M}\sum_{j=0}^{M-1}\sigma_{\omega_j}^2\right)^2\right), \\
\mathscr{H}_1 : \bar{E} \sim \mathscr{N}\left(\frac{N}{M}\sum_{j=0}^{M-1}\left(\sigma_{s_j}^2 + \sigma_{\omega_j}^2\right), \left(\frac{\sqrt{2N}}{M}\sum_{j=0}^{M-1}\left(\sigma_{s_j}^2 + \sigma_{\omega_j}^2\right)\right)^2\right).
\end{cases}
\tag{20}
$$

Then, we can get the remaining part of (15):

$$
\mathscr{P}\{\bar{E}_i \geq \lambda_{Hi}|\mathscr{H}_1\} = Q\left(\frac{\lambda_{Hi} - (N/M)\sum_{j=0}^{M-1}\left(\sigma_{s_{ij}}^2 + \sigma_{\omega_{ij}}^2\right)}{\left(\sqrt{2N}/M\right)\sum_{j=0}^{M-1}\left(\sigma_{s_{ij}}^2 + \sigma_{\omega_{ij}}^2\right)}\right),
\tag{21}
$$

$$\mathscr{P}\{\bar{E}_i \geq \lambda_{Li} | \mathscr{H}_1\} = Q\left(\frac{\lambda_{Li} - (N/M)\sum_{j=0}^{M-1}\left(\sigma_{s_{ij}}^2 + \sigma_{\omega_{ij}}^2\right)}{\left(\sqrt{2N}/M\right)\sum_{j=0}^{M-1}\left(\sigma_{s_{ij}}^2 + \sigma_{\omega_{ij}}^2\right)}\right), \tag{22}$$

$$\begin{aligned}
\mathscr{P}\{\lambda_{Li} < \bar{E}_i < \lambda_{Hi} | \mathscr{H}_1\} &= 1 - \mathscr{P}\{\bar{E}_i \geq \lambda_{Hi} | \mathscr{H}_1\} \\
&\quad - \mathscr{P}\{\bar{E}_i < \lambda_{Li} | \mathscr{H}_1\} \\
&= 1 - \mathscr{P}\{\bar{E}_i \geq \lambda_{Hi} | \mathscr{H}_1\} \\
&\quad - (1 - \mathscr{P}\{\bar{E}_i \geq \lambda_{Li} | \mathscr{H}_1\}) \\
&= Q\left(\frac{\lambda_{Li} - (N/M)\sum_{j=0}^{M-1}\left(\sigma_{s_{ij}}^2 + \sigma_{\omega_{ij}}^2\right)}{\left(\sqrt{2N}/M\right)\sum_{j=0}^{M-1}\left(\sigma_{s_{ij}}^2 + \sigma_{\omega_{ij}}^2\right)}\right) \\
&\quad - Q\left(\frac{\lambda_{Hi} - (N/M)\sum_{j=0}^{M-1}\left(\sigma_{s_{ij}}^2 + \sigma_{\omega_{ij}}^2\right)}{\left(\sqrt{2N}/M\right)\sum_{j=0}^{M-1}\left(\sigma_{s_{ij}}^2 + \sigma_{\omega_{ij}}^2\right)}\right),
\end{aligned} \tag{23}$$

$$\mathscr{P}\{\bar{E}_i \geq \lambda_{Si} | \mathscr{H}_1\} = Q\left(\frac{\lambda_{Si} - (N/M)\sum_{j=0}^{M-1}\left(\sigma_{s_{ij}}^2 + \sigma_{\omega_{ij}}^2\right)}{\left(\sqrt{2N}/M\right)\sum_{j=0}^{M-1}\left(\sigma_{s_{ij}}^2 + \sigma_{\omega_{ij}}^2\right)}\right). \tag{24}$$

Substituting equations (16), (18), (20), (22), and (23) into equation (14), the detailed expression for the detection probability is shown in

$$\begin{aligned}
\mathscr{P}_{di} &= Q\left(\frac{\lambda_{Hi} - N\left(\sigma_{s_i}^2 + \sigma_{\omega_i}^2\right)}{\sqrt{2N}\left(\sigma_{s_i}^2 + \sigma_{\omega_i}^2\right)}\right) \\
&\quad + \left[Q\left(\frac{\lambda_{Li} - N\left(\sigma_{s_i}^2 + \sigma_{\omega_i}^2\right)}{\sqrt{2N}\left(\sigma_{s_i}^2 + \sigma_{\omega_i}^2\right)}\right) \right. \\
&\qquad \left. - Q\left(\frac{\lambda_{Hi} - N\left(\sigma_{s_i}^2 + \sigma_{\omega_i}^2\right)}{\sqrt{2N}\left(\sigma_{s_i}^2 + \sigma_{\omega_i}^2\right)}\right)\right] \\
&\quad * \left\{Q\left(\frac{\lambda_{Hi} - (N/M)\sum_{j=0}^{M-1}\left(\sigma_{s_{ij}}^2 + \sigma_{\omega_{ij}}^2\right)}{\left(\sqrt{2N}/M\right)\sum_{j=0}^{M-1}\left(\sigma_{s_{ij}}^2 + \sigma_{\omega_{ij}}^2\right)}\right) \right. \\
&\qquad + \left[Q\left(\frac{\lambda_{Li} - (N/M)\sum_{j=0}^{M-1}\left(\sigma_{s_{ij}}^2 + \sigma_{\omega_{ij}}^2\right)}{\left(\sqrt{2N}/M\right)\sum_{j=0}^{M-1}\left(\sigma_{s_{ij}}^2 + \sigma_{\omega_{ij}}^2\right)}\right) \right. \\
&\qquad \quad \left. - Q\left(\frac{\lambda_{Hi} - (N/M)\sum_{j=0}^{M-1}\left(\sigma_{s_{ij}}^2 + \sigma_{\omega_{ij}}^2\right)}{\left(\sqrt{2N}/M\right)\sum_{j=0}^{M-1}\left(\sigma_{s_{ij}}^2 + \sigma_{\omega_{ij}}^2\right)}\right)\right] \\
&\qquad \left. * Q\left(\frac{\lambda_{Si} - (N/M)\sum_{j=0}^{M-1}\left(\sigma_{s_{ij}}^2 + \sigma_{\omega_{ij}}^2\right)}{\left(\sqrt{2N}/M\right)\sum_{j=0}^{M-1}\left(\sigma_{s_{ij}}^2 + \sigma_{\omega_{ij}}^2\right)}\right)\right\}.
\end{aligned} \tag{25}$$

In a similar way, the false alarm probability of the proposed algorithm is as follows:

$$\begin{aligned}
\mathscr{P}_{fi} &= P\{E_i \geq \lambda_{Hi} | H_0\} \\
&\quad + P\{\lambda_{Li} < E_i < \lambda_{Hi} | H_0\}\left(P\{\bar{E}_i \geq \lambda_{H_i} | H_0\} \right. \\
&\quad \left. + P\{\lambda_{Li} < \bar{E}_i < \lambda_{Hi} | H_0\} * P\{\bar{E}_i \geq \lambda_{Si} | H_0\}\right).
\end{aligned} \tag{26}$$

Then, every part of formula (26) is derivated as follows. From (6), we can get

$$\mathscr{P}\{E_i \geq \lambda_{Hi} | \mathscr{H}_0\} = Q\left(\frac{\lambda_{Hi} - N\sigma_{\omega_i}^2}{\sqrt{2N}\sigma_{\omega_i}^2}\right), \tag{27}$$

$$\mathscr{P}\{E_i \geq \lambda_{Li} | \mathscr{H}_0\} = Q\left(\frac{\lambda_{Li} - N\sigma_{\omega_i}^2}{\sqrt{2N}\sigma_{\omega_i}^2}\right), \tag{28}$$

$$\begin{aligned}
\mathscr{P}\{\lambda_{Li} < E_i < \lambda_{Hi} | \mathscr{H}_0\} \\
= 1 - \mathscr{P}\{E_i \geq \lambda_{Hi} | \mathscr{H}_0\} - \mathscr{P}\{E_i < \lambda_{Li} | \mathscr{H}_0\} \\
= 1 - \mathscr{P}\{E_i \geq \lambda_{Hi} | \mathscr{H}_0\} - (1 - \mathscr{P}\{E_i \geq \lambda_{Li} | \mathscr{H}_0\}) \\
= Q\left(\frac{\lambda_{Li} - N\sigma_{\omega_i}^2}{\sqrt{2N}\sigma_{\omega_i}^2}\right) - Q\left(\frac{\lambda_{Hi} - N\sigma_{\omega_i}^2}{\sqrt{2N}\sigma_{\omega_i}^2}\right),
\end{aligned} \tag{29}$$

$$\mathscr{P}\{\bar{E}_i \geq \lambda_{Hi} | \mathscr{H}_0\} = Q\left(\frac{\lambda_{Hi} - (N/M)\sum_{j=0}^{M-1}\sigma_{\omega_{ij}}^2}{\left(\sqrt{2N}/M\right)\sum_{j=0}^{M-1}\sigma_{\omega_{ij}}^2}\right), \tag{30}$$

$$\mathscr{P}\{\bar{E}_i \geq \lambda_{Li} | \mathscr{H}_0\} = Q\left(\frac{\lambda_{Li} - (N/M)\sum_{j=0}^{M-1}\sigma_{\omega_{ij}}^2}{\left(\sqrt{2N}/M\right)\sum_{j=0}^{M-1}\sigma_{\omega_{ij}}}\right), \tag{31}$$

$$\begin{aligned}
\mathscr{P}\{\lambda_{Li} < \bar{E}_i < \lambda_{Hi} | \mathscr{H}_0\} \\
= 1 - \mathscr{P}\{\bar{E}_i \geq \lambda_{Hi} | \mathscr{H}_0\} - \mathscr{P}\{\bar{E}_i < \lambda_{Li} | \mathscr{H}_0\} \\
= 1 - \mathscr{P}\{\bar{E}_i \geq \lambda_{Hi} | \mathscr{H}_0\} - (1 - \mathscr{P}\{\bar{E}_i \geq \lambda_{Li} | \mathscr{H}_0\}) \\
= Q\left(\frac{\lambda_{Li} - (N/M)\sum_{j=0}^{M-1}\sigma_{\omega_{ij}}^2}{\left(\sqrt{2N}/M\right)\sum_{j=0}^{M-1}\sigma_{\omega_{ij}}^2}\right) \\
- Q\left(\frac{\lambda_{Hi} - (N/M)\sum_{j=0}^{M-1}\sigma_{\omega_{ij}}^2}{\left(\sqrt{2N}/M\right)\sum_{j=0}^{M-1}\sigma_{\omega_{ij}}^2}\right),
\end{aligned} \tag{32}$$

$$\mathscr{P}\{\bar{E}_i \geq \lambda_{Si} | \mathscr{H}_0\} = Q\left(\frac{\lambda_{Si} - (N/M)\sum_{j=0}^{M-1}\sigma_{\omega_{ij}}^2}{\left(\sqrt{2N}/M\right)\sum_{j=0}^{M-1}\sigma_{\omega_{ij}}^2}\right). \tag{33}$$

Substituting equations (26), (28), (29), (31), and (32) into equation (26), the detailed expression for the detection probability is obtained in

$$
\begin{aligned}
\mathscr{P}_{fi} = {} & Q\left(\frac{\lambda_{Hi} - N\sigma_{\omega_i}^2}{\sqrt{2N}\sigma_{\omega_i}^2}\right) \\
& + \left[Q\left(\frac{\lambda_{Li} - N\sigma_{\omega_i}^2}{\sqrt{2N}\sigma_{\omega_i}^2}\right) - Q\left(\frac{\lambda_{Hi} - N\sigma_{\omega_i}^2}{\sqrt{2N}\sigma_{\omega_i}^2}\right)\right] \\
& * \left\{Q\left(\frac{\lambda_{Hi} - (N/M)\sum_{j=0}^{M-1}\sigma_{\omega_{ij}}^2}{\left(\sqrt{2N}/M\right)\sum_{j=0}^{M-1}\sigma_{\omega_{ij}}^2}\right)\right. \\
& + \left[Q\left(\frac{\lambda_{Li} - (N/M)\sum_{j=0}^{M-1}\sigma_{\omega_{ij}}^2}{\left(\sqrt{2N}/M\right)\sum_{j=0}^{M-1}\sigma_{\omega_{ij}}^2}\right) - Q\left(\frac{\lambda_{Hi} - (N/M)\sum_{j=0}^{M-1}\sigma_{\omega_{ij}}^2}{\left(\sqrt{2N}/M\right)\sum_{j=0}^{M-1}\sigma_{\omega_{ij}}^2}\right)\right] \\
& \left. * Q\left(\frac{\lambda_{Si} - (N/M)\sum_{j=0}^{M-1}\sigma_{\omega_{ij}}^2}{\left(\sqrt{2N}/M\right)\sum_{j=0}^{M-1}\sigma_{\omega_{ij}}^2}\right)\right\}.
\end{aligned}
\tag{34}
$$

Meanwhile, the missed detection probability can be calculated from the detection probability as

$$
\begin{aligned}
\mathscr{P}_{mi} = {} & P\{E_i < \lambda_{Li}|H_1\} + P\{\lambda_{Li} < E_i < \lambda_{Hi}|H_1\} \\
& * \left(P\{\bar{E}_i < \lambda_{L_i}|H_1\} + P\{\lambda_{Li} < \bar{E}_i < \lambda_{Hi}|H_1\}\right. \\
& \left. * P\{\bar{E}_i < \lambda_{Si}|H_1\}\right) \\
= {} & 1 - P\{E_i \geq \lambda_{Li}|H_1\} + P\{\lambda_{Li} < E_i < \lambda_{Hi}|H_1\} \\
& * \left[1 - P\{\bar{E}_i \geq \lambda_{L_i}|H_1\} + P\{\lambda_{Li} < \bar{E}_i < \lambda_{Hi}|H_1\}\right. \\
& \left. * \left(1 - P\{\bar{E}_i \geq \lambda_{Si}|H_1\}\right)\right].
\end{aligned}
\tag{35}
$$

Substituting equations (18), (19), (22), (23), and (24) into equation (26), the detailed expression for the missed detection probability is obtained in

$$
\begin{aligned}
\mathscr{P}_{mi} = {} & 1 - Q\left(\frac{\lambda_{Li} - N\left(\sigma_{\omega_s}^2 + \sigma_{\omega_i}^2\right)}{\sqrt{2N}\sigma_{\omega_i}^2}\right) \\
& + \left[Q\left(\frac{\lambda_{Li} - N\left(\sigma_{\omega_s}^2 + \sigma_{\omega_i}^2\right)}{\sqrt{2N}\left(\sigma_{\omega_s}^2 + \sigma_{\omega_i}^2\right)}\right) - Q\left(\frac{\lambda_{Hi} - N\left(\sigma_{\omega_s}^2 + \sigma_{\omega_i}^2\right)}{\sqrt{2N}\left(\sigma_{\omega_s}^2 + \sigma_{\omega_i}^2\right)}\right)\right] \\
& * \left\{1 - Q\left(\frac{\lambda_{Li} - (N/M)\sum_{j=0}^{M-1}\left(\sigma_{s_{ij}}^2 + \sigma_{\omega_{ij}}^2\right)}{\left(\sqrt{2N}/M\right)\sum_{j=0}^{M-1}\left(\sigma_{s_{ij}}^2 + \sigma_{\omega_{ij}}^2\right)}\right)\right. \\
& + \left[Q\left(\frac{\lambda_{Li} - (N/M)\sum_{j=0}^{M-1}\left(\sigma_{s_{ij}}^2 + \sigma_{\omega_{ij}}^2\right)}{\left(\sqrt{2N}/M\right)\sum_{j=0}^{M-1}\left(\sigma_{s_{ij}}^2 + \sigma_{\omega_{ij}}^2\right)}\right)\right. \\
& \left. - Q\left(\frac{\lambda_{Hi} - (N/M)\sum_{j=0}^{M-1}\left(\sigma_{s_{ij}}^2 + \sigma_{\omega_{ij}}^2\right)}{\left(\sqrt{2N}/M\right)\sum_{j=0}^{M-1}\left(\sigma_{s_{ij}}^2 + \sigma_{\omega_{ij}}^2\right)}\right)\right] \\
& \left. * \left[1 - Q\left(\frac{\lambda_{Si} - (N/M)\sum_{j=0}^{M-1}\sigma_{\omega_{ij}}^2}{\left(\sqrt{2N}/M\right)\sum_{j=0}^{M-1}\sigma_{\omega_{ij}}^2}\right)\right]\right\}.
\end{aligned}
\tag{36}
$$

5. Simulation Results

In this section, to evaluate the performance of the proposed history-based adaptive double-threshold energy detection algorithm (HBADT-ED), we present numerical results and compare with the traditional double-threshold energy detection algorithm (TDT-ED) in [10], the weighted double-threshold energy detection method (WDT-ED) modified from [11], the adaptive double-threshold energy detection scheme (ADT-ED) in [17], and the three consecutive time double-threshold energy detection method (TCTDT-ED) improved based on [7], respectively. On the basis of the original weighted coefficient of [11], the algorithm WDT-ED added the ratio of the current user SNR value to the average SNR value to increase the accuracy of the thresholds. And the TCTDT-ED scheme utilized the double threshold the same in TDT-ED to replace the single threshold in [7].

In the following simulations, we assume that the SNR range of the received signal is from -20 dB to 10 dB in the AWGN channel. The number of sampling $N = 150$, and the variance of noise σ_ω is set to be 1. We also assume that all the SUs use the "or" criterion to make the final decision in the fusion center and the number of SUs $L = 5$. In the proposed algorithm, we set the false alarm probability $\mathscr{P}_f = 0.05$ and the missed detection probability $\mathscr{P}_m = 0.01$. Moreover, the size of history energy queue $M = 5$ [34]. All the simulation results are obtained by averaging 10^5 Monte Carlo independent experiments in MATLAB.

First, we investigate the impact of different SNR conditions of the received signal on the detection probability P_d. It can be seen from Figure 3 that the proposed algorithm has the most obvious advantages than other methods. When the SNR grows to -9 dB, the detection probability of the proposed algorithm (HBADT-ED) in this paper is close to 1, while for the three consecutive time double-threshold energy detection method (TCTDT-ED) and the adaptive double-threshold energy detection scheme (ADT-ED), the SNR value is required to reach -7 dB and -5 dB, respectively, and for the traditional double-threshold algorithm (TDT-ED) and weighted double-threshold algorithm (WDT-ED), the SNR value needs to grow to 2 dB to keep the detection probability close to 1.

Among these methods, our proposed HBADT-ED scheme has the highest value of detection probability and the most slowly rising with increasing SNR value. Even when the SNR is low to -20 dB, the detection probability is very high. Although the double threshold is fixed in the TCTDT method, because the energy both before and after current sensing time is taken into account, it gets the second-best performance. The ADT-ED algorithm uses the average SNR value of all SUs to adjust the decision threshold of every user adaptively; it performs better than the WDT-ED and TDT-ED distinctly. The WDT-ED only improves the detection results according to the weight factors but does not deal with the decision threshold; therefore, as the SNR value increases, the advantage of the WDT-ED over the TDT-ED becomes smaller and smaller.

Figure 4 is a comparison of the detection probability of each algorithm with the number of cooperative detective
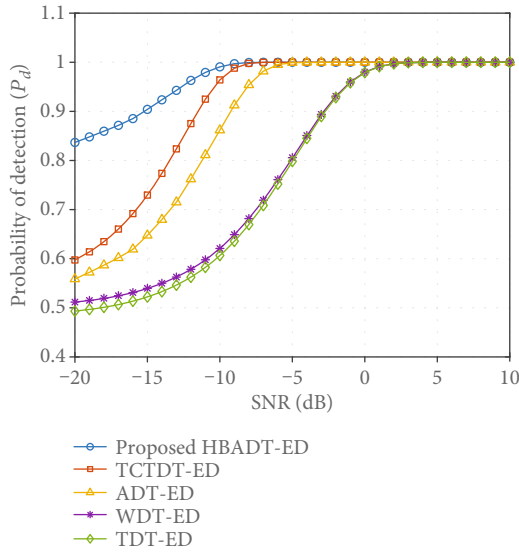
FIGURE 3: Probability of detection $(\mathscr{P}_d)$ vs. SNR (dB) for $L = 5$, $\mathscr{P}_f = 0.05$.
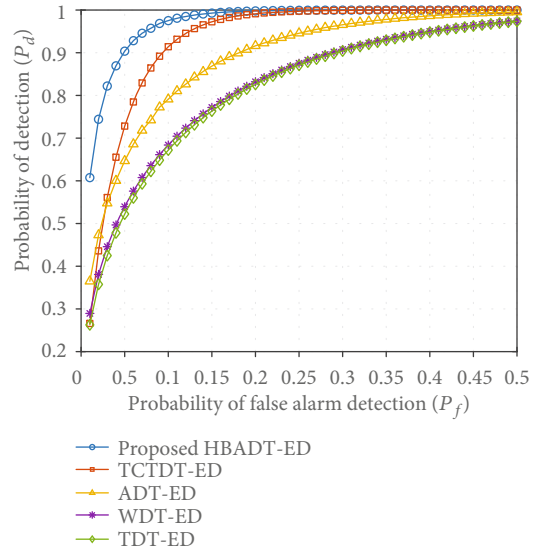
FIGURE 5: Probability of detection $(\mathscr{P}_d)$ vs. probability of false alarm detection $(\mathscr{P}_f)$ for SNR = -15 dB.
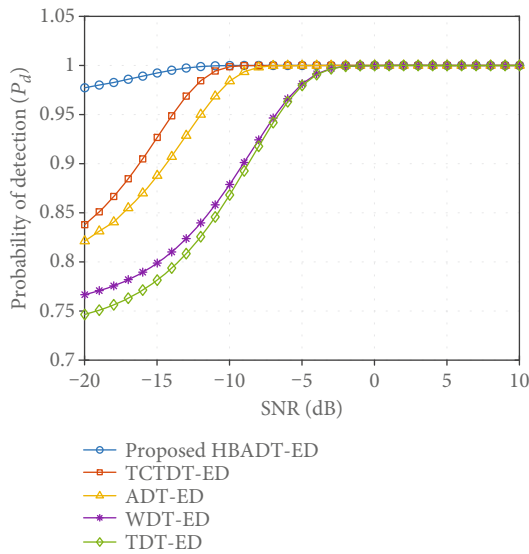
FIGURE 4: Probability of detection $(\mathscr{P}_d)$ vs. SNR (dB) for $L = 10$, $\mathscr{P}_f = 0.05$.
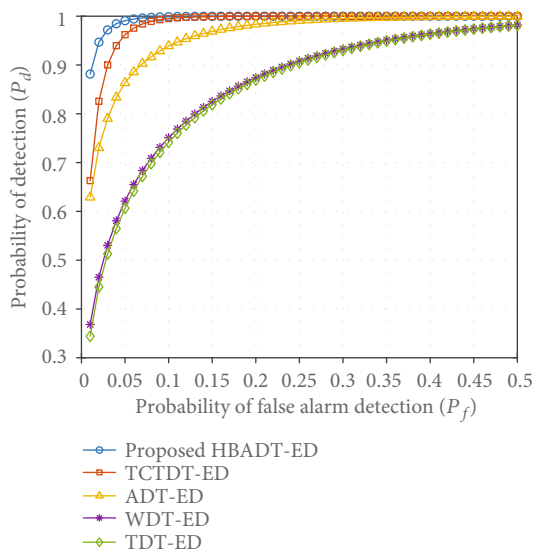
FIGURE 6: Probability of detection $(\mathscr{P}_d)$ vs. probability of false alarm detection $(\mathscr{P}_f)$ for SNR = -10 dB.

SUs changed to 10 under the same false alarm probability compared with Figure 3. Because the signal is affected by multipath effect and shadow fading in the actual transmission scenario, the SNR of each cognitive user must be different. Considering the "or" strategy adopted for the cooperative decision, using more cognitive nodes can effectively overcome the environmental impact and improve the detection performance of the system. As expected, the detection probabilities of all algorithms have been improved, and the overall performance comparison is consistent with Figure 3.

Figures 5 and 6 show the change of detection probabilities of five methods with false alarm probability under SNR $= -15$ dB and SNR $= -10$ dB, respectively. The higher the SNR is, the higher the detection probability is. When the

SNR is determined, the detection probability $\mathscr{P}_d$ goes up with the increase of false alarm probability. Moreover, under the same false alarm probability, the HBADT-ED algorithm proposed in this paper performs better than the other four methods, which can ensure a higher detection probability under the condition of lower false alarm probability. And the detection probability can approach 1 under a particularly small false alarm probability.

Figures 7 and 8 show the comparison of the number of cooperative nodes required as the detection probability of each algorithm is close to 1 when the SNR is -15 dB and -10 dB, respectively. Comparing Figures 7 and 8, it can be seen that the higher the SNR value, the fewer cognitive nodes required by the same algorithm. The algorithm HBADT-ED
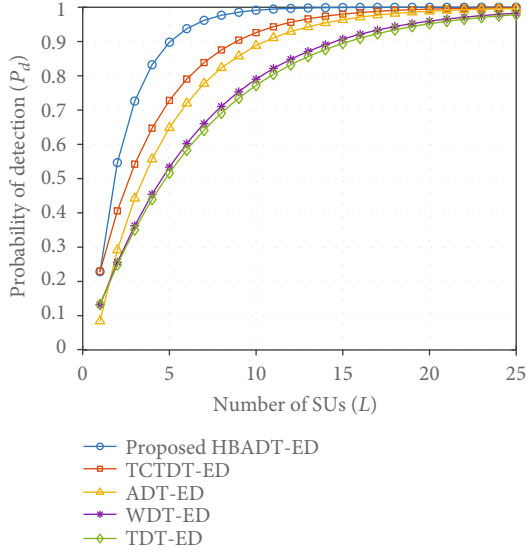
FIGURE 7: Probability of detection ($\mathscr{P}_d$) vs. the number of nodes (L) for SNR = −15 dB.
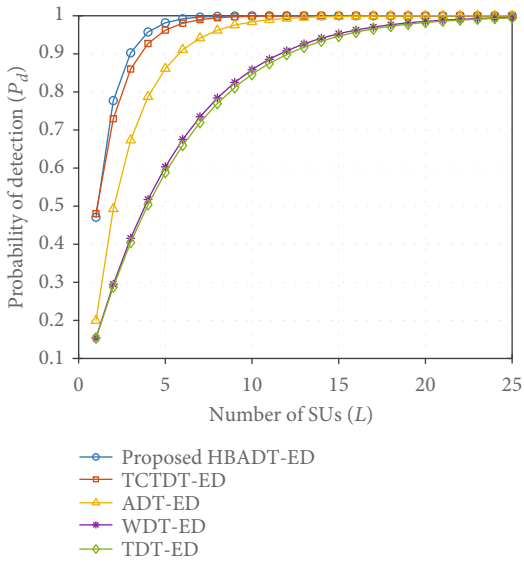
FIGURE 8: Probability of detection ($\mathscr{P}_d$) vs. the number of nodes (L) for SNR = −10 dB.

proposed in this paper only needs 11 (SNR = −15 dB) and 6 (SNR = −10 dB) cognitive nodes to make the detection probability close to 1. Moreover, the performance ranking of the five algorithms is consistent with the analysis from Figure 3. As a conclusion, the algorithm with good performance only needs fewer sensing nodes to achieve the expected detection probability, so the complexity of the system can be greatly simplified.

Furthermore, we observe the effect of the missed detection probability on the performance of the proposed algorithm. Figure 9 shows that no matter the value of SNR is, the probability of detection $\mathscr{P}_d$ always decreases with the increase of the missed detection probability$\mathscr{P}_m$. Meanwhile,
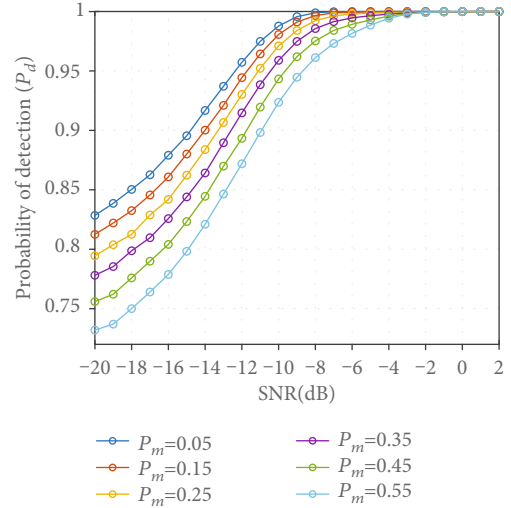
FIGURE 9: Probability of detection ($\mathscr{P}_d$) vs. SNR (dB) according to the different values of missed detection probability for $L = 5$, $\mathscr{P}_f = 0.05$, and $N = 150$ in the proposed HBADT-ED algorithm.

the decline degree of the detection probability becomes smaller and smaller with the increase of the SNR value gradually. For example, when $\mathscr{P}_m$ increases from 0.05 to 0.55, the value of $\mathscr{P}_d$ drops by 0.11 as SNR = −20 dB, while it decreases by 0.06 as SNR = −10 dB. Thus, we can conclude that the lower the value of SNR, the greater the effect on the performance by$\mathscr{P}_m$. We also find that at any $\mathscr{P}_m$ value, when the value of SNR is greater than -10db, the rise degree of $\mathscr{P}_d$ value decreases. This means when the SNR reach to a certain value, the effect on the performance by SNR will be a little decline. The reason is that when the SNR reaches a certain value, the probability of detection of each node will already be very close to 1, so even when the SNR increases continuously, the rise of the probability of detection will slow down.

At last, we also examine the impact of different sampling number N on the performance of the proposed algorithm. From Figure 10, it can be seen that no matter what is the value of SNR with the restraint, when the sampling number N grows up, the probability of detection $\mathscr{P}_d$ always increases except when it has already reached 1. Moreover, the improvement extent of the detection probability gets smaller and smaller with the growth of the SNR value. For example, when $ N $ increases from 100 to 500, the value of $\mathscr{P}_d$ is up by 0.17 under SNR = −20 dB and grows 0.6 under SNR = −10 dB. Therefore, it can be summarized that as the SNR is lower, the sampling number N would have a larger impact on the detection performance. Finally, the same reason as in Figure 9, at any fixed value of N, when the value of SNR reaches a certain value, the effect on the performance by SNR will be a little decline.

6. Conclusion

In this paper, based on history energy detection, an adaptive double-threshold energy detection cooperative spectrum sensing algorithm is proposed. The values of the double threshold are optimized adaptively according to
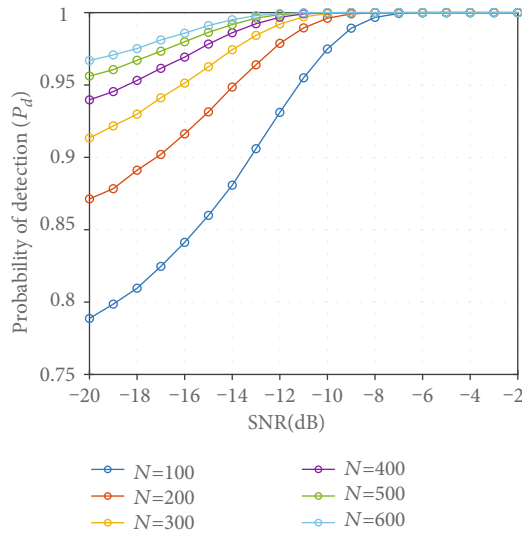
FIGURE 10: Probability of detection ($\mathscr{P}_d$) vs. SNR (dB) according to the different number of sampling for $L = 5$, $\mathscr{P}_f = 0.05$, and $\mathscr{P}_m = 0.01$ in the proposed HBADT-ED algorithm.

the weighting coefficient calculating by the SNR value of SUs. In the single cognitive node sensing process, when the detected energy is between the high and low thresholds, we utilize the average energy of history sensing times to complete subsequent judgment, which ensures that there must be an accurate decision in this situation of each sensing period. At last, the fusion center aggregates the detection results of each SU and obtains the final cooperative conclusion through the "or" criteria. In addition, we derive the exact closed-form expressions of the detection probability, the false alarm probability, and the missed detection probability base on the proposed scheme, respectively. Compared with the TDT-ED, WDT-ED, ADT-ED, and TCTDT-ED algorithms, the simulation result shows that the performance of the proposed HBADT-ED algorithm is the best especially in the case of low SNR. Moreover, the low complexity of the proposed algorithm ensured real-time performance simultaneously. In the future, we will pay more attention to the research of spectrum sensing methods under Rayleigh or other channel conditions which are closer to the actual situation.

Data Availability

No data were used to support this study.

Conflicts of Interest

The authors declare that there are no conflicts of interest regarding the publication of this paper.

Acknowledgments

References

[1] F. Hu, B. Chen, and K. Zhu, "Full spectrum sharing in cognitive radio networks toward 5G: a survey," *IEEE Access*, vol. 6, pp. 15754–15776, 2018.

[2] N. Zhao, F. R. Yu, H. Sun, and M. Li, "Adaptive power allocation schemes for spectrum sharing in interference-alignment-based cognitive radio networks," *IEEE Transactions on Vehicular Technology*, vol. 65, no. 5, pp. 3700–3714, 2016.

[3] A. Ali and W. Hamouda, "Advances on spectrum sensing for cognitive radio networks: theory and applications," *IEEE Communications Surveys & Tutorials*, vol. 19, no. 2, pp. 1277–1304, 2017.

[4] M. Amjad, M. H. Rehmani, and S. Mao, "Wireless multimedia cognitive radio networks: a comprehensive survey," *IEEE Communications Surveys & Tutorials*, vol. 20, no. 2, pp. 1056–1103, 2018.

[5] E. Chatziantoniou, B. Allen, and V. Velisavljevic, "Threshold optimization for energy detection-based spectrum sensing over hyper-Rayleigh fading channels," *IEEE Communications Letters*, vol. 19, no. 6, pp. 1077–1080, 2015.

[6] S. Atapattu, C. Tellambura, H. Jiang, and N. Rajatheva, "Unified analysis of low-SNR energy detection and threshold selection," *IEEE Transactions on Vehicular Technology*, vol. 64, no. 11, pp. 5006–5019, 2015.

[7] C. Vladeanu, C. V. Nastase, and A. Martian, "Energy detection algorithm for spectrum sensing using three consecutive sensing events," *IEEE Wireless Communications Letters*, vol. 5, no. 3, pp. 284–287, 2016.

[8] G. Mahendru, A. Shukla, and P. Banerjee, "A novel mathematical model for energy detection based spectrum sensing in cognitive radio networks," *Wireless Personal Communications*, vol. 110, no. 3, pp. 1237–1249, 2020.

[9] G. Yang, J. Wang, J. Luo et al., "Cooperative spectrum sensing in heterogeneous cognitive radio networks based on normalized energy detection," *IEEE Transactions on Vehicular Technology*, vol. 65, no. 3, pp. 1452–1463, 2016.

[10] X. Hu, G. Wu, and H. Hu, "Cooperative spectrum sensing with double threshold under noise uncertainty," *Computer Engineering and Applications*, vol. 48, no. 8, pp. 158–160, 2012.

[11] A. K. Sahu, A. Singh, and S. Nandakumar, "Improved adaptive cooperative spectrum sensing in cognitive radio networks," in *2018 2nd International Conference on Electronics, Materials Engineering & Nano- Technology (IEMENTech)*, pp. 1–5, Kolkata, India, May 2018.

[12] A. Nasrallah, A. Hamza, T. Boukaba, G. Baudoin, and A. Messani, "Energy detection with adaptive threshold for cognitive radio," in *2018 International Conference on Communications and Electrical Engineering (ICCEE)*, pp. 1–5, El Oued, Algeria, December 2018.

[13] A. Eslami and S. Karamzadeh, "Memory based energy detection spectrum sensing method in cognitive radio driven hospitals," in *2016 Advances in Wireless and Optical Communications (RTUWO)*, pp. 111–115, Riga, Latvia, November 2016.

[14] Z. Liu, X. Chen, and Z. Xie, "A novel double-threshold energy detection based on correlativity," in *2019 IEEE 9th International Conference on Electronics Information and Emergency Communication (ICEIEC)*, pp. 151–153, Beijing, China, July 2019.

[15] C. Fu, Y. Li, Y. He, M. Jin, G. Wang, and P. Lei, "An inter-frame dynamic double-threshold energy detection for spectrum

sensing in cognitive radios," *EURASIP Journal on Wireless Communications and Networking*, vol. 2017, no. 1, 2017.

[16] X. Huang, Y. Xu, J. Wu, and W. Zhang, "Noncooperative spectrum sensing with historical sensing data mining in cognitive radio," *IEEE Transactions on Vehicular Technology*, vol. 66, no. 10, pp. 8863–8871, 2017.

[17] J. Wang, S. Yu, and J. Liu, "Improved adaptive double threshold cooperative spectrum sensing algorithm," *Journal of Data Acquisition and Processing*, vol. 34, no. 6, pp. 986–991, 2019.

[18] S. Soofi, A. Potnis, and P. Diwivedy, "Efficient dynamic double threshold energy detection of cooperative spectrum sensing in cognitive radio," in *Emerging Research in Computing, Information, Communication and Applications. Advances in Intelligent Systems and Computing, vol 882*, N. Shetty, L. Patnaik, H. Nagaraj, P. Hamsavath, and N. Nalini, Eds., pp. 479–492, Springer, Singapore, 2019.

[19] C. C. Smriti, "Double threshold based cooperative spectrum sensing with consideration of history of sensing nodes in cognitive radio networks," in *2018 2nd International Conference on Power, Energy and Environment: Towards Smart Technology (ICEPE)*, pp. 1–9, Shillong, India, June 2018.

[20] C. Chen, Y. Chen, J. Qian, and J. Xu, "Triple-threshold cooperative spectrum sensing algorithm based on energy detection," in *2018 5th International Conference on Systems and Informatics (ICSAI)*, pp. 791–795, Nanjing, China, November 2018.

[21] K. V. Rop, H. Ouma, P. K. Langat, and H. A. Ouma, "Cluster based triple threshold energy detection for spectrum sensing in vehicular ad-hoc networks," *International Journal of Recent Technology and Engineering*, vol. 7, pp. 1495–1499, 2019.

[22] W. Zhao, H. Li, M. Jin, Y. Liu, and S. J. Yoo, "Enhanced detection algorithms based on eigenvalues and energy in random matrix theory paradigm," *IEEE Access*, vol. 8, pp. 9457–9468, 2020.

[23] Y. Gu, Q. Pei, and H. Li, "Dynamic matching-based spectrum detection in cognitive radio networks," *China Communications*, vol. 16, no. 4, pp. 47–58, 2019.

[24] X. L. Huang, Y. Gao, X. W. Tang, and S. B. Wang, "Spectrum mapping in large-scale cognitive radio networks with historical spectrum decision results learning," *IEEE Access*, vol. 6, pp. 21350–21358, 2018.

[25] M. K. Giri and S. Majumder, "Extreme learning machine based cooperative spectrum sensing in cognitive radio networks," in *2020 7th International Conference on Signal Processing and Integrated Networks (SPIN)*, pp. 636–641, Noida, India, February 2020.

[26] W. Wu, Z. Li, S. Ma, and J. Shi, "Performance improvement for machine learning-based cooperative spectrum sensing by feature vector selection," *IET Communications*, vol. 14, no. 7, pp. 1081–1089, 2020.

[27] M. Khayyeri and K. Mohammadi, "Cooperative wideband spectrum sensing in cognitive radio based on sparse real-valued fast Fourier transform," *IET Communications*, vol. 14, no. 8, pp. 1340–1348, 2020.

[28] X. Li, J. Li, Y. Liu, Z. Ding, and A. Nallanathan, "Residual transceiver hardware impairments on cooperative NOMA networks," *IEEE Transactions on Wireless Communications*, vol. 19, no. 1, pp. 680–695, 2020.

[29] W. U. Khan, F. Jameel, T. Ristaniemi, S. Khan, G. A. S. Sidhu, and J. Liu, "Joint spectral and energy efficiency optimization for downlink NOMA networks," *IEEE Transactions on Cognitive Communications and Networking*, vol. 6, no. 2, pp. 645–656, 2020.

[30] X. Li, M. Zhao, and L. Li, "Performance analysis of impaired SWIPT NOMA relaying networks over imperfect Weibull channels," *IEEE Systems Journal*, vol. 14, no. 1, pp. 669–672, 2020.

[31] W. U. Khan, Z. Yu, S. Yu, G. A. S. Sidhu, and J. Liu, "Efficient power allocation in downlink multi-cell multi-user NOMA networks," *IET Communications*, vol. 13, no. 4, pp. 396–402, 2019.

[32] X. Li, M. Liu, C. Deng, P. T. Mathiopoulos, Z. Ding, and Y. Liu, "Full-duplex cooperative NOMA relaying systems with I/Q imbalance and imperfect SIC," *IEEE Wireless Communications Letters*, vol. 9, no. 1, pp. 17–20, 2020.

[33] H. Urkowitz, "Energy detection of unknown deterministic signals," *Proceedings of the IEEE*, vol. 55, no. 4, pp. 523–531, 1967.

[34] M. López-Benítez and F. Casadevall, "Improved energy detection spectrum sensing for cognitive radio," *IET Communications*, vol. 6, no. 8, pp. 785–796, 2012.

WILEY | Hindawi

Research Article

A Heterogeneous Image Fusion Method Based on DCT and Anisotropic Diffusion for UAVs in Future 5G IoT Scenarios

Shuai Hao [ID],[1,2] **Beiyi An,**[2] **Hu Wen** [ID],[1] **Xu Ma,**[2] **and Keping Yu** [ID][3]

[1]*College of Safety Science and Engineering, Xi'an University of Science and Technology, Xi'an 710054, China*
[2]*College of Electrical and Control Engineering, Xi'an University of Science and Technology, Xi'an 710054, China*
[3]*Global Information and Telecommunication Institute, Waseda University, Tokyo 169-8050, Japan*

Correspondence should be addressed to Hu Wen; wenh@xust.edu.cn and Keping Yu; keping.yu@aoni.waseda.jp

Unmanned aerial vehicles, with their inherent fine attributes, such as flexibility, mobility, and autonomy, play an increasingly important role in the Internet of Things (IoT). Airborne infrared and visible image fusion, which constitutes an important data basis for the perception layer of IoT, has been widely used in various fields such as electric power inspection, military reconnaissance, emergency rescue, and traffic management. However, traditional infrared and visible image fusion methods suffer from weak detail resolution. In order to better preserve useful information from source images and produce a more informative image for human observation or unmanned aerial vehicle vision tasks, a novel fusion method based on discrete cosine transform (DCT) and anisotropic diffusion is proposed. First, the infrared and visible images are denoised by using DCT. Second, anisotropic diffusion is applied to the denoised infrared and visible images to obtain the detail and base layers. Third, the base layers are fused by using weighted averaging, and the detail layers are fused by using the Karhunen–Loeve transform, respectively. Finally, the fused image is reconstructed through the linear superposition of the base layer and detail layer. Compared with six other typical fusion methods, the proposed approach shows better fusion performance in both objective and subjective evaluations.

1. Introduction

Internet of Things (IoT) has attracted extensive attention in academics and industry ever since it was first proposed. IoT aims at integrating various technologies, such as body domain network systems, device-to-device (D2D) communication, and unmanned aerial vehicles (UAVs) and satellite networks, to provide a wide range of services in any location by using any network. This makes it highly useful for various civil and military applications. In recent years, however, the proliferation of intelligent devices used in IoT has given rise to massive amounts of data, which brings its own set of challenges to the smooth functioning of the wireless communication network. However, the emergence of the fifth-generation (5G) wireless communication technology has provided an effective solution to this problem. Many scholars are committed to the study of key 5G characteristics such as quality-of-

service (QoS) and connectivity [1, 2]. With the development of UAV technology and 5G wireless systems, the application field of IoT has expanded further [3–5]. Due to their characteristics of dynamic deployment, convenient configuration, and high autonomy, UAVs play an extremely important role in IoT. As some wireless devices suffer from limited transmission ranges, UAVs can be used as wireless relays to improve the network connection and extend the coverage of the wireless network. Meanwhile, due to their adjustable flight altitude and mobility, UAVs can easily and efficiently collect data from the users of IoT on the ground. At present, there exists an intelligent UAV management platform, which can operate several UAVs at the same time through various terminal devices. It is capable of customizing flight routes as needed and obtaining the required user data. Intelligent transportation systems (ITS) can use UAVs for traffic monitoring and law enforcement. UAVs can also be used as base

stations in the air to improve wireless network capacity. In 5G IoT, UAV wireless communication systems will play an increasingly important role [6, 7].

The perception layer, which is the basic layer of IoT, consists of different sensors. The UAVs collect the data of IoT users by means of airborne IoT devices, including infrared (IR) cameras and visible (VI) light cameras [8]. One of the key technologies affecting the reliability of the perception layer is the accurate acquisition of multisource signals and reliable fusion of data. In recent years, heterogeneous image fusion has become an important topic regarding the perception layer of IoT. IR and visible light sensors are the two most commonly used types of sensors. IR images taken by an IR sensor are usually less affected by adverse weather conditions such as bright sunlight and smog [9]. However, IR images lack sufficient details of the scene and have a lower spatial resolution than VI images. In contrast, VI images contain more detailed scene information, but are easily affected by illumination variation. IR and VI image fusion could produce a composite image, which is more interpretable to both human and machine perception. The goal of image fusion is to combine images obtained by different types of image sensors to generate an informative image. The fused image would be more consistent with the human visual perception system than the source image individually. It can be convenient for subsequent processing or decision-making. Nowadays, the image fusion technique is widely used in such fields as military reconnaissance [10], traffic management [11], medical treatment [12], and remote sensing [13, 14].

In recent decades, a variety of IR and VI image fusion approaches have been investigated. In general, based on the different levels of image representation, fusion methods could be classified into three categories: pixel-level, feature-level, and decision-level [15]. Pixel-level fusion, conducted on raw source images, usually generates more accurate, richer, and reliable details compared with other fusion methods. Feature-level image fusion first extracts various features (including colour, shape, and edge) from the multisource information of different sensors. Subsequently, the feature information obtained from multiple sensors is analysed and processed synthetically. Although this method could reduce the amount of data and retain most of the information, some details of the image are still lost. Decision-level fusion is used to fuse the recognition results of multiple sensors to make a global optimal decision on the basis of each sensor independently, thus, completing the decision or classification. Decision-level fusion has the advantage of good real-time performance, self-adaptability, and strong anti-interference; however, the fault-tolerance ability of the decision function directly affects the fusion classification performance. In this study, we focus on the pixel-level fusion method.

The remainder of this paper is organised as follows. In Section 2, we introduce related works and the motivation behind the present work. The proposed fusion method is described in Section 3. Experimental results on public datasets are covered in Section 4. The conclusions of this study are presented in Section 5.

2. Related Works

In general, the pixel-level fusion approach can be divided into two categories: space-based fusion methods and the transform domain technique. Space-based fusion methods usually address the fusion issue via pixel grayscale or pixel gradient. Although these methods are simple and effective, they easily lose spatial details [16]. Liu et al. [17] observed that this type of method is more suitable to fusion tasks of the same type of images. The transform domain technique usually takes the transform coefficient as the feature for image fusion. The fused image is obtained by the fusion and reconstruction of the transform coefficients. The image fusion method based on multiscale transformation has been widely investigated because of its compatibility with human visual perception. In recent years, a variety of fusion methods based on multiscale transform have been proposed, such as low-pass pyramid (RP) [18], gradient pyramid (GP) [19], nonsubsampled contourlet transform (NSCT) [20], discrete wavelet transform (DWT) [21], and dual-tree complex wavelet transform (DTCWT) [22]. However, image fusion methods based on multiscale transform are usually complex and suffer from long processing time and energy consumption issues, which limit their application.

Due to the aforementioned reasons, many researchers implemented image fusion methods by using discrete cosine transform (DCT). In [23], the authors pointed out that image fusion methods based on DCT were efficient due to their fast speed and low complexity. Cao et al. [24] proposed a multifocus image fusion algorithm based on spatial frequency in the DCT domain. The experimental results showed that it could improve the quality of the output image visually. Amin-Naji and Aghagolzadeh et al. [25] employed the correlation coefficient in the DCT domain for multifocus image fusion, proving that the proposed method could improve image quality and stability in noisy images. In order to provide better visual effects, Jin et al. [26] proposed a heterogeneous image fusion method by combining DSWT, DCT, and LSF. Jin et al. proved that the proposed method was superior to the conventional multiscale method. Although image fusion methods based on DCT have achieved superior performance, the fused results show undesirable side effects such as blocking artifacts [27]. While performing DCT, the image is usually required to be divided into small blocks prior, which causes discontinuities between adjacent blocks in the image. In order to address this problem, several filtering techniques have been proposed, such as weighted least square filter [28], bilateral filter [29], and anisotropic diffusion filter [30]. Xie and Wang [31] pointed out that the anisotropic diffusion processing of images could retain the image edge contour information. Compared with other fusion methods based on filtering, image fusion based on anisotropic diffusion could retain more edge profiles. It preferably suppresses noise and obtains better visual evaluation. However, most of the proposed methods for anisotropic diffusion models are based on the diffusion equation itself, ignoring the image's own feature information, which may lead to loss or blurring of image details (textures, weak edges, etc.). Inspired by the above research, a heterogeneous image fusion method
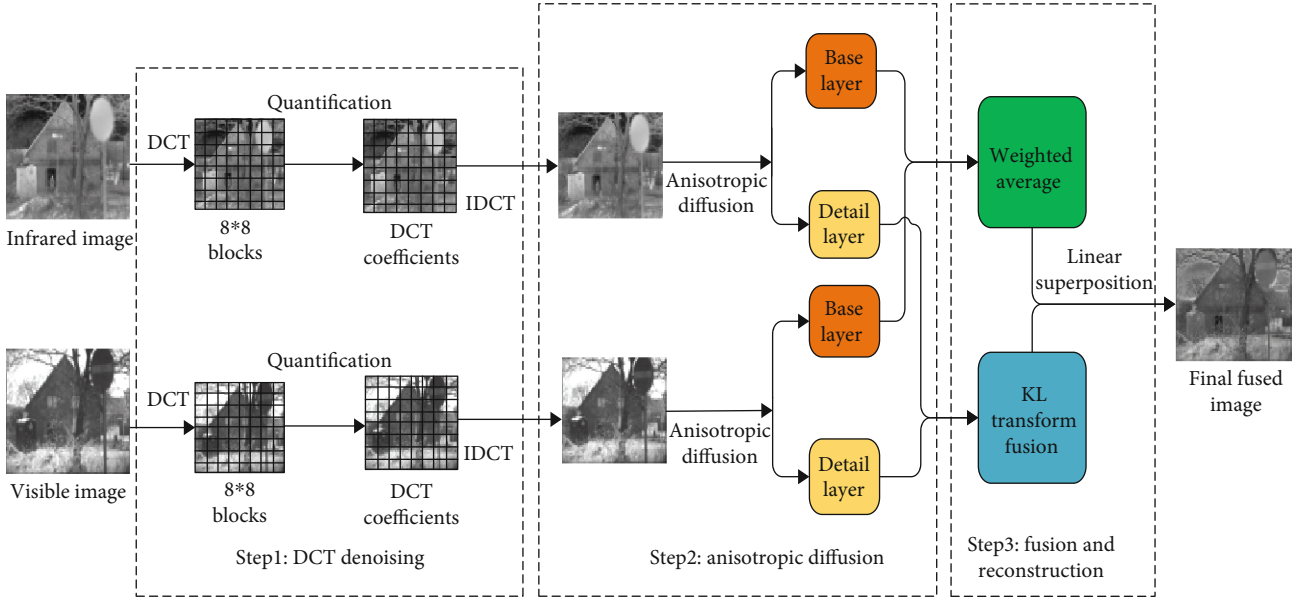
FIGURE 1: Flowchart of the proposed method framework.

based on DCT and anisotropic diffusion is proposed. The advantages of the proposed method mainly lie in the following three aspects:

(1) Due to the use of DCT transform, the fusion algorithm proposed in this paper shows good denoising ability

(2) The final fusion images show satisfactory detail resolution

(3) The proposed algorithm is easy to implement, and the real-time performance is very good, which is suitable for real-time requirements

3. Proposed Fusion Method

In this section, the operation mechanism of the proposed algorithm is described in detail. The proposed image fusion framework can be divided into three components, as shown in Figure 1. In the first step, in order to eliminate the noise in the original images, DCT and inverse discrete cosine transform are performed on the IR and VI images, respectively. In the second step, anisotropic diffusion is adopted to decompose IR and VI images to obtain the detail and base layers. In the third step, base layers are fused by using the weighted averaging, and detail layers are fused by using the Karhunen–Loeve transformation. Finally, the fused base and detail layers are linearly superimposed to obtain the final fusion result.

3.1. DCT. As an effective transform tool, DCT can transform the image information from the time domain to the frequency domain so as to effectively reduce the spatial redundancy of the image. In this study, the 2D DCT of an $N \times N$

image block $f(i, j)$ is defined as follows [32]:

$$F(u, v) = \frac{2}{N} c(u)c(v) \sum_{i=0}^{N-1} \sum_{j=0}^{N-1} f(i, j) \cos \left(\frac{(2i + 1)\pi u}{2N} \right)$$
$$\times \cos \left(\frac{(2j + 1)\pi v}{2N} \right), \text{ where } u, v = 0, 1, \cdots N - 1,$$
(1)

where $f(i, j)$ denotes the (i, j)-th image pixel value in the spatial domain and $F(u, v)$ denotes the (i, j)-th DCT coefficient in the frequency domain; $c(k)$ is a multiplication factor, defined as follows:

$$c(k) = \begin{cases} \dfrac{1}{\sqrt{2}}, & \text{if } u = 0, \\ 1 & \text{if } u \neq 0. \end{cases}$$
(2)

Similarly, the 2D inverse discrete cosine transform (IDCT) is defined as:

$$f(i, j) = \frac{2}{N} \sum_{u=0}^{N-1} \sum_{v=0}^{N-1} c(u)c(v)F(u, v) \cos \left(\frac{(2i + 1)\pi u}{2N} \right)$$
$$\times \cos \left(\frac{(2j + 1)\pi v}{2N} \right), \text{ where } i, j = 0, 1, \cdots N - 1.$$
(3)

When performing the DCT transform, most of the image information is concentrated on the DC coefficient and low-frequency spectrum nearby. Therefore, the coefficient close to 0 is deleted, and the coefficient containing the main information of the image is reserved for inverse transformation. The influence of noise can be effectively removed without

causing image distortion. In this study, if the coefficient obtained by the DCT transformation is less than 0.1, we set the coefficient as 0. The results of denoising by DCT are shown in Figure 2.

3.2. Anisotropic Diffusion. In computer vision, anisotropic diffusion is widely used to reduce noise while preserving image details. The model of anisotropic diffusion of an image I can be represented as follows [33]:

$$It = c(x, y, t)\Delta I + \nabla c \cdot \nabla I, \tag{4}$$

where $c(x, y, t)$ is rate of diffusion, ∇ and Δ are used to represent the gradient operator and the Laplacian operator, respectively, and t is time. Then, the equation (4) can be discretized as:

$$I_{i,j}^{t+1} = I_{i,j}^t + \lambda \left[c_N \cdot \Omega_N I_{i,j}^t + c_S \cdot \Omega_S I_{i,j}^t + c_E \cdot \Omega_E I_{i,j}^t + c_W \cdot \Omega_W I_{i,j}^t \right]. \tag{5}$$

In (5), $I_{i,j}^{t+1}$ is an image with coarse resolution at $t + 1$ scale. λ denotes a stability constant satisfying $0 \le \lambda \le 1/4$. The local image gradients along the north, south, east, and west directions are represented as:

$$\begin{cases} \Omega_N I_{i,j} = I_{i-1,j} - I_{i,j}, \\ \Omega_S I_{i,j} = I_{i+1,j} - I_{i,j}, \\ \Omega_E I_{i,j} = I_{i,j+1} - I_{i,j}, \\ \Omega_W I_{i,j} = I_{i,j-1} - I_{i,j}. \end{cases} \tag{6}$$

Similarly, the conduction coefficients along the four directions of north, south, east, and west can be defined as:

$$\begin{cases} c_{N_{i,j}}^t = g\left(\left\| (\nabla I)_{i+1/2,j}^t \right\| \right) = g\left(\left| \Omega_N I_{i,j}^t \right| \right), \\ c_{S_{i,j}}^t = g\left(\left\| (\nabla I)_{i-1/2,j}^t \right\| \right) = g\left(\left| \Omega_S I_{i,j}^t \right| \right), \\ c_{E_{i,j}}^t = g\left(\left\| (\nabla I)_{i,j+1/2}^t \right\| \right) = g\left(\left| \Omega_E I_{i,j}^t \right| \right), \\ c_{W_{i,j}}^t = g\left(\left\| (\nabla I)_{i,j-1/2}^t \right\| \right) = g\left(\left| \Omega_W I_{i,j}^t \right| \right). \end{cases} \tag{7}$$

In (7), $g(\cdot)$ is a decreasing function. In order to maintain smoothing and edge preservation, in this paper, we choose $g(\cdot)$ as:

$$g(\nabla I) = \begin{cases} \left[1 - \frac{(\|\nabla I\|)^2}{T^2} \right]^2, (\|\nabla I\|)^2 \le T^2, \\ 0, (\|\nabla I\|)^2 > T^2, \end{cases} \tag{8}$$

where T is an edge magnitude parameter.

Let $I_{IR}(x, y)$ and $I_{VI}(x, y)$ be IR and VI images, respectively, which have been coregistered. Anisotropic diffusion for an image I is denoted as $AD(I)$. The base layers $I_{IR}^B(x, y)$

and $I_{VI}^B(x, y)$ are obtained after performing anisotropic diffusion processes on $I_{IR}(x, y)$ and $I_{VI}(x, y)$, respectively, which are represented by:

$$\begin{cases} I_{IR}^B(x, y) = AD(I_{IR}(x, y)), \\ I_{VI}^B(x, y) = AD(I_{VI}(x, y)). \end{cases} \tag{9}$$

Then, the detail layers $I_{IR}^D(x, y)$ and $I_{VI}^D(x, y)$ are obtained by subtracting the base layers from the respective source images, which are shown in (10).

$$\begin{cases} I_{IR}^D(x, y) = I_{IR}(x, y) - I_{IR}^B(x, y), \\ I_{VI}^D(x, y) = I_{VI}(x, y) - I_{VI}^B(x, y). \end{cases} \tag{10}$$

The results obtained by the anisotropic diffusion of IR image and VI image are shown in Figure 3.

3.3. Construction and Fusion

3.3.1. Base Layer Fusion. The weighted average is adopted to fuse the base layers of IR and VI images. The fused base layer I_F^B is calculated by:

$$I_F^B = \omega_1 I_{IR}^B(x, y) + \omega_2 I_{VI}^B(x, y), \tag{11}$$

where ω_1 and ω_2 are normalized weighted coefficients, set to 0.5 in this paper.

3.3.2. Detail Layer Fusion. KL-transform can make the new sample set approximate to the original sample set distribution with minimum mean square error, and it eliminates the correlation between the original features. We use KL-transform to fuse the detail layers of IR and VI images. Let $I_{IR}^D(x, y)$ and $I_{VI}^D(x, y)$ be detail layers of the IR and VI images, respectively. The fused process based on KL-transform is described as follows.

Step 1. Arrange $I_{IR}^D(x, y)$ and $I_{VI}^D(x, y)$ as column vectors of a matrix, denoted as X.

Step 2. Calculate the autocorrelation matrix C of X.

Step 3. Calculate the eigenvalues λ_1 matrix λ_2, and eigenvectors $\mu_1 = [\mu_1(1) \ \mu_1(2)]^T$ and $\mu_2 = [\mu_2(1) \ \mu_2(2)]^T$ of C.

Step 4. Calculate the uncorrelated coefficients K_1 and K_2 corresponding to the largest eigenvalue λ_{max}, which is defined as:

$$\lambda_{max} = \max (\lambda_1, \lambda_2). \tag{12}$$

The eigenvector corresponding to λ_{max} is denoted as μ_{max}. And, K_1 and K_2 are given by:

$$\begin{cases} K_1 = \lambda_{max}(1) / \sum_i \lambda_{max}(i), \\ K_2 = \lambda_{max}(2) / \sum_i \lambda_{max}(i). \end{cases} \tag{13}$$

(a)

(b)

(c)

(d)

(e)

(f)
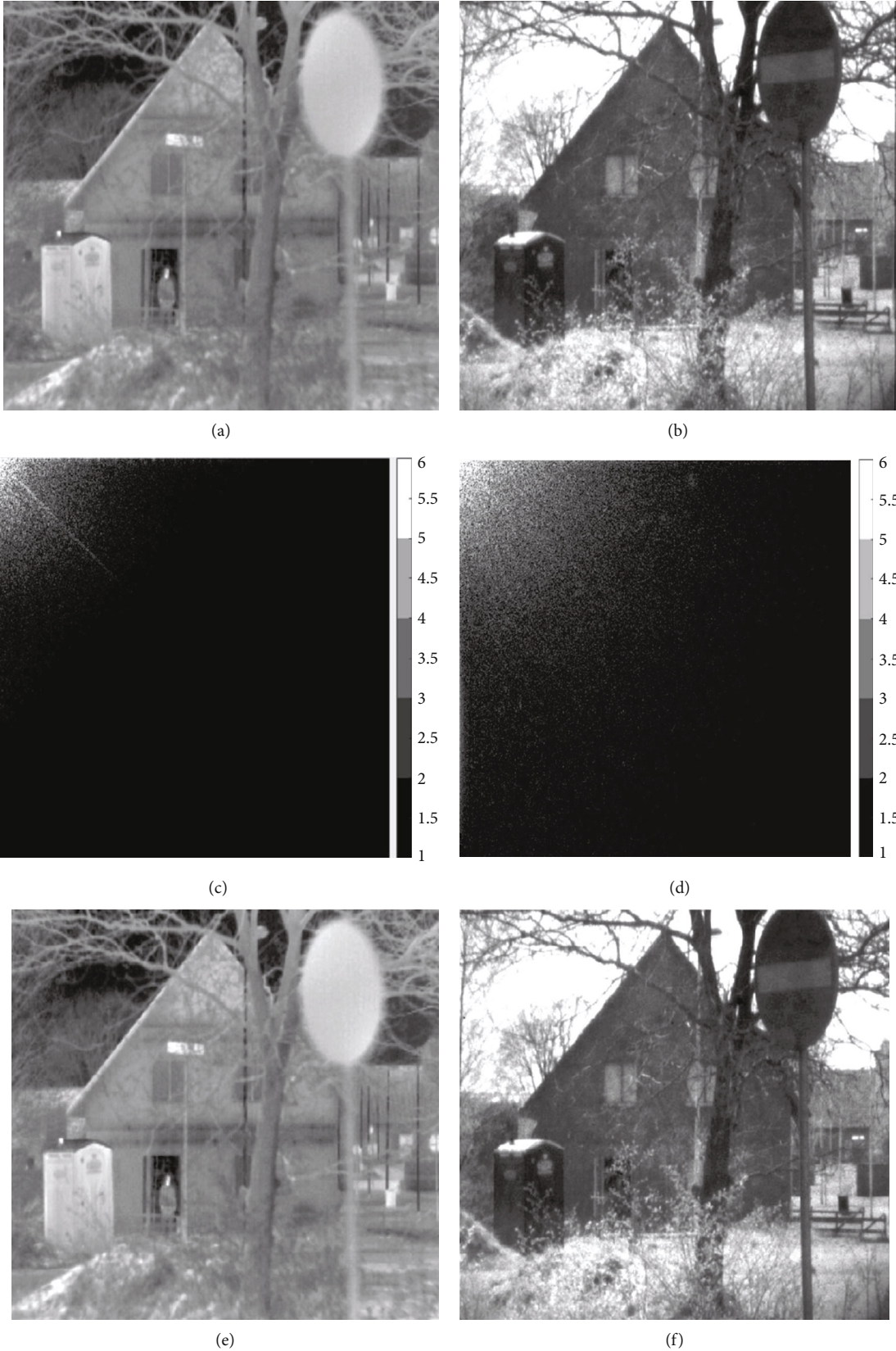
FIGURE 2: Results of denoising by DCT. (a) IR image. (b) VI image. (c) DCT coefficient matrix of the IR image. (d) DCT coefficient matrix of the VI image. (e) IR image after IDCT. (f) VI image after IDCT.

(a)

(b)

(c)

(d)

(e)

(f)
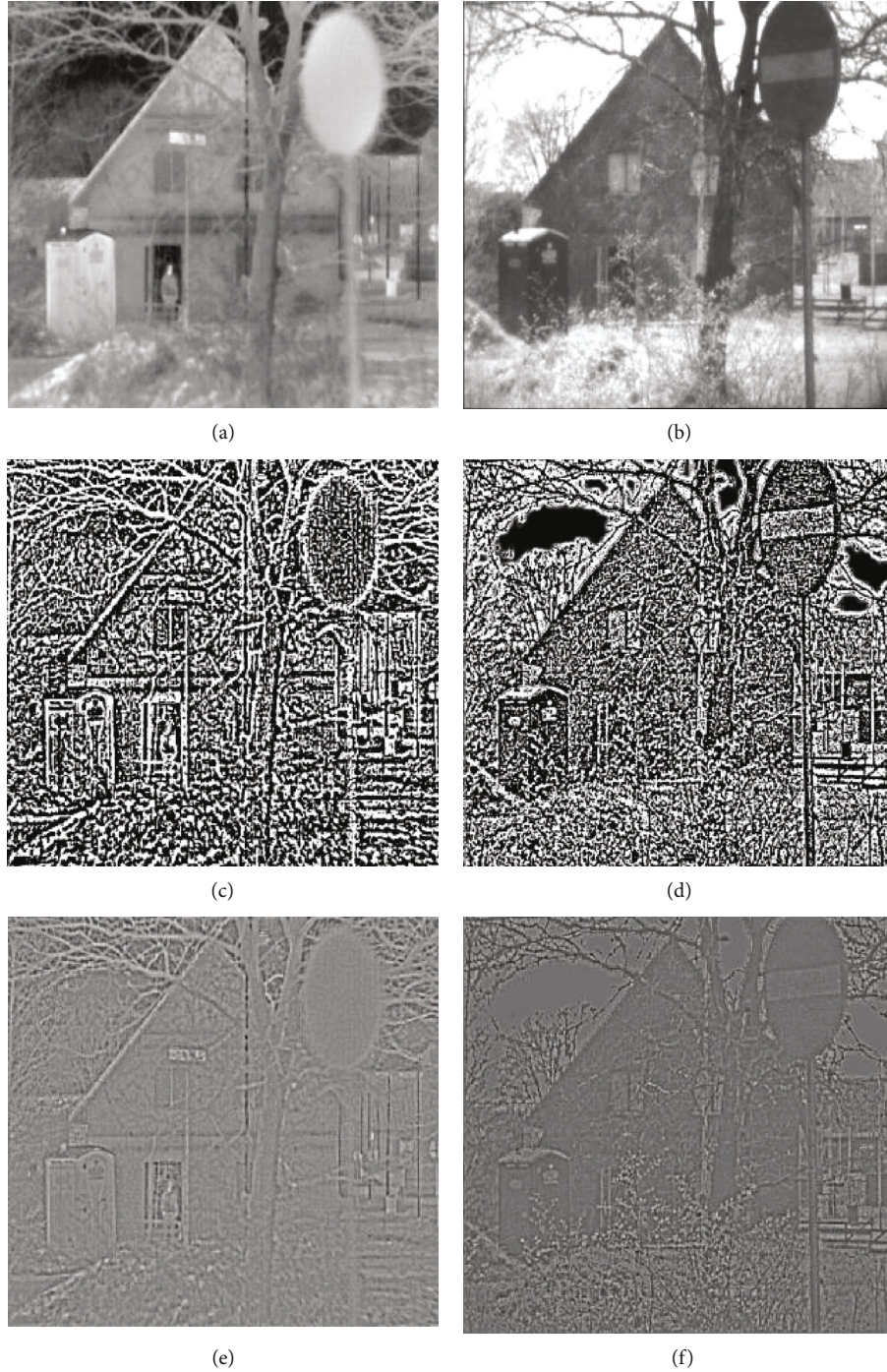
FIGURE 3: (a) IR image. (b) VI image. (c) Detail layer of the IR image. (d) Detail layer of the VI image. (e) Base layer of the IR image. (f) Base layer of the VI image.

Step 5. The fused detail layer I_F^D is calculated using:

$$I_F^D = K_1 I_{IR}^D(x, y) + K_2 I_{VI}^D(x, y). \tag{14}$$

3.3.3. Reconstruction. In this study, the final fused image is obtained by the linear superposition of I_F^B and I_F^D, as shown in equation (14).

$$I_F = I_F^B + I_F^D. \tag{15}$$

4. Experiment

In this section, the coregistered IR and VI images from the TNO image fusion dataset are used to evaluate our algorithm. This database provides a large number of coregistered infrared and visible images. All the experiments are implemented

(a) IR images

(b) VI images
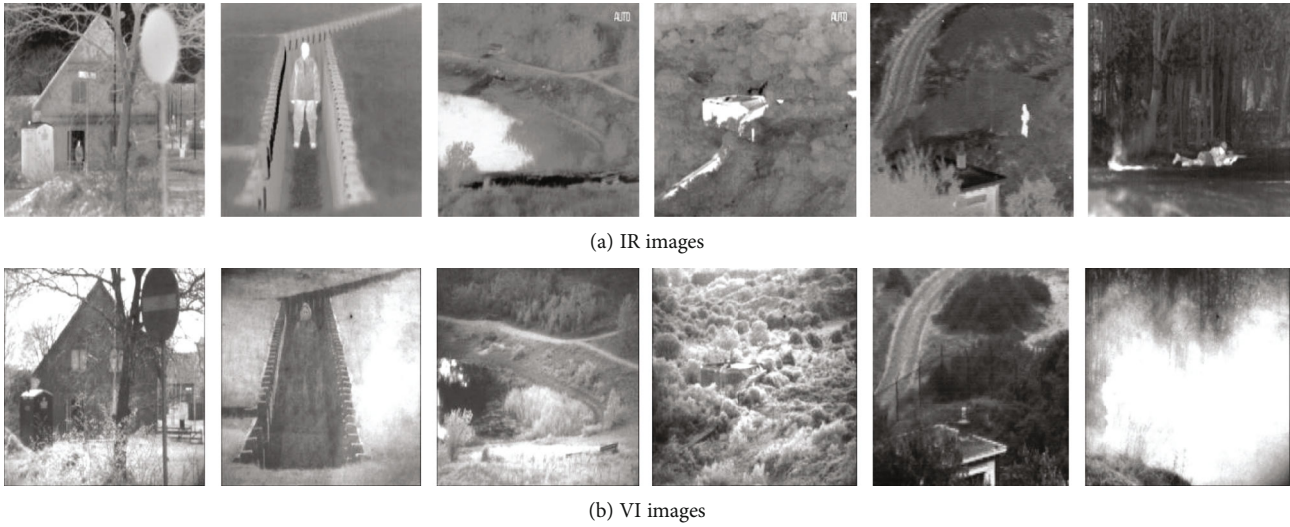
FIGURE 4: Source images used in the experiment.

in MATLAB 2019a on 1.8 GHz Intel(R) Core(TM) i7 CPU with 8 GB RAM. The proposed method is compared with six typical fusion methods: multiscale singular value representation (MSVD) [34], discrete harmonic wavelet transform (DCHWT) [35], discrete wavelet transform (DWT) [21], two-scale fusion (TS) [36], dual-tree complex wavelet transform (DTCWT) [22], and curvelet transform (CVT) [37]. In order to verify the advantages of the proposed method, the experimental verification is divided into two parts. Subjective evaluation results of the fused image are shown in the first part. In the second part, we compare the objective evaluation results of the proposed algorithm with six comparison algorithms. The six pairs of coregistered source images used in this experiment are depicted in Figure 4.

4.1. Subjective Evaluation. The fusion results obtained by the proposed method and six compared methods are shown in Figure 5. The fusion experimental results from pair 1 to pair 6 are represented from top to bottom, respectively.

In order to show a better comparison, the details in the fused images are highlighted with red boxes. As can be seen from Figure 5, our method preserves more detail information and contains less artificial noise in the red window. The image details in fused images obtained by MSVD, DWT, and TS are blurred, which are clearly seen from the first three pairs of the experiment. Compared with the above three fusion methods, the fusion results based on DCHWT preserve more detail information, while showing obvious VI artifacts in them (clearly visible in the last pair of the experiment). The fused images obtained by DTCWT, CVT, and the proposed method could preserve more detail information. Compared with DTCWT and CVT fusion methods, the fusion results of the proposed algorithm look more natural. In the next section, several different objective quality metrics are evaluated to demonstrate the advantages of the proposed method.

4.2. Objective Evaluation. In order to verify the advantages of the proposed method, cross entropy (CE) [38], mutual information (MI) [39], the average gradient (AG) [39], relative

standard deviation (RSD) [39], mean gradient (MG) [39], and running time are used as objective evaluation metrics. CE represents the cross entropy between the fused image and the source image. The smaller the cross entropy, the smaller the difference between the images. MI represents the calculation of mutual information between the fused image and the source image. The larger the value of MI, the higher the similarity between the two images. Calculating the average gradient of the image involves calculating the definition of the image, which reflects the expressive ability of the image to the detail contrast. RSD represents the relative standard deviation of the source image and the fused image, which reflects the degree of deviation from the true value. The smaller the relative standard deviation, the higher the fusion accuracy. The mean gradient represents the definition of the fused image. It refers to the clarity of each detail shadow and its boundary on the image. The objective evaluation results of the 6 pairs of the experiment in the "Subjective Evaluation" section are shown in Tables 1–3, and the best results are highlighted in bold.

The comparison results of the objective evaluation indexes of the first two pairs of experiments are given in Table 1. As seen from Table 1, the proposed method outperforms other fusion methods in terms of all metrics except for CE. Although the CE value of the proposed method is not the minimum value, it is very close to the minimum.

The comparison results of objective evaluation indexes of the third and fourth pairs of the experiment are shown in Table 2. As can be seen from Table 2, the fusion result of the proposed algorithm in this paper contains more information. The proposed method outperforms other methods as regards AG, RSD, MG, and running time. The CE values of the proposed method in the third pair of the experiment are very close to the best values produced by MSVD. In the fourth pair of the experiment, all fusion quality indexes of image fusion generated by the proposed method are the best.

The comparison results of the objective evaluation indexes of the last two pairs of the experiment are given in Table 3. As can be seen from Table 3, MI, RSD, MG, and

| (a) | (b) | (c) | (d) | (e) | (f) | (g) |
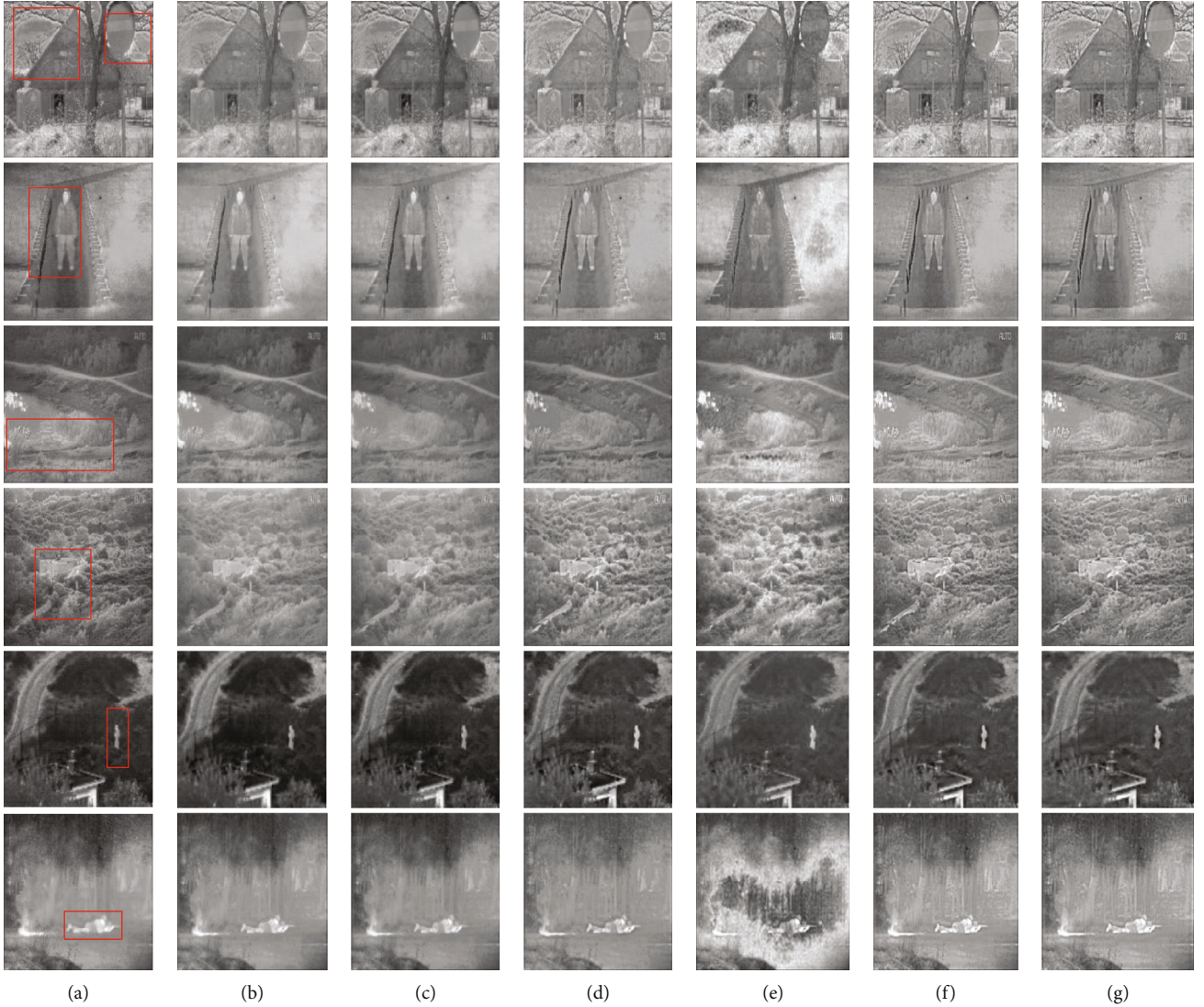
Figure 5: Comparison of the fusion results of various methods. (a) Proposed method; (b) MSVD; (c) DWT; (d) TS; (e) DCHWT; (f) DTCWT; (g) CVT.

Table 1: Objective evaluation results of the first and the second pair of fusion images.

| Method | Pair 1 | | | | | | Pair 2 | | | | | |
	CE	MI	AG	RSD	MG	Time	CE	MI	AG	RSD	MG	Time
Proposed	0.3214	0.1573	4.8756	0.2504	5.7140	0.7371	0.4494	0.3736	4.4364	0.0234	5.5580	0.7742
MSVD	0.5391	0.1384	2.8604	0.5931	3.4728	2.8533	0.8568	0.2637	3.0245	0.1651	3.9973	2.3541
DWT	0.4817	0.1342	3.4970	0.3698	4.2660	32.3347	0.4454	0.2662	2.9412	0.1340	3.9847	21.9847
TS	0.5264	0.1028	3.5827	0.4832	3.9747	1.9536	0.9366	0.2065	2.8596	0.3254	3.3589	0.9680
DCHWT	0.5510	0.0985	4.4494	0.4986	5.0204	5.4881	0.3876	0.2673	3.7730	0.4195	4.6367	5.4581
DTCWT	0.2203	0.1201	4.9425	0.3500	5.6020	0.7506	0.4819	0.2120	4.0197	0.2122	4.9407	0.8207
CVT	0.2456	0.1186	4.9845	0.3488	5.6325	1.5946	0.4815	0.2123	4.0254	0.2123	4.9427	1.3500

running time values of the proposed method are clearly better than that of the other six compared methods. The CE values and AG values of the proposed method in the last two pairs of the experiment are close to the best values separately.

As can be seen from Tables 1–3, MI, RSD, MG, and running time for the proposed method are better than those obtained for other fusion methods. Although the CE value and the AG values of the proposed method are not the best, they are very close to the best. The proposed fusion method

TABLE 2: Objective evaluation results of the third and the fourth pair of fusion images.

Method	Pair 3						Pair 4					
	CE	MI	AG	RSD	MG	Time	CE	MI	AG	RSD	MG	Time
Proposed	0.6179	0.3137	3.6422	0.3473	4.3254	0.7891	0.4129	0.1269	5.2188	0.1213	6.4463	0.907382
MSVD	0.4948	0.3561	1.9869	0.3458	2.3983	2.6334	0.8562	0.1167	3.4208	0.3490	4.5526	2.147643
DWT	1.0674	0.3396	1.9595	0.4984	2.3480	18.1276	0.6749	0.1217	2.8319	0.3167	3.6561	23.632156
TS	1.1629	0.2586	2.4866	0.5446	2.8115	0.861984	0.6039	0.0981	4.1365	0.2013	4.8300	1.765118
DCHWT	0.6763	0.3179	3.2024	0.4503	3.7068	7.161516	0.8383	0.1458	4.6607	0.3401	5.6594	6.912164
DTCWT	0.9942	0.2898	3.4753	0.4383	4.0355	0.8003	0.4626	0.1077	5.2010	0.1486	6.2683	1.0240
CVT	0.8881	0.2885	3.4959	0.4386	4.0508	1.6419	0.4835	0.1098	5.1896	0.1471	6.2543	1.8738

TABLE 3: Objective evaluation results of the fifth and the sixth pair of fusion images.

Method	Pair 5						Pair 6					
	CE	MI	AG	RSD	MG	Time	CE	MI	AG	RSD	RSD	Time
Proposed	0.3292	0.2950	2.5466	0.4469	3.2846	0.752436	1.2609	0.4962	3.3075	0.4887	4.1645	0.865061
MSVD	0.9859	0.2949	3.0297	0.3864	3.8383	3.382514	1.5970	0.4498	2.4004	0.5577	3.1041	3.234588
DWT	0.9207	0.2743	3.4283	0.4230	4.5347	8.195448	1.2014	0.4476	2.2759	0.5613	3.0004	11.950211
TS	0.4923	0.2458	3.3674	0.5271	4.0203	1.811981	4.0630	0.3963	2.2917	0.6697	2.6333	1.063052
DCHWT	0.3756	0.2173	2.6355	0.5991	3.1812	1.047889	2.3590	0.2674	3.9069	0.4493	4.7613	6.561848
DTCWT	0.2432	0.2138	2.5781	0.6611	3.1841	0.8231	2.2847	0.4043	3.8098	0.5344	4.7439	1.0223
CVT	0.2399	0.2276	2.6379	0.6494	3.2569	0.8582	2.0645	0.4057	3.8285	0.5334	4.7663	2.3507

in this paper can guarantee high fusion accuracy and a satisfactory real-time performance, which is suitable for real-time requirements.

5. Conclusions

Data fusion, which is a key technology in IoT, can effectively reduce the amount of data in the communication network and thus reduce the energy loss. In this article, we focused on the fusion of the IR image and the VI image and proposed a novel heterogeneous fusion approach. Considering that DCT has shown good denoising ability and anisotropic diffusion has shown satisfactory detail resolution, we fused the two algorithms through effective fusion strategies. Experimental results show that the proposed method can achieve better performance compared with other six state-of-the-art fusion approaches as regards both subjective and objective indexes.

However, IR and VI images in this experiment are all coregistered. The actual multisource data may be unregistered. In the future, we will focus on unregistered image fusion.

Data Availability

Experimental data can be found at https://figshare.com/articles/TN_Image_Fusion_Dataset/1008029.

Conflicts of Interest

The authors declare that there is no conflict of interest regarding the publication of this paper.

References

[1] X. Li, J. Li, Y. Liu, Z. Ding, and A. Nallanathan, "Residual transceiver hardware impairments on cooperative NOMA networks," *IEEE Transactions on Wireless Communications*, vol. 19, no. 1, pp. 680–695, 2020.

[2] X. Li, M. Liu, C. Deng, P. T. Mathiopoulos, Z. Ding, and Y. Liu, "Full-duplex cooperative NOMA relaying systems with I/Q imbalance and imperfect SIC," *IEEE Wireless Communications Letters*, vol. 9, no. 1, pp. 17–20, 2020.

[3] M. Mozaffari, W. Saad, M. Bennis, and M. Debbah, "Mobile unmanned aerial vehicles (UAVs) for energy-efficient internet of things Communications," *IEEE Transactions on Wireless Communications*, vol. 16, no. 11, pp. 7574–7589, 2017.

[4] F. A. Turjman and S. Alturjman, "5G/IoT-enabled UAVs for multimedia delivery in industry-oriented applications," *Multimedia Tools and Applications*, vol. 79, no. 13-14, pp. 8627–8648, 2020.

[5] X. Li, J. Li, and L. Li, "Performance analysis of impaired SWIPT NOMA relaying networks over imperfect weibull

channels," *IEEE Systems Journal*, vol. 14, no. 1, pp. 669–672, 2020.

[6] X. Li, Q. Wang, H. Peng et al., "A unified framework for HS-UAV NOMA Networks: performance analysis and location optimization," *IEEE Access*, vol. 8, pp. 13329–13340, 2020.

[7] T. Tang, T. Hong, H. Hong, S. Ji, S. Mumtaz, and M. Cheriet, "An improved UAV-PHD filter-based trajectory tracking algorithm for multi-UAVs in future 5G IoT scenarios," *Electronics*, vol. 8, no. 10, pp. 1188–1203, 2019.

[8] H. Li, S. Liu, Q. Duan, and W. Li, "Application of multi-sensor image fusion of internet of things in image processing," *IEEE Access*, vol. 6, pp. 50776–50787, 2018.

[9] H. Shakhatreh, A. Sawalmeh, A. Al-Fuqaha et al., "Unmanned aerial vehicles (UAVs): a survey on civil applications and key research challenges," *IEEE Access*, vol. 7, pp. 48572–48634, 2019.

[10] L. Meng, C. Liao, Z. Wang, and Z. Shen, "Development and military applications of multi-source image fusion technology," *Aerospace Electronic Warfare*, vol. 27, no. 3, pp. 17–19, 2011.

[11] D. Fan and Y. Cai, "Research on the fusion of dual-source traffic image based on transform domain and edge detection," *Infrared Technology*, vol. 39, no. 9, pp. 740–745, 2015.

[12] G. Luo, S. Dong, K. Wang, W. Zuo, S. Cao, and H. Zhang, "Multi-views fusion CNN for left ventricular volumes estimation on cardiac MR images," *IEEE Transactions on Biomedical Engineering*, vol. 65, no. 9, pp. 1924–1934, 2018.

[13] S. Li, H. Yin, and L. Fang, "Remote sensing image fusion via sparse representations over learned dictionaries," *IEEE Transactions on Geoscience and Remote Sensing*, vol. 51, no. 9, pp. 4779–4789, 2013.

[14] Z. Wu, Y. Huang, and K. Zhang, "Remote sensing image fusion method based on PCA and curvelet transform," *Journal of the Indian Society of Remote Sensing*, vol. 46, no. 5, pp. 687–695, 2018.

[15] J. Ma, C. Chen, C. Li, and J. Huang, "Infrared and visible image fusion via gradient transfer and total variation minimization," *Information Fusion*, vol. 31, pp. 100–109, 2016.

[16] N. Aishwarya and C. B. Thangammal, "Visible and infrared image fusion using DTCWT and adaptive combined clustered dictionary," *Infrared Physics & Technology*, vol. 93, pp. 300–309, 2018.

[17] Y. Liu, X. Chen, R. Ward, and Z. J. Wang, "Image fusion with convolutional sparse representation," *IEEE Signal Processing Letters*, vol. 23, no. 12, pp. 1882–1886, 2016.

[18] A. Toet, "Image fusion by a ratio of low-pass pyramid," *Pattern Recognition Letters*, vol. 9, no. 4, pp. 245–253, 1989.

[19] M. Li, Y. Dong, and X. Wang, "Image fusion algorithm based on gradient pyramid and its performance evaluation," *Applied Mechanics and Materials*, vol. 525, pp. 715–718, 2014.

[20] J. Liu, J. Zhang, and Y. Du, "A fusion method of multi-spectral image and panchromatic image based on NSCT transform and adaptive gamma correction," in *2018 3rd International Conference on Information Systems Engineering (ICISE)*, pp. 10–15, Shanghai, China, May 2018.

[21] H. Kaur and J. Rani, "Image fusion on digital images using Laplacian pyramid with DWT," in *2015 Third International Conference on Image Information Processing (ICIIP)*, pp. 393–398, Waknaghat, India, December 2015.

[22] A. Kushwaha, A. Khare, O. Prakash, J. I. Song, and M. Jeon, "3D medical image fusion using dual tree complex wavelet

transform," in *2015 International Conference on Control, Automation and Information Sciences (ICCAIS)*, pp. 251–256, Changshu, China, October 2015.

[23] M. Amin-Naji and A. Aghagolzadeh, "Multi-focus image fusion using VOL and EOL in DCT domain," in *Proceedings of the International Conference on New Research Achievements in Electrical and Computer Engineering (ICNRAECE'16)*, pp. 728–733, Tehran, Iran, May 2016.

[24] L. Cao, L. Jin, H. Tao, G. Li, Z. Zhuang, and Y. Zhang, "Multi-Focus image fusion based on spatial frequency in discrete cosine transform domain," *IEEE Signal Processing Letters*, vol. 22, no. 2, pp. 220–224, 2015.

[25] M. Amin-Naji and A. Aghagolzadeh, "Multi-focus image fusion in DCT domain based on correlation coefficient," in *2015 2nd International Conference on Knowledge-Based Engineering and Innovation (KBEI)*, pp. 632–639, Tehran, Iran, November 2015.

[26] X. Jin, Q. Jiang, S. Yao et al., "Infrared and visual image fusion method based on discrete cosine transform and local spatial frequency in discrete stationary wavelet transform domain," *Infrared Physics & Technology*, vol. 88, pp. 1–12, 2018.

[27] Y. A. V. Phamila and R. Amutha, "Discrete cosine transform based fusion of multi-focus images for visual sensor networks," *Signal Processing*, vol. 95, pp. 161–170, 2014.

[28] Y. Jiang and M. Wang, "Image fusion using multiscale edge-preserving decomposition based on weighted least squares filter," *IET Image Processing*, vol. 8, no. 3, pp. 183–190, 2014.

[29] G. Petschnigg, R. Szeliski, M. Agrawala, M. Cohen, H. Hoppe, and K. Toyama, "Digital photography with flash and no-flash image pairs," *ACM Transactions on Graphics*, vol. 23, no. 3, pp. 664–672, 2004.

[30] M. Alrefaya, "Adaptive speckle reducing anisotropic diffusion filter for positron emission tomography images based on anatomical prior," in *2018 4th International Conference on Computer and Technology Applications (ICCTA)*, pp. 194–201, Istanbul, Turkey, May 2018.

[31] M. Xie and Z. Wang, "Edge-directed enhancing based anisotropic diffusion denoising," *Acta Electronica Sinica*, vol. 34, no. 1, pp. 59–64, 2006.

[32] E. Vakaimalar, K. Mala, and S. R. Babu, "Multifocus image fusion scheme based on discrete cosine transform and spatial frequency," *Multimedia Tools and Applications*, vol. 78, no. 13, pp. 17573–17587, 2019.

[33] D. P. Bavirisetti and R. Dhuli, "Fusion of infrared and visible sensor images based on anisotropic diffusion and Karhunen-Loeve transform," *IEEE Sensors Journal*, vol. 16, no. 1, pp. 203–209, 2016.

[34] B. Liu, W. J. Liu, and Y. P. Wei, "Construction of the six channel multi-scale singular valuedecomposition and its application in multi-focus image fusion," *Systems Engineering & Electronics*, vol. 37, no. 9, pp. 2191–2197, 2015.

[35] B. K. Shreyamsha Kumar, "Multifocus and multispectral image fusion based on pixel significance using discrete cosine harmonic wavelet transform," *Signal, Image and Video Processing*, vol. 7, pp. 1125–1143, 2013.

[36] D. P. Bavirisetti and R. Dhuli, "Two-scale image fusion of visible and infrared images using saliency detection," *Infrared Physics & Technology*, vol. 76, pp. 52–64, 2016.

[37] F. Nencini, A. Garzelli, S. Baronti, and L. Alparone, "Remote sensing image fusion using the curvelet transform," *Information Fusion*, vol. 8, no. 2, pp. 143–156, 2007.

[38] S. Rajkumar and S. Kavitha, "Redundancy discrete wavelet transform and contourlet transform for multimodality medical image fusion with quantitative analysis," in *2010 3rd International Conference on Emerging Trends in Engineering and Technology*, pp. 134–139, Goa, India, November 2010.

[39] J. Ma, Y. Ma, and C. Li, "Infrared and visible image fusion methods and applications: a survey," *Information Fusion*, vol. 45, no. 2, pp. 153–178, 2019.

WILEY | Hindawi

Research Article

Stock Forecasting Model FS-LSTM Based on the 5G Internet of Things

Hui Li [ID],[1] **Jinjin Hua** [ID],[2] **Jinqiu Li,**[1] **and Geng Li** [ID] [1]

[1]*School of Physics and Electronic Information Engineering, Henan Polytechnic University, Jiaozuo 454000, China*
[2]*School of Electrical Engineering and Automation, Henan Polytechnic University, Jiaozuo 454000, China*

Correspondence should be addressed to Geng Li; ligeng@hpu.edu.cn

This paper analyzed the development of data mining and the development of the fifth generation (5G) for the Internet of Things (IoT) and uses a deep learning method for stock forecasting. In order to solve the problems such as low accuracy and training complexity caused by complicated data in stock model forecasting, we proposed a forecasting method based on the feature selection (FS) and Long Short-Term Memory (LSTM) algorithm to predict the closing price of stock. Considering its future potential application, this paper takes 4 stock data from the Shenzhen Component Index as an example and constructs the feature set for prediction based on 17 technical indexes which are commonly used in stock market. The optimal feature set is decided via FS to reduce the dimension of data and the training complexity. The LSTM algorithm is used to forecast closing price of stock. The empirical results show that compared with the LSTM model, the FS-LSTM combination model improves the accuracy of prediction and reduces the error between the real value and the forecast value in stock price prediction.

1. Introduction

The wide application of information technology gives rise to the increase in data flow and the number of intelligent terminals. As a result, the fifth-generation (5G) mobile services come into being. According to global telecom operators, 5G communication technology will be officially commercialized around 2020 [1]. Owing to the fast transmission network, the emergence of the 5G network will promote the innovation and development of the Internet of Things (IoT) technology. The 5G network is identified as a core contributing factor in meeting the growing needs for the future IoT services, including high data rate, multiple-device attachment, and low delay service [2]. As 5G mobile communication network technology can provide users with sufficient network communication, it can greatly improve the network communication speed and quality, making the network data transmission changes more reliable.

With its great adaptability, IoT technology can be applied to different scenarios, such as construction domain [3], smart cities environments [4], smart communities [5],

and other areas of society, bringing much convenience for people. The utility of IoT technology requires massive information connection and high-speed network communication. The emergence of the 5G network can promote the innovation and development of IoT technology. 5G has the advantages of fast data convey rate, strong robustness, wide transmission range, and good security [6]. Thus, the application of 5G wireless systems can effectively improve the communication quality of the IoT, making the IoT technology more powerful. 5G is the basic access technology for IoT utilization [7]. What is more, the use of 5G communication network infrastructure can also reduce the cost of IoT construction and investment, consequently improving the efficiency of IoT construction. The integration of the 5G mobile communication network and IoT enables the IoT to make full use of the advantages of the 5G mobile communication network and enhance its own advantages.

With the increasing exploitation of the IoT, the advantages of big data technology have gradually become prominent. Big data involves many key technologies, including
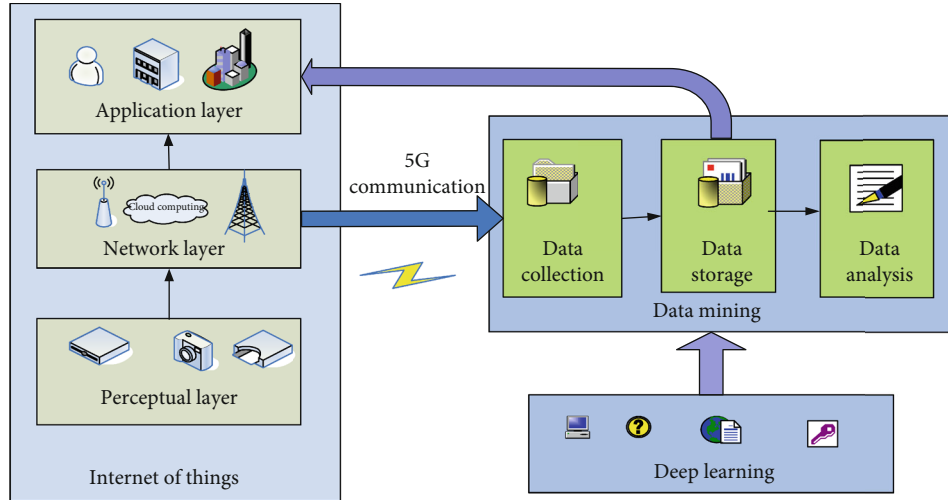
FIGURE 1: The relationship between 5G, IoT, and deep learning.

collection, storage, management, analysis, and mining. Big data usually relate to the use of predictive analytics, patral behavior research, or some other sophisticated data analysis tool, which can extract the valuable information from the massive data. 5G networks deal with big data at low cost. Besides, characteristics of 5G include low latency, high reliability, easy-to-update data, region spread, and improved mobile broadband [8]. The era of big data has aroused widespread interest in in-depth learning in different research fields. The deep integration with AI, cloud computing, big data, and deep learning is one of the important development directions of 5G.

Our contributions in this paper can be highlighted as follows:

(1) The development trend of 5G, IoT, and data mining and the influence of deep learning on data mining technology of IoT are analyzed

(2) A stock trend prediction method based on the feature selection (FS) and Long Short-Term Memory (LSTM) prediction model FS-LSTM to predict stock prices are put forth. First, we use the Tushare financial data package to obtain stock data. Then, the optimal feature set is selected to reduce the dimensionality of data. After that, the stock price is forecasted and the forecasting results are analyzed

(3) The application of 5G and IoT in stock forecasting is analyzed in aspects of data storage, efficiency, and processing speed

This paper falls into 6 parts. Section 2 describes some basic relevant algorithms related to the proposed idea. In Section 3, we illustrated in detail the design and implementation of the proposed prediction algorithm. The application of 5G and IoT in stock forecasting is analyzed in Section 4. Section 5 discusses the experimental results of our proposed FS-LSTM. Section 6 is the summary of the whole paper.

2. Related Work

2.1. The Integration Development of 5G, IoT, and Deep Learning. 5G is aimed at providing super ultralow delay technological schemes as well as fiber-like access data transmission speed, to connect over 100 billion facilities and deliver accordant experience across multiplex scenarios with improved capability and spend efficiency [9]. 5G mobile communication technology improves customer experience and system safety of communication technology, so it has been widely used in all walks of life [10]. A 5G-enabled IoT is devised to convey both 5G and IoT information and at the same time to reduce the whole IoT power consumption while maintaining 5G and IoT transmission rates steady [11]. 5G-enabled emotion-aware linked healthcare big data was designed. The proposed method will greatly promote 5G-based individualized and corresponding emotion-aware medical services [12]. With the development and popularization of 5G technology and IoT, new data mining algorithms were boosted [13]. Big data, IoT, and 5G are closely related to each other, for big data stems from the application of IoT technology.

5G will prove to be the mainstay of IoT, providing full links to all "things," surmounting place restrictions on time-space, and bringing about comprehensive, service-customized, and user-centric interconnections [14]. The relationship between 5G, IoT, and deep learning is shown in Figure 1. As shown in Figure 1, the entire system of the IoT constitutes three layers, namely, the perceptual layer, the transport layer, and the application layer. 5G communication provides technical support for network layer transmission. In the big data era, not all massive data are valuable. What is more important is to mine useful data via the deep learning algorithm. Among them, large data analysis methods based on deep learning have been developed more rapidly.

The development of 5G communication technology and IoT enables the application of the neural network and deep learning. IoT is extensively used in various fields, such as intelligent logistics, smart healthcare, pilotless driving,

industrial automation, and global positioning system (GPS) data aggregation [15]. Based on 5G communication agreements and data interchange criterion, with the convergence of the IoT and artificial intelligence (AI), the smart network performs much better communicating ability. To build an efficient intrusion detection system over big data, literature [16] proposed a classification algorithm based on data clustering and data reduction. IoT, as an expansion of Internet applications, is in a great stage of development. To cut down the resource expenditure with a reasonable implementation planning, an IoT-based smart energy consumption controlling and energy supervisory method has been proposed by investigating the energy use of a house [17]. Literature [18] designed a refreshing pattern, 5G Intelligent Internet of Things (5G I-IoT), to handle big data and promote communication channels effectively. IoT is a catalyst for the generation of big data because big data originates from the application of IoT. The use of IoT gives birth to large amount of data which contains significant information. The fast development of IoT and big data is owing to 5G communication.

2.2. Research on Stock Forecasting.
As an important part of capital market construction, the change of stock market is of extraordinary significance to national macroeconomic development, financial institutions, and individuals. The high instability and nondeterminacy of stock price make it a difficult matter in the domain of finance and data mining. Thus, forecasting stock prices in order to avoid the investment risk to the greatest extent and improve the investment returns becomes the latest research focus.

Traditional forecasting methods have the limitations to balance the randomness and regularity of controlling price changes [19]. In recent years, the artificial neural network (ANN) has achieved remarkable results in the field of artificial intelligence algorithm whose predictive analysis capability has greatly promoted the application of technologies like big data. So stock forecasting methods based on ANN and related technologies have been widely studied, which make up for the shortcomings of traditional forecasting techniques and increase the reliability and accuracy of stock forecasting [20]. Literature [21] implements an LSTM model on time series trend forecasting problems, and the results outperform that of the conventional autoregression models. Moreover, some portfolio models have been applied to stock trend prediction. They all achieved good results. Literature [22] combines price prediction based on historical and real-time data along with news analysis, and LSTM was used for predicting; this approach incorporated into the existing strategies will encourage quant traders to invest and maximize their profit. In literature [23], a deep learning method for stock price prediction was proposed. In this literature, a total of 14 different deep learning models were presented and all stocks in the Standard & Poor's (S&P) BSE-BANKEX index were evaluated.

3. Stock Prediction Algorithms

3.1. Feature Selection.
Machine learning is a process of data processing and model training. Data processing includes feature extraction and feature representation. In model training, there are a set of processes such as training strategy, training model, and algorithm correlation. A good prediction model is closely related to feature selection and feature representation. The method of feature selection is to select a subset from the original feature data set to reduce the number of attributes in the feature data set. The purpose of feature selection is to increase the accuracy of prediction, to design an efficient prediction model, and to have a better understanding and interpretation of the model as well.

Optimal feature subset selection was performed using a correlation coefficient and feature importance ranking. The correlation coefficient is a quantity that studies the degree of linear correlation between variables. It is usually expressed by the letter r, which is shown in

$$r(X, Y) = \frac{\text{cov}(X, Y)}{\sqrt{\text{var}[X] \text{var}[Y]}} \tag{1}$$

$$\text{cov}(X, Y) = \frac{\sum_{i=1}^{n}(x_i - \bar{x})(yi - \bar{y})}{n - 1} \tag{2}$$

where $\text{cov}(X, Y)$ is the covariance of X and Y, $\text{var}[X]$ is the variance of X, and $\text{var}[Y]$ is the variance of Y. $r(X, Y)$ is a quantity that can characterize the degree of a close linear relationship between X and Y. If X and Y are not related, $r(X, Y) = 0$. It is generally considered that there is no linear relationship between X and Y. If $r(X, Y) \leq 1$, it is generally considered that there is a linear relationship between X and Y. The closer the value of $r(X, Y)$ is to 1, the more linear the two variables are. For each pair of highly correlated features, one of them is identified and removed.

3.2. LSTM Network.
LSTM is a special type of recurrent neural network (RNN). It solves the problem of gradient explosion and gradient disappearance in the process of long-sequence RNN training. When the number of network layers increases, the perception ability of the following nodes to the front nodes becomes weak and the phenomenon that the previous information will be forgotten over time appears. LSTM adds memory units to each neuron unit of the hidden layer on the basis of ordinary RNN, so that the memory information on time series can be controlled. The schematic diagram of memory units of LSTM is shown in Figure 2. C_{t-1} and h_{t-1} represent the state of the memory unit at the last moment; C_t and h_t represent the state of the hidden layer, respectively.

Each time the input gate i_t, the forget gate f_t, and the output gate o_t are passed between the units, the memory and forgetting of the previous information and the current information can be controlled.

The calculation formulas of the forget gate f_t, the input gate i_t, and the output gate o_t are defined in

$$f_t = \sigma\left(W_{xf}x_t + W_{hf}h_{t-1} + b_f\right),$$

$$i_t = \sigma\left(W_{xi}x_t + W_{hi}h_{t-1} + b_i\right), \tag{3}$$

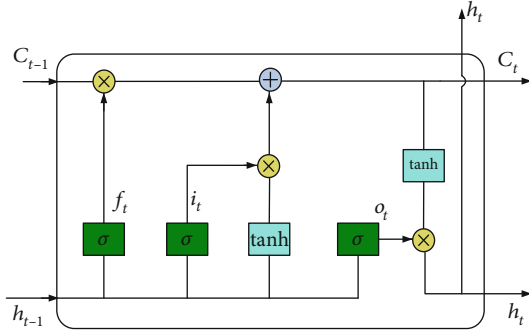$$o_t = \sigma\left(W_{xo}x_t + W_{ho}h_{t-1} + b_o\right).$$

Figure 2: LSTM memory unit structure diagram.

Among them, σ is the sigmoid activation function, x_t is the input at time t, W_{xf} is the weight matrix from the input x to the forget gate f_t, W_{hf} is the weight matrix from the hidden layer state to the forgetting gate, and b_f is the linear bias of the forgetting gate. W_{xi} is the weight matrix from the input x to the input gate, W_{hi} is the weight matrix from the hidden state to the input gate, and b_i is the linear bias of the input gate. W_{xo} is the weight matrix from the input to the output gate, W_{ho} is the weight matrix from the hidden state to the output gate, and b_o is the linear bias of the output gate.

The state value of t time memory unit c_t consists of two parts: one is the state value of the memory unit at the previous time c_{t-1} and the other is the input gate waiting for update information $\tilde{c}_t$, which is controlled by the input gate and the forgetting gate, respectively. The current state of the memory unit c_t can be obtained by calculating the following formula:

$$
\begin{aligned}
\tilde{c}_t &= \tanh\left(W_{xc}x_t + W_{hc}h_{t-1} + b_c\right), \\
c_t &= i_t * \tilde{c}_t + f_t * c_{t-1}.
\end{aligned}
\tag{4}
$$

Among them, W_{xc} is the weight matrix from input X to the memory unit, W_{hc} is the weight matrix from the hidden layer to the memory unit, and b_c is the linear bias of the memory unit.

Finally, the current state of the hidden layer h_t is determined by the state of the output gate o_t and the current storage unit c_t. The calculation formula is shown in

$$
h_t = o_t * \tanh\left(c_t\right).
\tag{5}
$$

4. Application of 5G and IoT in Stock Forecasting

IoT technology has penetrated into people's production and life. With IoT technology, different types of data are exchanged and communicated through sensor nodes. Under the continuous development of IoT technology, IoT-based stock forecasting will become a new trend. It proves that it is feasible to mine useful information from stock historical data for stock prediction. The combination of 5G and IoT will promote the rapid development of stock forecasting industry. The application of 5G and IoT in stock forecasting is mainly reflected in the following aspects:

(1) In order to carry out data mining, data must be stored first. Unlike previous data storage methods, IoT stores scattered data in different network nodes to form virtual storage. Distributed storage makes it possible to exchange and share data between different regions and networks

(2) With the development of IoT, traditional methods will be replaced for it is hard to meet the requirements of data management and processing. The integration of 5G communication and IoT can build a secure, fast, and reliable transmission channel, therefore improving the time and efficiency of stock forecasting

(3) The IoT and 5G will continuously promote the automation of the stock forecasting system. By pushing relevant content to users' mobile apps or other communication platforms, users can get the latest and most relevantly firsthand information at the fastest speed

5. Empirical Analysis

5.1. Data Preprocessing. From the Shenzhen Component Index market, this paper chooses the transaction data of Ping An Bank, Shenzhen Component Index, Petrochemical Machinery, and Jidian Shares from December 2, 2016, to May 31, 2019, as experimental subjects. The original data in this paper are all derived from the Tushare financial data package, which contains 608 trading days of transaction information. The first 90% data is selected as the training set and the last 10% data as the test set.

Owing to the characteristics of intuition, concreteness, and easy application when judging the trend of stock market, technical indicators are widely used in stock market forecasting and analysis. Different technical indicators have their own scope of application and constraints. In the process of stock trend feature representation, a single technical index cannot guarantee the comprehensiveness and accuracy of the feature representation. Therefore, selecting several representative and easy-to-quantify technical indicators can improve the complementarity of data and the accuracy of feature representation. This paper constructs a feature set for forecasting based on 17 technical indicators (MA, CCI, ADX, RSI, ROC, AROONOSC, MOM, ATR, OSC, OBV, BOP, ULTOSC, MFI, ATR, K%, BETA, and CR) commonly used in stock market. These indicators comprehensively reflect the information of stock trend change and can include most of the influencing factors of stock trend forecasting. The final optimal feature subset is MA, RSI, CCI, K%, and CR, which can summarize most

of the information of the original data. The expression of MA, RSI, CCI, K%, and CR is shown in

$$MA = \sum_{i=1}^{n} \frac{C_n}{n},$$

$$RSI = 100 - \frac{100}{\left(1 + \left(\sum_{i=0}^{n-1} U_{p_{t-1}}/n\right)\right)/\left(\sum_{i=0}^{n-1} D_{w_{t-i}}/n\right)},$$

$$CCI = \frac{M_t - SM_{t-1}}{0.015 D_t},$$ (6)

$$K\% = \frac{\sum_{i=1}^{n} (2K_{i-1} + RSV_i)}{3},$$

$$CR = \frac{\sum_{i=0}^{n-1} (H_i - M_i)}{\sum_{i=0}^{n-1} (M_i - L_i)} \times 100,$$

where n denotes n day and C_n denotes the sum of n day closing prices. U_{p_t} is the increase of the first day compared with the previous day. D_{w_t} is the decline of the first day compared with the previous day. M_t is the average of the highest, lowest, and closing prices. H_t and L_t indicate the highest and lowest price of t day, respectively.

The selected data are used to construct the feature set. As the calculation methods of each index are different, the feature set constructed according to the technical index presents different range of values, of which the range varies greatly. The huge quantity difference will lead to the complexity of parameter optimization of the algorithm model, making it easy to overfit, which will have a negative impact on the final prediction results. Therefore, this paper uses formula (7) to normalize the feature quantities and convert each dimension feature component to $[-1, 1]$.

$$x_d = \frac{v_d - v_{d\_min}}{v_{d\_max} - v_{d\_min}}.$$ (7)

In the formula, v_{d_min} is the minimum value of the d-dimensional eigenvalue and v_{d_max} is the maximum value of the d-dimensional eigenvalue.

5.2. Stock Price Forecast. In order to test the effectiveness of the proposed method, the optimal feature subset is taken as input variable, the input time span is 30 days, and the opening price of the day is taken as output variable. The model consists of four layers: one LSTM layer and three dense layers. When training the LSTM model, dropout parameters and regular terms are added to avoid overfitting. The stock price of the test set is predicted by the trained model, and the traditional LSTM prediction model was compared. Mean absolute error (MAE), mean square error (MSE), and root mean square error (RMSE) were used as evaluation indexes to evaluate the validity of the
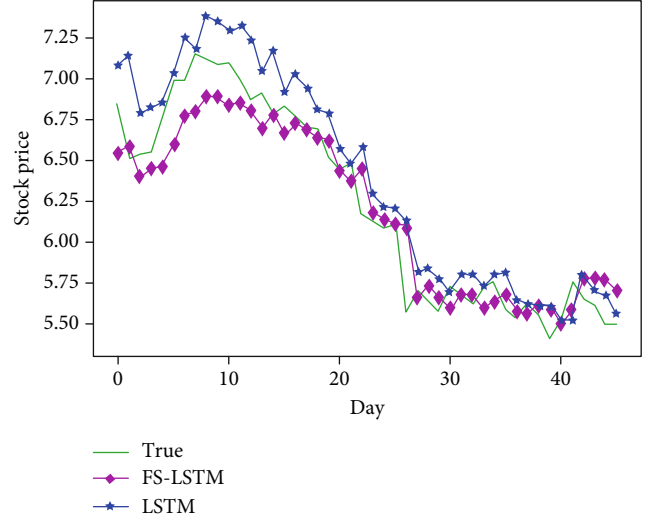
FIGURE 3: Prediction result of Shenzhen Zhenye (Group).
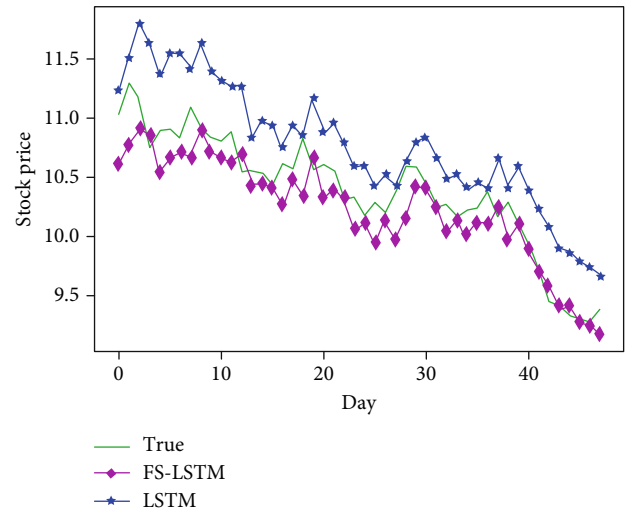
FIGURE 4: Prediction result of Ping An Bank.

model. The formulas for calculating the three evaluation indexes are shown in

$$MAE = \frac{1}{N} \sum_{i=1}^{N} |y_i - \hat{y}_i|,$$

$$MSE = \frac{1}{N} \sum_{i=1}^{N} (y_i - \hat{y}_i)^2,$$ (8)

$$RMSE = \sqrt{\frac{1}{N} \sum_{i=1}^{N} (y_i - \hat{y}_i)^2}.$$

Among them, Y_i and $\hat{Y}_i$ represent the true value and the predicted value, respectively.

The predicted results of these four stocks are shown in Figures 3–6, and the error analysis is shown in Tables 1 and
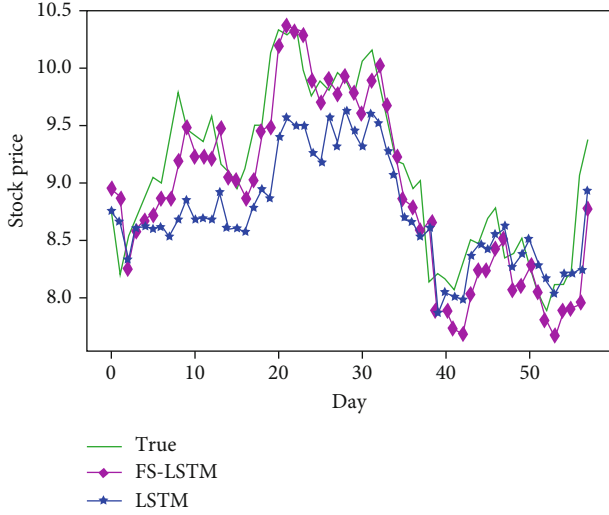
FIGURE 5: Prediction result of Sinopec Oilfield Equipment Corporation.
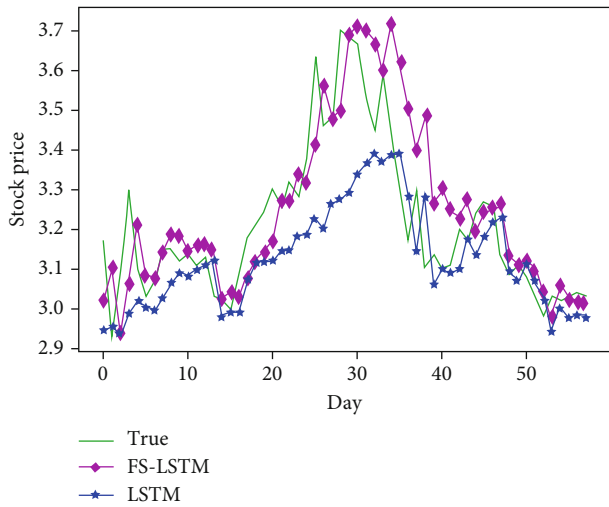
FIGURE 6: Prediction result of Jilin Electric Power.

TABLE 1: Stock prediction error table (LSTM).

Stock name	Sinopec Oilfield Equipment Corporation	Jilin Electric Power	Ping An Bank	Shenzhen Zhenye (Group)
MSE	0.260	0.023	0.190	0.052
MAE	0.423	0.113	0.388	0.184
RMSE	0.510	0.152	0.437	0.229

2. From Figures 3–6, it can be seen that the model can accurately predict the overall trend of four stock prices with different market capitalization scales. The predicted value of the FS-LSTM model is closer to the real value, indicating a better overall fitting effect. As can be seen from Tables 1 and 2, the prediction error of the FS-LSTM model is smaller

TABLE 2: Stock prediction error table (FS-LSTM).

Stock name	Sinopec Oilfield Equipment Corporation	Jilin Electric Power	Ping An Bank	Shenzhen Zhenye (Group)
MSE	0.123	0.016	0.052	0.033
MAE	0.280	0.093	0.179	0.143
RMSE	0.351	0.012	0.230	0.182

compared with that of the traditional LSTM model. Comparatively, the prediction effect of the Shenzhen Component Index is the best which is attributed to the small stock price volatility. Using this model, the overall trend of stocks with different market values can also be accurately predicted, proving that the model can not only predict the stock price but also reliably predict the stock price of different scales, demonstrating its generalization and reliability. The application of the FS-LSTM model in stock forecasting can fully analyze the original data of stock and improve the forecasting accuracy of stock price. The experiment shows that the combination model has obvious advantages in dealing with data with many indexes and complex noise.

6. Conclusion

Firstly, this paper analyzes the impact of 5G development on the IoT. The integration of 5G, IoT, and deep learning is a new development trend. 5G and IoT have many advantages in stock forecasting. Then, this paper presents a FS-LSTM combination model based on feature selection and LSTM prediction for stock trend prediction. The optimal feature subset for stock trend prediction is obtained through feature selection. The prediction effect of the optimal feature subset is verified by the test set. The experimental results show that the forecasting model proposed in this paper is superior to the traditional LSTM forecasting model in terms of forecasting effect. Using this method, the best feature subset for forecasting can be found and the impact of redundant information on stock trend forecasting can be reduced. As a result, the accuracy of forecasting is improved. Finally, the application of 5G and IoT in stock forecasting is analyzed.

Stock market is a complex and dynamic system. The shortcoming of this work is that this paper is only based on technical indicators and does not consider other factors. The future work involves including newly developed computing models. The future work also involves minimizing computation time of FS-LSTM. It is concluded that 5G, IoT, and stock forecasting will be more closely linked in the future.

Data Availability

The research data used to support the findings of this study have been deposited in the Tushare repository (http://tushare.org/).

Conflicts of Interest

The authors declare that they have no conflicts of interest.

Acknowledgments

References

[1] Y. Zikria, S. Kim, M. Afzal, H. Wang, and M. Rehmani, "5G mobile services and scenarios: challenges and solutions," *Sustainability*, vol. 10, no. 10, pp. 3626–3629, 2018.

[2] J. Ni, X. Lin, and X. S. Shen, "Efficient and secure service-oriented authentication supporting network slicing for 5G-enabled IoT," *IEEE Journal on Selected Areas in Communications*, vol. 36, no. 3, pp. 644–657, 2018.

[3] V. K. Reja and K. Varghese, "Impact of 5G technology on IoT applications in construction project management," in *36th International Symposium on Automation and Robotics in Construction (ISARC 2019)*, pp. 209–217, 2019.

[4] D. Minoli and B. Occhiogrosso, "Practical aspects for the integration of 5G networks and IoT applications in smart cities environments," *Wireless Communications and Mobile Computing*, vol. 2019, 30 pages, 2019.

[5] C. Tsai and M. Moh, "Load balancing in 5G cloud radio access networks supporting IoT communications for smart communities," in *2017 IEEE International Symposium on Signal Processing and Information Technology (ISSPIT)*, pp. 259–264, Bilbao, Spain, 2017.

[6] G. Yan, "Simulation analysis of key technology optimization of 5G mobile communication network based on Internet of things technology," *International Journal of Distributed Sensor Networks*, vol. 15, no. 6, pp. 1–11, 2019.

[7] S. Borkar and H. Pande, "Application of 5G next generation network to Internet of things," in *2016 International Conference on Internet of Things and Applications (IOTA)*, pp. 443–447, Pune, India, 2016.

[8] S. Rashid and S. A. Razak, "Big data challenges in 5G networks," *2019 Eleventh International Conference on Ubiquitous and Future Networks (ICUFN)*, 2019, pp. 152–157, Zagreb, Croatia, Croatia, 2019.

[9] A. Younis, N. Abuzgaia, R. Mesleh, and H. Haas, "Quadrature spatial modulation for 5G outdoor millimeter-wave communications: capacity analysis," *IEEE Transactions on Wireless Communications*, vol. 16, no. 5, pp. 2882–2890, 2017.

[10] M. Qiu, D. Cao, H. Su, and K. Gai, "Data transfer minimization for financial derivative pricing using Monte Carlo simulation with GPU in 5G," *International Journal of Communication Systems*, vol. 29, no. 16, pp. 2364–2374, 2015.

[11] X. Liu and X. Zhang, "Rate and energy efficiency improvements for 5G-based IoT with simultaneous transfer," *IEEE Internet of Things Journal*, vol. 6, no. 4, pp. 5971–5980, 2019.

[12] M. S. Hossain and G. Muhammad, "Emotion-aware connected healthcare big data towards 5G," *IEEE Internet of Things Journal*, vol. 5, no. 4, pp. 2399–2406, 2018.

[13] Z. Wang, W. Liang, Y. Zhang et al., "Data mining in IoT era: a method based on improved frequent items mining algorithm," in *2019 5th International Conference on Big Data and Information Analytics (BigDIA)*, pp. 120–125, Kunming, China, China, 2019.

[14] M. R. Palattella, M. Dohler, A. Grieco et al., "Internet of things in the 5G era: enablers, architecture, and business models," *IEEE Journal Selected Areas Communications*, vol. 34, no. 3, pp. 510–527, 2016.

[15] A. A. Khan, M. H. Rehmani, and A. Rachedi, "Cognitive-radio-based Internet of things: applications, architectures, spectrum related functionalities, and future research directions," *IEEE Wireless Communications*, vol. 24, no. 3, pp. 17–25, 2017.

[16] Q. Wang, X. Ouyang, and J. Zhan, "A classification algorithm based on data clustering and data reduction for intrusion detection system over big data," *KSII Transactions on Internet and Information Systems*, vol. 13, no. 7, 2019.

[17] M. Taştan, "Internet of things based smart energy management for smart home," *KSII Transactions on Internet and Information Systems*, vol. 13, no. 6, pp. 2781–2798, 2019.

[18] D. Wang, D. Chen, B. Song, N. Guizani, X. Yu, and X. du, "From IoT to 5G I-IoT: the next generation IoT-based intelligent algorithms and 5G technologies," *IEEE Communications Magazine*, vol. 56, no. 10, pp. 114–120, 2018.

[19] W. Lertyingyod and N. Benjamas, "Stock price trend prediction using artificial neural network techniques: case study: Thailand stock exchange," in *2016 International Computer Science and Engineering Conference (ICSEC)*, pp. 1–6, 2016.

[20] N. Srinivasan and C. Lakshmi, "Stock prediction and analysis using intermittent training data with artificial neural networks," in *2017 International Conference on Innovations in Information, Embedded and Communication Systems (ICIIECS)*, pp. 1–4, Coimbatore, India, 2017.

[21] Y. Liu, Z. Su, H. Li, and Y. Zhang, "An LSTM based classification method for time series trend forecasting," in *2019 14th IEEE Conference on Industrial Electronics and Applications (ICIEA)*, pp. 402–406, 2019.

[22] S. Sarode, H. G. Tolani, P. Kak, and L. CS, "Stock price prediction using mechine learning techniques," in *International Conference on Intelligent Sustainable Systems (ICISS 2019)*, pp. 177–181, 2019.

[23] A. J. Balaji, D. S. H. Ram, and B. B. Nair, "Applicability of deep learning models for stock price forecasting an empirical study on BANKEX data," *Procedia Computer Science*, vol. 143, pp. 947–953, 2018.

Research Article

Channel Estimation Performance Analysis of FBMC/OQAM Systems with Bayesian Approach for 5G-Enabled IoT Applications

Han Wang [iD],[1,2] **Wencai Du** [iD],[2] **Xianpeng Wang**,[3] **Guicai Yu**,[1] and **Lingwei Xu** [iD][4]

[1]*College of Physical Science and Engineering, Yichun University, 576 Xuefu Road, Yichun, Jiangxi 336000, China*
[2]*Institute of Data Science, City University of Macau, Avenida Padretomas Pereira, Taipa, Macau 999078, China*
[3]*State Key Laboratory of Marine Resource Utilization in South China Sea, Hainan University, 58 Renming Road, Haikou, Hainan 570228, China*
[4]*Department of Information Science and Technology, Qingdao University of Science and Technology, 99 Songling Road, Qingdao, Shandong 266061, China*

Correspondence should be addressed to Han Wang; hanwang1214@gmail.com and Wencai Du; georgedu@city.mo

A filter bank multicarrier (FBMC) with offset quadrature amplitude modulation (OQAM) (FBMC/OQAM) is considered to be one of the physical layer technologies in future communication systems, and it is also a wireless transmission technology that supports the applications of Internet of Things (IoT). However, efficient channel parameter estimation is one of the difficulties in realization of highly available FBMC systems. In this paper, the Bayesian compressive sensing (BCS) channel estimation approach for FBMC/OQAM systems is investigated and the performance in a multiple-input multiple-output (MIMO) scenario is also analyzed. An iterative fast Bayesian matching pursuit algorithm is proposed for high channel estimation. Bayesian channel estimation is first presented by exploring the prior statistical information of a sparse channel model. It is indicated that the BCS channel estimation scheme can effectively estimate the channel impulse response. Then, a modified FBMP algorithm is proposed by optimizing the iterative termination conditions. The simulation results indicate that the proposed method provides better mean square error (MSE) and bit error rate (BER) performance than conventional compressive sensing methods.

1. Introduction

To date, the application of mobile communication systems in the field of Internet of Things (IoT) is not in-depth [1, 2]. Although Fourth Generation (4G) has greatly improved the network speed, there is still much room for improvement in network reliability and latency. Fifth Generation (5G) systems [3–8] are now being deployed which can well meet the demands of IoT, such as low latency, high reliability network, and large bandwidth. The full opening of the 5G era is accelerating the application and popularization of IoT, artificial intelligence (AI), and other technologies [9–12]. However, the development of IoT requires suitable infrastructure [13, 14] including sensors for data acquisition and wireless communication technology. Currently, multicarrier modulation has been widely used in wireless communication systems. The filter bank multicarrier (FBMC) with offset quadrature

amplitude modulation (OQAM), denoted as FBMC/OQAM, has captured significant attention [15, 16], due to its potential as an option to orthogonal frequency division multiplexing (OFDM). Although the Third Generation Partnership Project (3GPP) has indicated that filtered OFDM will be utilized in 5G systems, interest in FBMC for future mobile communication systems has not declined [17, 18].

FBMC technology employs a good time-frequency prototype filter, which has many features such as low spectral side lobes, high spectrum efficiency, and robustness to frequency offset [19]. However, the nonstrict orthogonality of the system leads to the existence of imaginary interference. This interference can be mitigated during channel estimation (CE), but this requires that the channel coefficients be estimated in the complex domain. Interference reduction is challenging in FBMC systems, particularly when multiple-input multiple-output (MIMO) communications are involved.

There has been significant effort to overcome this problem, and both preamble-based [20–27] and compressive sensing-(CS-) based approaches have been proposed [28–33].

Numerous preamble-based schemes have been proposed for CE. The interference approximation method (IAM) [20] and interference cancellation method (ICM) [21] are two well-known algorithms for interference mitigation. They reduce the imaginary interference or exploit this interference to improve CE performance. Combined with these methods, a novel preamble structure for FBMC systems was proposed in [22]. Because more channel coefficients need to be determined, CE in MIMO systems is more complicated than in single-input single-output (SISO) systems. In addition, imaginary interference from multiple antennas makes CE in MIMO-FBMC systems difficult. Thus, there has been significant research on CE for MIMO systems. In [23], IAM preamble variants were investigated and the characteristic due to the extension to MIMO systems was studied. An optimized preamble for a frequency division multiplexing MIMO system was proposed in [24]. In [25], an interference elimination MIMO preamble structure was proposed to improve CE performance. In addition, an efficient sequence design for a MIMO-FBMC system was proposed in [26]. However, the use of a preamble reduces spectrum efficiency, and it is difficult to remove the intrinsic interference. There is consensus [27] that preamble-based CE for MIMO systems is inefficient.

Many works had been devoted to improve the CE performance in FBMC systems. In [34], the authors proposed a blind CE method by utilizing spatial diversity to introduce data redundancy. However, the method could not provide satisfactory CE performance. By utilizing the sparse channel characteristics, the CS approach is explored to promote the CE performance. Most works [35–37] were reported on CE in OFDM systems. Only few studies can be found for FBMC systems. In [28], a traditional orthogonal matching pursuit (OMP) method was utilized for CE. The results obtained showed that compared with the traditional preamble structure scheme, this approach could significantly improve the CE performance. In [29], a sparse adaptive CS algorithm was put forward for high CE. This algorithm is based on the compressive sampling matching pursuit (CoSaMP) and sparsity adaptive matching pursuit (SAMP) methods. Besides, a scattered pilot CE method based on CS for FBMC was proposed in [30] by utilizing the wireless channel sparsity. In [31], the authors developed two distinctive compressive sensing algorithms to estimate channel frequency response in FBMC systems. Simulations verified the superiority of the two algorithms. In [32], an effective CS-based CE method was given for MIMO systems. A sparse adaptive scheme for CE in MIMO systems was proposed in [33]. However, no work has been reported on Bayesian compressive sensing (BCS) for CE in FBMC systems. As a special CS method, BCS, which utilizes statistical information of sparse channels as prior knowledge, can achieve better recovery effect than traditional CS methods in many applications [38, 39].

Motivated by those above, in this paper, we explore the statistical information of sparse channels for CE. The main contributions of this paper are listed as follows:

(1) Based on Bayesian CS approach, we propose an iterative fast Bayesian matching pursuit approach for high channel estimation in FBMC and its MIMO scenario. As far as we know, the Bayesian approach for high CE in FBMC systems has not yet been investigated

(2) To evaluate the performance of the proposed Bayesian approach, well-known CS methods and the least square (LS) method are utilized for comparison. Moreover, mean square error (MSE) and bit error rate (BER) are adopted to assess the CE performance. Simulations verify that the Bayesian approach can offer better both MSE and BER performance than other well-known CS approaches

The rest of this paper is organized as follows. Section 2 presents the system model, including FBMC and MIMO-FBMC systems. Section 3 reviews the CS-based channel estimation method. In Section 4, a fast Bayesian matching pursuit channel estimation approach is proposed. In Section 5, the simulation comparisons are carried out and the results are analyzed. Finally, Section 6 gives the conclusions.

2. System Model

2.1. FBMC System. The FBMC signal can be expressed as

$$s(t) = \sum_{m=0}^{N-1} \sum_{n} d_{m,n} g_{m,n}(t), \tag{1}$$

where N denotes the number of subcarriers, $g_{m,n}(t)$ represents the time-frequency prototype filter, and $d_{m,n}$ represents the real-valued OQAM symbol. The $(.)_{m,n}$, in which m represents the subcarrier index and n represents the symbol time index, denotes the (m, n)th frequency-time (FT) point.

The filter functions $g_{m,n}$ are orthogonal in the real domain with

$$\Re\left\{\left\langle g_{m,n} \big| g_{m_0,n_0}\right\rangle\right\} = \Re\left\{\sum_{t} g_{m,n}(t) g_{m_0,n_0}^*(t)\right\} = \delta_{m,m_0}\delta_{n,n_0}, \tag{2}$$

where $\Re(\cdot)$ represents the real part of a complex number and δ is the Kronecker delta function with $\delta_{m,m_0} = 1$, if $m = m_0$ and $\delta_{m,m_0} = 0$. Note that even without channel distortion, there is still imaginary intercarrier interference at the output of the filter bank. The weight of the interference is given by

$$\langle g \rangle_{m,n}^{m_0,n_0} = -j\left\langle g_{m,n} \big| g_{m_0,n_0}\right\rangle, \tag{3}$$

where $\langle g_{m,n} | g_{m_0,n_0}\rangle$ denotes an imaginary term for $(m, n) \neq (m_0, n_0)$. The values of interference weights can be

calculated based on the prototype filter g, and thus, for all m, the interference weights are given by

$$
\begin{matrix}
(-1)^m \varepsilon & 0 & -(-1)^m \varepsilon, \\
(-1)^m \delta & -\beta & (-1)^m \delta, \\
-(-1)^m \gamma & d_{m,n} & (-1)^m \gamma, \\
(-1)^m \delta & \beta & (-1)^m \delta, \\
(-1)^m \varepsilon & 0 & -(-1)^m \varepsilon.
\end{matrix} \quad (4)
$$

Generally, $\beta, \gamma > \delta$. In simulation, $\gamma = 0.5004$, $\beta = 0.3183$, $\delta = 0.2501$, and $\varepsilon = 0$ for the design of g.

Then, the received signal is given by

$$
r(t) = \sum_{k}^{K-1} s(t-k)h(t) + w(t), \quad (5)
$$

where K is the number of channel taps, $w(t)$ is the additive white Gaussian noise (AWGN), and $h(t)$ is the time domain impulse response of the multipath channel. The channel can be described as

$$
h(t) = \sum_{k=0}^{K-1} a_k(t)\delta(\tau - \tau_k), \quad (6)
$$

where $a_k(t)$ denotes the complex amplitude of the kth path, $\delta(\cdot)$ is the Kronecker delta, and τ_k represents the delay of the kth path. It is assumed that it is a complex Gaussian process of wide-sensing stationary (WSS), and the channel paths are independent. Assuming that the length of channel impulse response is L, and the channel $\mathbf{h} = [h_0, h_1, \cdots h_{L-1}]^T$.

2.2. MIMO-FBMC System. For a $N_t \times N_r (N_t \leq N_r)$ spatial multiplexing MIMO system, the baseband signal on the n_tth branch can be expressed as

$$
s^{n_t}(t) = \sum_{m=0}^{N-1} \sum_{n} d_{m,n}^{n_t} g_{m,n}(t), \quad (7)
$$

where $n_t = [1, 2, \cdots, N_t]$ and $d_{m,n}^{n_t}$ is the real-valued FBMC/-OQAM symbol on the n_tth transmit antenna conveyed by subcarrier m during symbol time n. N is the number of subcarriers, and

$$
g_{m,n}(t) = g(t - n\tau_0)e^{i2\pi m F_0 t}e^{j\phi_{m,n}}, \quad (8)
$$

where $g(t)$ is a symmetric real-valued pulse filter, F_0 is the subcarrier spacing with $F_0 = 1/T_0 = 1/2\tau_0$, and $\phi_{m,n}$ is an additional phase term. T_0 is the OFDM symbol duration, and τ_0 denotes the time offset between the real and imaginary parts of an FBMC/OQAM symbol.

The received signal can be expressed as

$$
r^{n_r}(t) = \sum_{n_t=1}^{N_t} \sum_{m=0}^{N-1} \sum_{n} H_{m,n}^{n_r,n_t}(t) d_{m,n}^{n_t} g_{m,n}(t) + \eta^{n_r}(t), \quad (9)
$$

with

$$
H_{m,n}^{n_r,n_t}(t) = \int_0^{\tau_{\max}} h_{m,n}^{n_r,n_t}(t,\tau)e^{-2j\pi m F_0 \tau}d\tau, \quad (10)
$$

where $h_{m,n}^{n_r,n_t}(t,\tau)$ denotes the channel impulse response; n_r and n_t denote the receive and transmit antennas, respectively; $\eta^{n_r}(t)$ is the channel noise; and $H_{m,n}^{n_r,n_t}(t)$ is the complex channel response at time t. We assume a slowly varying channel, so we omit t for brevity giving $H_{m,n}^{n_r,n_t}(t) = H_{m,n}^{n_r,n_t}$.

3. CS-Based Channel Estimation

Classical CS theory indicated that a K-spare signal h could be stably reestablished as

$$
y = \Phi h + w, \quad (11)
$$

with the precondition that Φ should meet the Restricted Isometry Property (RIP), Φ is a matrix with M rows and N columns, $M \ll N$, and w is noise.

Equation (5) in matrix form can be expressed as

$$
R = XH + W, \quad (12)
$$

with $R = [r(0), r(1), \cdots, r(N-1)]^T$, $X = \text{diag}(x(0), x(1), \cdots, x(N-1))$, W represents a $N \times N$ dimension noise matrix with zero mean and σ^2 variance, and $H = F_{NL}h$ is the channel frequency response, with F_{NL} being an L-row discrete Fourier transform matrix, and L denotes the channel length.

Let P be the number of pilot signals and φ the $P \times N$ pilot matrix with $\varphi = (e_{s_1}, e_{s_2}, \cdots, e_{s_p})$. For the N_c subcarriers, φ is used to select the position of the pilot, and $s_i (i = 1, 2, \cdots, P)$ represents the position of the ith pilot. Then, equation (12) can be written as follows:

$$
R_P = X_P F_p h + W_P, \quad (13)
$$

where R_P denotes the LS estimation channel value, $R_P = \varphi R$, and $W_P = \varphi W$. X_P denotes a diagonal matrix, with $X_P = \varphi X \varphi^T$, and the diagonal elements are pilot values, $F_P = \varphi F_{NL}$.

Convert (13) to

$$
R_P = Fh + W_P, \quad (14)
$$

where $F = X_P F_P$, R_P and F are available during transmission, and h represents the multipath channel impulse response. Then, the CS recovery algorithm can be used to recover h.

Similarly, in MIMO systems, the CS method is also based on the above analysis. The received signal in (7) can be written as

$$R^{n_r} = X^{n_t} H^{n_r, n_t} + \eta^{n_r}, \tag{15}$$

where H^{n_r, n_t} is the channel frequency response given by $H^{n_r, n_t} = F_{NL} h^{n_r, n_t}$, $X^{n_t} = \text{diag}\,(x^1(0), x^2(1), \cdots, x^{n_t}(N-1))$, $R^{n_r} = [r^1(0), r^2(1), \cdots, r^{n_r}(N-1)]^T$, F_{NL} is the $N \times L$ discrete Fourier transform matrix, and η^{n_r} is an $N \times N$ noise matrix with zero mean and variance σ^2.

Letting P be the number of pilot signals, equation (15) can be rewritten as

$$R_P^{n_r} = X_P^{n_t} F_p h^{n_r, n_t} + \eta_P, \tag{16}$$

where $R_P^{n_r} = \varphi R^{n_r}$ is the received pilot signals, $R_P^{n_r}$ is the LS estimated channel values, $\eta_P = \varphi \eta^{n_r}$, $X_P^{n_t}$ is a diagonal matrix with $X_P^{n_t} = \varphi X^{n_t} \varphi^T$, and the pilot values are $F_P = \varphi F_{NL}$. Equation (16) can be expressed as

$$R_P^{n_r} = F h^{n_r, n_t} + \eta_P, \tag{17}$$

where $F = X_P^{n_t} F_p$ and h^{n_r, n_t} is the channel impulse response. If $R_P^{n_r}$ and F are available, then h^{n_r, n_t} can be employed in the CS reconstruction algorithm.

Considering all receive antennas, equation (17) can be written as

$$R = Xh + \eta, \tag{18}$$

where $X = I_{N_r} \otimes [\text{diag}\,(x^1) F_{NL}, \text{diag}\,(x^2) F_{NL}, \cdots, \text{diag}\,(x^{N_t}) F_{NL}]$, $R = [(R^1)^T (R^2)^T \cdots (R_0^{N_r})^T]^T$, $\eta = [(\eta^1)^T \quad (\eta^2)^T \cdots (\eta^{N_r})^T]^T$,

$$h = \begin{bmatrix} h^{1,1} & h^{1,2} & \cdots & h^{1,N_t} \\ h^{2,1} & h^{2,2} & \cdots & h^{2,N_t} \\ \vdots & \vdots & \ddots & \vdots \\ h^{N_r,1} & h^{N_r,2} & \cdots & h^{N_r,N_t} \end{bmatrix}. \tag{19}$$

4. Proposed Bayesian Matching Pursuit Method

It is considered that $\mathbf{h}$ is a Gaussian mixture process, the parametric vector $\mathbf{z}$ is introduced to reflect the sparsity of $\mathbf{h}$, and the position of nonzero elements is the same as that of $\mathbf{h}$. $h[n]$ is defined as the nth element of vector $\mathbf{h}$, and $z[n] \in \{0, 1\}$ is used to express whether $h[n]$ is a nonzero element, since $h[n]$ is a Gaussian process with a mean of 0 and a variance of σ^2:

$$h[n]|\{z[n] = q\} \sim CN\left(0, \sigma_q^2\right), \tag{20}$$

where $z[n] = 0$, $\sigma_0^2 \triangleq 0$, $h[n] = 0$, $z[n] = 1$, $h[n] \neq 0$, and $p(z[n] = 1) = p_1$ and $p(z[n] = 0) = 1 - p_1$.

The vector form of equation (20) can be expressed as follows:

$$\mathbf{h}|\mathbf{z} \sim CN(0, \mathbf{R_{zz}}), \tag{21}$$

with $\mathbf{R_{zz}} = E\{\mathbf{z}\mathbf{z^H}\}$.

Using Bayesian rule,

$$p(\mathbf{y}, \mathbf{h}|\mathbf{z}) = \frac{p(\mathbf{y}, \mathbf{h}, \mathbf{z})}{p(\mathbf{z})} = p(\mathbf{y}|\mathbf{z}, \mathbf{h})p(\mathbf{h}|\mathbf{z}) = p(\mathbf{y}|\mathbf{h})p(\mathbf{h}|\mathbf{z}), \tag{22}$$

if $\mathbf{h}$ is given, $\mathbf{z}$ can be completely determined, then $p(\mathbf{y}|\mathbf{z}, \mathbf{h}) = p(\mathbf{y}|\mathbf{h}, \mathbf{z}) = p(\mathbf{y}|\mathbf{h})$.

$$\begin{bmatrix} \mathbf{y} \\ \mathbf{h} \end{bmatrix} \bigg| \mathbf{z} = \begin{bmatrix} \mathbf{y}|\mathbf{z} \\ \mathbf{h}|\mathbf{z} \end{bmatrix} \sim CN\left(0, \begin{bmatrix} \varphi(\mathbf{z}) & \Phi\mathbf{R_{zz}} \\ \mathbf{R_{zz}}\Phi^H & \mathbf{R_{zz}} \end{bmatrix}\right), \tag{23}$$

where $\varphi(\mathbf{z}) \triangleq \Phi\mathbf{R_{zz}}\Phi^H + \sigma_n^2 \mathbf{I_M}$.

According to the description of the above model, the selection of the support set for $\mathbf{h}$ can be simplified to the selection of the support set for $\mathbf{z}$. Using the Bayesian rule, the posterior probability could be written as

$$p(\mathbf{z}|\mathbf{y}) = \frac{p(\mathbf{y}|\mathbf{z})p(\mathbf{z})}{\sum_{z' \in \Lambda} p\left(\mathbf{y}|\mathbf{z}'\right)p\left(|\mathbf{z}'\right)}, \tag{24}$$

where $\Lambda \in \{0, 1\}^L$. $p(\mathbf{z}|\mathbf{y})$ can be obtained by solving $p(\mathbf{y}|\mathbf{z})p(\mathbf{z})$; considering that Λ has a relatively large value, it is still difficult to solve $p(\mathbf{y}|\mathbf{z})p(\mathbf{z})$. If one can find a smaller set Λ^* to approximate Λ, the amount of calculation could be reduced. In order to choose Λ^*, we first take the logarithm of $p(\mathbf{y}|\mathbf{z})p(\mathbf{z})$,

$$\begin{aligned} v(\mathbf{z}) &\triangleq \ln p(\mathbf{y}|\mathbf{z})p(\mathbf{z}) = \ln p(\mathbf{y}|\mathbf{z}) + \ln \prod_{n=1}^{L} p(z_n) \\ &= \ln p(\mathbf{y}|\mathbf{z}) + \|\mathbf{z}\|_0 \ln p_1 + (N - \|\mathbf{z}\|_0) \ln (1 - p_1), \end{aligned} \tag{25}$$

where $\ln p(\mathbf{y}|\mathbf{z}) = -(L/2) \ln 2\pi - (1/2) \ln \det (\varphi(\mathbf{z})) - (1/2) \mathbf{y}^H \varphi(\mathbf{z})^{-1} \mathbf{y}$ and $v(\mathbf{z})$ is the selection criterion for Λ^*. Then, an effective way is taken to estimate $\mathbf{z}$ by utilizing $v(\mathbf{z})$, and we call this method as the fast Bayesian matching pursuit (FBMP) [32].

More specifically, suppose $\mathbf{z_n}$ means that the vector is the same as the vector $\mathbf{z}$ except for the nth element, with $z_n[n] = 1, z[n] = 0$. Then, calculate the gain of $v(\mathbf{z_n})$, with $\Delta_n(\mathbf{z_n}) = v(\mathbf{z_n}) - v(\mathbf{z})$. According to (23), $\varphi(0) = \sigma_n^2 I_M$. Notice the initialization state of $\mathbf{z}$; when $\mathbf{z} = 0$, $v(0) = -(L/2) \ln 2\pi - M \ln \sigma_n - (1/2\sigma_n^2)\|y\|_2^2 + L \ln (1 - p_1)$. In order to get the gain of $v(\mathbf{z_n})$, we first calculate

$$\begin{aligned} \varphi(\mathbf{z_n}) &= \Phi\mathbf{R_{znzn}}\Phi^H + \sigma_n^2 \mathbf{I_M} = \Phi(\mathbf{R_{zz}} + \mathbf{A})\Phi^H + \sigma_n^2 \mathbf{I_M} \\ &= \varphi(\mathbf{z}) + \sigma_1^2 \Phi_n \Phi_n^H, \end{aligned} \tag{26}$$

where $\mathbf{A}$ is an $L \times L$ matrix; it has zero elements except for $A[n, n]$, and $A[n, n] = \sigma_{zn}^2 = \sigma_1^2$. Φ_n represents the nth column of matrix Φ. Then, according to the principle of matrix transpose

$$\varphi(\mathbf{z}_n)^{-1} = \varphi(\mathbf{z})^{-1} - \varphi(\mathbf{z})^{-1}\Phi_n\left(\Phi_n^H\varphi(\mathbf{z})^{-1}\Phi_n + \sigma_1^{-2}\right)^{-1}\Phi_n^H\varphi(\mathbf{z})^{-1}. \tag{27}$$

Define that $\mathbf{b}_n \triangleq \varphi(\mathbf{z})^{-1}\Phi_n$ and $\beta_n \triangleq \sigma_1^2(1 + \sigma_1^2\Phi_n^H\mathbf{b}_n)^{-1}$. Then, equation (27) can be rewritten as

$$\varphi(\mathbf{z}_n)^{-1} = \varphi(\mathbf{z})^{-1} - \beta_n\mathbf{b}_n\mathbf{b}_n^H. \tag{28}$$

Through calculation, we can finally get that

$$\Delta_n(\mathbf{z}_n) = v(\mathbf{z}_n) - v(\mathbf{z}) = \frac{1}{2}\ln\left(\frac{\beta_n}{\sigma_1^2}\right) + \frac{1}{2}\beta_n|\mathbf{y}^H\mathbf{b}_n|^2 + \ln\frac{p_1}{1 - p_1}, \tag{29}$$

where $\Delta_n(\mathbf{z}_n)$ is the gain of $\mathbf{z}$ after changing at the nth position.

According to the above method, the main support set Λ^* can be found. The steps of the algorithm are shown below:

Initialization: $\Omega = \varnothing$, $\mathbf{z} = 0$, $\mathbf{R}_{zz} = 0$, and $v(0)$. Use (23) to obtain $\varphi(\mathbf{z})$, and use (26) to initialize $\mathbf{b}_n$, $n = 1, 2, \cdots, L$, and β_n.

First, starting with $\mathbf{z} = 0$, use (29) to calculate $\Delta_n(\mathbf{z}_n)$, $n = 1 : L$, find the location element with the largest $v(\mathbf{z}_n) = v(0) + \Delta_n(\mathbf{z}_n)$, $n = 1 : L$, and record it as $n^{(1)}$; add it to the set $\Omega = \Omega \cup \{n^{(1)}\}$, then update $\Psi = \{1, 2, \cdots, L\}/\Omega$.

Then, update $\mathbf{b}_n$ and β_n, use (29) to calculate $\Delta_n(\mathbf{z}_n)$, $n = 1 : L$, find the location element with the largest $v(\mathbf{z}_n) = v(\mathbf{z}) + \Delta_n(\mathbf{z}_n)$, $n = 1 : L$, and record it as $n^{(2)}$.

Until the number of elements in the selection Ω reaches $\widehat{K}$, set $\widehat{K}$ to be slightly greater than the expected position of nonzero elements, with $E\{\|\mathbf{z}\|_0\} = Lp_1$. Therefore, the probability that the actual sparsity is greater than the estimated sparsity $\widehat{K}$ is lower, and $P_0 = p(\|\mathbf{z}\|_0 > \widehat{K}) = (1/2)\,\mathrm{erfc}\left((\widehat{K} - Lp_1)/\sqrt{2Np_1(1 - p_1)}\right)$; $\widehat{K}$ could be calculated as $\widehat{K} = [\mathrm{erfc}^{-1}(2p_0)\sqrt{2Lp_1(1 - p_1)} + Lp_1]$.

In the proposed algorithm, by giving the value of P_0, use the above formula to calculate $\widehat{K}$, until the number of elements in Ω reaches $\widehat{K}$. By optimizing the number of loops, the iteration will be stopped until the requirements are met.

After estimating the parameter vector $\mathbf{z}$, the estimated channel is given as

$$\widehat{\mathbf{h}} = \sum_{\Lambda^*} E\{\mathbf{h}|\mathbf{y}, \mathbf{z}\}p(\mathbf{z}|\mathbf{y}), \tag{30}$$

where $\{\mathbf{h}|\mathbf{y}, \mathbf{z}\} = \mathbf{R}_{zz}\Phi^H\Phi(\mathbf{z}_n)^{-1}\mathbf{y}$. Figure 1 shows the flowchart of the proposed algorithm.
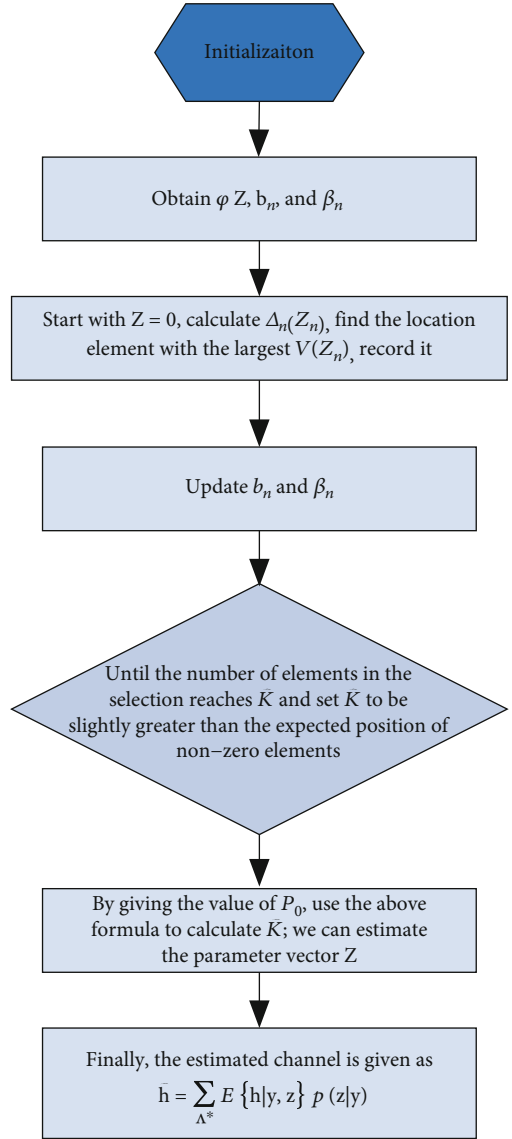
FIGURE 1: The flowchart of the proposed algorithm.

5. Simulation Results

In this section, we consider FBMC systems using $N = 512$ subcarriers. A square root-raised cosine filter is adopted for the pulse filter. The LS approach adopts the IAM preamble structure. The length of the channel is $L = 240$, the number of nonzero elements $K = 6$, K is also expressed as sparsity, and set $P_0 = 0.01$. It is clearly that $p_1 = 0.025$. The number of iterations is 5. MSE and BER are used to evaluate the CE performance. Conventional LS, OMP, and regularized OMP (ROMP) methods are used to compare with the proposed method, where the OMP and ROMP are the two well-known CS recovery algorithms.

Figures 2 and 3 give the MSE and BER with five methods for a SISO-FBMC system. These results show that the proposed scheme outperforms the other four schemes in terms of both the MSE and BER. The CS-based approaches provide significant MSE performance improvement over the
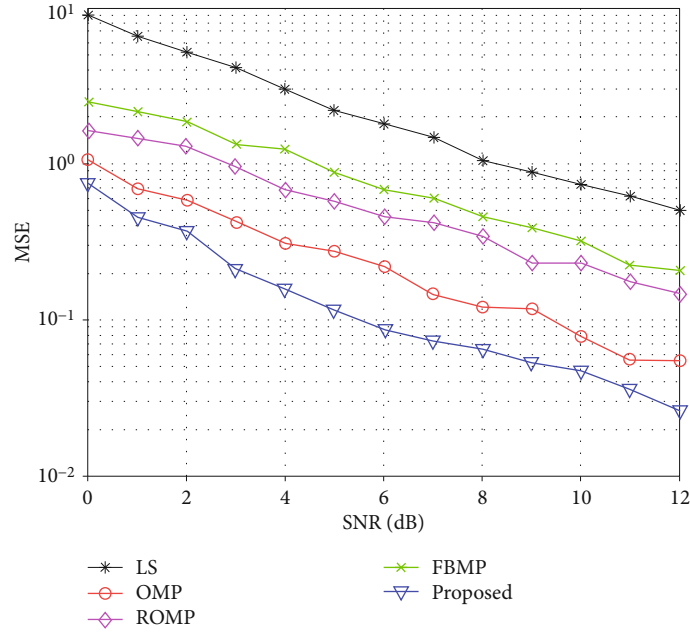
FIGURE 2: MSE with five methods for a SISO system.
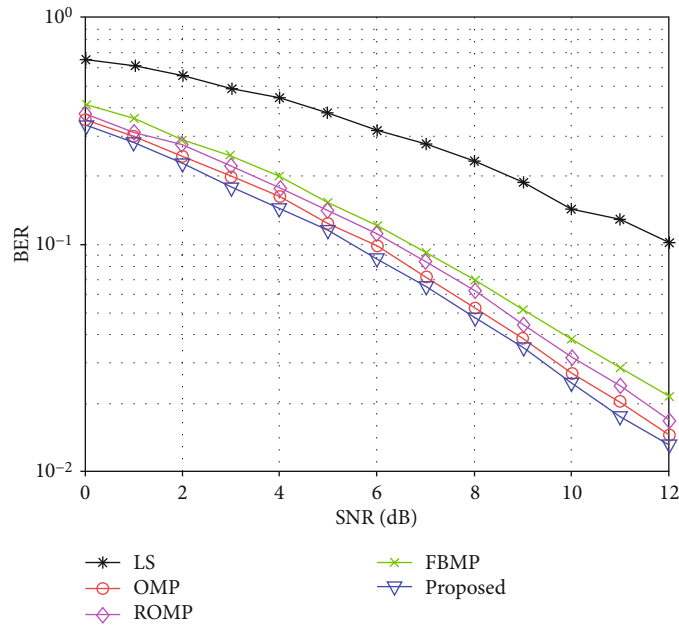
FIGURE 3: BER with five methods for a SISO system.

conventional LS method. Due to the change of iteration conditions, the proposed method is significantly better than the conventional FBMP method.

Figure 2 depicts the MSE performance curves for five channel estimation methods. The results show that our proposed algorithm exhibits a better MSE performance than the other four methods. The conventional FBMP method outperforms the LS method but is worse than the traditional CS method. The MSE performance for CE can be significantly improved by the proposed method.

In Figure 3, the BER performance curves for five channel estimation methods are given. It is obvious that the proposed method gives the best BER values among the five methods. More specifically, our proposed approach improves the BER performance of the OMP, ROMP, and FBMP by 0.5, 0.8, and 1.2 dB, respectively, when $BER = 10^{-1}$ is considered.
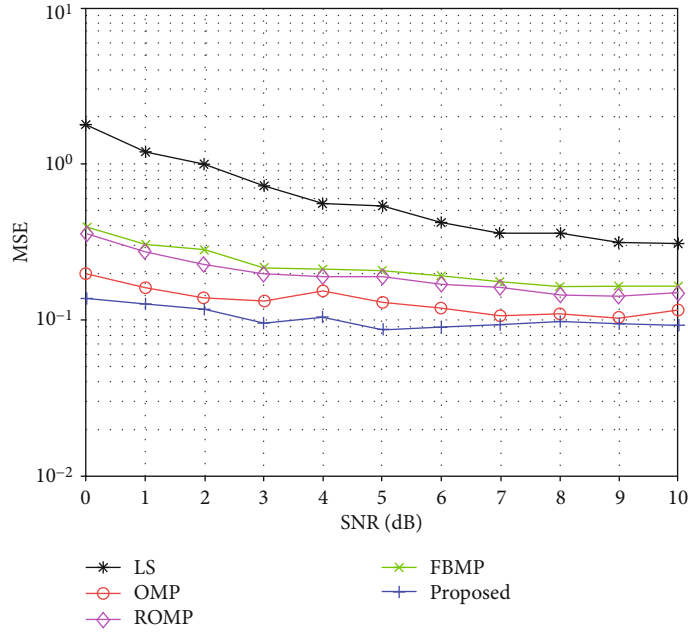
FIGURE 4: MSE with five methods for a 2×2 MIMO system.
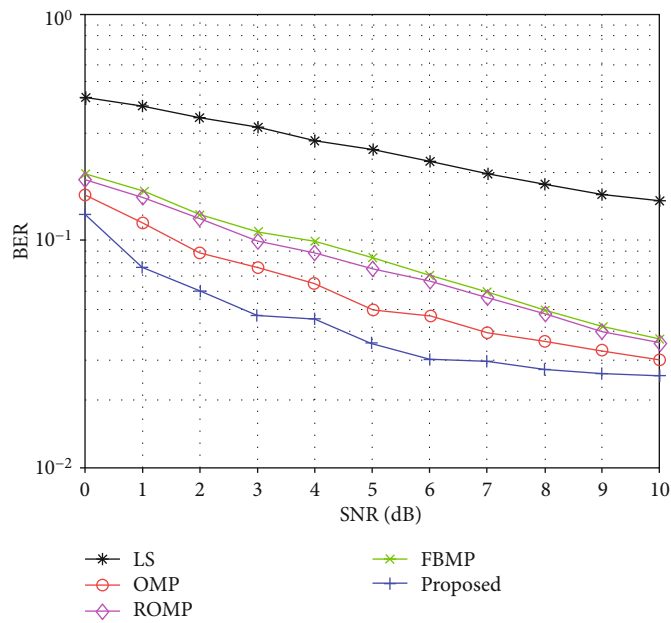
FIGURE 5: BER with five methods for a 2×2 MIMO system.

We also study the CE performance of a MIMO-FBMC system. Figures 4 and 5 give the MSE and BER of the five methods for a 2×2 MIMO-FBMC system. Compared with the SISO system, the performance of all methods in the MIMO system is decreased. And these results also demonstrate that the proposed method outperforms the other four schemes in terms of both the MSE and BER in a MIMO case.

Figure 4 gives the MSE performance curves for five channel estimation methods in a MIMO case. Compared with the performance in Figure 2, the OMP method offers slightly better MSE values than the FBMP method in Figure 4. The error floor of the CS-based approaches is due to the inherent interference from the MIMO-FBMC system.

Figure 5 shows that the CS approach outperforms the conventional LS scheme in terms of the BER, and the proposed method provides the best performance. More specifically, the proposed approach improves the BER performance of the OMP, ROMP, and FBMP by 1.1,

2.6, and 3.6 dB, respectively, when BER = 10^{-1} is considered. The BER performance improvement of the proposed method in a MIMO system is better than that in a SISO system.

6. Conclusions

In this paper, we had studied the FBMP algorithm for channel estimation. A modified FBMP algorithm was proposed by optimizing the iterative termination conditions for FBMC sparse channel estimation. The proposed algorithm was compared with the LS, OMP, ROMP, and FBMP methods. The simulation results obtained showed that our proposed approach achieved better MSE and BER performance than LS and the other well-known CS-based approaches. However, the shortcoming is that the computational complexity of the proposed method is increased. In the future, low-complexity Bayesian sparse CE approach for FBMC systems will be studied.

Data Availability

The data used to support the findings of this study are available from the corresponding author upon reasonable request and with permission from the funders.

Conflicts of Interest

The authors declare that there is no conflict of interests regarding the publication of this paper.

Acknowledgments

References

[1] L. Xu, J. Wang, H. Wang, T. Aaron Gulliver, and K. N. le, "BP neural network-based ABEP performance prediction for mobile Internet of Things communication systems," *Neural Computing and Applications*, 2019.

[2] L. Chettri and R. Bera, "A comprehensive survey on Internet of Things (IoT) toward 5G wireless systems," *IEEE Internet of Things Journal*, vol. 7, no. 1, pp. 16–32, 2020.

[3] F. Wen, J. Shi, and Z. Zhang, "Joint 2D-DOD, 2D-DOA, and polarization angles estimation for bistatic EMVS-MIMO radar via PARAFAC analysis," *IEEE Transactions on Vehicular Technology*, vol. 69, no. 2, pp. 1626–1638, 2020.

[4] F. Wen, J. Wang, J. Shi, and G. Gui, "Auxiliary vehicle positioning based on robust DOA estimation with unknown mutual coupling," *IEEE Internet of Things Journal*, 2020.

[5] L. Lyu, C. Chen, S. Zhu, and X. Guan, "5G enabled codesign of energy-efficient transmission and estimation for industrial IoT systems," *IEEE Transactions on Industrial Informatics*, vol. 14, no. 6, pp. 2690–2704, 2018.

[6] X. Li, J. Li, and L. Li, "Performance analysis of impaired SWIPT NOMA relaying networks over imperfect Weibull channels," *IEEE Systems Journal*, vol. 14, no. 1, pp. 669–672, 2020.

[7] X. Li, M. Liu, C. Deng, P. T. Mathiopoulos, Z. Ding, and Y. Liu, "Full-duplex cooperative NOMA relaying systems with I/Q imbalance and imperfect SIC," *IEEE Wireless Communications Letters*, vol. 9, no. 1, pp. 17–20, 2020.

[8] X. Li, J. Li, Y. Liu, Z. Ding, and A. Nallanathan, "Residual transceiver hardware impairments on cooperative NOMA networks," *IEEE Transactions on Wireless Communications*, vol. 19, no. 1, pp. 680–695, 2020.

[9] L. Xu, J. Wang, Y. Liu, W. Shi, and T. A. Gulliver, "Outage performance for IDF relaying mobile cooperative networks," *Mobile Networks and Applications*, vol. 23, no. 6, pp. 1496–1501, 2018.

[10] X. Wang, L. Wan, M. Huang, C. Shen, and K. Zhang, "Polarization channel estimation for circular and non-circular signals in massive MIMO systems," *IEEE Journal of Selected Topics in Signal Processing*, vol. 13, no. 5, pp. 1001–1016, 2019.

[11] H. Wang, L. Wan, M. Dong, K. Ota, and X. Wang, "Assistant vehicle localization based on three collaborative base stations via SBL-based robust DOA estimation," *IEEE Internet of Things Journal*, vol. 6, no. 3, pp. 5766–5777, 2019.

[12] X. Wang, L. Wan, M. Huang, C. Shen, Z. Han, and T. Zhu, "Low-complexity channel estimation for circular and noncircular signals in virtual MIMO vehicle communication systems," *IEEE Transactions on Vehicular Technology*, vol. 69, no. 4, pp. 3916–3928, 2020.

[13] K. Zheng, Z. Yang, K. Zhang, P. Chatzimisios, K. Yang, and W. Xiang, "Big data-driven optimization for mobile networks toward 5G," *IEEE Network*, vol. 30, no. 1, pp. 44–51, 2016.

[14] X. Zhang and Q. Zhu, "Information-centric virtualization for software-defined statistical QoS provisioning over 5G multimedia big data wireless networks," *IEEE Journal on Selected Areas in Communications*, vol. 37, no. 8, pp. 1721–1738, 2019.

[15] R. Nissel and M. Rupp, "OFDM and FBMC-OQAM in doubly-selective channels: calculating the bit error probability," *IEEE Communications Letters*, vol. 21, no. 6, pp. 1297–1300, 2017.

[16] L. Zhang, P. Xiao, A. Zafar, A. Quddus, and R. Tafazolli, "FBMC system: an insight into doubly dispersive channel impact," *IEEE Transactions on Vehicular Technology*, vol. 66, no. 5, pp. 3942–3956, 2016.

[17] R. Nissel, S. Schwarz, and M. Rupp, "Filter bank multicarrier modulation schemes for future mobile communications," *IEEE Journal on Selected Areas in Communications*, vol. 35, no. 8, pp. 1768–1782, 2017.

[18] D. Chen, Y. Tian, D. Qu, and T. Jiang, "OQAM-OFDM for wireless communications in future internet of things: a survey on key technologies and challenges," *IEEE Internet of Things Journal*, vol. 5, no. 5, pp. 3788–3809, 2018.

[19] D. Gregoratti and X. Mestre, "Uplink FBMC/OQAM-based multiple access channel: distortion analysis under strong

frequency selectivity," *IEEE Transactions on Signal Processing*, vol. 64, no. 16, pp. 4260–4272, 2016.

[20] J. F. Du and S. Signeel, "Novel preamble-based channel estimation for OFDM/OQAM systems," in *Proceedings 2009 IEEE International Conference on Communications*, pp. 1–6, Dresden, Germany, June 2009.

[21] E. Kofidis and D. Katselis, "Improved interference approximation method for preamble-based channel estimation in FBMC/OQAM," in *Proceedings IEEE European Signal Process. Conference*, pp. 1603–1607, Barcelona, Spain, September 2011.

[22] H. Wang, W. C. Du, and L. W. Xu, "Novel preamble design for channel estimation in FBMC/OQAM systems," *KSII Transactions on Internet and Information Systems*, vol. 10, no. 8, pp. 3672–3688, 2016.

[23] E. Kofidis, "Preamble-based estimation of highly frequency selective channels in FBMC/OQAM systems," *IEEE Transactions on Signal Processing*, vol. 65, no. 7, pp. 1855–1868, 2017.

[24] W. Liu, D. Chen, K. Luo, T. Jiang, and D. Qu, "FDM-structured preamble optimization for channel estimation in MIMO-OQAM/FBMC systems," *IEEE Transactions on Wireless Communications*, vol. 17, no. 12, pp. 8433–8443, 2018.

[25] H. Wang, L. Xu, X. Wang, and S. Taheri, "Preamble design with interference cancellation for channel estimation in MIMO-FBMC/OQAM systems," *IEEE Access*, vol. 6, pp. 44072–44081, 2018.

[26] J. Zhang, S. Hu, Z. Liu, P. Wang, P. Xiao, and Y. Gao, "Real-valued orthogonal sequences for iterative channel estimation in MIMO-FBMC systems," *IEEE Access*, vol. 7, pp. 68742–68751, 2019.

[27] Z. L. Liu, P. Xiao, and S. Hu, "Low-PAPR preamble design for FBMC systems," *IEEE Transactions on Vehicular Technology*, vol. 68, no. 8, pp. 7869–7876, 2019.

[28] X. M. Liu, Z. W. Cai, A. L. Jia, and J. L. Ou, "A novel channel estimation method based on compressive sensing for OFDM/OQAM systems," *The Journal of Computer Information Systems*, vol. 9, no. 15, pp. 5955–5963, 2013.

[29] H. Wang, W. du, and L. Xu, "A new sparse adaptive channel estimation method based on compressive sensing for FBMC/OQAM transmission network," *Sensors*, vol. 16, no. 7, p. 966, 2016.

[30] L. Xiaopeng, C. Xihong, X. Zedong, Z. Kai, and T. Ningning, "Scattered pilots aided channel estimation based on compressed sensing in OQAM/OFDM system," *Journal of National University of Defense Technology*, vol. 39, no. 5, pp. 102–107, 2017.

[31] Z. He, L. Zhou, Y. Yang, Y. Chen, X. Ling, and C. Liu, "Compressive sensing-based channel estimation for FBMC-OQAM system under doubly selective channels," *IEEE Access*, vol. 7, pp. 51150–51158, 2019.

[32] M. Lin, Y. Li, L. Xiao, and J. Wang, "A compressive sensing channel estimation for MIMO FBMC/OQAM system," *Wireless Personal Communications*, vol. 96, no. 3, pp. 3345–3360, 2017.

[33] H. Wang, "Sparse channel estimation for MIMO-FBMC/OQAM wireless communications in smart city applications," *IEEE Access*, vol. 6, pp. 60666–60672, 2018.

[34] H. Wang, J. Liao, L. Xu, and X. Wang, "Blind channel estimation for FBMC/OQAM systems based on subspace approach," *Information*, vol. 9, no. 3, p. 58, 2018.

[35] J. Meng, W. Yin, Y. Li, N. T. Nguyen, and Z. Han, "Compressive sensing based high-resolution channel estimation for OFDM system," *IEEE Journal of Selected Topics in Signal Processing*, vol. 6, no. 1, pp. 15–25, 2012.

[36] C. Qi and L. Wu, "Uplink channel estimation for massive MIMO systems exploring joint channel sparsity," *Electronics Letters*, vol. 50, no. 23, pp. 1770–1772, 2014.

[37] R. Mohammadian, A. Amini, and B. H. Khalaj, "Compressive sensing-based pilot design for sparse channel estimation in OFDM systems," *IEEE Communications Letters*, vol. 21, no. 1, pp. 4–7, 2017.

[38] Z. Sadeghigol, M. H. Kahaei, and F. Haddadi, "Generalized beta Bayesian compressive sensing model for signal reconstruction," *Digital Signal Processing*, vol. 60, no. 1, pp. 163–171, 2017.

[39] S. Liu, S. Wu, and Y. Li, "Application of Bayesian compressive sensing in IRUWB channel estimation," *China Communications*, vol. 14, no. 5, pp. 30–37, 2017.

Research Article

Nonorthogonal Multiple Access for Visible Light Communication IoT Networks

Chun Du,[1] Shuai Ma [iD],[1] Yang He,[1] Songtao Lu,[2] Hang Li,[3] Han Zhang,[4] and Shiyin Li [iD] [1]

[1]*School of Information and Control Engineering, China University of Mining and Technology, Xuzhou 221116, China*
[2]*IBM Research AI, IBM Thomas J. Watson Research Center, Yorktown Heights, New York 10598, USA*
[3]*Shenzhen Research Institute of Big Data, Shenzhen 518172, China*
[4]*Department of Electrical and Computer Engineering, University of California, Davis, CA 95616, USA*

Correspondence should be addressed to Shuai Ma; mashuai001@cumt.edu.cn

In this study, we investigated the nonorthogonal multiple access (NOMA) for visible light communication (VLC) Internet of Things (IoT) networks and provided a promising system design for 5G and beyond 5G applications. Specifically, we studied the capacity region of a practical uplink NOMA for multiple IoT devices with discrete and continuous inputs, respectively. For discrete inputs, we proposed an entropy approximation method to approach the channel capacity and obtain the discrete inner and outer bounds. For the continuous inputs, we derived the inner and outer bounds in closed forms. Based on these results, we further investigated the optimal receiver beamforming design for the multiple access channel (MAC) of VLC IoT networks to maximize the minimum uplink rate under receiver power constraints. By exploiting the structure of the achievable rate expressions, we showed that the optimal beamformers are the generalized eigenvectors corresponding to the largest generalized eigenvalues. Numerical results show the tightness of the proposed capacity regions and the superiority of the proposed beamformers for VLC IoT networks.

1. Introduction

As the wireless data traffic exponentially increased in 5G, traditional radio frequency- (RF-) based Internet of Things (IoT) network suffers from a limited data rate and network capacity due to the shortage of RF spectra and massive IoT devices. With its vast unlicensed bandwidth, visible light communication (VLC) is a promising complementary solution to meet the growing wireless traffic demands for IoT networks [1, 2]. By exploiting the widespread deployment of the light-emitting diodes (LEDs) as transmitters, VLC has attracted an increasing interest due to its dual functionality: communication and illumination [3–5]. Besides a wider spectrum, VLC has other inherent advantages such as high spatial reuse, high energy efficiency, no electromagnetic radiation, and inherent security [6, 7].

Thus far, traditional IoT networks have generally utilized orthogonal multiple access (OMA) techniques such as frequency division multiple access (FDMA) and time division multiple access (TDMA). In OMA, the resources are allocated orthogonally to multiple users, and it cannot provide sufficient resource reuse. In contrast, the nonorthogonal multiple access (NOMA) technique exploits the power domain for multiple access and is able to serve multiple users at the same time frequency-code resource [8–10], which has recently been included into the 3GPP long-term evolution advanced standard [11–13] and is widely recognized as a promising candidate for the MAC scheme in 5G-enabled IoT applications.

Recently, uplink NOMA has received significant research attention [14–20]. Based on the theory of the Poisson cluster process, the authors in [14] have provided a framework to analyze the rate coverage probability. In [15], the optimal user pairing was investigated for various uplink NOMA scenarios. In [16], the joint subchannel assignment and power allocation problem were investigated. In [17], an interference balance power control scheme was derived. By using stochastic geometry, a signal alignment-based framework

was developed in [18] for both multiple-input, multiple-output- (MIMO-) NOMA downlink and uplink transmissions. In [19], a theoretical framework was proposed to analyze the outage probability and the average achievable rate in NOMA downlink and uplink multicell wireless systems. In [20], a phase predistorted joint detection method was proposed to reduce the bit error ratio (BER) for uplink NOMA in VLC systems. Most of the aforementioned research works focused on the RF uplink NOMA [14–19], while the VLC uplink NOMA is not well discussed [20]. Until now, the achievable rate expression of VLC uplink NOMA is still unknown, which makes it great difficult to undertake the optimal NOMA beamforming design for VLC IoT networks.

Different from the RF communications, VLC generally adopts intensity modulation and direct detection (IM/DD), where the messages are modulated to the intensity of the signals. Therefore, the transmitted VLC signals are real and nonnegative, which differ from the RF complex-valued signals. Additionally, due to the eye safety standards and physical limitations, both the peak and average amplitudes of VLC signals are restricted. Hence, the classic Shannon capacity formula with Gaussian input [21] cannot quantify the capacity of VLC IoT networks.

This study is aimed at providing a solution to the above-mentioned issues in the area of VLC IoT networks. First, we investigated the capacity region of MAC in VLC IoT networks. Then, we further studied the optimal beamforming design in a practical NOMA uplink. The main contributions of this study are summarized as follows:

(i) Due to the peak optical power constraint, the optimal input is discrete [22]. Thus, we supposed that the input follows a discrete distribution and develops both the inner and outer bounds of the capacity region of uplink NOMA in VLC IoT networks. Specifically, finding the capacity region was formulated as an entropy maximization problem which is a mixed discrete optimization problem. To overcome the challenge, we proposed an entropy maximization approximation method and obtained the capacity bounds

(ii) Based on the continuous inputs, a closed-form expression for the achievable rate of uplink NOMA of VLC IoT networks is presented. Specifically, with the continuous inputs, the channel capacity of uplink NOMA in VLC IoT networks can be approximated as a differential entropy maximization problem. The corresponding optimal continuous distributions were ABG distributions, and we obtained both the inner and outer bounds in closed forms. To the best of our knowledge, the proposed inner and outer bounds are the first theoretical bounds of the channel capacity region for uplink NOMA of VLC IoT networks

(iii) Finally, based on the obtained results of NOMA, we further studied the optimal receiver beamforming design for VLC IoT. Specifically, we first extended the ABG inner bound to a single-input, multiple-output (SIMO) uplink NOMA case and then maximized the minimum uplink rate of multiple users under receiver power constraints. By exploiting the structure of the achievable rate expression, we equivalently reformulated this problem as a generalized eigenvalue maximization problem, and the optimal beamformers are the generalized eigenvectors corresponding to the largest generalized eigenvalues

The rest of this paper is organized as follows. In Section 2, the capacity regions of the discrete and continuous distribution for uplink NOMA of VLC IoT networks are presented. In Section 3, the achievable rate of multi-LED and optimal beamforming design derived for uplink NOMA of VLC IoT networks is described. In Section 4, the simulation results of the capacity regions and optimal beamforming design in NOMA VLC IoT networks are presented. Finally, the conclusions are presented in Section 5.

2. Capacity Region of Uplink NOMA for VLC IOT Networks

As shown in Figure 1, N single-LED users (IoT devices) simultaneously transmit its own information to a single-PD base station (BS) over the same channel. Let s_i be the message of the ith user, where $|s_i| \leq A_i$, $\mathbb{E}\{s_i\} = 0$, and $\mathbb{E}\{s_i^2\} = \varepsilon_i$.

The transmitted signal of the ith user is given by

$$x_i = \sqrt{p_i}s_i + b_i, \tag{1}$$

where p_i is the transmit power of the ith user and b_i is the direct current (DC) bias of the ith user. To ensure that the transmitted signal is nonnegative, the DC bias needs to satisfy $b_i \geq \sqrt{p_i}A_i$.

As the received signal power is dominated by the power from the line-of-sight (LOS) link [23, 24], the diffuse link can be neglected. Thus, the channel gain between user i and the BS is given by [25]

$$g_i = \begin{cases} \dfrac{(m+1)A_R}{2\pi d_\kappa^2} \cos^m(\phi_k) \cos(\psi_k), & \text{if } |\psi_k| \leq \psi_{\text{FOV}}; \\ 0, & \text{otherwise}, \end{cases} \tag{2}$$

where m is the Lambertian index of the LED, which depends on the semiangle $\phi_{1/2}$ by $m = -\log 2/(\log(\cos(\phi_{1/2})))$; d_i denotes the distance between user i and the receiver; ϕ is the angle of irradiance; ψ_i is the angle of incidence; ψ_{FOV} is the field of vision (FOV) semiangle of the receiver; and A_R denotes the effective area of the PD.

The received signal at the BS is given by

$$y = \sum_{i=1}^{N} g_i(\sqrt{p_i}s_i + b_i) + z, \tag{3}$$

where $z \sim \mathcal{N}(0, \sigma^2)$ represents the sum of contributions from the shot noise and the thermal noise [26, 27]. At the BS, the
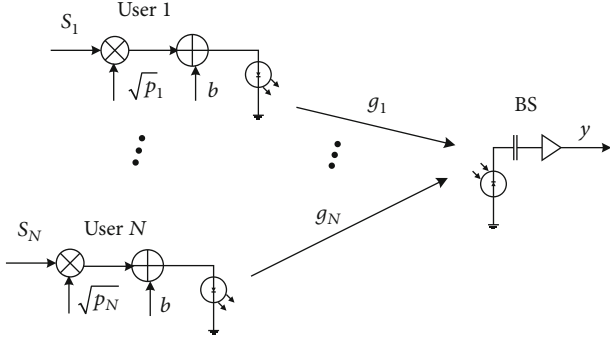
Figure 1: Schematic of an uplink NOMA of VLC IoT network.

multiple received signals may cause interference to each other. To mitigate the interference, the BS applies SIC to decode and remove the partial interference. Without the loss of generality, we assume that the terms $\{g_i^2 \varepsilon_i\}_{i=1}^N$ satisfy a descending order, i.e., $g_1^2 \varepsilon_1 \geq g_2^2 \varepsilon_2 \geq \cdots \geq g_N^2 \varepsilon_N$. The BS adopts the SIC technique to decode the received signals in a descending order [28–31], i.e., from s_1 to s_N. Specifically, when the BS decodes s_i, it first decodes the signal intended for user s_k with the order $k \leq i$ and then subtracts it from y.

Thus far, the capacity region of uplink NOMA for VLC IoT networks has been an open problem, which is a major barrier for signal processing in VLC IoT networks. To overcome the challenge, we derived both the inner and outer bounds of the channel capacity region for uplink NOMA of VLC IoT networks.

2.1. Capacity Region with Discrete Inputs. As in the previous section, we assumed that the signal s_i is a discrete random variable with M_i real values $\{a_{i,m}\}_{1 \leq m \leq M_i}$.

Specifically, the signal s_i satisfies

$$\Pr \{s_i = a_{i,m}\} = p_{i,m}, m = 1, \cdots, M_i, \tag{4a}$$

$$\mathbb{E}\{s_i\} = \sum_{m=1}^{M_i} p_{i,m} a_{i,m} = 0, \tag{4b}$$

$$\mathbb{E}\{s_i^2\} = \sum_{m=1}^{M_i} p_{i,m} a_{i,m}^2 = \varepsilon_i, \tag{4c}$$

$$\sum_{m=1}^{M_i} p_{i,m} = 1, -A_i \leq a_{i,m} \leq A_i, k = 1, \cdots, M_i, \tag{4d}$$

where $a_{i,m}$ denotes the mth point for signal s_i and $p_{i,m}$ denotes the corresponding probability.

2.1.1. Inner Bound with Discrete Inputs. Let R_i denote the capacity of user i, where $1 \leq i \leq N$, the capacity of R_i can be

written as

$$
\begin{aligned}
R_i &= \max_{\{P(s_i)\}} I(y ; s_i | s_1, \cdots, s_{i-1}), \\
&= \max_{\{P(s_i)\}} h(y | s_1, \cdots, s_{i-1}) - h(y | s_1, \cdots, s_i), \\
&= \max_{\{P(s_i)\}} h\left(\sum_{k=i}^N g_k \sqrt{p_k} s_k + z \right) - h\left(\sum_{j=i+1}^N g_j \sqrt{p_j} s_j + z \right), \\
&\geq \max_{\{P(s_i)\}} \frac{1}{2} \log_2 \sum_{k=i}^N 2^{2h(\widehat{y}_k)} - \frac{1}{2} \log_2 2\pi e \left(\sum_{j=i+1}^N g_j^2 p_j \varepsilon_j + \sigma^2 \right),
\end{aligned}
\tag{5}
$$

where $\widehat{y}_k = g_k \sqrt{p_k} s_k + \widehat{z}_k$, $\sum_{k=i}^K \widehat{z}_k = z$, due to the entropy power inequality (EPI) [21] and $h(Q) \leq 1/2 \log 2\pi e \operatorname{var}(Q)$ for a random variable with variance, $\operatorname{var}(Q)$.

Based on (5), the discrete inner bound uplink NOMA of VLC can be obtained by maximizing the entropy $h(\widehat{y}_i)$, i.e.,

$$h(\widehat{y}_i) = -\int_{-\infty}^{\infty} f_{\widehat{Y}_i}(y) \log_2 f_{\widehat{Y}_i}(y) dy. \tag{6}$$

As the noise $\widehat{z}_{k,i}$ follows the Gaussian distribution with zero mean and σ^2/K variance, the probability density function (PDF) $f_Y(y)$ is given by

$$f_{\widehat{Y}_i}(y) = \frac{\sqrt{K}}{\sqrt{2\pi}\sigma} \sum_{m=1}^{M_i} p_{i,m} e^{-K(y - g_i \sqrt{p_i} a_{i,m})^2 / 2\sigma^2}. \tag{7}$$

Thus, the entropy $h(\widehat{y}_i)$ maximization problem is given by

$$
\min_{M_i, \{a_{i,m}\}, \{p_{i,m}\}} \int_{-\infty}^{\infty} f_{\widehat{Y}_i}(y) \log_2 f_{\widehat{Y}_i}(y) dy \tag{8}
$$
$$
\text{s.t.} \quad (4a), (4b), (4c), (4d).
$$

Problem (8) is a mixed discrete and nonconvex problem that is generally difficult to solve.

To handle Problem (8), we first defined some vectors as follows:

$$\mathbf{a}_i \triangleq [a_{i,1}, \cdots, a_{i,M_i}]^T,$$

$$\mathbf{p}_i \triangleq [p_{i,1}, \cdots, p_{i,M_i}]^T,$$

$$\mathbf{q}_i \triangleq \frac{\sqrt{K}}{\sqrt{2\pi}\sigma} \left[e^{-K(y - g_i \sqrt{p_i} a_{i,1})^2 / 2\sigma^2}, \cdots, e^{-K(y - g_i \sqrt{p_i} a_{i,M_i})^2 / 2\sigma^2} \right]^T. \tag{9}$$

Based on the above mentioned definitions in (9), we

reformulated Problem (8) as

$$\min_{M_i, \mathbf{a}_i, \mathbf{p}_i} \int_{-\infty}^{\infty} \mathbf{p}_i \mathbf{q}_i \log_2 \mathbf{p}_i \mathbf{q}_i dy,$$

$$\text{s.t. } \mathbf{p}_i^T \mathbf{a}_i = 0,$$
$$\mathbf{p}_i^T (\mathbf{a}_i \odot \mathbf{a}_i) = \varepsilon_i,$$
$$\mathbf{p}_i^T 1 M_i = 1,$$
$$\mathbf{p}_i \geq 0, \tag{10}$$

where $\odot$ denotes the Hadamard product. Note that given both M_i and $\mathbf{a}_i$, Problem (10), is convex with respect to $\mathbf{p}_i$, which can be solved efficiently using the available interior-point algorithms [32, 33].

Without the loss of generality, we assumed the space among the M_i points $\{a_{i,m}\}_{m=1}^{M_i}$ is equally placed in the range of $[-A_i, A_i]$, i.e.,

$$a_{i,m} = \frac{2A_i}{M_i - 1}(m_i - 1) - A_i. \tag{11}$$

Note that when M_i is larger than the optimal values M_i^*, redundant points exist in $\{a_{i,m}\}_{m=1}^{M_i}$. However, the effects of the redundant points can be eliminated by optimizing the PDF $\mathbf{p}_i$. Thus, for a sufficiently large M_i, the maximum entropy $h(\hat{y}_i)$ can be approximated by solving Problem (10) under condition (11). In summary, the proposed entropy $h(\hat{y}_i)$ approximation method is listed in Algorithm 1.

Let $h^*(\hat{y}_i)$ denote the entropy $h(\hat{y}_i)$ computed by Algorithm 1. Substituting $h^*(\hat{y}_i)$ to, we obtained the discrete inner bound of NOMA VLC as

$$R_i \geq \frac{1}{2} \log_2 \frac{\sum_{k=1}^{N} 2^{2h^*(\hat{y}_k)}}{2\pi e \left(\sum_{j=i+1}^{N} g_j^2 p_j \varepsilon_j + \sigma^2 \right)}. \tag{12}$$

Let $\mathscr{R}_{\text{dis}}^{\text{inner}}$ denote the achievable rate region of NOMA VLC IoT networks bounded by (12), which is given by

$$\mathscr{R}_{\text{dis}}^{\text{inner}} \triangleq \left\{ \begin{array}{c} r_1, \cdots, r_N | r_i \in \mathbb{R}, \\ r_i \geq \frac{1}{2} \log_2 \frac{\sum_{k=i}^{N} 2^{2h^*(\hat{y}k)}}{2\pi e \left(\sum_{j=i+1}^{N} g_j^2 p_j \sigma^2 \right)}, \\ i = 1, \cdots, N. \end{array} \right\} \tag{13}$$

2.1.2. Outer Bound with Discrete Inputs. In this subsection, the outer bound of the channel capacity region of the NOMA VLC IoT network with discrete input is proposed. The upper bound of the achievable rate R_i is given by

$$R_i = \max_{\{P(s_i)\}} h \left(\sum_{k=i}^{N} g_k \sqrt{p_k} s_k + z \right) - h \left(\sum_{j=i+1}^{N} g_j \sqrt{p_j} s_j + z \right), \tag{14a}$$

$$\leq \frac{1}{2} \log_2 2\pi e \text{ var} \left(\sum_{k=i}^{N} g_k \sqrt{p_k} s_k + z \right) - \max_{\{f(s_i)\}} \frac{1}{2} \log_2 \sum_{j=i+1}^{N} 2^{2h(\hat{y}_i)}, \tag{14b}$$

$$= \frac{1}{2} \log_2 \frac{2\pi e \sigma^2 + 2\pi e \sum_{k=i}^{N} g_k^2 p_k \varepsilon_k}{\sum_{j=i+1}^{N} 2^{2h(\hat{y}_j)}}, \tag{14c}$$

where the inequality (14a) follows the EPI [21] and $h(x) \leq 1/2 \log 2\pi e \text{ var}(x)$ and $h^*(\hat{y}_i)$ is calculated by Algorithm $\mathscr{R}_{\text{dis}}^{\text{outer}}$ denotes the channel capacity region of NOMA VLC IoT networks bounded, which is given by

$$\mathscr{R}_{\text{dis}}^{\text{outer}} \triangleq \left\{ \begin{array}{c} r_1, \cdots, r_N | r_i \in \mathbb{R}, \\ r_i \leq \frac{1}{2} \log_2 \frac{2\pi e \sigma^2 + 2\pi e \sum_{j=i}^{N} g_j^2 p_j \varepsilon_j}{\sum_{k=i+1}^{N} 2^{2h^*(\hat{y}_k)}}, \\ i = 1, \cdots, N. \end{array} \right\} \tag{15}$$

2.2. Capacity Region with Continuous Inputs. Although the discrete inner and outer bounds are obtained, they are not in closed-forms, which is the main obstacle in determining the capacity region. To this end, we assumed that the input signal s_i follows a continuous distribution and derived the ABG inner bound of NOMA VLC IoT networks in closed-form expressions.

2.2.1. ABG Inner Bound. Let $f(s_i)$ denote the pdf of s_i which satisfies the following peak optical power (Equation (16a)), average optical power (Equation (16b)), and electrical power constraints (Equation (16c)), i.e.,

$$\int_{-A_i}^{A_i} f(s_i) ds_i = 1, \tag{16a}$$

$$\int_{-A_i}^{A_i} s_i f(s_i) ds_i = 0, \tag{16b}$$

$$\int_{-A_i}^{A_i} s_i^2 f(s_i) ds_i = \varepsilon_i. \tag{16c}$$

Then, for $1 \leq i \leq N$, the lower bound of the achievable rate, R_i, is given by

$$R_i = \max_{\{f(s_i)\}} I(y; s_i | s_1, \cdots, s_{i-1}), \tag{17a}$$

$$= \max_{\{P(s_i)\}} h \left(\sum_{k=i}^{N} g_k \sqrt{p_k} s_k + z \right) - h \left(\sum_{j=i+1}^{N} g_j \sqrt{p_j} s_j + z \right), \tag{17b}$$

> 1 initialization: Set $n = 0$, $h_0 = 0$; set c_1 as the stopping parameter, choose $M_i \geq 2$;
> 2 let $n = n + 1$, and compute a_i according to (11);
> 3 compute the entropy $h_n = h(\hat{y}_i)$ by solving Problem (10);
> 4 if $|h_n - h_n - 1| \leq c_1$, stop, and output h_n; otherwise, $M_i = M_i + 1$, and go to step 2.

ALGORITHM 1. Entropy $h(\hat{y}_i)$ approximation method.

$$\geq \max_{\{f(s_i)\}} \frac{1}{2} \log_2 \left(\sum_{k=i}^{N} 2^{2h(s_k) + \log_2 g_k^2 p_k} + 2^{2h(z)} \right)$$
$$- \frac{1}{2} \log_2 2\pi e \, \mathrm{var} \left(\sum_{j=i+1}^{N} g_j \sqrt{p_j} s_j + z \right), \tag{17c}$$

$$= \frac{1}{2} \log_2 \frac{\sum_{k=i}^{N} p_k g_k^2 e^{1+2(\alpha_k + \gamma_k \varepsilon_k)} + 2\pi\sigma^2}{2\pi \sum_{j=i+1}^{N} p_j g_j^2 \varepsilon_j + 2\pi\sigma^2}, \tag{17d}$$

where the inequality (17c) is true due to the EPI [21] and $h(Q) \leq 1/2 \log 2\pi e \, \mathrm{var}(Q)$ for a random variable with variance, $\mathrm{var}(Q)$. The equality (17d) holds because the corresponding input distribution (termed ABG distribution) [34] maximizes the differential entropy and is given by

$$f_i(s_i) = \begin{cases} e^{-1-\alpha_i - \beta_i s_i - \gamma_i s_i^2}, & -A_i \leq s_i \leq A_i; \\ 0, & \text{otherwise}, \end{cases} \tag{18}$$

where the parameters α_i, β_i, and γ_i are the solutions of the following equations:

$$T_i(A_i) - T_i(-A_i) = e^{1+\alpha_i},$$
$$\beta_i \left(e^{A_i(\beta_i - \gamma_i A_i)} - e^{1+\alpha_i} - e^{-A_i(\beta_i + \gamma_i A_i)} \right) = 0,$$
$$e^{A_i(\beta_i - \gamma_i A_i)} \left((\beta_i - 2\gamma_i A_i) e^{-2A_i \beta_i} - \beta_i - 2\gamma_i A_i \right) + \left(\beta_i^2 + 2\gamma_i \right) e^{1+\alpha_i}$$
$$= 4\gamma_i^2 \varepsilon_i e^{1+\alpha i}, \tag{19}$$

$$T_i(X) = \sqrt{\pi} \frac{e^{\beta_i^2/4\gamma_i} \, \mathrm{erf} \, \left(\beta_i + 2\gamma_i X/2\sqrt{\gamma_i} \right)}{2\sqrt{\gamma_i}}. \tag{20}$$

For $k = N$, the upper bound R_k is given by

$$R_N = \frac{1}{2} \log_2 \left(1 + \frac{p_N g_N^2 e^{1+2(\alpha_N + \gamma N \varepsilon N)}}{2\pi\sigma^2} \right) \tag{21}$$

Let $\mathscr{R}_{\mathrm{con}}^{\mathrm{inner}}$ denote the achievable rate region of NOMA

VLC, which is given by

$$\mathscr{R}_{\mathrm{con}}^{\mathrm{inner}} \triangleq \left\{ \begin{array}{c} r_1, \cdots, r_K | r_i \in \mathbb{R}, \\ r_i \geq \frac{1}{2} \log_2 \frac{\sum_{k=i}^{N} p_k g_k^2 e^{1+2(\alpha_k + \gamma_k \varepsilon_k)} + 2\pi\sigma^2}{2\pi \sum_{j=i+1}^{N} p_j g_j^2 \varepsilon_j + 2\pi\sigma^2}, \\ i = 1, \cdots, K. \end{array} \right\} \tag{22}$$

2.2.2. ABG Outer Bound. Finally, we developed the ABG outer bound of uplink NOMA of VLC IoT networks in closed-form expressions for the continuous input. The upper bound of the maximum achievable rate, R_i, is given by

$$R_i = \max_{\{f(s_i)\}} h \left(\sum_{k=i}^{N} g_k \sqrt{p_k} s_k + z \right) - h \left(\sum_{j=i+1}^{N} g_j \sqrt{p_j} s_j + z \right), \tag{23a}$$

$$\leq \frac{1}{2} \log_2 2\pi e \, \mathrm{var} \left(\sum_{k=i}^{N} g_k \sqrt{p_k} s_k + z \right)$$
$$- \max_{\{f(s_i)\}} \frac{1}{2} \log_2 \left(\sum_{j=i+1}^{N} 2^{2h(s_j) + \log_2 g_j^2 p_j} + 2^{2h(z)} \right), \tag{23b}$$

$$= \frac{1}{2} \log_2 \frac{2\pi\sigma^2 + 2\pi \sum_{k=i}^{N} g_k^2 p_k \varepsilon_k}{\sum_{j=i+1}^{N} p_j g_j^2 e^{1+2(\alpha_j + \gamma_j \varepsilon_j)} + 2\pi\sigma^2}, \tag{23c}$$

where the inequality (23b) follows the EPI [21] and $h(Q) \leq 1/2 \log 2\pi e \, \mathrm{var}(x)$ and the equality (23c) holds because s_i follows the ABG distribution [34].

Let $\mathscr{R}_{\mathrm{con}}^{\mathrm{outer}}$ denote the channel capacity region of NOMA VLC IoT networks bounded by (23c), which is given by

$$\mathscr{R}_{\mathrm{con}}^{\mathrm{outer}} \triangleq \left\{ \begin{array}{c} r_1, \cdots, r_N | r_i \in \mathbb{R}, \\ r_i \leq \frac{1}{2} \log_2 \frac{2\pi\sigma^2 + 2\pi \sum_{j=i}^{N} g_j^2 p_j \varepsilon_j}{\sum_{k=i+1}^{N} p_k g_k^2 e^{1+2(\alpha_k + \gamma_k \varepsilon_k)}_j + 2\pi\sigma^2}, \\ i = 1, \cdots, K \end{array} \right\}. \tag{24}$$

3. Optimal Beamforming Design for Uplink NOMA of VLC IOT Networks

In this section, we further considered a single-input, multiple-output (SIMO) uplink NOMA for a VLC IoT network as illustrated in Figure 2, which includes N single
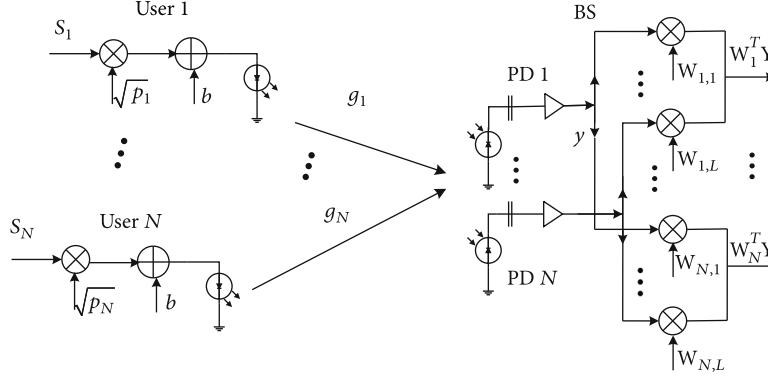
Figure 2: Schematic of SIMO NOMA of a VLC IoT network.

LED users (IoT devices) and a L PDs BS. Let s_i denote the transmitted message from user i, where the definition of s_i is similar to that in the previous SISO scenario. Thus, the received signal at BS can be expressed as

$$\mathbf{y} = \sum_{k=1}^{N} \mathbf{g}_k \sqrt{p_k} s_k + \mathbf{z}, \tag{25}$$

where $\mathbf{g}_i \in \mathbb{R}^{L \times 1}$ denotes the channel vector between user i and BS, $p_i \varepsilon_i \geq 0$ is the transmitted power of user i, and $\mathbf{z} \sim \mathcal{N}(\mathbf{0}, \sigma^2 \mathbf{I})$ represents the additive white Gaussian noise vector.

For message s_i, the BS invokes a linear receive beamformer $\mathbf{w}_i \in \mathbb{R}^L$ to the received signals $\mathbf{y}$ as follows:

$$\hat{y}_i = \mathbf{w}_i^T \mathbf{y} = \sum_{k=1}^{N} \mathbf{w}_i^T \mathbf{g}_k \sqrt{p_k} s_k + \mathbf{w}_i^T \mathbf{z}, \ i = 1, \cdots, N. \tag{26}$$

Without the loss of generality, we assumed that the terms $\{ \| \mathbf{g}_i^T \sqrt{p_i \varepsilon_i} \| \}_{i=1}^{N}$ satisfy a descending order, i.e., $\| \mathbf{g}_1^T \sqrt{p_1 \varepsilon_1} \| \geq \| \mathbf{g}_2^T \sqrt{p_2 \varepsilon_2} \| \geq \cdots \geq \| \mathbf{g}_N^T \sqrt{p_N \varepsilon_N} \|$. Then, the BS adopts the SIC technique to decode the received signals in a descending order [35], i.e., from s_1 to s_N. Specifically, let R_i denote the achievable rate of decoding message s_i, $1 \leq i \leq N$.

When $1 \leq i < N$, R_i is given by

$$R_i = \max_{\{f(s_i)\}} I(\hat{y}; s_i | s_1, \cdots, s_{i-1}), \tag{27a}$$

$$= \max_{\{f(s_i)\}} h(\hat{y} | s_1, \cdots, s_{i-1}) - h(\hat{y} | s_1, \cdots, s_i), \tag{27b}$$

$$= \max_{\{f(s_i)\}} h\left(\sum_{j=i}^{N} \mathbf{w}_i^T \mathbf{g}_j \sqrt{p_j} s_j + \mathbf{w}_i^T \mathbf{z} \right) \\ - h\left(\sum_{m=i+1}^{N} \mathbf{w}_k^T \mathbf{g}_m \sqrt{p_m} s_m + \mathbf{w}_i^T \mathbf{z} \right), \tag{27c}$$

$$\geq \max_{\{f(s_i)\}} \frac{1}{2} \log_2 \left(\sum_{j=i}^{N} 2^{2h(s_j)} + \log_2 \left| \mathbf{w}_i^T \mathbf{g}_j \right|^2 p_j + 2^{2h(\mathbf{w}_i^T \mathbf{z})} \right) \\ - \frac{1}{2} \log_2 2\pi e \operatorname{var} \left(\sum_{m=i+1}^{N} \left| \mathbf{w}_i^T \mathbf{g}_m \right|^2 + p_m s_m + \| \mathbf{w}_i \|^2 \sigma^2 \right), \tag{27d}$$

$$= \frac{1}{2} \log_2 \frac{\sum_{j=i}^{N} \left| \mathbf{w}_i^T \mathbf{g}_j \right|^2 p_j e^{1+2(\alpha_j + \gamma_j \varepsilon_j)} + 2\pi \| \mathbf{w}_i \|^2 \sigma^2}{2\pi \sum_{m=i+1}^{N} \left| \mathbf{w}_i^T \mathbf{g}_m \right|^2 p_m \varepsilon_m + 2\pi \| \mathbf{w}_i \|^2 \sigma^2}, \tag{27e}$$

where the inequality (27d) holds due to the EPI [21] and $h(Q) \leq (1/2) \log 2\pi e \operatorname{var}(Q)$ for a random variable with variance, $\operatorname{var}(Q)$. The equality (27e) holds because the corresponding input distribution (termed ABG distribution) [34] maximizes the differential entropy. For $k = N$, R_N is given by

$$R_N = \frac{1}{2} \log_2 \left(1 + \frac{\left| \mathbf{w}_N^T \mathbf{g}_N \right|^2 p_N e^{1+2(\alpha_N + \gamma_N \varepsilon_N)}}{2\pi \sigma^2} \right). \tag{28}$$

Therefore, for $1 \leq i \leq N$, the expression of the lower bound R_i can be expressed as

$$R_i = \frac{1}{2} \log_2 \frac{\sum_{j=i}^{N} \left| \mathbf{w}_i^T \mathbf{g}_j \right|^2 p_j e^{1+2(\alpha_j + \gamma_j \varepsilon_j)} + 2\pi \| \mathbf{w}_i \|^2 \sigma^2}{2\pi \Gamma_i \sum_{m=i+1}^{N} \left| \mathbf{w}_i^T \mathbf{g}_m \right|^2 p_m \varepsilon_m + 2\pi \| \mathbf{w}_i \|^2 \sigma^2}, \tag{29}$$

where Γ_i is an indicator function as follows:

$$\Gamma_i \triangleq \begin{cases} 1, & \forall_i \neq N, \\ 0, & i = N. \end{cases} \tag{30}$$

Based on the explicit achievable rate expression in (29), we investigated the optimal receiver beamformers' design to maximize the minimum achievable rates which satisfies the
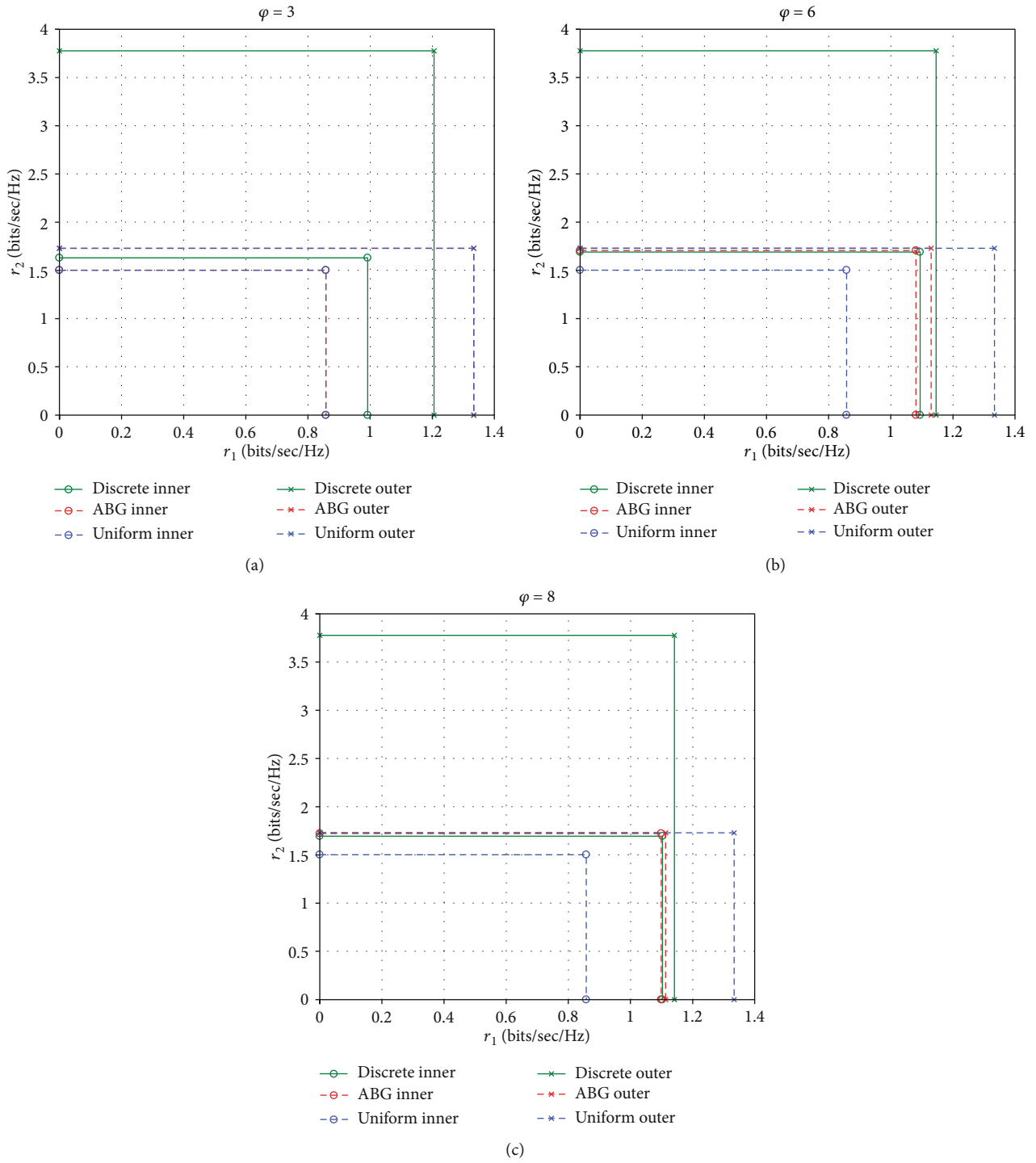
Figure 3: Outer and inner bounds of the capacity region for MAC NOMA in VLC IoT networks with (a) $\varphi = 3$, (b) $\varphi = 6$, and (c) $\varphi = 8$, respectively.

power constraints as follows:

$$\max_{\mathbf{w}_i} \frac{1}{2} \log_2 \frac{\sum_{j=i}^{N} \left|\mathbf{w}_i^T \mathbf{g}_j\right|^2 p_j e^{1+2\left(\alpha_j+\gamma_j\varepsilon_j\right)} + 2\pi\|\mathbf{w}_i\|^2\sigma^2}{2\pi\Gamma_i\sum_{m=i+1}^{N}\left|\mathbf{w}_i^T \mathbf{g}_m\right|^2 p_m\varepsilon_m + 2\pi\|\mathbf{w}_i\|^2\sigma^2} \quad (31)$$

$$\text{s.t.}\|\mathbf{w}_i\|^2 \le 1, 1 \le i \le N.$$

Note that Problem (31) is nonconvex which is hard to solve. To deal with this difficulty, we first define some variables as follows:

$$\widehat{p}_i = \sqrt{p_i e^{1+2(\alpha_i+\gamma_i\varepsilon_i)}},$$
$$\mathbf{G}_i \triangleq [0, \cdots, \widehat{p}_i\mathbf{g}_i, \cdots, \widehat{p}_N\mathbf{g}_N],$$
$$\bar{\mathbf{G}}_i \triangleq 2\pi[\mathbf{0}, \cdots, \Gamma_i\sqrt{p_{i+1}\varepsilon_{i+1}}\mathbf{g}_i, \cdots, \Gamma_i\sqrt{p_N\varepsilon_N}\mathbf{g}_N], \quad (32)$$
$$c \triangleq 2\pi\sigma^2.$$

With the introduced variables in (32), we can equivalently rewrite Problem (31) to a concise form as follows:

$$\max_{\mathbf{w}_i} \frac{1}{2} \log_2 \left(\frac{\mathbf{w}_i^T \mathbf{G}_i\mathbf{G}_i^T \mathbf{w}_i + c\mathbf{w}_i^T\mathbf{w}_i}{\mathbf{w}_i^T \bar{\mathbf{G}}_i\bar{\mathbf{G}}_i^T \mathbf{w}_i + c\mathbf{w}_i^T\mathbf{w}_i}\right), \quad (33)$$

$$\text{s.t.}\|\mathbf{w}_i\|^2 \le 1, 1 \le i \le N,$$

which is a quadratically constrained quadratic problem (QCQP). As the logarithmic function is monotonically increasing, Problem (33) can be further reformulated as follows:

$$\max_{\mathbf{w}_i} \frac{\mathbf{w}_i^T \left(\mathbf{G}_i\mathbf{G}_i^T + c\mathbf{I}\right)\mathbf{w}_i}{\mathbf{w}_i^T \left(\mathbf{G}_i\mathbf{G}_i^T + c\mathbf{I}\right)\mathbf{w}_i} \quad (34)$$

$$\text{s.t.}\|\mathbf{w}_i\|^2 \le 1, 1 \le i \le N.$$

Let $\lambda_{i,\max}$ denote the largest generalized eigenvalue of matrix $\mathbf{A}_i$ and matrix $\mathbf{B}_i$, where $\mathbf{A}_i \triangleq \mathbf{G}_i\mathbf{G}_i^T + c\mathbf{I}$ and $\mathbf{B}_i \triangleq \bar{\mathbf{G}}_i\bar{\mathbf{G}}_i^T + c\mathbf{I}$.

Furthermore, let $\mathbf{w}_{i,\max}$ denote the generalized eigenvector corresponding to the largest eigenvalue $\lambda_{i,\max}$, which satisfies $\mathbf{A}_i\mathbf{w}_{i,\max} = \lambda_{i,\max}\mathbf{B}_i\mathbf{w}_{i,\max}$. Thus, for the NOMA VLC uplink, the optimal beamformer $\mathbf{w}_i$ of Problem (34) is given by

$$\mathbf{w}_i^{\text{opt}} = \frac{\mathbf{w}_{i,\max}}{\left\|\mathbf{w}_{i,\max}\right\|}, \quad (35)$$

and the maximum achievable rate of message s_i is $\log_2\lambda_{i,\max}$.

4. Numerical Results

In this section, the performance of the capacity region and the optimal beamforming design for uplink NOMA in VLC IoT networks are evaluated using numerical results.

In the following, we present the performance of the discrete inner and outer bounds and the ABG inner and outer

Figure 4: Sum rates $r_1 + r_2$ (bits/sec/Hz) of the discrete inner and outer bounds, ABG inner and outer bounds, and uniform inner and outer bounds versus SNR(dB) with $\varphi = 6$.
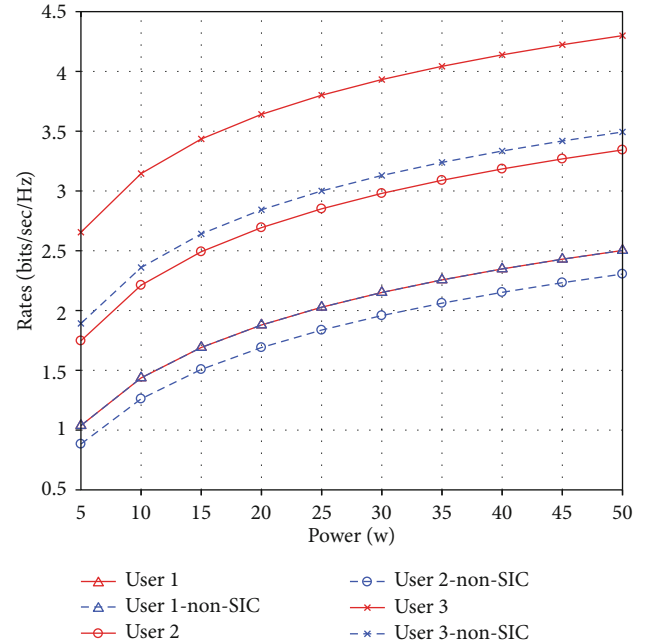
Figure 5: Maximum rates of users versus transmit power.

bounds of the capacity region for the MAC NOMA in VLC IoT networks. Assume that $g_1 = 1$, $g_2 = 1/2$, $A \triangleq A_1 = A_2$, and $\varepsilon \triangleq \varepsilon_1 = \varepsilon_2$. Let $\varphi \triangleq A^2/\varepsilon$ denote the amplitude-to-variance ratio, and define SNR as $\triangleq \varepsilon/\sigma^2$. Moreover, both the uniform inner and outer bounds of the capacity region of MAC NOMA of VLC IoT networks are also presented

for comparison, where the input signals follow a uniform distribution [36–38].

Figures 3(a)–3(c) show the inner and outer bounds for the channel capacity region of uplink NOMA in VLC IoT networks with SNR = 10 dB, $\varphi = 3$, 6, and 8, respectively. Figure 3(a) shows that the ABG inner bound is identical to the uniform inner bound. A similar case is observed for the outer bound; this is because the ABG has a uniform distribution for $\varphi = 3$. Moreover, the inner bound with discrete inputs is larger than the ABG inner bound, while the outer bound with discrete inputs cannot dominate the ABG outer bound. Figures 3(b) and 3(c) show that the inner bound with discrete inputs is the highest among the three types of inner bounds, while the ABG outer bound is the lowest among the three types of outer bounds for $\varphi = 6$ and 8. Comparing Figures 3(a)–3(c), it can be seen that as the value of φ increases, the gap between the inner bound with discrete input and the ABG inner bound decreases, and the gap between the ABG inner bound and the ABG outer bound also decreases.
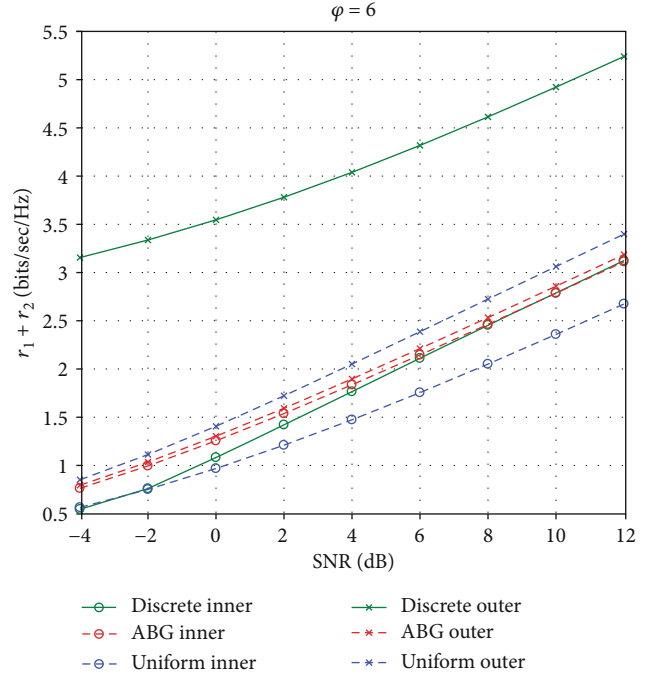
Figure 4 compares the sum rates $r_1 + r_2$ (bits/sec/Hz) of the discrete inner and outer bounds, the ABG inner and outer bounds, and the uniform and inner bounds against SNR(dB) with $\phi = 6$. As shown in Figure 4, the sum rate of each bound increases as the SNR gets larger, and the ABG inner bound is higher than those with the discrete inputs and the uniform inner bound, while the ABG outer bound is lower than the one with discrete inputs and the uniform outer bound. Additionally, we can observe that the gap between the proposed ABG inner bound and ABG outer bound increases as the SNR increases.

Figure 5 shows the achievable rates of three users with respect to the transmit power. We can see that the rate of each user increases as the rate of the transmit power increases. Furthermore, the rate for each user of the proposed method is larger than that of the users of the non-SIC methods.

5. Conclusions

In this paper, we investigated the NOMA transmission for VLC IoT networks. Specifically, the channel capacity region of the practical NOMA VLC IoT networks was established with discrete and continuous inputs, respectively. To the best of our knowledge, the proposed inner and outer bounds are the first theoretical bounds of the channel capacity region for uplink NOMA of VLC IoT networks. Furthermore, we developed the optimal receiver NOMA beamforming design for VLC IoT networks and showed that the optimal beamformers are the generalized eigenvectors corresponding to the largest generalized eigenvalues.

Data Availability

The data of the numerical results can be obtained by emailing the author (mashuai001@cumt.edu.cn).

Conflicts of Interest

The authors declare that they have no conflicts of interest.

References

[1] T. Komine and M. Nakagawa, "Fundamental analysis for visible-light communication system using LED lights," *IEEE Transactions on Consumer Electronics*, vol. 50, no. 1, pp. 100–107, 2004.

[2] H. Elgala, R. Mesleh, and H. Haas, "Indoor optical wireless communication: potential and state-of-the-art," *IEEE Communications Magazine*, vol. 49, no. 9, pp. 56–62, 2011.

[3] S. Arnon, J. Barry, G. Karagiannidis, R. Schober, and M. Uysal, *Advanced Optical Wireless Communication Systems*, Cambridge Univ, Cambridge, U.K., 1st edition, 2012.

[4] A. Jovicic, J. Li, and T. Richardson, "Visible light communication: opportunities, challenges and the path to market," *IEEE Communications Magazine*, vol. 51, no. 12, pp. 26–32, 2013.

[5] P. H. Pathak, X. Feng, P. Hu, and P. Mohapatra, "Visible light communication, networking, and sensing: a survey, potential and challenges," *IEEE Communications Surveys & Tutorials*, vol. 17, no. 4, pp. 2047–2077, 2015.

[6] D. Karunatilaka, F. Zafar, V. Kalavally, and R. Parthiban, "LED based indoor visible light communications: state of the art," *IEEE Communications Surveys & Tutorials*, vol. 17, no. 3, pp. 1649–1678, 2015.

[7] J. Luo, L. Fan, and H. Li, "Indoor positioning systems based on visible light communication: state of the art," *IEEE Communications Surveys & Tutorials*, vol. 19, no. 4, pp. 2871–2893, 2017.

[8] L. Dai, B. Wang, Y. Yuan, S. Han, Chih-lin I, and Z. Wang, "Non-orthogonal multiple access for 5G: solutions, challenges, opportunities, and future research trends," *IEEE Communications Magazine*, vol. 53, no. 9, pp. 74–81, 2015.

[9] X. Li, J. Li, Y. Liu, Z. Ding, and A. Nallanathan, "Residual transceiver hardware impairments on cooperative NOMA networks," *IEEE Transactions on Wireless Communications*, vol. 19, no. 1, pp. 680–695, 2019.

[10] X. Li, M. Liu, C. Deng, P. T. Mathiopoulos, Z. Ding, and Y. Liu, "Full-duplex cooperative noma relaying systems with i/q imbalance and imperfect sic," *IEEE Wireless Communications Letters*, vol. 9, no. 1, pp. 17–20, 2019.

[11] Z. Ding, Y. Liu, J. Choi et al., "Application of non-orthogonal multiple access in LTE and 5G networks," *IEEE Communications Magazine*, vol. 55, no. 2, pp. 185–191, 2017.

[12] W. Hao, Z. Chu, F. Zhou, S. Yang, G. Sun, and K. Wong, "Green communication for NOMA-based CRAN," *IEEE Internet of Things Journal*, vol. 6, no. 1, pp. 666–678, 2019.

[13] X. Li, J. Li, and L. Li, "Performance analysis of impaired swipt noma relaying networks over imperfect weibull channels," *IEEE Systems Journal*, vol. 14, no. 1, pp. 669–672, 2020.

[14] H. Tabassum, E. Hossain, and J. Hossain, "Modeling and analysis of uplink non-orthogonal multiple access (NOMA) in large-scale cellular networks using poisson cluster processes," *IEEE Transactions on Communications*, vol. 65, no. 8, pp. 1–3570, 2017.

[15] M. A. Sedaghat and R. R. Mller, "On user pairing in uplink NOMA," *IEEE Transactions on Wireless Communications*, vol. 17, no. 5, pp. 3474–3486, 2018.

[16] R. Ruby, S. Zhong, H. Yang, and K. Wu, "Enhanced uplink resource allocation in non-orthogonal multiple access systems," *IEEE Transactions on Wireless Communications*, vol. 17, no. 3, pp. 1432–1444, 2018.

[17] N. Zhang, T. Ding, and G. Kang, "Interference balance power control for uplink non-orthogonal multiple access," *IEEE Communications Letters*, vol. 23, no. 3, pp. 470–473, 2019.

[18] Z. Ding, R. Schober, and H. V. Poor, "A general MIMO framework for NOMA downlink and uplink transmission based on signal alignment," *IEEE Transactions on Wireless Communications*, vol. 15, no. 6, pp. 4438–4454, 2016.

[19] Z. Zhang, H. Sun, and R. Q. Hu, "Downlink and uplink non-orthogonal multiple access in a dense wireless network," *IEEE Journal on Selected Areas in Communications*, vol. 35, no. 12, pp. 2771–2784, 2017.

[20] X. Guan, Q. Yang, and C. Chan, "Joint detection of visible light communication signals under non-orthogonal multiple access," *IEEE Photonics Technology Letters*, vol. 29, no. 4, pp. 377–380, 2017.

[21] T. M. Cover and J. A. Thomas, *Elements of information theory*, Wiley, New York, 2nd edition, 2006.

[22] J. G. Smith, "The information capacity of amplitude- and variance-constrained sclar gaussian channels," *Information and Control*, vol. 18, no. 3, pp. 203–219, 1971.

[23] T. Fath and H. Haas, "Performance comparison of MIMO techniques for optical wireless communications in indoor environments," *IEEE Transactions on Communications*, vol. 61, no. 2, pp. 733–742, 2013.

[24] T. Q. Wang, Y. A. Sekercioglu, and J. Armstrong, "Analysis of an optical wireless receiver using a hemispherical lens with application in MIMO visible light communications," *Journal of Lightwave Technology*, vol. 31, no. 11, pp. 1744–1754, 2013.

[25] J. Kahn and J. Barry, "Wireless infrared communications," *Proceedings of the IEEE*, vol. 85, no. 2, pp. 265–298, 1997.

[26] S. M. Moser, "Capacity results of an optical intensity channel with input-dependent Gaussian noise," *IEEE Transactions on Information Theory*, vol. 58, no. 1, pp. 207–223, 2012.

[27] Q. Gao, C. Gong, and Z. Xu, "Joint transceiver and offset design for visible light communications with input-dependent shot noise," *IEEE Transactions on Wireless Communications*, vol. 16, no. 5, pp. 2736–2747, 2017.

[28] C. Gong, A. Tajer, and X. Wang, "Interference channel with constrained partial group decoding," *IEEE Transactions on Communications*, vol. 59, no. 11, pp. 3059–3071, 2011.

[29] X. Zhang, Q. Gao, C. Gong, and Z. Xu, "User grouping and power allocation for NOMA visible light communication multi-cell networks," *IEEE Communications Letters*, vol. 21, no. 4, pp. 777–780, 2017.

[30] Z. Yang, W. Xu, and Y. Li, "Fair non-orthogonal multiple access for visible light communication downlinks," *IEEE Wireless Communications Letters*, vol. 6, no. 1, pp. 66–69, 2017.

[31] Z. Ding, L. Dai, and H. V. Poor, "MIMO-NOMA design for small packet transmission in the Internet of Things," *IEEE Access*, vol. 4, pp. 1393–1405, 2016.

[32] J. F. Sturm, "Using SeDuMi 1.02, a Matlab toolbox for optimization over symmetric cones," *Optimization Methods and Software*, vol. 11, no. 1-4, pp. 625–653, 1999.

[33] M. Grant and S. Boyd, "CVX: Matlab software for disciplined convex programming," June 2009, http://stanford.edu/boyd/cvx.

[34] S. Ma, R. Yang, H. Li, Z.-L. Dong, H. Gu, and S. Li, "Achievable rate with closed-form for SISO channel and broadcast channel in visible light communication networks," *Journal of Lightwave Technology*, vol. 35, no. 14, pp. 2778–2787, 2017.

[35] M. Mollanoori and M. Ghaderi, "Uplink scheduling in wireless networks with successive interference cancellation," *IEEE Transactions on Mobile Computing*, vol. 13, no. 5, pp. 1132–1144, 2014.

[36] T. V. Pham and A. T. Pham, "Max-Min fairness and sum-rate maximization of MU-VLC local networks," in *2015 IEEE Globecom Workshops (GC Wkshps)*, pp. 1–6, San Diego, CA, USA, December 2015.

[37] T. V. Pham, H. L. Minh, and A. T. Pham, "Multi-cell VLC: multiuser downlink capacity with coordinated precoding," in *2017 IEEE International Conference on Communications Workshops (ICC Workshops)*, Paris, France, 2017.

[38] H. Shen, Y. Deng, W. Xu, and C. Zhao, "Rate-maximized zero-forcing beamforming for VLC multiuser MISO downlinks," *IEEE Photonics Journal*, vol. 8, no. 1, pp. 1–13, 2016.

Research Article

Competition of Duopoly MVNOs for IoT Applications through Wireless Network Virtualization

Wanli Zhang,[1] **Xianwei Li** [ID],[1] **Liang Zhao,**[2] **and Xiaoying Yang**[1]

[1]*School of Information Engineering, Suzhou University, 234000, China*
[2]*School of Computer Science, Shenyang Aerospace University, 110136, China*

Correspondence should be addressed to Xianwei Li; lixianwei163@163.com

Network performance is of great importance for processing Internet of Things (IoT) applications in the fifth-generation (5G) communication system. With the increasing number of the devices, how network services should be provided with better performances is becoming a pressing issue. The static resource allocation of wireless networks is becoming a bottleneck for the emerging IoT applications. As a potential solution, network virtualization is considered a promising approach to enhancing the network performance and solving the bottleneck issue. In this paper, the problem of wireless network virtualization is investigated where one wireless infrastructure provider (WIP), mobile virtual network operators (MVNOs), and IoT devices coexist. In the system model under consideration, with the help of a software-defined network (SDN) controller, the WIP can divide and reconfigure its radio frequency bands to radio frequency slices. Then, two MVNOs, $MVNO_1$ and $MVNO_2$, can lease these frequency slices from the WIP and then provide IoT network services to IoT users under competition. We apply a two-stage Stackelberg game to investigate and analyze the relationship between the two MVNOs and IoT users, where $MVNO_1$ and $MVNO_2$ firstly try to maximize their profits by setting the optimal network service prices. Then, IoT users make decisions on which network service they should select according to the performances and prices of network services. Two competition cases between $MVNO_1$ and $MVNO_2$ are considered, namely, Stackelberg game (SG) where $MVNO_1$ is the leader whose price of network service is set firstly and $MVNO_2$ is the follower whose network service price is set later and noncooperative strategic game (NSG) under which the service prices of $MVNO_1$ and $MVNO_2$ are simultaneously set. Each IoT user decides whether and which MVNO to select on the basis of the network service prices and qualities. The numerical results are provided to show the effectiveness of our game model and the proposed solution method.

1. Introduction

With the technologies of the Internet of Things (IoT) growing rapidly, more and more IoT devices will be connected in the fifth-generation (5G) communication networks. It was predicted that smart objects would reach with the number 50 billion by 2020 [1]. In recent years, we have witnessed a wide adoption of IoT in many areas, such as health care, landslide detection, and environmental monitoring [2–4]. As shown in Figure 1, the number of connected things by the Internet had been over the population of people by the end of the year 2008 [5]. The radio frequency (RF) spectrum has become crowded due to the rapid increase in the number of IoT devices [7]. Furthermore, the demand from IoT

devices for wireless data services is growing exponentially in recent years. From a recent report released by Cisco, in the year of 2021, the number of global mobile data traffic will reach 49 exabytes per month [8, 9], and part of these data traffic may be generated by unmanned aerial vehicle (UAV) [10]. The wireless spectrum is the scarce and precious radio resource in the 5G communication networks [11]. In general, the government statically allocates the licensed spectrum resource. Recent studies have shown that the static spectrum allocation scheme cannot handle the data generated by these smart devices [12, 13]. The paradox that IoT devices are in a great need for wireless network services and the spectrum has not been fully utilized indicates that the current static spectrum resource allocation policy has some shortcomings.
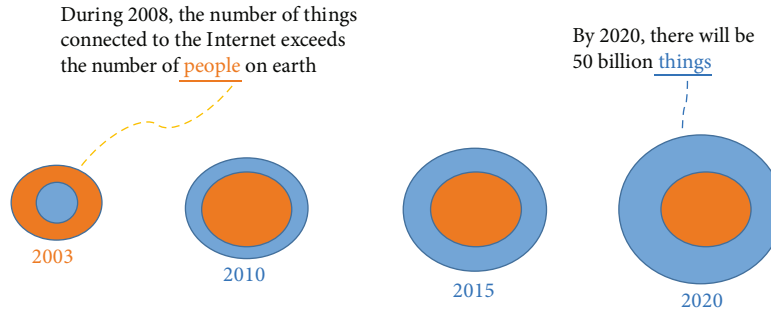
FIGURE 1: The prediction of the number of "things" [5, 6].

Traditionally, the Internet service providers adopted middleboxes to provide network services to users, which is inflexible and results in high Capital Expenses (CAPEX) and Operating Expenses (OPEX) [14]. Fortunately, a SDN and Network Function Virtualization (NFV) have appeared to address these problems. By using the technology of NFV, Virtual Network Functions (VNFs) can replace the middleboxes in traditional networks. The SDN is one of the most important technologies in the 5G commutation systems, and it is considered an emerging paradigm for applications in the IoT [15–18]. In the SDN, with the help of an OpenFlow protocol and SDN controller, the wireless infrastructure providers (WIPs) could programmatically divide and reconfigure their radio frequency bands to frequency slices, and the mobile virtual network operators (MVNOs) can lease these frequency slices from the WIPs in order to provide virtual network services in a fine-grained way [12, 16]. It should be pointed out that the WIP can also adopt NFV to provide virtual network services.

Today, MVNOs have received successful operations in many countries, such as the Google-Fi project. In Japan, IIJ-mio and LINE MOBILE are two MVNOs. They lease radio frequency slices from DOCOMO, which is one of the three WIPs in Japan, to provide network services. The market of global virtual operators is expected to grow with an annual rate of 7.4% and will reach 75.25 billion US $ by 2023 [19]. Although a lot of existing works have studied the network provision of MVNOs, many of them put more focus on the technical aspects, like energy-efficient spectrum allocation protocols for end users [20]. In this paper, we study from the economic perspective of wireless networks' network service provision. Besides, unlike the previous works that simply analyze homogeneous IoT users, in which all the IoT users are of the same valuation for the wireless network services, in our study, IoT users are divided into different types according to their different tastes for the wireless network service quality, which is more realistic than the previous works. For example, the IoT users might have stricter requirements for the latency in the applications of vehicular communications [17, 21] [22].

This study investigates IoT network service selection from two MVNOs leasing radio frequency slices from the WIP and compete for the users of IoT devices, aiming to maximize their profits. The interaction of the MVNOs and IoT users is modelled as a Stackelberg game with two stages,
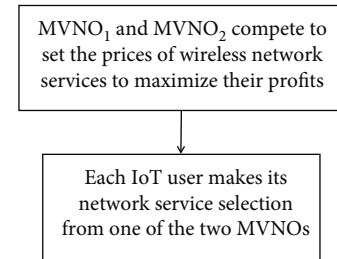
FIGURE 2: Two-level structure between MVNOs and IoT users.

where the two MVNOs set network service price strategies firstly aiming to get their maximized profits, and each IoT user will determine which MVNO it will select service from according to the network service prices and qualities, as Figure 2 illustrates. As far as the competition between the two MVNOs is considered, we analyze two cases: (1) Stackelberg game (SG) case where $MVNO_1$ acts firstly to set the network service price, and then, $MVNO_2$ sets the network service price, and (2) noncooperative strategic game (NSG), also called simultaneous-play game, under which the two MVNOs set the network service prices at the same time. The SG case means that an MVNO will enter an IoT network service market whose incumbent MVNO has better service quality, and the NSG case is that two MVNOs with different qualities of services offer network services at the same time.

The contributions that this study mainly made are summarized as follows:

(i) We study network service selection from two MVNOs, who lease radio frequency slices from WIP and compete to maximize their profits by providing network services. IoT users choose to buy services from one of the two MVNOs based on their offered IoT network service prices and qualities

(ii) The interaction of the two MVNOs and the IoT users is modelled by using the Stackelberg game with two stages, which can be analyzed and solved by leveraging the backward induction method

(iii) We studied and analyzed two competition cases between the two MVNOs, which are known as SG and NSG, respectively. A unique equilibrium for each case is proved to be obtained

(iv) Numerical results are provided to verify the analysis the system models proposed in this paper. Specifically, several parameters are considered to show their impacts on the profits, prices, and service demands of $MVNO_1$ and $MVNO_2$

The rest of this paper is structured as follows. The related work is reviewed and discussed in Section 2. The system model is introduced in Section 3. Service selection is analyzed in Section 3.1. We conduct numerical results and present our analysis results in Section 3.2. Section 4 gives the conclusions of this paper and shows several future research directions.

2. Related Work

Game theory-based techniques have been widely adopted for managing resources in wireless communication networks and cloud computing systems. In a femtocell communication system with two service providers, the authors explored the problem of spectrum sharing scheme decisions from the viewpoint of an entrant service provider [23]. As the IoT users exhibit different valuations for IoT data services, Li et al. investigated price and service selection in IoT data service market, where two service providers buy raw data from a data owner to provision data services to the end users [24]. As the increase in mobile data traffic may cause service quality, a mixed pricing model combined with usage-based and fixed free pricing is proposed in [25] to solve this problem. In [26], the authors studied opportunistic computation offloading in the cloud-enabled IOV by proposing a scheme based on a two-stage Stackelberg game. In [27], Li et al. studied pricing and service selection in mobile cloud architecture, under which the edge cloud and public cloud coexist. They also proposed a two-stage Stackelberg game-based approach to analyze the interactions of the service providers and the mobile users. In [28], the authors analyzed the prioritized sharing between a value MVNO and multiple MNOs. In [29], Wang et al. studied virtual resource management in the virtualized networks with ultradense small cells by using the hierarchical game.

The study of spectrum resource allocation for IoT and IoT service pricing has received a great deal of amount of attention in the past few years. In [30], Ejaz and Ibnkahla proposed a spectrum resource allocation scheme for IoT under the cognitive 5G communication systems. An optimization problem was formulated to solve the spectrum sensing and allocation problem. In [31], Ansere et al. studied energy-efficient spectrum allocation in the cognitive radio network systems. They proposed two dynamic spectrum algorithms to improve the efficiency of the network systems. In [1], a business model including WSNs, multiple service providers, and the end users was presented and analyzed by Guijarro et al. The service providers buy the sensed data from the owners of Wireless Sensor Networks (WSNs) and provide services to the end users in a competitive oligopoly IoT data service market. In [32], Ghosh and Sarkar studied IoT service provision in a monopoly IoT market that consists of IoT service provider (IoTSP), wireless service provider (WSP), and cloud service provider (CSP). Three kinds of interactions

are analyzed among these providers. The authors in [33] studied how the MVNOs should make pricing decisions when others' inventory information is known or unknown. For the known case, they proposed an optimal pricing scheme for maximizing the revenue of each other. For the unknown case, a distributed coalition formation algorithm is developed to maximize each MVNO's revenue. In [34], a market-oriented model was proposed for IoT service delivery. A multileader multifollower Stackelberg game-based approach was proposed to study and analyze the relationship between the IoT service provider and users. In [35], the authors studied two service providers provisioning WSN-based services under competition.

Spectrum resource management in cognitive radio networks (CRNs) has been extensively studied by using game theory. The related works on price competitions in CRNs can be divided into two categories. The first category consists of a competition between the primary network operator who is the licensed spectrum owner and the secondary network operator who has no spectrum license. The second category is the competition between secondary operators who lease the spectrum from the spectrum holder to offer network services to secondary users. A spectrum sharing-method was proposed to set the appropriate price in [36] to maximize users' throughput and the profit of operators. Duan et al. studied price competition and spectrum leasing between two MVNOs in a secondary spectrum market [13]. They assumed that the two secondary operators set prices simultaneously to serve a number of SUs. Tran et al. first studied spectrum access control—based on price in a CRN, where two secondary operators use shared-use and exclusive-use DSA paradigms, respectively, to set prices simultaneously to provision services to delay-sensitive SUs via pricing strategies [37]. However, the costs of spectrum leasing are overlooked and channel quality is not thoroughly analyzed in these works. In [38], the authors studied duopoly service pricing competition in the secondary spectrum market, in which two MVNOs offer network services to the SUs under a competitive environment. However, they only considered one competition case.

Based on the above analysis of previous works on network service provision under competition, it can be obviously found that many of them only considered either one competition scenario or the revenues of MVNOs ignoring the operating costs, such as the leasing cost of a radio frequency slice. Although [39] studied two competition scenarios, the spectrum leasing costs and users' different valuations on network services are not considered.

The system model that this paper analyzed is mainly motivated by [12, 40, 41]. In [12], the authors studied the virtualization of the wireless network to create MVNOs who offer IoT network services to IoT users using the leased frequency slices from WIPs. They formulated a three-layer game where the interactions among WIPs, MVNOs, and IoT users are investigated. In [40], the authors proposed a spectrum access scheme based on price to solve the problem of duopoly competition in a secondary spectrum market, in which two MVNOs lease idle spectrums whose channel qualities are different from the
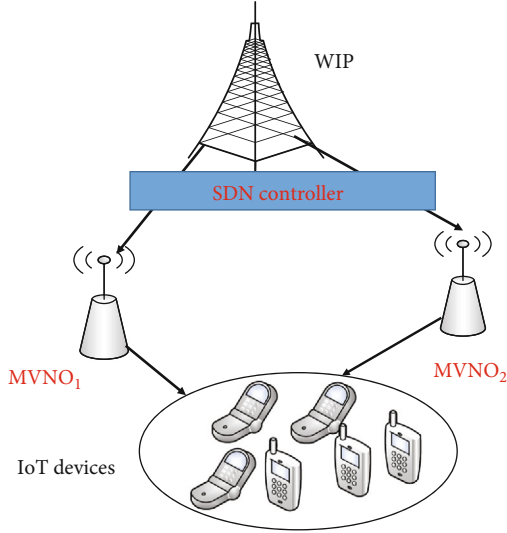
Figure 3: System model.

spectrum owner. In [41], Zhao et al. also studied the duopoly competition in a secondary spectrum market and analyzed the selection dynamics of SUs by using evolutionary game theory. Our study differs from the two previous works in the following aspects. First, the above works only considered one competition scenario, which is the simultaneous-play game scenario. Second, [40] assumed that the secondary users must choose network service from one of the operators, which is not valid in practice, as IoT users might refuse to subscribe to services from any of them if their obtained utilities are negative [37, 42]. Although [41] considered the practical case that some users might refuse to use networks services, the operating costs of the two MVNOs were not considered. Besides, different from [12] that considered a three-layer game among IPs, MVNOs, and IoT users, we mainly focus the two-layer game between two MVNOs and IoT users. Specifically, we analyzed two practical competition cases between the two MVNOs.

3. System Model

In this section, the system model is presented consisting of one WIP, two MVNOs, and a number of IoT users, as illustrated in Figure 3. Under the help of the SDN controller [12, 15–18], the WIP can divide and reconfigure its radio frequency band into slices. These radio frequency slices are of different qualities caused by different interference levels, as can be shown in Figure 4. The two MVNOs, denoted by $MVNO_1$ and $MVNO_2$, respectively, lease radio frequency slices from one WIP and provide network services to a number of IoTs. We assume that each IoT user has one device. Therefore, we use IoT users and IoT devices interchangeably throughout the paper. The system model of this paper is mainly inspired by [12] but is extended to consider two competition scenarios. Different from [12] that studied three-layer game among WIP, MVNOs, and IoT users, the only two-layer game between MVNOs and IoT users is considered in this study. We assume that each IoT user purchases one slice and has its preference when choosing network service.
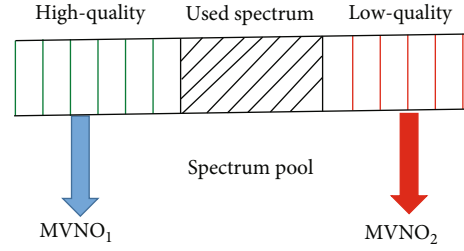

Figure 4: Radio frequency slices with two kinds of qualities.

We suppose that the slice with higher network quality denoted as C_1 is leased to $MVNO_1$, and the one with lower quality denoted as C_2 is leased to $MVNO_2$. The channel quality C_i is expressed as

$$C_i = B \log_2 \left(1 + \frac{\rho}{I_i} \right), \tag{1}$$

where B, ρ, and I_i, respectively, denote bandwidth, the received power of the SU, and the channel interference.

3.1. IoT Users' Model. To represent IoT users' different valuations of the network service, these users are divided into different types according to their tastes for the network service qualities. Suppose that the type of IoT user k is denoted by using the parameter α_k, whose value has uniform distribution in the range $[0, 1]$ whose probability distribution function (PDF) is $f(\cdot)$ and cumulative distribution function (CDF) is $F(\cdot)$. One of the main reasons for the assumption of the uniform distribution is just for convenience. It should be noted that other forms of distribution can also be adopted without affecting our analysis results. The parameter of α_k reflects this IoT user's preference for network service quality, and a higher value of α_k means this IoT user has a higher preference for network service quality. For a type α_k IoT user that selects service from $MVNO_i$, its utility function is given as [12, 40, 41]

$$U_{i,k} = \alpha_k C_i - p_i, i = 1, 2, \tag{2}$$

where C_i and p_i denote the network service quality and price, respectively.

3.2. MVNOs' Model. Assume that there are two network service operators, denoted as $MVNO_1$ and $MVNO_2$, competing to attract a standard number of IoT users. The objective of the MVNOs is to set optimal network service prices p_1 and p_2, respectively, to maximize their profits. For an $MVNO_i$, $i = \{1, 2\}$, its profit is denoted as the revenue it can obtain minus the cost of leasing radio frequency slices from the WIP, which is given as

$$\pi_i = (p_i - \mu_i), i = 1, 2, \tag{3}$$

where μ_i and D_i are the operating cost including radio frequency slice leasing cost and user demands of $MVNO_i$, respectively.

Notation	Description
i	$i \in \{1, 2\}$, which is a MVNO set
k	Subscript of a mobile user
p_i	The network service price of $MVNO_i$, for $i = 1, 2$
D_i	The demands of IoT users for services from $MVNO_i$
C_i	The network service quality of $MVNO_i$
p_i^s	The equilibrium price of $MVNO_i$ in SG scenario
p_i^n	The equilibrium price of $MVNO_i$ in NSG scenario
π_i^s	The profit of $MVNO_i$ in SG scenario
π_i^n	The profit of $MVNO_i$ in NSG scenario
α_k	IoT user k's preference for network service quality
$f(\cdot)$	PDF of IoT users' type
$F(\cdot)$	CDF of IoT users' preference parameter
μ_i	The operating cost of $MVNO_i$
α_i	The marginal IoT type
$\alpha^{\sim}$	The marginal type
$U_{i,k}$	The utility that type α_k IoT user gets from $MVNO_i$

For ease of analysis, we summarize the notations of this paper in Table 1.

4. Price and Service Selection

In this section, we analyze price and service selection in a wireless network service market where two MVNOs compete for IoT users through the set of optimal prices of their network services to have maximized profits. The relationship between MOVNOs and IoT users can be characterized by using the Stackelberg game with two stages, and it is solved by making use of the technique of backward induction [43, 44]. We first analyze the network service selection of IoT users in stage II and then analyze how the network service prices are determined in stage I.

For the service selection and price from the two MVNOs, we consider two cases: (1) the Stackelberg game (SG) case where one MVNO sets network service price firstly and the other one sets later and (2) noncooperative strategic game (NSG) [43, 45], also known as simultaneous-play game, where the network service prices are simultaneously set by the two MVNOs. The SG case means that an entrant MVNO who plans to offer network service competes with an incumbent MVNO whose quality of network service is better, and the NSG case means that two MVNOs whose network service prices and qualities are different compete simultaneously.

4.1. IoT Users' Demand Decision. Based on the prices and service qualities of the two MVNOs, each of the IoT users will make a network service demand decision to buy network service from one of the two MVNOs or neither. We denote the demands of IoT users for network services from $MVNO_1$ and $MVNO_2$ as $D_1(p_1, p_2)$ and $D_2(p_1, p_2)$,

respectively. Two critical types of IoT users denoted as α_1 and α_2 are considered, such that

$$U_{1,k} = \alpha_1 C_1 - p_1 = 0, \tag{4}$$

$$U_{2,k} = \alpha_2 C_2 - p_2 = 0. \tag{5}$$

From Equations (4) and (5), we get

$$\alpha_1 = \frac{p_1}{C_1}, \tag{6}$$

$$\alpha_2 = \frac{p_2}{C_2}. \tag{7}$$

We also denote an indifferent IoT user by $\alpha \sim$ such that $U_{1,k} = U_{2,k}$; that is,

$$\alpha \sim C_1 - p_1 = \alpha \sim C_2 - p_2. \tag{8}$$

Then, from Equation (8), $\alpha \sim$ is calculated as

$$\alpha \sim = \frac{p_1 - p_2}{C_1 - C_2}. \tag{9}$$

IoT users are assumed to be self-interested, which means that they choose service access from $MVNO_i$ ($i = 1, 2$) if their utilities are not only positive but also higher than the other one. Therefore, the following results can be obtained.

Proposition 1. *An IoT user with type α_k will choose network services according to the following conditions:*

(i) It chooses service from $MVNO_1$ if $U_{1,k}(\alpha_k, p_1) > U_{2,k}(\alpha_k, p_2)$ and $U_{1,k}(\alpha_k, p_1) > 0$, requiring $\alpha_k < \alpha^{\sim}$ and $\alpha_k < \alpha_1$

(ii) It chooses service from $MVNO_2$ if $U_{2,k}(\alpha_k, p_2) > U_{1,k}(\alpha_k, p_1)$, and $U_{2,k}(\alpha_k, p_2) > 0$, requiring $\alpha^{\sim} < \alpha_k < \alpha_2$

(iii) It chooses no service if $U_{1,k}(\alpha_k, p_1) < 0$ and $U_{2,k}(\alpha_k, p_2) < 0$, requiring $\alpha_k > \alpha_1$ and $\alpha_k > \alpha_2$

According to the results of Proposition 1, the service demand decisions of IoT users from $MVNO_1$ and $MVNO_2$ are, respectively, given as

$$D_1 = F_1(\alpha) = \int_{\max\{\alpha_1, \alpha \sim\}}^{1} f(\alpha) d\alpha, \tag{10}$$

$$D_2 = F_2(\alpha) = \int_{\alpha_2}^{\alpha \sim} f(\alpha) d\alpha. \tag{11}$$

From Equations (10) and (11), the following proposition can be obtained.

Proposition 2. *For network service prices (p_1, p_2), a unique pair of equilibrium demands D^e_1 and D^e_2 exist at $MVNO_1$ and $MVNO_2$, respectively:*

(1) If $\alpha_2 > \alpha_1$, then $\alpha_1 > \alpha\sim$ and $\alpha_2 > \alpha\sim$. We have $F_1(\alpha) = 0$ and $F_2(\alpha_2) = F(\alpha_2)$

(2) If $\alpha_1 > \alpha_2$, then $\alpha\sim > \alpha_1$ and $\alpha\sim > \alpha_2$. We have $F_1(\alpha) = 1 - F(\alpha\sim)$ and $F_2(\alpha_2) = F(\alpha_2) - F(\alpha\sim)$

(3) This corresponds to the case that $MVNO_1$ and $MVNO_2$ coexist to offer network services. Therefore, the demands for network services from $MVNO_1$ and $MVNO_2$ in equilibrium are, respectively, given as

$$D_1 = 1 - F_1(\alpha) = 1 - \frac{p_1 - p_2}{C_1 - C_2}, \tag{12}$$

$$D_2 = F_2(\alpha\sim) - F_2(\alpha) = \frac{p_1 - p_2}{C_1 - C_2} - \frac{p_2}{C_2}. \tag{13}$$

4.2. Two Competition Cases. After the network service demands of IoT users are given, the two MVNOs will compete to get their maximized profits through setting optimal network service prices. Therefore, the profits of the two MVNOs can be, respectively, expressed as

$$\pi_1 = (p_1 - \mu_1)D_1(p_1, p_2) = (p_1 - \mu_1)\left(1 - \frac{p_1 - p_2}{C_1 - C_2}\right), \tag{14}$$

$$\pi_2 = (p_2 - \mu_2)D_2(p_1, p_2) = (p_2 - \mu_2)\left(\frac{p_1 - p_2}{C_1 - C_2} - \frac{p_2}{C_2}\right). \tag{15}$$

The competition of the two MVNOs can be modelled and analyzed by using the one-shot game, which is formulated as follows:

Players: $MVNO_1$ and $MVNO_2$
Strategies: prices $p_i > 0$, $i = 1, 2$
Payoff: profits π_i, $i = 1, 2$

4.3. Stackelberg Game (SG) Case. In this case, the competition of the two MVNOs is modelled and analyzed by using the Stackelberg game (SG), where $MVNO_1$ is the leader, whereas $MVNO_2$ is the follower. $MVNO_1$ moves firstly to set the optimal network service price to get the maximized profit by anticipating the choice on p_2 of $MVNO_2$.

The problem that maximizes the profit of $MVNO_1$ is expressed as follows.

Problem 3.

$$\begin{aligned} \max\ &\pi_1 = (p_1 - \mu_1)D_1(p_1, p_2), \\ &p_1 \geq 0 \end{aligned} \tag{16}$$

where $D_1(p_1, p_2)$ is given by Equation (10).

After getting $MVNO_1$'s price p_1, $MVNO_2$ tries to solve the following profit optimization problem to get its price p_2.

Problem 4.

$$\begin{aligned} \max\ &\pi_2 = (p_2 - \mu_2)D_2(p_1, p_2), \\ &p_2 \geq 0, \end{aligned} \tag{17}$$

where $D_2(p_1, p_2)$ is given in Equation (11).

From solving Problem 3 and Problem 4 sequentially, Proposition 5 is obtained, and the proof is shown in Appendix A.

Proposition 5. *A unique pair of the price (p^s_1, p^s_2) is obtained in equilibrium in the SG case.*

According to the results of Proposition 5, Corollary 6 can be obtained.

Corollary 6. *In the SG case, the profits that $MVNO_1$ and $MVONO_2$ get are, respectively, expressed as*

$$\pi^s_1 = (p^s_1 - \mu_1)D^s_1, \tag{18}$$

$$\pi^s_2 = (p^s_2 - \mu_1)D^s_2. \tag{19}$$

4.4. Noncooperative Strategic Game (NSG) Case. Noncooperative strategic game (NSG), which is also known as simultaneous-play game [46], is the case that $MVNO_1$ and $MVNO_2$ simultaneously set their service prices in order to get their maximized profits.

The problem that tries to solve the maximized profit of $MVNO_1$ is expressed as follows.

Problem 7.

$$\begin{aligned} \max\ &\pi_1 = (p_1 - \mu_1)D_1(p_1, p_2), \\ &p_1 \geq 0, \end{aligned} \tag{20}$$

where $D_1(p_1, p_2)$ is shown in Equation (10).

The problem that tries to solve the maximized profit of $MVNO_2$ is expressed as follows.

Problem 8.

$$\begin{aligned} \max\ &\pi_2 = (p_2 - \mu_2)D_2(p_1, p_2), \\ &p_2 \geq 0, \end{aligned} \tag{21}$$

where $D_2(p_1, p_2)$ is shown in Equation (11).

From solving Problem 7 and Problem 8 jointly, the following results are obtained; the proof is given in Appendix B.

Proposition 9. *In the NSG case, a unique price pair (p_1^n, p_2^n) exists in equilibrium.*

According to Proposition 9, Corollary 10 is obtained.

$$\pi_1^n = (p_1^n - \mu_1) D_1^n, \tag{22}$$

$$\pi_2^n = (p_2^n - \mu_1) D_2^n. \tag{23}$$

Corollary 10. *In SG case, the profits that MVNO$_1$ and MVONO$_2$ get are, respectively, expressed as*

5. Numerical Results

This section provides numerical results to verify the analysis presented in the prior sections. We consider an IoT environment with two MVNOs who lease radio frequency slices from a WIP and provision network services to a number of IoT users under two competition cases. Specifically, we analyze the sensitivity of network service prices and profits in equilibrium with respect to different parameters, like the quality of slice and cost coefficient. We assume $\mu_i = \beta C_i$, for $i = 1, 2$, where β is the cost coefficient. Unless otherwise specified, the set of parameter values is mainly referred to as [12, 40] $\beta = 0.2, 0.1 \leq C_2 \leq C_1 \leq 3$ (bps). We use the tool of MATLAB to develop the simulation environment.

5.1. Impact of Slice Quality. First, we analyze how the quality of radio frequency slice impacts the network service prices, IoT user demands, and profits of the two MVNOs in equilibrium under the two competition cases.

Figure 5 shows the impact of slice quality C_1 on the network prices of MVNO$_1$ in equilibrium under the two competition cases, where C_2 is fixed as 0.3. Figure 6 shows the impact of slice quality C_2 on network prices of MVNO$_2$ in equilibrium under two competition cases, where C_1 is fixed as 3. The cost efficient β is set as 0.2 in the two figures. From Figures 5 and 6, it can be observed that, in equilibrium, the network service prices that MVNO$_1$ and MVNO$_2$ get are higher in the NSG competition case than those in the SG competition case. Figures 5 and 6 suggest that MVNOs can achieve higher network service prices with respect to their qualities of leased frequency slice increasing. From the two figures, it can also be observed that MVNO$_1$ can get higher network prices than MVNO$_2$ in equilibrium under the two competition cases due to its leased quality of frequency slice which is higher.

Figures 7 and 8, respectively, show the profits of MVNO$_1$ and MVNO$_2$ versus slice qualities C_1 and C_2 in the SG scenario. We set β as 0.2 in the two figures, $C_2 = 0.3$ in Figure 7 and $C_1 = 3$ in Figure 8. From Figure 7, it can be found that the profits of MVNO$_1$ and MVNO$_2$ will increase if the better slice quality of MVNO$_1 C_1$ is leased from WIP. It can be found from this figure that the obtained profit of MVNO$_2$ is larger than that of MVNO$_1$. This is because MVNO$_1$ has a higher operating cost. From Figure 8, it can be observed that the profit of MVNO$_1$ increases while the profit of MVNO$_2$ first increases then decreases with respect to the increase in radio frequency quality C_2 increasing.

Figures 9 and 10 show, respectively, the profits that MVNO$_1$ and MVNO$_2$ obtain versus the slice qualities C_1 and C_2 in NSG case. We set β as 0.2 in the two figures, $C_2 =$
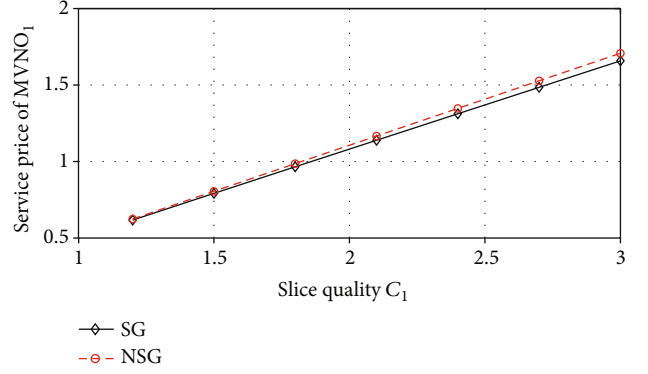
FIGURE 5: The equilibrium network price of MVNO$_1$ versus slice quality C_1 in two cases.
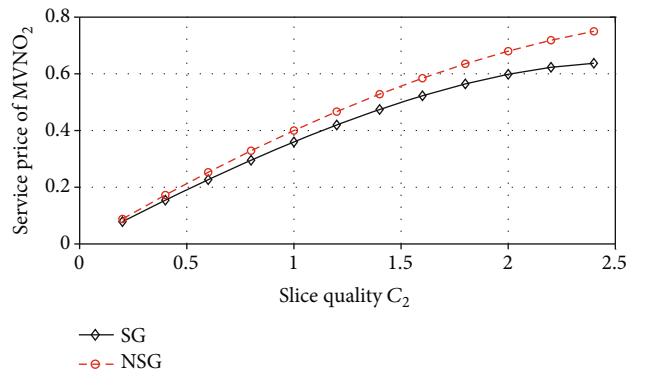
FIGURE 6: The equilibrium network price of MVNO$_2$ versus slice quality C_2 in two cases.
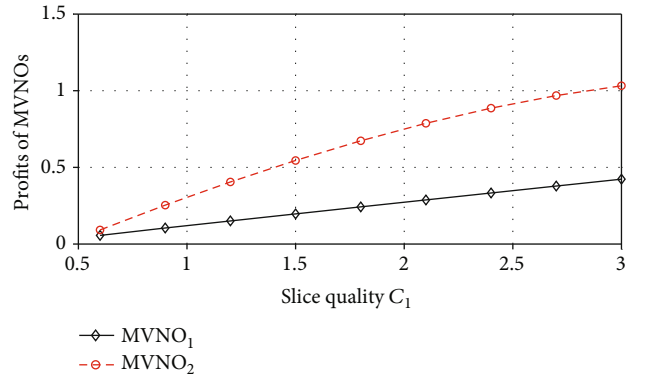
FIGURE 7: The profits of MVNO$_1$ and MVNO$_2$ versus slice quality C_1 in the SG case.

0.3 in Figure 9 and $C_1 = 3$ in Figure 10. Figure 9 shows that the profits of MVNO$_1$ and MVNO$_2$ decrease with the slice quality of MVNO$_1$ increasing. Although the slice quality of MVNO$_1$ increases, the profit of this MVNO decreases, due to the reason that less IoT users choose MVNO$_1$ for the higher network price, which can be observed from Figure 5. From Figure 10, it can be observed that the profit of MVNO$_2$ increases if it leases better slice quality from the WIP, as more

FIGURE 8: The profits of $MVNO_1$ and $MVNO_2$ versus slice quality C_2 in the SG case.
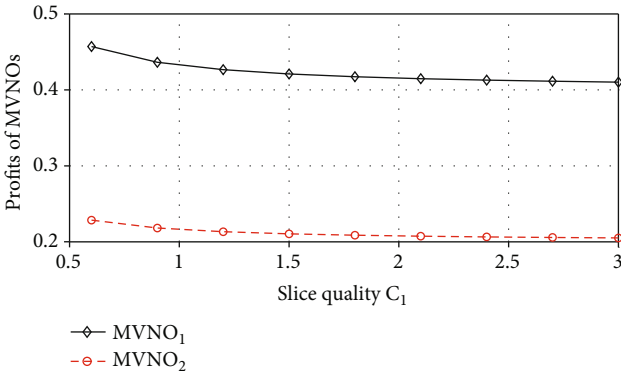
FIGURE 9: The profits of $MVNO_1$ and $MVNO_2$ versus slice quality C_1 in the NSG case.
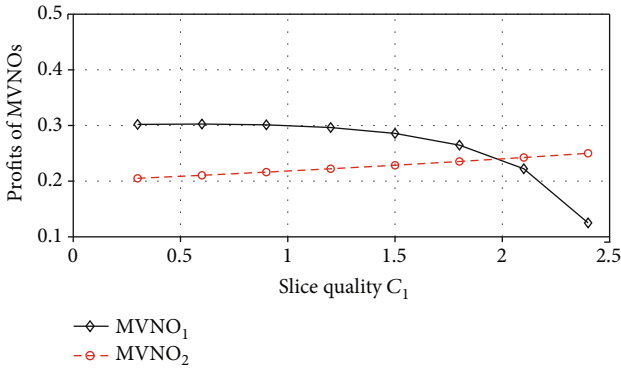
FIGURE 10: The profits of $MVNO_1$ and $MVNO_2$ versus slice quality C_2 in the NSG case.

IoT users will choose the service from $MVNO_2$, which can be found in Figure 6.

5.2. Impact of Operating Cost. This part analyzes how the operating cost impacts the network service prices and profits of $MVNO_1$ and $MVNO_2$ in equilibrium under the two competition cases. Figures 11 and 12 show the profits of the two MVNOs versus cost coefficient β, respectively, under the SG and NSG cases with $C1 = 2$ and $C_2 = 0.7$. Figure 11
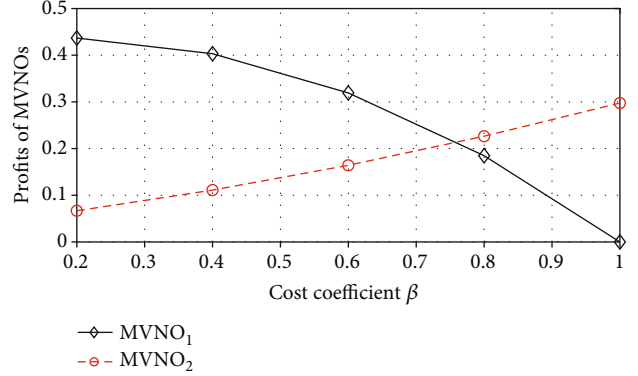
FIGURE 11: The profits of $MVNO_1$ and $MVNO_2$ versus cost coefficient β in the SG case.
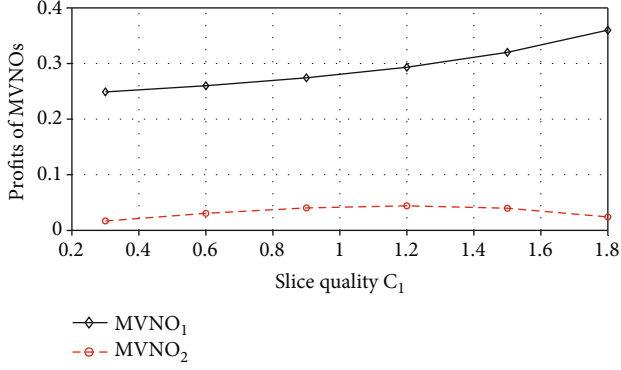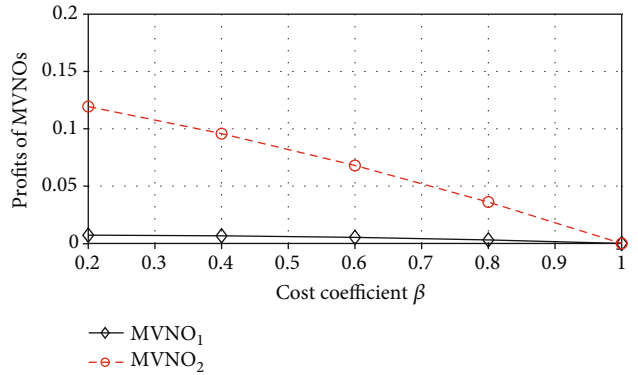

FIGURE 12: The profits of $MVNO_1$ and $MVNO_2$ versus cost coefficient β in the NSG case.

illustrates that with the cost coefficient β increasing, unlike $MVNO_2$ whose profit increases, the profit of $MVNO_1$ under the SG case decreases indicating that $MVNO_2$ benefits more from this competition case when the cost coefficient β increases. The profit of $MVNO_2$ will be larger than that of $MVNO_1$ with the increase of β. Figure 12 indicates that, in the NSG case, the profits of the $MVNO_1$ and $MVNO_2$ decrease with respect to the increasing cost coefficient β. A higher value of cost coefficient means that the two MVNOs should afford more operating costs.

6. Conclusions and Future Works

This paper has studied a two-layer game in an IoT network service environment aiming to get the maximized MVNOs' profits by taking IoT users' heterogeneous tastes for the service qualities into account. We investigated and analyzed network service pricing competition of $MVNO_1$ and $MVNO_2$ by using NSG and SG, respectively, and a unique equilibrium is obtained in each game case. The numerical results show that, in equilibrium, $MVNO_1$ and $MVNO_2$ can charge their network services with higher prices if they leased better slice qualities from the WIP, and they charge higher network service prices in the SG case than in the NSG case. The numerical results also indicated that IoT users are not prone to pay to use network services even if the two MVNOs provide

network services with better slice qualities. We got the conclusion that with the increase in operating cost, the profit of $MVNO_1$ decreased in the two competition cases while the profit of $MVNO_2$ increases in the SG case and decreases in the NSG case.

Several research directions still remained to be further studied as future works. First, the duopoly competition scenario can be extended to the oligopoly one where multiple MVNOs exist provisioning network services. For the oligopoly case where there are more than two MVNOs, we can apply the model in [47]. Second, we can investigate and analyze the three-layer game by incorporating the interaction between the WIP and the two MVNOs. Third, the MVNOs can improve their profits through price differentiation, i.e., charging network service with different prices according to the different types of IoT users.

Appendix

A. Proof of Proposition 5

Given the network service price of $MVNO_1$, by setting the first derivative of π_2 concerning p_2 to zero,

$$\frac{\partial \pi_2}{\partial p_2} = \frac{C_1 p_1 - 2C_1 p_2 + C_1 \mu_2}{C_2(C_1 - C_2)} = 0. \tag{A.1}$$

From Equation (A.1), p_2 is calculated as

$$p_2 = \frac{C_2 p_1 + C_1 \mu_2}{2C_1}. \tag{A.2}$$

After substituting Equation (A.1) into Equation (14), π_1 is calculated as

$$\pi_1 = (p_1 - \mu_1)\left[1 - \frac{2C_1 p_1 - C_2 p_1 - C_1 \mu_2}{2C_1(C_1 - C_2)}\right]. \tag{A.3}$$

Equation (A.3) is convex; therefore, by setting the derivative of π_2 with respect to p_2 to zero,

$$\frac{\partial \pi_1}{\partial p_1} = 1 - \frac{4C_1 p_1 - 2C_2 p_1 - C_1 \mu_2 + C_2 \mu_1}{2C_1(C_1 - C_2)} = 0. \tag{A.4}$$

From Equation (A.4), the best response of $MVNO_1$ is

$$p_1^s = \frac{2C_1(C_1 - C_2) + 2\mu_1 C_1 + C_1 \mu_2 - C_2 \mu_1}{2(2C_1 - C_2)}. \tag{A.5}$$

By substituting Equation (A.5) into Equation (A.2), the best response of $MVNO_2$ is

$$p_2^s = \frac{C_2[2C_1(C_1 - C_2) + 2\mu_1 C_1 + C_1 \mu_2 - C_2 \mu_1]}{4C_1(2C_1 - C_2)} + \frac{\mu_2}{2}. \tag{A.6}$$

Accordingly, by, respectively, substituting Equations (A.5) and (A.6) into Equations (12) and (13), the service

demands from $MVNO_1$ and $MVNO_2$ in the SG case are denoted, respectively, as

$$D_1^s = \frac{2C_1(C_1 - C_2) - 2\mu_1 C_1 + C_1 \mu_2 + C_2 \mu_1}{4C_1(C_1 - C_2)}, \tag{A.7}$$

$$D_2^s = \frac{2C_1(C_1 - C_2) - 2\mu_1 C_1 + C_1 \mu_2 + C_2 \mu_1}{4(2C_1 - C_2)(C_1 - C_2)}. \tag{A.8}$$

B. Proof of Proposition 9

The objective function for Problem 3 is easily proved as convex; hence, by setting the derivative of π_1 with respect to p_1 to zero,

$$\frac{\partial \pi_1}{\partial p_1} = 1 - \frac{2p_1 - p_2 - \mu_1}{C_1 - C_2} = 0. \tag{B.1}$$

From Equation (B.1), p_1 is calculated as

$$p_1 = \frac{C_1 - C_2 + p_2 + \mu_1}{2}. \tag{B.2}$$

Similarly, by setting the derivative of π_2 with respect to p_2 to zero,

$$\frac{\partial \pi_2}{\partial p_2} = \frac{C_1 p_1 - 2C_1 p_2 + C_1 \mu_2}{C_2(C_1 - C_2)} = 0. \tag{B.3}$$

From Equation (B.2), p_2 is calculated as

$$p_2 = \frac{p_1 C_2 + C_1 \mu_2}{2C_1}. \tag{B.4}$$

By solving Equations (B.2) and (B.4), the optimal service prices of $MVNO_1$ and $MVNO_2$ are, respectively, denoted as

$$p_1^n = \frac{2C_1(C_1 - C_2) + C_1(2\mu_1 + \mu_2)}{4C_1 - C_2}, \tag{B.5}$$

$$p_2^n = \frac{C_1 C_2 - C_2^2 + C_2 \mu_1 + 2\mu_2 C_1}{4C_1 - C_2}. \tag{B.6}$$

Accordingly, by, respectively, substituting Equations (B.5) and (B.6) into Equations (12) and (13), the service demands from $MVNO_1$ and $MVNO_2$ in NSG case are, respectively, denoted as

$$D_1^n = \frac{2C_1(C_1 - C_2) - 2\mu_1 C_1 + C_1 \mu_2 + C_2 \mu_1}{(4C_1 - C_2)(C_1 - C_2)}, \tag{B.7}$$

$$D_2^n = \frac{C_1[\mu_2(C_2 - 2C_1) + C_2(\mu_1 + C_1 - C_2)]}{C_2(4C_1 - C_2)(C_1 - C_2)}. \tag{B.8}$$

Data Availability

The data and programme of this study can be available from the corresponding author upon reasonable request.

Conflicts of Interest

The authors declare that there is no conflict of interest regarding the publication of this paper.

Acknowledgments

References

[1] L. Guijarro, V. Pla, J. R. Vidal, and M. Naldi, "Game theoretical analysis of service provision for the Internet of Things based on sensor virtualization," *IEEE Journal on Selected Areas in Communications*, vol. 35, no. 3, pp. 691–706, 2017.

[2] M. Huang, Y. Liu, N. Zhang et al., "A services routing based caching scheme for cloud assisted CRNs," *IEEE Access*, vol. 6, pp. 15787–15805, 2018.

[3] M. Dong, K. Ota, A. Liu, and M. Guo, "Joint optimization of lifetime and transport delay under reliability constraint wireless sensor networks," *IEEE Transactions on Parallel and Distributed Systems*, vol. 27, no. 1, pp. 225–236, 2016.

[4] Z. Liu, T. Tsuda, H. Watanabe, S. Ryuo, and N. Iwasawa, "Data driven cyber-physical system for landslide detection," *Mobile Networks and Applications*, vol. 24, no. 3, pp. 991–1002, 2019.

[5] D. Miorandi, S. Sicari, F. de Pellegrini, and I. Chlamtac, "Internet of things: vision, applications and research challenges," *Ad Hoc Networks*, vol. 10, no. 7, pp. 1497–1516, 2012.

[6] C. Perera, A. Zaslavsky, P. Christen, and D. Georgakopoulos, "Sensing as a service model for smart cities supported by Internet of Things," *Transactions on Emerging Telecommunications Technologies*, vol. 25, no. 1, pp. 81–93, 2014.

[7] X. Wang, Z. Liu, Y. Gao, X. Zheng, Z. Dang, and X. Shen, "A near-optimal protocol for the grouping problem in RFID systems," *IEEE Transactions on Mobile Computing*, 2020.

[8] Cisco Systems, *Cisco visual networking index: forecast and methodology, 2016-2021*, 2017, https://www.reinvention.be/webhdfs/v1/docs/complete-white-paper-c11-481360.pdf.

[9] H. Hu, Z. Liu, and J. An, "Mining mobile intelligence for wireless systems: a deep neural network approach," *IEEE Computational Intelligence Magazine*, vol. 15, no. 1, pp. 24–31, 2020.

[10] J. Wu, L. Zou, L. Zhao, A. al-Dubai, L. Mackenzie, and G. Min, "A multi-uav clustering strategy for reducing insecure communication range," *Computer Networks*, vol. 158, pp. 132–142, 2019.

[11] Y. Fan, L. Yang, D. Zhang, G. Han, and D. Zhang, "An angle rotate-QAM aided differential spatial modulation for 5G ubiquitous mobile networks," *Mobile Networks and Applications*, 2019.

[12] D. B. Rawat, A. Alshaikhi, A. Alshammari, C. Bajracharya, and M. Song, "Payoff optimization through wireless network virtualization for IoT applications: a three layer game approach," *IEEE Internet of Things Journal*, vol. 6, no. 2, pp. 2797–2805, 2019.

[13] X. Zhao, Y. Zhang, S. Geng, F. du, Z. Zhou, and L. Yang, "Hybrid precoding for an adaptive interference decoding SWIPT system with full-duplex IoT devices," *IEEE Internet of Things Journal*, vol. 7, no. 2, pp. 1164–1177, 2020.

[14] J. Pei, P. Hong, M. Pan, J. Liu, and J. Zhou, "Optimal VNF placement via deep reinforcement learning in SDN/NFV-enabled networks," *IEEE Journal on Selected Areas in Communications*, vol. 38, no. 2, pp. 263–278, 2020.

[15] Z. Zhou, J. Gong, Y. He, and Y. Zhang, "Software defined machine-to-machine communication for smart energy management," *IEEE Communications Magazine*, vol. 55, no. 10, pp. 52–60, 2017.

[16] G. Li, J. Wu, J. Li, Z. Zhou, and L. Guo, "SLA-aware fine-grained QoS provisioning for multi-tenant software-defined networks," *IEEE Access*, vol. 6, pp. 159–170, 2018.

[17] D. Zhang, Y. Liu, L. Dai, A. K. Bashir, A. Nallanathan, and B. Shim, "Performance analysis of FD-NOMA-based decentralized V2X systems," *IEEE Transactions on Communications*, vol. 67, no. 7, pp. 5024–5036, 2019.

[18] C. Gong, D. Yu, L. Zhao, X. Li, and X. Li, "An intelligent trust model for hybrid DDoS detection in software defined networks," *Concurrency and Computation: Practice and Experience*, 2019.

[19] J. Yu, M. H. Cheung, and J. Huang, "Spectrum investment under uncertainty: a behavioral economics perspective," *IEEE Journal on Selected Areas in Communications*, vol. 34, no. 10, pp. 2667–2677, 2016.

[20] S. Agarwal and S. De, "eDSA: energy-efficient dynamic spectrum access protocols for cognitive radio networks," *IEEE Transactions on Mobile Computing*, vol. 15, no. 12, pp. 3057–3071, 2016.

[21] L. Zhao, X. Li, B. Gu et al., "Vehicular communications: standardization and open issues," *IEEE Communications Standards Magazine*, vol. 2, no. 4, pp. 74–80, 2018.

[22] C. Wu, Z. Liu, D. Zhang, T. Yoshinaga, and Y. Ji, "Spatial intelligence toward trustworthy vehicular IoT," *IEEE Communications Magazine*, vol. 56, no. 10, pp. 22–27, 2018.

[23] S. Ren, J. Park, and M. van der Schaar, "Entry and spectrum sharing scheme selection in femtocell communications markets," *IEEE/ACM Transactions on Networking*, vol. 21, no. 1, pp. 218–232, 2013.

[24] X. Li, L. Zhao, Z. Zhou et al., "Duopoly price competition in wireless sensor network-based service provision," *Sensors*, vol. 18, no. 12, p. 4422, 2018.

[25] M. Cho and M. Choi, "Pricing for mobile data services considering service evolution and change of user heterogeneity," *IEICE Transactions on Communications*, vol. E96.B, no. 2, pp. 543–552, 2013.

[26] M. Liwang, J. Wang, Z. Gao, X. du, and M. Guizani, "Game theory based opportunistic computation offloading in cloud-enabled iov," *IEEE Access*, vol. 7, pp. 32551–32561, 2019.

[27] X. Li, C. Zhang, B. Gu, K. Yamori, and Y. Tanaka, "Optimal pricing and service selection in the mobile cloud architectures," *IEEE Access*, vol. 7, pp. 43564–43572, 2019.

[28] Y. Zhu, H. Yu, R. A. Berry, and C. Liu, "Cross-network prioritized sharing: an added value MVNO's perspective," in *IEEE INFOCOM 2019 - IEEE Conference on Computer Communications*, pp. 1549–1557, Paris, France, 2019.

[29] L. Wang, C. Yang, X. Wang, F. R. Yu, and V. C. M. Leung, "User oriented resource management with virtualization: a

hierarchical game approach," *IEEE Access*, vol. 6, pp. 37070–37083, 2018.

[30] W. Ejaz and M. Ibnkahla, "Multiband spectrum sensing and resource allocation for IoT in cognitive 5G networks," *IEEE Internet of Things Journal*, vol. 5, no. 1, pp. 150–163, 2018.

[31] J. A. Ansere, G. Han, H. Wang, C. Choi, and C. Wu, "A reliable energy efficient dynamic spectrum sensing for cognitive radio IoT networks," *IEEE Internet of Things Journal*, vol. 6, no. 4, pp. 6748–6759, 2019.

[32] A. Ghosh and S. Sarkar, "Pricing for profit in internet of things," *IEEE Transactions on Network Science and Engineering*, vol. 6, no. 2, pp. 130–144, 2019.

[33] C. Li, J. Li, Y. Li, and Z. Han, "Pricing game with complete or incomplete information about spectrum inventories for mobile virtual network operators," *IEEE Transactions on Vehicular Technology*, vol. 68, no. 11, pp. 11118–11131, 2019.

[34] Y. Zhang, Z. Xiong, D. Niyato, P. Wang, H. V. Poor, and D. I. Kim, "A game-theoretic analysis for complementary and substitutable IoT services delivery with externalities," *IEEE Transactions on Communications*, vol. 68, no. 1, pp. 615–629, 2020.

[35] A. Sanchis-Cano, J. Romero, E. Sacoto-Cabrera, and L. Guijarro, "Economic feasibility of wireless sensor network-based service provision in a duopoly setting with a monopolist operator," *Sensors*, vol. 17, no. 12, p. 2727, 2017.

[36] K. Kinoshita, Y. Maruyama, K. Kawano, and T. Watanabe, "A spectrum sharing method based on users' behavior and providers' profit," *IEICE Transactions on Communications*, vol. E100.B, no. 10, pp. 1928–1938, 2017.

[37] N. H. Tran, Choong Seon Hong, Zhu Han, and Sungwon Lee, "Optimal pricing effect on equilibrium behaviors of delay-sensitive users in cognitive radio networks," *IEEE Journal on Selected Areas in Communications*, vol. 31, no. 11, pp. 2566–2579, 2013.

[38] L. Duan, J. Huang, and B. Shou, "Duopoly competition in dynamic spectrum leasing and pricing," *IEEE Transactions on Mobile Computing*, vol. 11, no. 11, pp. 1706–1719, 2012.

[39] J. Elias, F. Martignon, Lin Chen, and E. Altman, "Joint operator pricing and network selection game in cognitive radio networks: equilibrium, system dynamics and price of anarchy," *IEEE Transactions on Vehicular Technology*, vol. 62, no. 9, pp. 4576–4589, 2013.

[40] F. Li, Z. Sheng, J. Hua, and L. Wang, "Preference-based spectrum pricing in dynamic spectrum access networks," *IEEE Transactions on Services Computing*, vol. 11, no. 6, pp. 922–935, 2018.

[41] S. Zhao, Q. Zhu, G. Zhu, and H. Zhu, "Competitions and dynamics of MVNOs in spectrum sharing: an evolutionary game approach," *IEICE Transactions on Communications*, vol. E96.B, no. 1, pp. 69–72, 2013.

[42] N. H. Tran, L. B. Le, S. Ren, Z. Han, and C. S. Hong, "Joint pricing and load balancing for cognitive spectrum access: non-cooperation versus cooperation," *IEEE Journal on Selected Areas in Communications*, vol. 33, no. 5, pp. 972–985, 2015.

[43] D. Fudenberg and J. Tirole, *Game Theory*, MIT Press, Cambridge, MA, USA, 1991.

[44] Z. Han, D. Niyato, W. Saad, T. Basar, and A. Hjorungnes, *Game Theory in Wireless and Communication Networks: Theory, Models, and Applications*, Cambridge University Press, Cambridge, UK, 2011.

[45] L. Xianwei, G. Bo, C. Zhang, Z. Liu, K. Yamori, and Y. Tanaka, "Optimal pricing for service provision in heterogeneous cloud market," *IEICE Transactions on Communications*, vol. E102–B, no. 6, pp. 1148–1159, 2018.

[46] D. Niyato and E. Hossain, "A game theoretic analysis of service competition and pricing in heterogeneous wireless access networks," *IEEE Transactions on Wireless Communications*, vol. 7, no. 12, pp. 5150–5155, 2008.

[47] C. Zhang, G. Bo, K. Yamori, X. Sugang, and Y. Tanaka, "Oligopoly competition in time-dependent pricing for improving revenue of network service providers with complete and incomplete information," *IEICE Transactions on Communications*, vol. E98.B, no. 1, pp. 20–32, 2015.

WILEY | Hindawi

Research Article

Performance Analysis of Cooperative NOMA Systems with Incremental Relaying

Zhenling Wang ⓘ**, Zhangyou Peng** ⓘ**, Yongsheng Pei** ⓘ**, and Haojia Wang** ⓘ

Key Laboratory of Specialty Fiber Optics and Optical Access Networks, Shanghai University, Shanghai 200444, China

Correspondence should be addressed to Zhangyou Peng; zypeng@shu.edu.cn

In this paper, we investigate the performance of the non-orthogonal multiple access (NOMA) system with incremental relaying, where the relay is employed with amplify-and-forward (AF) or decode-and-forward (DF) protocols. To characterize the outage behaviors of the incremental cooperative NOMA (ICN) system, new closed-form expressions of both exact and asymptotic outage probability for two users are derived. In addition, the performance of the conventional cooperative NOMA (CCN) system is analyzed as a benchmark for the the purpose of comparison. We confirm that the outage performance of the distant user is enhanced when ICN system is employed. Numerical results are presented to demonstrate that (1) the near user of the ICN system achieves better outage behavior than that of the CCN system in the low signal-to-noise ratio (SNR) region; (2) the outage performance of distant user for the DF-based ICN system is superior to that of the AF-based ICN system when the system works in cooperative NOMA transmission mode; and (3) in the low SNR, the throughput of the ICN system is higher than that of the CCN system.

1. Introduction

With the rapid development of the Internet of Things (IoT), spectrum efficiency becomes a key factor in guaranteeing the quality of service (QoS) of IoT applications. Nonorthogonal multiple access (NOMA) (NOMA schemes can be classified into two categories, namely, power-domain NOMA and code-domain NOMA. In this paper, we focus on power-domain NOMA and use NOMA to represent power-domain NOMA.) technology has been a revolutionary multiple access technology to enhance spectrum efficiency, user access ability, and user fairness [1–3]. Compared with the previous orthogonal multiple access technology (OMA), i.e., time division multiple access and frequency division multiple access, the key characteristic of NOMA is that multiuser signals are multiplexed in the same time/frequency/code resources with different power factors. Superposition coding and successive interference cancellation (SIC) has been used at the transmitter and receivers [4], respectively. The NOMA schemes has been proved to achieve higher spectral efficiency and system throughput in large-scale heterogeneous data traffic [5–7].

The initial research focused on the point-to-point downlink NOMA system extensively [8–10]. The outage behavior and ergodic rate of NOMA users were investigated where the users were deployed randomly [8]. In addition, the authors of [9] have researched the performance of a downlink single-cell NOMA network when assuming imperfect channel state information (CSI) and second-order statistics. Furthermore, the authors in [10] consider the scenario that each user only feedback one bit of its CSI to a base station (BS) and analyzed the outage performance. Apart from these researches, there are a lot of studies on improving the secrecy performance of multiple users [11, 12], where the external and internal eavesdropping scenarios have been considered.

Up to now, NOMA has been extended to cooperative communication systems [13, 14], as the higher diversity and extended coverage can be obtained in wireless networks. The authors have analyzed the outage performance of NOMA system with decode and forward (DF) relay employing full-duplex (FD) and half-duplex (HD) mode, where the near user was selected as a relay to deliver information and improve transmission reliability of distance users [15]. Inspired by this, simultaneous wireless information and

power transfer have been applied to cooperative NOMA from the perspective of enhancing spectrum efficiency and energy efficiency [16, 17]; the main feature is that the user relay harvests energy from BS. Especially, the system performance of [16] was comprehensively analyzed with considering DF and amplify-and-forward (AF) protocols. Moreover, cooperative NOMA schemes with dedicated relays have been widely investigated. The authors of [18, 19] have investigated the cooperative NOMA systems with dedicated AF relays, and it was proved that the performance of the NOMA system is obviously superior to that of the cooperative NOMA. Additionally, the performance of the cooperative NOMA system with dedicated DF relay has been researched by evaluating outage probability and sum rate over Nakagami-m fading [20]. The authors of [21] have researched a unified framework for hybrid satellite/unmanned aerial vehicle (UAV) terrestrial NOMA networks, where satellite communicated with ground users with the aid of a DF-UAV relay. In [22], the CSI was available in the cooperative NOMA system to determine the decoding order of cell-edge users data, where the outage behaviors have been analyzed under considering DF and AF relaying protocols. To further improve spectral efficiency, the FD mode has been employed in cooperative NOMA systems. The outage probability and ergodic rate of two-way relay NOMA system have been investigated [23]. In addition, the performance of FD cooperative NOMA systems in the presence of in-phase and quadrature-phase imbalance and imperfect SIC is analyzed and evaluated [24]. Furthermore, the authors have researched relay selection schemes to take advantages of space diversity and enhance spectral efficiency in cooperative NOMA systems [25, 26]. Very recently, the impact of residual transceiver hardware impairments on cooperative NOMA networks has been investigated in [27], which has also been researched in satellite-terrestrial cooperative NOMA networks [28] and two-way multiple relay NOMA networks [29].

The conventional cooperative NOMA (CCN) system described above can enhance the spectral efficiency, whether cooperative NOMA system employs the HD or FD. However, there are still some problems in the CCN system. On the one hand, the HD relay in the CCN system leads to a decline in spectral efficiency, as the HD relay needs half of the communication time to forward information compared to noncooperative NOMA networks. On the other hand, the existence of loop interference (LI) in the CCN system with FD relay will seriously affect the diversity gain. Recall that the the incremental relaying (IR) protocol [30] is widely adopted in conventional cooperative networks, since it can achieve higher spectral efficiency by introducing a negligible one-bit-feedback overhead. Specifically, the IR protocol invokes a relay for cooperation only when the source to destination channel gain is below a predetermined threshold. Driven by this, the performance of cooperative systems with IR protocol has been investigated in NOMA systems [31, 32], which has the higher throughput compared to the conventional cooperative communications.

1.1. Motivation and Contributions. While the aforementioned research on cooperative NOMA and user relay

NOMA systems with IR protocol has laid a solid foundation for understanding the IR protocol [31–33], the incremental cooperative NOMA (ICN) system is still under exploration. It is worth pointing out that, from a practical perspective, the NOMA communication networks can be employed to support IoT scenarios, especially when two NOMA users are classified into two types by their quality of service (QoS) [25], i.e., the nearby user and distant user. The nearby user requires a high targeted rate and can be served opportunistically; e.g., it is to download video files or perform some background tasks and so on. The distant user should be served quickly for a small packet with a lower target date rate, as a further example, which is as a medical sensor to send the pivotal safety information containing such as pulse and heart rates in a few bytes. Hence, it is important to further enhance the communication reliability of the distant user in the NOMA systems. Moreover, there are some issues in cooperative systems, i.e., HD relay systems restrict the enhancement of spectral efficiency, while the LI of FD relay seriously affects the diversity gain. Motivated by these, we specifically consider a cooperative NOMA system with IR protocol (i.e., ICN system), where the dedicated relay is used when source to weak user channel gain is below the predetermined threshold. More specifically, the performance of our proposed system is characterized when AF and DF protocols are implemented at the relay, respectively. The main contributions of our paper are summarized as follows:

(1) We derive the outage probability expressions of two users for AF-based ICN system. To get further insights, the asymptotic outage probability of two users is derived. Based on the analytical results, we acquire the diversity orders of two users for AF-based ICN system. We confirm that the use of the ICN system is able to improve the outage performance of the distant user

(2) We also investigate the outage behaviors of the DF-based ICN system. We further derive the closed-form and asymptotic expressions of outage probability for two users. Additionally, we obtain the diversity orders of two users. The distant user in the DF-based ICN system is capable of achieving better outage behavior than that of the CCN system

(3) We confirm that the near user of ICN system achieves better outage behavior than that of the CCN system in the low signal-to-noise ratio (SNR) region. The outage performance of distant user for DF-based NOMA system is superior to that of the AF-based NOMA system. Furthermore, better system throughput of the ICN system is achieved in the low SNR region over delay-limited transmission

1.2. Organization. The rest of this paper is organized as follows. In Section 2, the model of the ICN system is presented. In Section 3, the outage behaviors of two users for AF-based ICN system are investigated. Furthermore, the outage behaviors of two users for DF-based ICN system are studied in Section 4. In Section 5, numerical results are provided for

performance evaluation and comparison. Finally, Section 6 concludes the paper.

2. System Model

2.1. Network Description. Consider a downlink cooperative NOMA network including one BS, one relay R and two users, i.e., the nearby user D_1 and distant user D_2, as shown in Figure 1. Moreover, the AF and DF protocols are considered at R. The relay employs HD mode and all nodes in the network have a single antenna. All wireless channels in the scenario considered are assumed to be independent nonselective block Rayleigh fading and are disturbed by additive white Gaussian noise with mean power σ^2. $h_{1,b} \sim CN(0, \Omega_{1,b})$, $h_{2,b} \sim CN(0, \Omega_{2,b})$, and $h_{r,b} \sim CN(0, \Omega_{r,b})$ denote the complex channel coefficient of $BS \longrightarrow D_1$, $BS \longrightarrow D_2$, and $BS \longrightarrow R$, respectively. Similarly, $h_{r,1} \sim CN(0, \Omega_{r,1})$ and $h_{r,2} \sim CN(0, \Omega_{r,2})$ are the complex channel coefficient of $R \longrightarrow D_1$ and $R \longrightarrow D_2$, respectively. In addition, we assume $d_{1,b}$, $d_{r,b}$, and $d_{2,b}$ denote the distance from BS to D_1, R, and D_2, respectively; $d_{r,1}$ and $d_{r,2}$ are the distance from R to D_1 and D_2, respectively. Without loss of generality, assuming that $d_{1,b} > d_{r,b} > d_{2,b}$ and $\Omega_{1,b} > \Omega_{r,b} > \Omega_{2,b}$. In the next subsection, the ICN system and communication process will be introduced in detail.

2.2. ICN System. The transmission process of the ICN system is described as follows. At the beginning of each transmission block, BS broadcasts a pilot signal to D_1, R, and D_2. Based on the received pilot signal, D_2 performs channel estimation of $h_{2,b}$ and compares with a predefined threshold. If D_2 judges that it can correctly decode its desired information through direct transmission, it feedbacks 1-bit positive acknowledgement to BS and R. After receiving the positive feedback, BS adopts a direct NOMA transmission mode, i.e., it sends the superimposed signal directly to D_1 and D_2 within the whole transmission block. If D_2 observes that it is unable to decode its desired message without cooperation, it feedbacks 1-bit negative acknowledge to BS and R. Upon hearing the negative feedback, BS adopts a cooperative NOMA transmission mode, i.e., BS broadcasts the superimposed signal in the first half of the transmission block, and then R forwards the superimposed signal to the two users in the second half of the transmission block. Different from ICN system, the transmission block of CCN system is divided into two phases with equal duration. During the first phase, BS sends the superimposed signal to D_1, D_2, and R; then, R will forward it to users in the second phase. Obviously, the ICN system is an adaptive system, which can adaptively switch between the direct NOMA transmission mode and cooperative NOMA transmission mode based on the 1-bit indicator.

2.3. Signal Model

2.3.1. Direct NOMA Transmission Mode. In the first time slot, BS broadcasts the superposed signal $\sqrt{a_1 P_s} x_1 + \sqrt{a_2 P_s} x_2$ to D_1, D_2, and R according to NOMA principle, where x_1 and x_2 are the unit power signals for D_1 and D_2, respectively. The corresponding power allocation coefficients of D_1 and
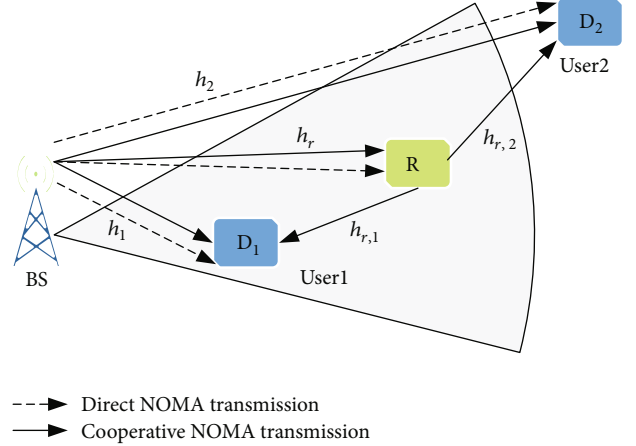
Figure 1: An illustration of cooperative NOMA system with IR protocol.

D_2 are a_1 and a_2, respectively. Specially, we assume that $a_1 \leq a_2$ with $a_1 + a_2 = 1$ to ensure better user fairness and QoS requirements between the users, which is also consistent with many existing NOMA contributions [6]. Therefore, the received signal at D_1, D_2, and R can be given by

$$y_1 = \sqrt{a_1 P_s} h_{1,b} x_1 + \sqrt{a_2 P_s} h_{1,b} x_2 + \omega_1, \tag{1}$$

$$y_2 = \sqrt{a_1 P_s} h_{2,b} x_1 + \sqrt{a_2 P_s} h_{2,b} x_2 + \omega_2, \tag{2}$$

$$y_r = \sqrt{a_1 P_s} h_{r,b} x_1 + \sqrt{a_2 P_s} h_{r,b} x_2 + \omega_r, \tag{3}$$

respectively; where P_s represents normalized transmission power of BS. ω_1, ω_2, and ω_r denote the Gaussian noise with zero mean and variance σ^2 at D_1, D_2, and R, respectively.

The SIC scheme is first employed at D_1 to detect the signal x_2 of D_2. Hence, the received signal-to-interference-plus-noise ratio (SINR) at D_1 to detect x_2 is given by

$$\gamma_{1,2} = \frac{a_2 \rho_s |h_{1,b}|^2}{a_1 \rho_s |h_{1,b}|^2 + 1}, \tag{4}$$

where $\rho_s = P_s/\sigma^2$ is the transmit SNR of the link between BS and users and R. After decoding the message of D_2 and subtracting it, D_1 is further to detect its own information with the following SNR:

$$\gamma_1 = a_1 \rho_s |h_{1,b}|^2. \tag{5}$$

The received SINR at D_2 to detect its own message is given by

$$\gamma_2 = \frac{a_2 \rho_s |h_{2,b}|^2}{a_1 \rho_s |h_{2,b}|^2 + 1}. \tag{6}$$

2.3.2. Cooperative NOMA Transmission Mode. In cooperative NOMA transmission mode, the entire transmission

block consists of two phases with equal duration. In the first phase, the received signal and SINR at D_1, D_2, and R is the same as described in direct NOMA transmission mode. Then, in the second phase, R forwards the received signal y_r to users with transmit power P_r, which is assumed $P_r = P_s$. Specially, the observations from the BS and the relaying node are combined at the users with selection combining. More importantly, as the relay is employed with AF and DF modes, the transmission process for AF and DF protocols will be explained in the next part in detail, respectively.

(1) Amplify-and-Forward. For AF case, R amplifies and forwards its received signals to D_1 and D_2 in the second time slot. Therefore, the observation at D_1 and D_2 in the second phase can be given as

$$y_1^{AF} = Gh_{r,1}y_r + n_1, \tag{7}$$

$$y_2^{AF} = Gh_{r,2}y_r + n_2, \tag{8}$$

respectively, where $G = \sqrt{P_r/(P_s|h_{r,b}|^2 + \sigma^2)}$ is the amplifying factor of the AF relay. Similarly, the received SINR at D_1 to detect x_2 with SIC scheme is given by

$$\gamma_{1,2}^{AF} = \frac{a_2\rho_s|h_{r,b}|^2|h_{r,1}|^2}{a_1\rho_s|h_{r,b}|^2|h_{r,1}|^2 + |h_{r,1}|^2 + |h_{r,b}|^2 + (1/\rho_s)}, \tag{9}$$

After decoding the message of D_2 and subtracting it, D_1 is further to detect its own information with the following SNR:

$$\gamma_1^{AF} = \frac{a_1\rho_s|h_{r,b}|^2|h_{r,1}|^2}{|h_{r,1}|^2 + |h_{r,b}|^2 + (1/\rho_s)}. \tag{10}$$

The received SINR at D_2 to detect its own message is given by

$$\gamma_2^{AF} = \frac{a_2\rho_s|h_{r,b}|^2|h_{r,2}|^2}{a_1\rho_s|h_{r,b}|^2|h_{r,2}|^2 + |h_{r,2}|^2 + |h_{r,b}|^2 + (1/\rho_s)}. \tag{11}$$

(2) Decode-and-Forward. For simplicity, assuming that R is capable of decoding the two NOMA users information, therefore, the observation at D_1 and D_2 in the second slot can be expressed as

$$y_1^{DF} = \sqrt{a_1 P_r}h_{r,1}x_1 + \sqrt{a_2 P_r}h_{r,1}x_2 + n_1, \tag{12}$$

$$y_2^{DF} = \sqrt{a_1 P_r}h_{r,2}x_1 + \sqrt{a_2 P_r}h_{r,2}x_2 + n_2, \tag{13}$$

respectively, where n_1 and n_2 are the AWGN at D_1 and D_2 with zero mean and variance σ^2.

By using SIC scheme, the received SINR at D_1 to detect x_2 is given by

$$\gamma_{1,2}^{DF} = \frac{a_2\rho_s|h_{r,1}|^2}{a_1\rho_s|h_{r,1}|^2 + 1}. \tag{14}$$

Then, D_1 further detects its own information with the following SINR:

$$\gamma_1^{DF} = a_1\rho_s|h_{r,1}|^2. \tag{15}$$

The received SINR at D_2 to detect its own message is given by

$$\gamma_2^{DF} = \frac{a_2\rho_s|h_{r,2}|^2}{a_1\rho_s|h_{r,2}|^2 + 1}. \tag{16}$$

3. Outage Performance Evaluation for AF-Based NOMA System

In this section, the outage behaviors are characterized for AF-based ICN and CCN systems, which are detailed in the following.

3.1. Outage Performance Analysis of ICN System. In this subsection, the outage behaviors of the AF-based ICN system are investigated.

3.1.1. Outage Probability of D_1. According to the ICN protocol, the outage probability of D_1 can be expressed as

$$P_{1,AF}^{ICN} = \Pr(\gamma_2 \geq \gamma_{th2})[1 - \Pr(\gamma_{1,2} \geq \gamma_{th2}, \gamma_1 \geq \gamma_{th1})] + \Pr(\gamma_2 < \gamma_{th2})P_{1,AF}^{CNT}, \tag{17}$$

where $P_r(\gamma_2 \geq \gamma_{th2})$ represents the system works in the direct NOMA transmission mode, and $P_r(\gamma_2 < \gamma_{th2})$ indicates that the system works in the cooperative NOMA transmission mode. In addition, $\gamma_{th1} = 2^{R_1} - 1$ and $\gamma_{th2} = 2^{R_2} - 1$ are the decoding threshold under direct NOMA transmission mode with R_1 and R_2 being the target rate of D_1 and D_2. Besides, $P_{1,AF}^{CNT}$ is the outage probability of D_1 with AF relay in the cooperative NOMA transmission mode, which can be given as

$$P_{1,AF}^{CNT} = \left[1 - \Pr\left(\gamma_{1,2} \geq \gamma_{th2}', \gamma_1 \geq \gamma_{th1}'\right)\right] \times \left[1 - \Pr\left(\gamma_{1,2}^{AF} \geq \gamma_{th2}', \gamma_1^{AF} \geq \gamma_{th1}'\right)\right], \tag{18}$$

where $\gamma'_{th1} = 2^{2R_1} - 1$ and $\gamma'_{th2} = 2^{2R_2} - 1$ are the decoding threshold with R_1 and R_2 being the target rate of D_1 and D_2 in cooperative NOMA transmission mode.

The following theorem provides the outage probability of D_1 in the AF-based ICN system.

Theorem 1. *The closed-form expression of outage probability for D_1 in the AF-based ICN system is given as*

$$
P_{1,AF}^{ICN} = \begin{cases}
1 - e^{-\tau/\Omega_{2,b}} e^{-\theta/\Omega_{1,b}} - \left(1 - e^{-\tau/\Omega_{2,b}}\right) \\
\quad \times \left[e^{-\theta'/\Omega_{1,b}} + \left(1 - e^{-\theta'/\Omega_{1,b}}\right) e^{-\theta'/\Omega_{r,b} - \theta'/\Omega_{r,1}} \right. \\
\quad \times \left. \sqrt{\dfrac{4\theta'\left(\rho_s\theta' + 1\right)}{\rho_s\Omega_{r,1}\Omega_{r,b}}} K_1\left(\sqrt{\dfrac{4\theta'\left(\rho_s\theta' + 1\right)}{\rho_s\Omega_{r,1}\Omega_{r,b}}} \right) \right], \dfrac{a_2}{a_1} > \gamma'_{th2}, \\
1 - e^{-\tau/\Omega_{2,b}} e^{-\theta/\Omega_{1,b}}, \gamma_{th2} < \dfrac{a_2}{a_1} \le \gamma'_{th2} \\
1, 0 < \dfrac{a_2}{a_1} \le \gamma_{th2},
\end{cases}
$$

$$(19)$$

where $\tau = \gamma_{th2}/(\rho_s(a_2 - a_1\gamma_{th2}))$, $\sigma = \gamma_{th1}/a_1\rho_s$, and $\theta = \max(\tau, \sigma)$; $\tau' = \gamma'_{th2}/(\rho_s(a_2 - a_1\gamma'_{th2}))$, $\sigma' = \gamma'_{th1}/a_1\rho_s$, and $\theta' = \max(\tau', \sigma')$. $K_1(\cdot)$ is the first-order modified Bessel function of the second kind.

Proof. See Appendix A.

3.1.2. Outage Probability of D_2. Based on the ICN protocol, the outage event cannot occur when $\gamma_2 \ge \gamma_{th2}$. Hence, the outage event can only occur in cooperative NOMA transmission mode, i.e., the information of D_2 failed to be successfully decoded in the first and second phases when $\gamma_2 < \gamma_{th2}$. The outage probability of D_2 in AF-based NOMA system can be expressed as

$$
P_{2,AF}^{ICN} = \Pr\left(\gamma_2 < \gamma_{th2}, \gamma_2 < \gamma'_{th2}, \gamma_2^{AF} < \gamma'_{th2}\right). \quad (20)
$$

As $\gamma_{th2} < \gamma'_{th2}$, (20) can be further rewritten as

$$
P_{2,AF}^{ICN} = \Pr\left(\gamma_2 < \gamma_{th2}, \gamma_2^{AF} < \gamma'_{th2}\right). \quad (21)
$$

Similar to the proof process of Theorem 1, the following theorem provides the outage probability of D_2 in the AF-based ICN system.

Theorem 2. *The closed-form expression of outage probability for D_2 in the AF-based ICN system is given as*

$$
P_{2,AF}^{ICN} = \begin{cases}
\left(1 - e^{-\tau/\Omega_{2,b}}\right)\left[1 - e^{-\tau'/\Omega_{r,b}} e^{-\tau'/\Omega_{r,2}} \sqrt{\dfrac{4\tau'\left(\rho_s\tau' + 1\right)}{\rho_s\Omega_{r,2}\Omega_{r,b}}} \right. \\
\quad \times \left. K_1\left(\sqrt{\dfrac{4\tau'\left(\rho_s\tau' + 1\right)}{\rho_s\Omega_{r,2}\Omega_{r,b}}} \right) \right], \dfrac{a_2}{a_1} > \gamma'_{th2} \\
\left(1 - e^{-\tau/\Omega_{2,b}}\right), \gamma_{th2} < \dfrac{a_2}{a_1} \le \gamma'_{th2} \\
1, 0 < \dfrac{a_2}{a_1} \le \gamma_{th2},
\end{cases}
$$

$$(22)$$

Proof. See Appendix B.

From the above derivations, it is obvious that $P_{1,AF}^{ICN}$ and $P_{2,AF}^{ICN}$ are both equal to one when $0 < a_2/a_1 \le \gamma_{th2}$. Thus, in the following, we only focus on the remaining region, i.e., $a_2/a_1 > \gamma_{th2}$.

3.1.3. Diversity Analysis. To gain more insights, the outage probability in high SNR region is investigated in this section, and the diversity order achieved by the users can be obtained based on the above analytical results. The diversity order [26] is defined as

$$
d = -\lim_{\rho \to \infty} \frac{\log\left(P(\rho)\right)}{\log \rho}. \quad (23)
$$

(1) Diversity Order of D_1. When $\rho \longrightarrow \infty$, according to $K_1(x) \approx 1/x$ and $e^{-x} \approx 1 - x(x \longrightarrow 0)$, we can derive the asymptotic outage probability of D_1 for the AF-based ICN system in the following corollary.

Corollary 3. *The asymptotic outage probability of D_1 in the AF-based ICN system is given as*

$$
P_{1,AF}^{ICN,\infty} = \begin{cases}
\dfrac{\theta}{\Omega_{1,b}} + \dfrac{\tau}{\Omega_{2,b}} \dfrac{\theta'}{\Omega_{1,b}} \left(\dfrac{\theta'}{\Omega_{r,b}} + \dfrac{\theta'}{\Omega_{r,1}} \right), \dfrac{a_2}{a_1} > \gamma'_{th2} \\
\dfrac{\tau}{\Omega_{2,b}} + \dfrac{\theta}{\Omega_{1,b}} - \dfrac{\tau\theta}{\Omega_{1,b}\Omega_{2,b}}, \gamma_{th2} < \dfrac{a_2}{a_1} \le \gamma'_{th2}.
\end{cases}
$$

$$(24)$$

Substituting (24) into (23), we can obtain the diversity order of D_1 in the AF-based ICN system as

$$
d_{1,AF}^{ICN} = 1, \quad (25)
$$

Remark 4. The diversity order of D_1 is one, which is obtained with direct link. It indicates that the performance of D_1 mainly depends on the direct link in the AF-base NOMA ICN system.

(2) Diversity Order of D_2. Similarly, we can derive the asymptotic outage probability of D_2 for the AF-based ICN system in the following corollary.

Corollary 5. *The closed-form expression of outage probability for D_2 in the AF-based ICN system is given as*

$$P_{2,AF}^{ICN,\infty} = \begin{cases} \dfrac{\tau}{\Omega_{2,b}}\left(\dfrac{\tau'}{\Omega_{r,b}} + \dfrac{\tau'}{\Omega_{r,2}}\right), \dfrac{a_2}{a_1} > \gamma'_{th2} \\ \dfrac{\tau}{\Omega_{2,b}}, \gamma_{th2} < \dfrac{a_2}{a_1} \le \gamma'_{th2}. \end{cases} \quad (26)$$

Substituting (26) into (23), we can obtain the diversity order of D_2 in the AF-based ICN system as

$$d_{2,AF}^{ICN} = \begin{cases} 2, \dfrac{a_2}{a_1} > \gamma'_{th2} \\ 1, \gamma_{th2} < \dfrac{a_2}{a_1} \le \gamma'_{th2}, \end{cases} \quad (27)$$

where (26) and (27) are also derived on the condition of $a_2/a_1 > \gamma_{th2}$.

Remark 6. When $a_2/a_1 > \gamma'_{th2}$, the diversity order of D_2 is two, which is obtained with direct link and relaying link. When $\gamma_{th2} < a_2/a_1 \le \gamma'_{th2}$, the diversity order of D_2 is one, which is obtained with direct link.

3.1.4. Throughput Analysis. In this section, the throughput will be considered in delay-limited transmission for AF-based ICN system. In our considered system, the BS transmits information at a constant rate, which is subject to the effect of outage probability due to wireless fading channels. The system throughput for AF-based ICN system is given as

$$R_{AF}^{ICN} = \left(1 - P_{1,AF}^{ICN}\right)R_1 + \left(1 - P_{2,AF}^{ICN}\right)R_2, \quad (28)$$

where $P_{1,AF}^{ICN}$ ang $P_{2,AF}^{ICN}$ are obtained from (19) and (22), respectively.

3.2. Outage Performance Analysis with CCN Protocol. In this subsection, the outage behaviors of the AF-based CCN system are investigated, which will be served as a benchmark for the outage performance employing ICN protocol.

3.2.1. Outage Probability of D_1. According to the CCN protocol, the expression of the outage probability for D_1 is the same with (18). Hence, the closed-form expression of outage probability for D_1 in the AF-based NOMA system with CCN protocol is given as

$$P_{1,AF}^{CCN} = \left(1 - e^{-\theta'/\Omega_{1,b}}\right)\left[1 - e^{-\theta'/\Omega_{r,b} - \theta'/\Omega_{r,1}}\sqrt{\dfrac{4\theta'\left(\rho_s\theta' + 1\right)}{\rho_s\Omega_{r,1}\Omega_{r,b}}}\right. $$
$$\left. \times K_1\left(\sqrt{\dfrac{4\theta'\left(\rho_s\theta' + 1\right)}{\rho_s\Omega_{r,1}\Omega_{r,b}}}\right)\right], \quad (29)$$

where (29) is derived on the condition of $a_2/a_1 > \gamma'_{th2}$, otherwise $P_{1,AF}^{CCN} = 1$.

Comparing (17) and (18) or (19) and (29), it is impossible to judge directly that the performance of D_1 for the ICN system is better than that of the CCN system. However, the derivation results can be used for simulation verification and comparison.

3.2.2. Outage Probability of D_2. According to the CCN protocol, the expression of the outage probability for D_2 can be given as

$$P_{2,AF}^{CCN} = \Pr\left(\gamma_2 < \gamma'_{th2}\right)\Pr\left(\gamma_2^{AF} < \gamma'_{th2}\right). \quad (30)$$

The closed-form expression of outage probability for D_2 in the AF-based NOMA system with CCN protocol is given as

$$P_{2,AF}^{CCN} = \left(1 - e^{-\tau'/\Omega_{2,b}}\right)\left[1 - e^{-\tau'/\Omega_{r,b}}e^{-\tau'/\Omega_{r,2}}\right.$$
$$\left. \times \sqrt{\dfrac{4\tau'\left(\rho_s\tau' + 1\right)}{\rho_s\Omega_{r,2}\Omega_{r,b}}}K_1\left(\sqrt{\dfrac{4\tau'\left(\rho_s\tau' + 1\right)}{\rho_s\Omega_{r,2}\Omega_{r,b}}}\right)\right], \quad (31)$$

where (30) is also derived on the condition of $a_2/a_1 > \gamma'_{th2}$, otherwise $P_{2,AF}^{CCN} = 1$.

Remark 7. It is obvious that $P_{2,AF}^{ICN} < P_{2,AF}^{CCN}$, i.e., the outage behavior of D_2 in the cooperative NOMA system is enhanced by employing ICN protocol.

Proof. See Appendix C.

3.2.3. Diversity Analysis

(1) Diversity Order of D_1. When $\rho \longrightarrow \infty$, based on $K_1(x) \approx 1/x$ and $e^{-x} \approx 1 - x(x \longrightarrow 0)$, the asymptotic outage probability of D_1 for the AF-based CCN system is given as

$$P_{1,AF}^{CCN,\infty} = \frac{\theta'}{\Omega_{1,b}} \left(\frac{\theta'}{\Omega_{r,b}} + \frac{\theta'}{\Omega_{r,1}} \right). \tag{32}$$

Substituting (32) into (23), we can obtain $d_{1,AF}^{CCN} = 2$.

(2) Diversity Order of D_2. Similarly, the asymptotic outage probability of D_2 for the AF-based CCN system can be obtained as

$$P_{2,AF}^{CCN,\infty} = \frac{\tau'}{\Omega_{2,b}} \left(\frac{\tau'}{\Omega_{r,b}} + \frac{\tau'}{\Omega_{r,2}} \right). \tag{33}$$

Substituting (33) into (23), we can obtain $d_{2,AF}^{CCN} = 2$. It is noting that (32) and (33) are derived on the condition of $a_2/a_1 > \gamma'_{th2}$. One observation is that D_1 of CCN system can obtain higher diversity order than that of ICN system. Another observation is that D_2 of CCN and ICN systems obtains the same diversity order.

3.2.4. Throughput Analysis. Similarly, the throughput in delay-limited transmission for AF-based CCN system is given by

$$R_{AF}^{CCN} = \left(1 - P_{1,AF}^{CCN} \right) R_1 + \left(1 - P_{2,AF}^{CCN} \right) R_2. \tag{34}$$

where $P_{1,AF}^{CCN}$ and $P_{1,AF}^{CCN}$ are obtained from (29) and (31), respectively.

4. Outage Performance Evaluation for DF-Based NOMA System

In this section, the outage behaviors are characterized for DF-based ICN and CCN systems, which are detailed in the following.

4.1. Outage Performance Analysis with ICN Protocol. In this subsection, the outage behaviors of the DF-based ICN system are investigated.

4.1.1. Outage Probability of D_1. According to the ICN protocol, the outage probability of D_1 can be expressed as

$$P_{1,DF}^{ICN} = \Pr \left(\gamma_2 \geq \gamma_{th2} \right) \left[1 - \Pr \left(\gamma_{1,2} \geq \gamma_{th2}, \gamma_1 \geq \gamma_{th1} \right) \right] \\ + \Pr \left(\gamma_2 < \gamma_{th2} \right) P_{1,DF}^{CNT}, \tag{35}$$

where $P_{1,DF}^{CNT}$ is the outage probability of D_1 in the CNT mode, which can be given as

$$P_{1,DF}^{CNT} = \left[1 - \Pr \left(\gamma_{1,2} \geq \gamma'_{th2}, \gamma_1 \geq \gamma'_{th1} \right) \right] \\ \times \left[1 - \Pr \left(\gamma_{1,2}^{DF} \geq \gamma'_{th2}, \gamma_1^{DF} \geq \gamma'_{th1} \right) \right]. \tag{36}$$

Referring to the proof process of Theorem 1, the following theorem provides the outage probability of D_1 in the DF-based ICN system.

Theorem 8. *The closed-form expression of outage probability for D_1 in the DF-based ICN system is given as*

$$P_{1,DF}^{ICN} = \begin{cases} 1 - e^{-\tau/\Omega_{2,b}} e^{-\theta/\Omega_{1,b}} - \left(1 - e^{-\tau/\Omega_{2,b}} \right) \\ \times \left(e^{-\theta'/\Omega_{1,b}} + e^{-\theta'/\Omega_{r,1}} \left(1 - e^{-\theta'/\Omega_{1,b}} \right) \right), \frac{a_2}{a_1} > \gamma'_{th2} \\ 1 - e^{-\tau/\Omega_{2,b}} e^{-\theta/\Omega_{1,b}}, \gamma_{th2} < \frac{a_2}{a_1} \leq \gamma'_{th2} \\ 1, 0 < \frac{a_2}{a_1} \leq \gamma_{th2}. \end{cases} \tag{37}$$

4.1.2. Outage Probability of D_2. Similar to the case of AF-based NOMA system, the outage probability of D_2 can be expressed as

$$P_{2,DF}^{ICN} = \Pr \left(\gamma_2 < \gamma_{th2}, \gamma_2 < \gamma'_{th2}, \gamma_2^{DF} < \gamma'_{th2} \right). \tag{38}$$

As $\gamma_{th2} < \gamma'_{th2}$, (39) can be further rewritten as

$$P_{2,DF}^{ICN} = \Pr \left(\gamma_2 < \gamma_{th2}, \gamma_2^{DF} < \gamma'_{th2} \right). \tag{39}$$

Similarly, referring to the proof process of Theorem 2, the following theorem provides the outage probability of D_2 in the DF-based ICN system.

Theorem 9. *The closed-form expression of outage probability for D_2 in the DF-based ICN system is given as*

$$P_{2,DF}^{ICN} = \begin{cases} \left(1 - e^{-\tau/\Omega_{2,b}} \right) \left(1 - e^{-\tau'/\Omega_{r,2}} \right), \frac{a_2}{a_1} > \gamma'_{th2} \\ 1 - e^{-\tau/\Omega_{2,b}}, \gamma_{th2} < \frac{a_2}{a_1} \leq \gamma'_{th2} \\ 1, 0 < \frac{a_2}{a_1} \leq \gamma_{th2} \end{cases} \tag{40}$$

Similar to the AF-based ICN system, we only focus on the remaining region $a_2/a_1 > \gamma_{th2}$ in the following.

4.1.3. Diversity Analysis. Similarly, the outage probability in high SNR region is investigated in this section, and the diversity order achieved by the users can be obtained based on the above analytical results.

(1) Diversity Order of D_1. When $\rho \longrightarrow \infty$, according to $e^{-x} \approx 1 - x (x \longrightarrow 0)$, we can derive the asymptotic outage probability of D_1 for the DF-based ICN system in the following corollary.

Corollary 10. *The asymptotic outage probability of D_1 in the DF-based ICN system is given as*

$$P_{1,DF}^{ICN,\infty} = \begin{cases} \dfrac{\tau}{\Omega_{2,b}} + \dfrac{\theta}{\Omega_{1,b}} - \dfrac{\tau\theta}{\Omega_{1,b}\Omega_{2,b}} \\ \quad - \dfrac{\tau}{\Omega_{2,b}} \left[1 - \dfrac{\theta'^2}{\Omega_{1,b}\Omega_{r,1}} \right], \dfrac{a_2}{a_1} > \gamma'_{th2} \\ \dfrac{\tau}{\Omega_{2,b}} + \dfrac{\theta}{\Omega_{1,b}} - \dfrac{\tau}{\Omega_{2,b}}\dfrac{\theta}{\Omega_{1,b}}, \gamma_{th2} < \dfrac{a_2}{a_1} \le \gamma'_{th2} \end{cases} . \quad (41)$$

Substituting (41) into (23), we can obtain the diversity order of D_1 in the DF-based ICN system as

$$d_{1,DF}^{ICN} = 1, \quad (42)$$

Remark 11. The diversity order of D_1 in DF-based ICN system is one, which is the same as the diversity order of D_1 in AF-based ICN system.

(2) Diversity Order of D_2. Similarly, we can derive the asymptotic outage probability of D_2 for the DF-based ICN system in the following corollary.

Corollary 12. *The closed-form expression of outage probability for D_2 in the DF-based ICN system is given as*

$$P_{2,DF}^{ICN,\infty} = \begin{cases} \dfrac{\tau\tau'}{\Omega_{r,2}\Omega_{2,b}}, \dfrac{a_2}{a_1} > \gamma'_{th2} \\ \dfrac{\tau}{\Omega_{2,b}}, \gamma_{th2} < \dfrac{a_2}{a_1} \le \gamma'_{th2} \end{cases} . \quad (43)$$

Substituting (43) into (23), we can obtain the diversity order of D_2 in the DF-based ICN system as

$$d_{2,DF}^{ICN} = \begin{cases} 2, \dfrac{a_2}{a_1} > \gamma'_{th2} \\ 1, \gamma_{th2} < \dfrac{a_2}{a_1} \le \gamma'_{th2} \end{cases} . \quad (44)$$

Remark 13. The diversity order of D_2 in DF-based ICN system is the same as the diversity order in AF-based ICN system.

4.1.4. Throughput Analysis. Similarly, the throughput is considered in delay-limited transmission for DF-based ICN system, which can be given as

$$R_{DF}^{ICN} = \left(1 - P_{1,DF}^{ICN} \right) R_1 + \left(1 - P_{2,DF}^{ICN} \right) R_2, \quad (45)$$

where $P_{1,DF}^{ICN}$ and $P_{2,DF}^{ICN}$ are obtained from (37) and (40), respectively.

4.2. Outage Performance Analysis with CCN Protocol. As a benchmark for the outage behaviors of ICN system, the outage behaviors of the DF-based CCN system are investigated.

4.2.1. Outage Probability of D_1. According to the description of the CCN system, the expression of the outage probability for D_1 is the same with (36). Hence, the closed-form expression of outage probability for D_1 in the DF-based CCN system is given as

$$P_{1,DF}^{CCN} = 1 - e^{-\theta'/\Omega_{1,b}} - e^{-\theta'/\Omega_{r,1}} + e^{-\theta'/\Omega_{1,b}} e^{-\theta'/\Omega_{r,1}}, \quad (46)$$

where (46) is derived on the condition of $a_2/a_1 > \gamma'_{th2}$, otherwise $P_{1,DF}^{CCN} = 1$.

4.2.2. Outage Probability of D_2. According to the CCN protocol, the expression of the outage probability for D_2 can be given as

$$P_{2,DF}^{CCN} = \Pr\left(\gamma_2 < \gamma'_{th2} \right) \Pr\left(\gamma_2^{DF} < \gamma'_{th2} \right). \quad (47)$$

The closed-form expression of outage probability for D_2 in the DF-based CCN system is given as

$$P_{2,DF}^{CCN} = \left(1 - e^{-\tau'/\Omega_{2,b}} \right)\left(1 - e^{-\tau'/\Omega_{r,2}} \right), \quad (48)$$

where (48) is also derived on the condition of $a_2/a_1 > \gamma'_{th2}$, otherwise, $P_{2,DF}^{CCN} = 1$. Similar to AF-based NOMA system, it is obvious that the outage behavior of D_2 for ICN system outperforms CCN system.

4.2.3. Diversity Analysis

(1) Diversity Order of D_1. When $\rho \longrightarrow \infty$, based on $e^{-x} \approx 1 - x (x \longrightarrow 0)$, the asymptotic outage probability of D_1 for the DF-based CCN system is given as

$$P_{1,DF}^{CCN,\infty} \approx \frac{\theta'^2}{\Omega_{1,b}\Omega_{r,1}}. \quad (49)$$

Substituting (49) into (23), we can obtain $d_{1,DF}^{CCN} = 2$.

(2) Diversity Order of D_2. Similarly, the asymptotic outage probability of D_2 for the DF-based CCN system can be obtained as

$$P_{2,DF}^{CCN,\infty} \approx \frac{\tau'^2}{\Omega_{2,b}\Omega_{r,2}}. \quad (50)$$

Substituting (50) into (23), we can obtain $d_{2,\text{DF}}^{\text{CCN}} = 2$, where (49) and (50) are also derived on the condition of $a_2/a_1 > \gamma'_{th2}$, otherwise, $P_{2,\text{DF}}^{\text{CCN}} = 1$. It is obvious that the diversity orders of two uses for DF-based ICN and CCN systems are the same as that of the AF-based ICN and CCN systems, respectively.

Remark 14. When $\gamma_{th2} < a_2/a_1 \leq \gamma'_{th2}$, the outage behavior of two users for AF-based ICN system is the same as the DF-based ICN system, as the two users for AF-/DF-based ICN systems works in direct NOMA transmission mode. Furthermore, the outage behavior of two users for ICN system is superior to that of the CCN system when $\gamma_{th2} < a_2/a_1 \leq \gamma'_{th2}$, as the outage probability of two users for CCN system is one under the condition of $\gamma_{th2} < a_2/a_1 \leq \gamma'_{th2}$.

4.2.4. Throughput Analysis. Similarly, the throughput in delay-limited transmission for DF-based system with CCN protocol is given by

$$R_{\text{DF}}^{\text{CCN}} = \left(1 - P_{1,\text{DF}}^{\text{CCN}}\right)R_1 + \left(1 - P_{2,\text{DF}}^{\text{CCN}}\right)R_2. \quad (51)$$

where $P_{1,\text{DF}}^{\text{CCN}}$ and $P_{2,\text{DF}}^{\text{CCN}}$ are obtained from (46) and (48), respectively.

5. Numerical Results

In this section, simulation results are provided to evaluate the outage performance of users for AF/DF-based NOMA systems. Monte Carlo simulation parameters used in this section are given as follows. The power allocation coefficients [15] of D_1 and D_2 are $a_1 = 0.2$ and $a_2 = 0.8$ (In this paper, the power allocation factor is taken fixed value, optimizing the power allocation factor is capable of further improving the system secrecy performance, which motivates us to investigate optimal power allocation algorithms in our future work.), respectively. Additionally, the target rate [25] of D_1 and D_2 are $R_1 = 1.5$ BPCU and $R_2 = 0.5$ BPCU, respectively, where BPCU is an abbreviation for bit per channel use. We assume $\Omega_{i,j} = (d_{i,j}/d_0)^{-\alpha}$ [34], in which $d_{i,j}$ denotes the distance between i and j, d_0 is a reference distance, and α is a path loss exponent. The parameters correspond to $d_{1,b} = 50$ m, $d_{2,b} = 85$ m, $d_{r,b} = d_{r,1} = d_{r,2} = 63$ m for $d_0 = 40$ m, and $\alpha = 3$. Especially, α is the path loss exponent usually satisfying $2 \leq \alpha \leq 6$. To ensure the validity of numerical results, the numerical results of the outage probability with different path loss exponent are also presented in the following. Apart from the performance of AF/DF-based ICN system, the performance of CCN system is also considered as a benchmark for comparison, where the total communication process is completed in two slots. The BS sends information x_1 and x_2 to relay R in the first slot. In the second slot, R forwards the information x_1 and x_2 to D_1 and D_2, respectively. The above parameters are set on the general condition of $a_2/a_1 > \gamma'_{th2}$, as the outage probability of the two users for the CCN system is one when $a_2/a_1 \leq \gamma'_{th2}$. The following simulation results are first given on the general condition of $a_2/a_1 > \gamma'_{th2}$.
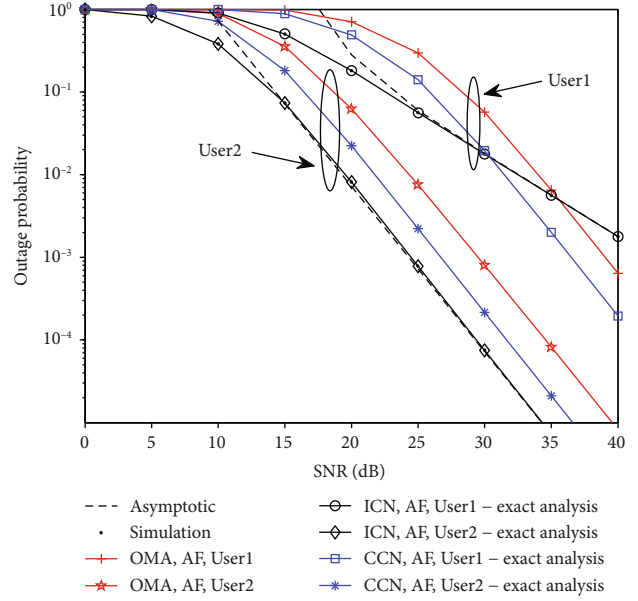

FIGURE 2: The outage probability versus transmit SNR for AF-based NOMA system with $a_1 = 0.2$, $a_2 = 0.8$, $R_1 = 1.5$ BPCU, $R_2 = 0.5$ BPCU, and $\alpha = 3$.

Figures 2 and 3 plot the outage probability of two users versus SNR for AF-based and DF-based ICN/CCN system, respectively. The black and blue curves represent the outage performance for ICN and CCN systems, respectively. In these two figures, the exact theoretical curves of D_1 and D_2 for AF- and DF-based ICN system are plotted according to (19), (22) and (37), (40), respectively. Obviously, the Monte Carlo simulation verifies the accuracy of our derivation. In addition, the blue curves of D_1 and D_2 for AF- and DF-based CCN system are plotted according to (29), (31) and (46), (48), respectively; which served as a benchmark for comparison. It is shown that the outage performance of D_2 for ICN system outperforms CCN system, which verifies the conclusion in Remark 7. We can observed that D_1 of the ICN system is able to achieve better outage performance in the low SNR region, since the possibility that the relay does not participate in communication is greater in high SNR. Besides, the red simulation curves represent the outage probability of D_1 and D_2 for cooperative NOMA systems, which is also used as a benchmark. We can observe that the outage behaviors of the cooperative NOMA system outperform NOMA systems. Furthermore, the asymptotic outage probability curves of D_1 and D_2 for AF- and DF-based ICN systems are plotted according to (24), (26) and (41), (43), respectively. As can be observed from the figures, the asymptotic curves approximate the exact curves well in the high SNR region.

Figure 4 plots the outage probability of two users versus SNR for ICN systems with different targeted data rates. One can observe that the outage probability of D_1 becomes worse with increasing R_1. The reason is that the threshold for decoding increases as R_1 increases. However, the outage behaviors of D_1 are hardly affected by R_2 adjustment. This phenomenon can be explained as that D_2 should be quickly connected with a low data rate, while D_1 should be served
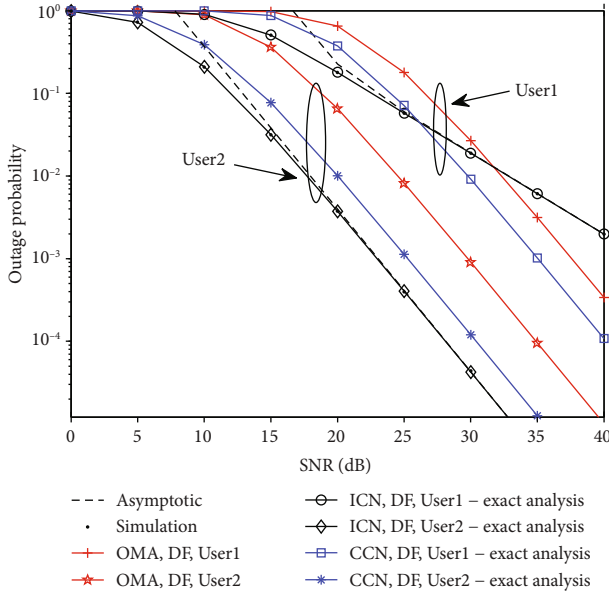
FIGURE 3: The outage probability versus transmit SNR for DF-based NOMA system with $a_1 = 0.2$, $a_2 = 0.8$, $R_1 = 1.5$ BPCU, $R_2 = 0.5$ BPCU, and $\alpha = 3$.
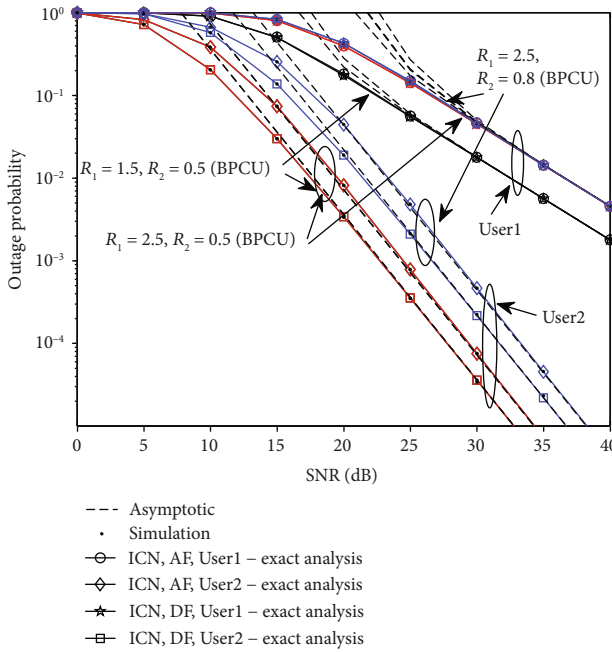

FIGURE 4: The outage probability versus transmit SNR for ICN system with different target rates, $a_1 = 0.2$, $a_2 = 0.8$, and $\alpha = 3$.
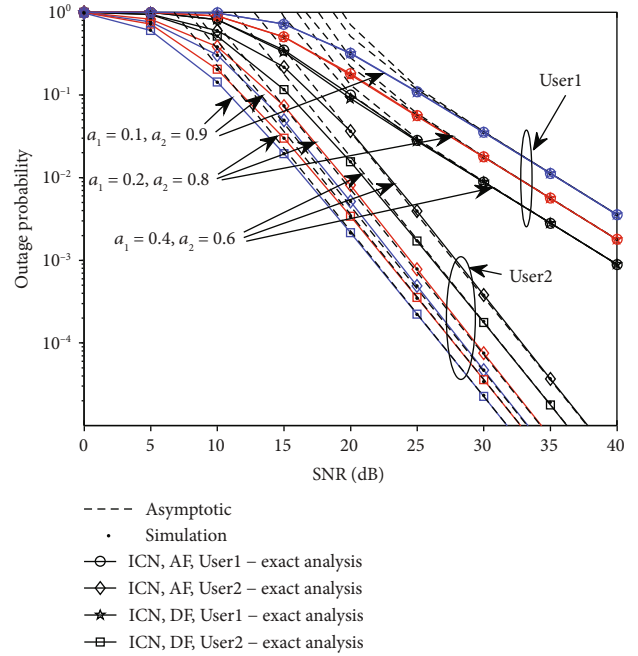

FIGURE 5: The outage probability versus transmit SNR for ICN system with different power allocation coefficients, $R_1 = 1.5$ BPCU, $R_2 = 0.5$ BPCU, and $\alpha = 3$.

tion is that the outage performance of D_2 for DF protocol is better than that of AF protocol. Because the signal x_1, which is considered as noise, is amplified while the AF relay amplifies the useful signal x_2; i.e., the enhancement of interference affects the decoding performance of the relay link between relay and D_2. The reason is that when the useful signal x_2 is amplified by AF relay, the signal x_1 as the noise signal is also amplified; i.e., the interference affects the decoding performance of D_2 with relaying link (the link between R and D_2).

Figure 5 plots the outage probability of two users versus SNR for ICN system with different power allocation coefficients. The black, red, and blue solid curves represent the outage probability of two users with $a_1 = 0.4$, $a_1 = 0.2$, and $a_1 = 0.1$, respectively. The figure shows that the outage behavior of D_1 deteriorates with the decrease of a_1. Moreover, the outage performance of D_2 is improved with the decrease of a_1 (i.e., the increase of a_2). Obviously, each user's performance will become better as the increase of the transmission power allocated to each user. In summary, the dynamic power allocation factor affects the outage behavior of two users. This phenomenon indicates that it is significant to select beneficial system parameters. Especially in NOMA communication systems, when users are generally classified into the nearby users and distant users by their quality of service, where the nearby users require a high date rate, and the distant users may only require a predetermined low data rate. Without loss of generality, it is best to assign a higher power to the distance user in order to ensure the higher priority (higher communication reliability) of the distance user.

As a further development, Figure 6 plots the outage probability of two users versus SNR for ICN system with different

opportunistically according to the definition of the cooperative NOMA, i.e., D_2 is easy to be successfully decoded. Therefore, the outage performance of D_1 can successfully decode the information of D_2, and it will not be affected by R_2 adjustment. Besides, the outage behaviors of D_2 deteriorates as R_2 increases, but it does not depend on changes in R_1, which verifies the derivation in (22) and (40). This is due to the fact that the information of D_1 is not decoded and is regarded as noise when D_2 decoding its own message. Another observa-
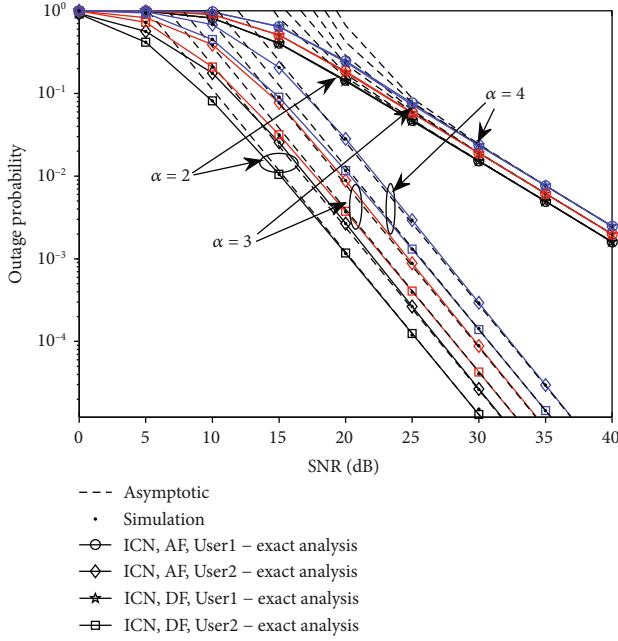
FIGURE 6: The outage probability versus transmit SNR for ICN system with different path loss exponent, $a_1 = 0.2$, $a_2 = 0.8$, $R_1 = 1.5$ BPCU, and $R_2 = 0.5$ BPCU.

FIGURE 7: The outage probability versus transmit SNR for ICN system with different distance $d_{r,b}$, $a_1 = 0.2$, $a_2 = 0.8$, $R_1 = 1.5$ BPCU, $R_2 = 0.5$ BPCU, and $\alpha = 3$.

path loss exponent. The black, red, and blue solid curves represent the outage probability of two users with $\alpha = 2$, $\alpha = 3$, and $\alpha = 4$, respectively. It is obvious that the performance of two users for the ICN system is strongly affected by the path loss exponent. As shown in Figure 6, the performance of the ICN system deteriorates as the path loss exponent increases. However, it is worth noting that the curves with different path loss exponent have the same slopes, which verifies the conclusions in Remark 4, Remark 6, Remark 11, and Remark 13, i.e., the diversity orders of D_1 are one, and the diversity orders of D_2 are two under the condition of $a_2/a_1 > \gamma'_{th2}$.

Figure 7 plots the outage probability of two users versus SNR for ICN system with different distance $d_{r,b}$. One can observe that the outage behavior of D_1 is hardly affected by the distance between BS and relay. This is mainly due to the performance of near user D_1 which mainly depends on the direct link (the link between BS and D_1) when $a_2/a_1 > \gamma'_{th2}$. We also can observe that the outage behavior of D_2 for AF relaying case deteriorates as the distance $d_{r,b}$ becomes larger. The reason is that $E\{|h_{r,b}|^2\}$ becomes smaller when the $d_{r,b}$ becomes larger, which leads to the received SINR at D_2 with relaying link decrease in AF relaying case according to (11). In contrast, the performance of D_2 for DF relaying case is almost unchanged, which verifies the derivation in equation (40). The reason is that we have assumed the relay is capable of decoding the two users's information successfully for simplicity.

Figure 8 plots the system throughput versus SNR in delay-limited transmission mode for ICN and CCN systems, which are plotted according to (28), (34), (45), and (51), respectively. We can observe that the throughput of the ICN system is higher than that of the CCN system in low SNR region, since
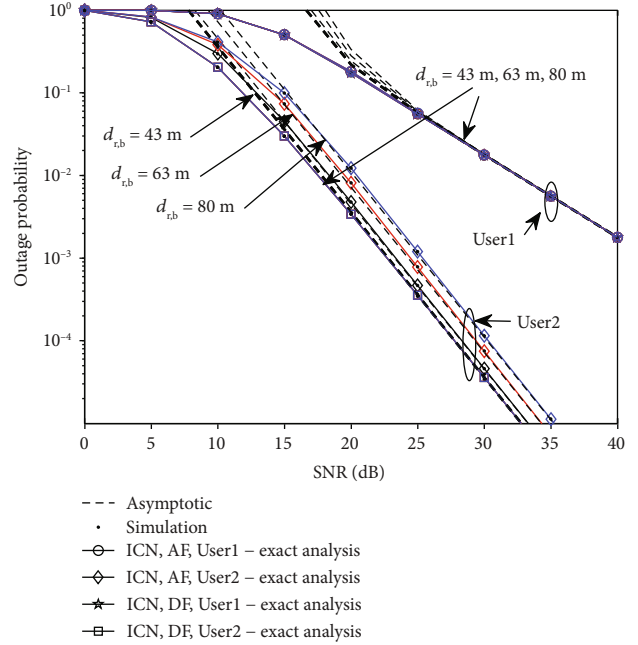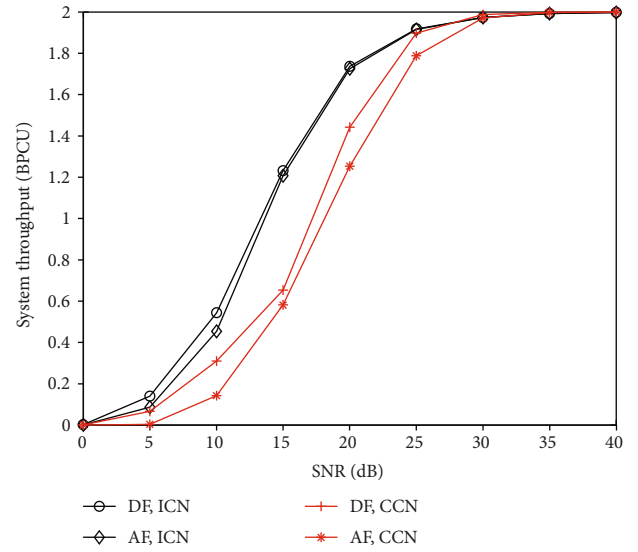

FIGURE 8: The system throughput versus transmit SNR for ICN and CCN systems with $a_1 = 0.2$, $a_2 = 0.8$, $R_1 = 1.5$ BPCU, $R_2 = 0.5$ BPCU, and $\alpha = 3$.

the outage performance of the users for the ICN system is better than that of the CCN system. It is noting that this superiority is more pronounced at low SNR. Another observation is that throughput ceilings exist in the ICN and CCN systems in the high SNR region. The reason is that the outage probability tends zero, and the throughput almost depends on the target data rate in the high SNR region.

The above simulation results are under general condition $a_2/a_1 > \gamma'_{th2}$. To verify the accuracy of the analysis under special condition $\gamma_{th2} < a_2/a_1 \leq \gamma'_{th2}$, the power allocation
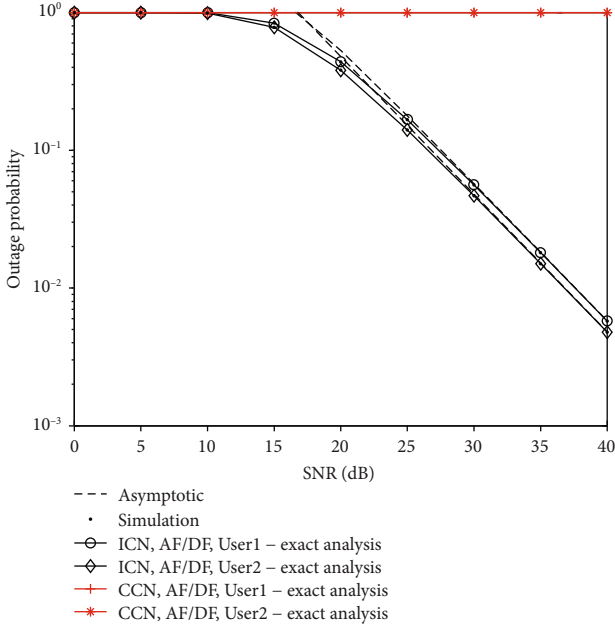
FIGURE 9: The outage probability versus transmit SNR for AF-/DF-based ICN and CCN systems with $a_1 = 0.4$, $a_2 = 0.6$, $R_1 = 1.5$ BPCU, $R_2 = 1$ BPCU, and $\alpha = 3$.

coefficients of D_1 and D_2 are reset to $a_1 = 0.4$ and $a_2 = 0.6$, respectively. Simultaneously, the target rates of D_1 and D_2 are reset to $R_1 = 1.5$ BPCU and $R_2 = 1$ BPCU, respectively. The remaining parameters are unchanged. Figure 9 plots the outage probability of two users versus SNR for AF-/DF-based ICN and CCN systems when $\gamma_{th2} < a_2/a_1 \leq \gamma'_{th2}$. As the conclusion in Remark 14, the outage behavior of two users for AF-based ICN system is the same as the DF-based ICN system. The black and red curves represent the outage performance for ICN and CCN systems, respectively. As can be observed from the figures, the Monte Carlo simulation verifies the accuracy of our derivation. One can observe that the asymptotic curves approximate the exact curves well in the high SNR region. It is worth noting that the curves have the same slopes, which verifies the conclusions in Remark 4, Remark 6, Remark 11, and Remark 13, i.e., the diversity order of D_1 for ICN system is one, and the diversity order of D_2 for ICN system under the condition of $\gamma_{th2} < a_2/a_1 \leq \gamma'_{th2}$ is also one. Obviously, when $\gamma_{th2} < a_2/a_1 \leq \gamma'_{th2}$, the outage behavior of two users for ICN system is superior to that of CCN system, as the outage probability of two users for CCN system is one, which verifies the conclusions in Remark 14. Similarly, the system throughput in delay-limited transmission mode for ICN system is also higher than that of the CCN system when $\gamma_{th2} < a_2/a_1 \leq \gamma'_{th2}$. The rest of the performance analysis, which is similar to the performance analysis under general condition $a_2/a_1 > \gamma'_{th2}$, will not be discussed.

6. Conclusion

In this paper, the ICN system has investigated insightfully. The outage behavior of the proposed system has been charac-

terized based on AF and DF relaying, respectively. New closed form expressions of outage probability for two users have been derived. Based on the analytical results, the diversity orders achieved by the nearby and distant users were obtained. Additionally, the performance of the CCN system has also been analyzed, which has been served as a benchmark for the purpose of comparison. Numerical results have verified that the distant user of the ICN system achieved better outage behavior than that of CCN system. The nearby user for the ICN system was capable of achieving better performance than that of CCN system in the low SNR region, and the outage performance of distant user for DF-based ICN system was superior to AF-based ICN system, when the system worked in cooperative NOMA transmission mode. Furthermore, the throughput of the ICN system was higher than that of CCN system in the low SNR region.

Appendix

A. Proof of Theorem 1

The expression (17) can be rewritten as

$$P_{1,\text{AF}}^{\text{ICN}} = 1 - \underbrace{\Pr\left(\gamma_2 \geq \gamma_{th2}\right)}_{Q_1} \underbrace{\Pr\left(\gamma_{1,2} \geq \gamma_{th2}, \gamma_1 \geq \gamma_{th1}\right)}_{Q_2} \tag{A.1}$$
$$- \Pr\left(\gamma_2 < \gamma_{th2}\right)\left(1 - P_{1,\text{AF}}^{\text{CCN}}\right).$$

Combining (6) and Q_1, Q_1 can be rewritten as

$$Q_1 = \Pr\left(\frac{a_2\rho_s|h_{2,b}|^2}{a_1\rho_s|h_{2,b}|^2 + 1} \geq \gamma_{th2}\right)$$
$$= \Pr\left(|h_{2,b}|^2 \geq \frac{\gamma_{th2}}{\rho_s(a_2 - a_1\gamma_{th2})}\right) = e^{-\tau/\Omega_{2,b}}, \tag{A.2}$$

where $\tau = \gamma_{th2}/(\rho_s(a_2 - a_1\gamma_{th2}))$ with $a_2 > a_1\gamma_{th2}$. Note that (A.2) is derived on the condition of $a_2 > a_1\gamma_{th2}$, otherwise, $Q_1 = 0$.

Similarly, combining (4), (5), and Q_2, Q_2 can be rewritten as

$$Q_2 = \Pr\left(\frac{a_2\rho_s|h_{1,b}|^2}{a_1\rho_s|h_{1,b}|^2 + 1} \geq \gamma_{th2}, a_1\rho_s|h_{1,b}|^2 \geq \gamma_{th1}\right)$$
$$= \Pr\left(|h_{1,b}|^2 \geq \frac{\gamma_{th2}}{\rho_s(a_2 - a_1\gamma_{th2})}, |h_{1,b}|^2 \geq \frac{\gamma_{th1}}{a_1\rho_s}\right) = e^{-\theta/\Omega_{1,b}}, \tag{A.3}$$

where $\theta = \max(\tau, \sigma)$ and $\sigma = \gamma_{th1}/a_1\rho_s$ with $a_2 > a_1\gamma_{th2}$. Note that (A.3) is derived on the condition of $a_2 > a_1\gamma_{th2}$, otherwise, $Q_2 = 0$.

Then, we derive the closed-form expression of $P_{1,\text{AF}}^{\text{CCN}}$, i.e., the closed-form expression of (18), which can be rewritten as

$$
P_{1,\text{AF}}^{\text{CCN}} = \left[1 - \underbrace{\Pr\left(\gamma_{1,2} \geq \gamma'_{th2}, \gamma_1 \geq \gamma'_{th1}\right)}_{Q_3} \right]
$$
$$
\times \left[1 - \underbrace{\Pr\left(\gamma_{1,2}^{AF} \geq \gamma'_{th2}, \gamma_1^{AF} \geq \gamma'_{th1}\right)}_{Q_4} \right]. \tag{A.4}
$$

Combining (4), (5), and Q_3, applying some algebraic manipulations, Q_3 can be rewritten as

$$
Q_3 = \Pr\left(\frac{a_2 \rho_s |h_{1,b}|^2}{a_1 \rho_s |h_{1,b}|^2 + 1} \geq \gamma'_{th2}, a_1 \rho_s |h_{1,b}|^2 \geq \gamma'_{th1} \right)
$$
$$
= \Pr\left(|h_{1,b}|^2 \geq \frac{\gamma'_{th2}}{\rho_s \left(a_2 - a_1 \gamma'_{th2}\right)}, |h_{1,b}|^2 \geq \frac{\gamma'_{th1}}{a_1 \rho_s} \right) \tag{A.5}
$$
$$
= e^{-\theta'/\Omega_{1,b}},
$$

where $\theta' = \max(\tau', \sigma')$ and $\tau' = \gamma'_{th2}/(\rho_s(a_2 - a_1\gamma'_{th2}))$, $\sigma' = \gamma'_{th1}/a_1\rho_s$ with $a_2 > a_1\gamma'_{th2}$. Note that (A.3) is derived on the condition of $a_2 > a_1\gamma'_{th2}$, otherwise, $Q_3 = 0$.

Similarly, Combining (9), (10), and Q_4, Q_4 can be rewritten as

$$
Q_4 = \Pr\left(\frac{a_2 \rho_s |h_{r,b}|^2 |h_{r,1}|^2}{a_1 \rho_s |h_{r,b}|^2 |h_{r,1}|^2 + |h_{r,1}|^2 + |h_{r,b}|^2 + (1/\rho_s)} \right.
$$
$$
\left. \geq \gamma'_{th2}, \frac{a_1 \rho_s |h_{r,b}|^2 |h_{r,1}|^2}{|h_{r,1}|^2 + |h_{r,b}|^2 + (1/\rho_s)} \geq \gamma'_{th1} \right)
$$
$$
= \Pr\left(|h_{r,1}|^2 \geq \frac{\theta'\left(\rho_s |h_{r,b}|^2 + 1\right)}{\rho_s\left(|h_{r,b}|^2 - \theta'\right)}, |h_{r,b}|^2 \geq \theta' \right)
$$
$$
= \int_0^\infty \frac{1}{\Omega_{r,b}} e^{-x+\theta'/\Omega_{r,b}} e^{-\theta'\left(\rho_s(x+\theta')+1\right)/x\rho_s\Omega_{r,1}} dx
$$
$$
= e^{-\theta'/\Omega_{r,b} - \theta'/\Omega_{r,1}} \sqrt{\frac{4\theta'\left(\rho_s\theta'+1\right)}{\rho_s\Omega_{r,1}\Omega_{r,b}}} K_1\left(\sqrt{\frac{4\theta'\left(\rho_s\theta'+1\right)}{\rho_s\Omega_{r,1}\Omega_{r,b}}} \right), \tag{A.6}
$$

where (A.6) is derived according to ([35], Eq.(3.324.1)), it is noting that (A.5) is derived on the condition of $a_2 > a_1\gamma'_{th2}$, otherwise, $Q_4 = 0$.

Substituting (A.2), (A.3), (A.4), and (A.5) into (A.1), we can obtain (19). The proof is completed.

B. Proof of Theorem 2

We can rewrite (21) as

$$
P_{2,\text{AF}}^{ICN} = \underbrace{\Pr\left(\gamma_2^{AF} < \gamma'_{th2}\right)}_{\Lambda_1} \underbrace{\Pr\left(\gamma_2 < \gamma_{th2}\right)}_{\Lambda_2}. \tag{B.1}
$$

Substituting (11) into Λ_1, after some algebraic manipulations, Λ_1 can be rewritten as

$$
\Lambda_1 = \Pr\left(|h_{r,b}|^2 < \tau' \right)
$$
$$
+ P_r\left(|h_{r,2}|^2 < \frac{\tau'\left(\rho_s |h_{r,b}|^2 + 1\right)}{\rho_s\left(|h_{r,b}|^2 - \tau'\right)}, |h_{r,b}|^2 \geq \tau' \right)
$$
$$
= \left(1 - e^{-\tau'/\Omega_{r,b}} \right) + \int_{\tau'}^\infty \frac{1}{\Omega_{r,b}} e^{-y/\Omega_{r,b}} dy
$$
$$
- \int_{\tau'}^\infty \frac{1}{\Omega_{r,b}} e^{-y/\Omega_{r,b}} e^{-\tau'(\rho_s y + 1)/\rho_s(y-\tau')\Omega_{r,2}} dy
$$
$$
= 1 - e^{-\tau'/\Omega_{r,b}} e^{-\tau'/\Omega_{r,2}} \frac{1}{\Omega_{r,b}} \int_0^\infty e^{-x/\Omega_{r,b}} e^{-\tau'\left(\rho_s\tau'+1\right)/\rho_s x\Omega_{r,2}} dy
$$
$$
= 1 - e^{-\tau'/\Omega_{r,b}} e^{-\tau'/\Omega_{r,2}} \sqrt{\frac{4\tau'\left(\rho_s\tau'+1\right)}{\rho_s\Omega_{r,2}\Omega_{r,b}}}
$$
$$
\times K_1\left(\sqrt{\frac{4\tau'\left(\rho_s\tau'+1\right)}{\rho_s\Omega_{r,2}\Omega_{r,b}}} \right), \tag{B.2}
$$

where ((B.2) is derived according to ([35], Eq.(3.324.1)), it is noting that (B.2) is derived on the condition of $a_2 > a_1\gamma'_{th2}$, otherwise, $\Lambda_1 = 1$.

Substituting (6) into Λ_2, the closed-form expression of Λ_2 can be given as

$$
\Lambda_2 = 1 - e^{-\tau/\Omega_{2,b}}. \tag{B.3}
$$

Note that (B.3) is derived on the condition of $a_2 > a_1\gamma_{th2}$, otherwise, $\Lambda_2 = 1$.

Substituting (B.2) and (B.3) into (B.1), we can obtain (22). The proof is completed.

C. Proof of Remark 7

We have obtain the outage probability of D_2 for AF-based ICN system as shown in (21), which can be rewritten as

$$
P_{2,\text{AF}}^{ICN} = \Pr\left(\gamma_2 < \gamma_{th2}\right) P_r\left(\gamma_2^{AF} < \gamma'_{th2}\right). \tag{C.1}
$$

Since $\gamma_{th2} = 2^{R_2} - 1$, $\gamma'_{th2} = 2^{2R_2} - 1$, and $R_2 > 0$, we can obtain

$$
\gamma_{th2} < \gamma'_{th2}. \tag{C.2}
$$

And we can further obtain that

$$\Pr\left(\gamma_2 < \gamma_{th2}\right) < \Pr\left(\gamma_2 < \gamma_{th2}'\right). \qquad \text{(C.3)}$$

According to (C.3), compared to (C.1) and the outage probability $P_{2,AF}^{CCN}$ in (31), we can obtain $P_{2,AF}^{ICN} < P_{2,AF}^{CCN}$. The proof is completed.

Data Availability

If the data are needed during the process of reviewing or publishing, they are provided by the author Zhenling Wang (Email: wangzhenling@shu.du.cn).

Conflicts of Interest

The authors declare that they have no conflicts of interest.

Acknowledgments

References

[1] K. David and H. Berndt, "6G vision and requirements: is there any need for beyond 5G?," *IEEE Vehicular Technology Magazine*, vol. 13, no. 3, pp. 72–80, 2018.

[2] Y. Cai, Z. Qin, F. Cui, G. Y. Li, and J. A. McCann, "Modulation and multiple access for 5G networks," *IEEE Communications Surveys & Tutorials*, vol. 20, no. 1, pp. 629–646, 2018.

[3] Z. Ding, X. Lei, G. K. Karagiannidis, R. Schober, J. Yuan, and V. K. Bhargava, "A survey on non-orthogonal multiple access for 5G networks: research challenges and future trends," *IEEE Journal on Selected Areas in Communications*, vol. 35, no. 10, pp. 2181–2195, 2017.

[4] T. M. Cover and J. A. Thomas, *Elements of Information Theory*, Wiley, 1991.

[5] Y. Liu, Z. Qin, M. Elkashlan, Z. Ding, A. Nallanathan, and L. Hanzo, "Nonorthogonal multiple access for 5G and beyond," *Proceedings of the IEEE*, vol. 105, no. 12, pp. 2347–2381, 2017.

[6] Z. Ding, Y. Liu, J. Choi et al., "Application of non-orthogonal multiple access in LTE and 5G networks," *IEEE Communications Magazine*, vol. 55, no. 2, pp. 185–191, 2017.

[7] X. Yue, Z. Qin, Y. Liu, S. Kang, and Y. Chen, "A unified framework for non-orthogonal multiple access," *IEEE Transactions on Communications*, vol. 66, no. 11, pp. 5346–5359, 2018.

[8] Z. Ding, Z. Yang, P. Fan, and H. V. Poor, "On the performance of non-orthogonal multiple access in 5G systems with randomly deployed users," *IEEE Signal Processing Letters*, vol. 21, no. 12, pp. 1501–1505, 2014.

[9] Z. Yang, Z. Ding, P. Fan, and G. K. Karagiannidis, "On the performance of non-orthogonal multiple access systems with partial channel information," *IEEE Transactions on Communications*, vol. 64, no. 2, pp. 654–667, 2016.

[10] P. Xu, Y. Yuan, Z. Ding, X. Dai, and R. Schober, "On the outage performance of non-orthogonal multiple access with 1-bit feedback," *IEEE Transactions on Wireless Communications*, vol. 15, no. 10, pp. 6716–6730, 2016.

[11] Y. Liu, Z. Qin, M. Elkashlan, Y. Gao, and L. Hanzo, "Enhancing the physical layer security of non-orthogonal multiple access in large-scale networks," *IEEE Transactions on Wireless Communications*, vol. 16, no. 3, pp. 1656–1672, 2017.

[12] X. Yue, Y. Liu, Y. Yao, X. Li, R. Liu, and A. Nallanathan, "Secure communications in a unified non-orthogonal multiple access framework," *IEEE Transactions on Wireless Communications*, p. 1, 2020.

[13] Z. Ding, M. Peng, and H. V. Poor, "Cooperative non-orthogonal multiple access in 5G systems," *IEEE Communications Letters*, vol. 19, no. 8, pp. 1462–1465, 2015.

[14] Z. Zhang, Z. Ma, M. Xiao, Z. Ding, and P. Fan, "Full-duplex device-to-device-aided cooperative nonorthogonal multiple access," *IEEE Transactions on Vehicular Technology*, vol. 66, no. 5, pp. 4467–4471, 2017.

[15] X. Yue, Y. Liu, S. Kang, A. Nallanathan, and Z. Ding, "Exploiting full/half-duplex user relaying in NOMA systems," *IEEE Transactions on Communications*, vol. 66, no. 2, pp. 560–575, 2018.

[16] Z. Wang, X. Yue, and Z. Peng, "Full-duplex user relaying for NOMA system with self-energy recycling," *IEEE Access*, vol. 6, pp. 67057–67069, 2018.

[17] X. Li, J. Li, and L. Li, "Performance analysis of impaired swipt NOMA relaying networks over imperfect weibull channels," *IEEE Systems Journal*, vol. 14, no. 1, pp. 669–672, 2020.

[18] X. Liang, Y. Wu, D. W. K. Ng, Y. Zuo, S. Jin, and H. Zhu, "Outage performance for cooperative NOMA transmission with an AF relay," *IEEE Communications Letters*, vol. 21, no. 11, pp. 2428–2431, 2017.

[19] X. Yue, Y. Liu, S. Kang, and A. Nallanathan, "Performance analysis of NOMA with fixed gain relaying over Nakagami-m fading channels," *IEEE Access*, vol. 5, pp. 5445–5454, 2017.

[20] T. M. C. Chu and H. Zepernick, "Performance of a non-orthogonal multiple access system with full-duplex relaying," *IEEE Communications Letters*, vol. 22, no. 10, pp. 2084–2087, 2018.

[21] X. Li, Q. Wang, H. Peng et al., "A unified framework for HS-UAV NOMA networks: performance analysis and location optimization," *IEEE Access*, vol. 8, pp. 13329–13340, 2020.

[22] D. Wan, M. Wen, F. Ji, Y. Liu, and Y. Huang, "Cooperative NOMA systems with partial channel state information over Nakagami- m fading channels," *IEEE Transactions on Communications*, vol. 66, no. 3, pp. 947–958, 2018.

[23] X. Wang, M. Jia, I. W. Ho, Q. Guo, and F. C. M. Lau, "Exploiting full-duplex two-way relay cooperative non-orthogonal multiple access," *IEEE Transactions on Communications*, vol. 67, no. 4, pp. 2716–2729, 2019.

[24] X. Li, M. Liu, C. Deng, P. T. Mathiopoulos, Z. Ding, and Y. Liu, "Full-duplex cooperative NOMA relaying systems with I/Q imbalance and imperfect SIC," *IEEE Wireless Communications Letters*, vol. 9, no. 1, pp. 17–20, 2019.

[25] X. Yue, Y. Liu, S. Kang, A. Nallanathan, and Z. Ding, "Spatially random relay selection for full/half-duplex cooperative NOMA networks," *IEEE Transactions on Communications*, vol. 66, no. 8, pp. 3294–3308, 2018.

[26] Z. Wang and Z. Peng, "Secrecy performance analysis of relay selection in cooperative NOMA systems," *IEEE Access*, vol. 7, pp. 86274–86287, 2019.

[27] X. Li, J. Li, Y. Liu, Z. Ding, and A. Nallanathan, "Residual transceiver hardware impairments on cooperative NOMA networks," *IEEE Transactions on Wireless Communications*, vol. 19, no. 1, pp. 680–695, 2019.

[28] X. Tang, K. An, K. Guo, Y. Huang, and S. Wang, "Outage analysis of non-orthogonal multiple access-based integrated satellite-terrestrial relay networks with hardware impairments," *IEEE Access*, vol. 7, pp. 141258–141267, 2019.

[29] X. Tang, K. An, K. Guo et al., "On the performance of two-way multiple relay non-orthogonal multiple access-based networks with hardware impairments," *IEEE Access*, vol. 7, pp. 128896–128909, 2019.

[30] J. N. Laneman, D. N. C. Tse, and G. W. Wornell, "Cooperative diversity in wireless networks: efficient protocols and outage behavior," *IEEE Transactions on Information Theory*, vol. 50, no. 12, pp. 3062–3080, 2004.

[31] S. S. Ikki and M. H. Ahmed, "Performance analysis of incremental relaying cooperative-diversity networks over rayleigh fading channels," *IET Communications*, vol. 5, no. 3, pp. 337–349, 2011.

[32] "Performance analysis of cooperative diversity with incremental best-relay technique over rayleigh fading channels," *IEEE Transactions on Communications*, vol. 59, no. 8, pp. 2152–2161, 2011.

[33] G. Li, D. Mishra, and H. Jiang, "Cooperative noma with incremental relaying: performance analysis and optimization," *IEEE Transactions on Vehicular Technology*, vol. 67, no. 11, pp. 11291–11295, 2018.

[34] J. Kim and I. Lee, "Non-orthogonal multiple access in coordinated direct and relay transmission," *IEEE Wireless Communications Letters*, vol. 19, no. 11, pp. 2037–2040, 2015.

[35] I. S. Gradshteyn and I. M. Ryzhik, *Table of Integrals, Series and Products*, Academic Press, New York, NY, USA, 6th edition, 2000.